University of Groningen

Molecular line tracers of high-mass star forming regions

Nagy, Zsofia

IMPORTANT NOTE: You are advised to consult the publisher's version (publisher's PDF) if you wish to cite from it. Please check the document version below.

Document Version
Publisher's PDF, also known as Version of record

Publication date:
2013

Link to publication in University of Groningen/UMCG research database

Citation for published version (APA):
Nagy, Z. (2013). *Molecular line tracers of high-mass star forming regions*. s.n.

Copyright
Other than for strictly personal use, it is not permitted to download or to forward/distribute the text or part of it without the consent of the author(s) and/or copyright holder(s), unless the work is under an open content license (like Creative Commons).

The publication may also be distributed here under the terms of Article 25fa of the Dutch Copyright Act, indicated by the "Taverne" license. More information can be found on the University of Groningen website: https://www.rug.nl/library/open-access/self-archiving-pure/taverne-amendment.

Take-down policy
If you believe that this document breaches copyright please contact us providing details, and we will remove access to the work immediately and investigate your claim.

Downloaded from the University of Groningen/UMCG research database (Pure): http://www.rug.nl/research/portal. For technical reasons the number of authors shown on this cover page is limited to 10 maximum.

Download date: 05-05-2023

rijksuniversiteit
groningen

Molecular line tracers of high-mass star forming regions

Proefschrift

ter verkrijging van het doctoraat in de
Wiskunde en Natuurwetenschappen
aan de Rijksuniversiteit Groningen
op gezag van de
RectorMagnificus, dr. E. Sterken,
in het openbaar te verdedigen op
maandag 23 september 2013
om 14.30 uur

door

Zsófia Nagy
geboren op 3 juli 1986
te Miskolc, Hongarije

Promotor: Prof. dr. F.F.S. van der Tak

Beoordelingscommissie: Prof. dr. G.A. Fuller
Prof. dr. M. Gerin
Prof. dr. I. Kamp

ISBN 978-90-367-6378-3
ISBN 978-90-367-6379-0 (electronic version)

Front cover - Background: ^{13}CO 3-2 integrated intensity map of the Orion Bar and Ridge region observed with the James Clerk Maxwell Telescope (JCMT). The data are from the JCMT archive (`http://www1.cadc-ccda.hia-iha.nrc-cnrc.gc.ca/jcmt`). The CH$^+$ J=1-0 spectra observed with *Herschel*/HIFI analysed in this thesis are overlaid toward the observed positions (CO$^+$ peak of the Orion Bar and Orion S).

Back cover - Background: Image of the Orion Nebula made with the NASA/ESA Hubble Space Telescope. Credit: *Image Data* - Hubble Legacy Archive (`http://hla.stsci.edu`), *Processing* - Robert Gendler. The molecules in the foreground are from the website of Wikimedia Commons (`https://commons.wikimedia.org/wiki`). The molecules (from top to bottom): CH_3OH, SO_2, and H_2CO. The foreground pictures apart from the molecules are based on photos by the author.

Contents

1

Introduction

1.1 Star formation and the interstellar medium

The interstellar medium (ISM) is a key component of a galaxy as it is the place of birth of future generations of stars. The ISM itself is dependent on earlier generations of stars that influence its chemical composition and physical structure over the life-time of galaxies (see reviews by Draine 2011, Tielens 2005). Star-formation occurs in molecular clouds consisting of atoms, molecules, ions, and dust. Its structure and chemical composition is affected by previous populations of stars through supernova explosions, outflows, stellar winds, and irradiation. Star-formation in molecular clouds can occur in isolation (typically low-mass stars, $M \lesssim 8\ M_{\odot}$) or in clusters (typically high-mass stars, $M \gtrsim 8\ M_{\odot}$). The type of star-formation set in a cloud is dependent on its physical parameters (e.g. Kennicutt & Evans 2012, and references therein). Dark molecular clouds are ideal sites for the formation of low-mass stars. These clouds range from globules with sizes of a few pc up to dark clouds or cloud complexes with sizes of $\gtrsim$10 pc. The formation of massive stars typically occurs in the densest parts of $\sim$40 pc size Giant Molecular Clouds (GMCs). These star-forming sites and their properties are the subject of the current thesis. The young massive stars formed in GMCs largely affect their physical and chemical structure through their radiation and mechanical feedback (such as outflows or stellar winds). We focus on these feedback effects in this thesis, based on molecular line surveys.

In this chapter we give a general overview of the interstellar medium (Section 1.1.1) and star-formation (Sect. 1.1.2), focusing on the formation of high-mass stars (Sect. 1.1.3). We discuss the structure of high-mass star forming regions with two examples that are analysed in the thesis. We discuss commonly used tools for the interpretation of molecular line observations, such as radiative transfer and chemical models (Sect. 1.2). We give a summary of the most important results of the thesis in Section 1.3.

1.1.1 Phases of the interstellar medium

The gas in the ISM has different phases including ionized, neutral atomic, and molecular (Draine 2011, Tielens 2005 and references therein). The *coronal gas* represents a hot ($T \sim 10^5 - 10^6$ K) and diffuse ($n = 0.003$ cm^{-3}) phase of the ISM. It is traced by optical / UV absorption lines of highly ionized species such as O VI, N V, C IV; and X-ray emission.

The warm ionized medium (WIM) corresponds to discrete H^+ regions with $T \sim 8000$ K and $n \sim 0.1$ cm^{-3} that can be traced by hydrogen recombination lines, optical / ultraviolet absorption lines of ionized species, and the dispersion of pulsar signals as passing through the WIM. Apart from the WIM, HII gas can also be found around hot massive O-type stars (HII regions). HII regions have average densities of $n_{\rm H} \sim 10^4$ cm^{-3} and their lifetimes are around 3-10 Myr.

The *neutral atomic gas* includes the cold neutral medium (CNM) corresponding to clouds with 100 K temperatures and the warm neutral medium (WNM) corresponding to intercloud gas at $T = 8000$ K. It is observable through the 21 cm line of neutral hydrogen and by optical/UV absorption lines toward background stars.

The *molecular phase* of the ISM is most commonly observed in rotational transitions of CO. Around 180 molecules have been detected up to now in the ISM and in circumstellar shells, based on the Cologne Database for Molecular Spectroscopy[1] (CDMS, Müller et al. 2005). Dense molecular material is present in GMCs with properties of $T = 10 - 50$ K, $n_{\rm H} \sim 10^3 - 10^6$ cm^{-3}, typical sizes of $D = 40$ pc and masses of $M = 4 \times 10^5$ $M_\odot$. Parts of GMCs and variations in physical parameters are discussed in more details in Sect. 1.1.3. Molecular gas can also be found in diffuse clouds that have sufficient densities and column densities so that H_2 molecules can be abundant. These clouds have temperatures of ∼50 K and densities of $n_{\rm H}$ ∼100 cm^{-3}. The pressure of diffuse clouds also has non-thermal contributions as a result of supersonic turbulence. See Hennebelle & Falgarone (2012) for a recent review on the structure of molecular clouds in relation with turbulence.

Interstellar dust represents another component of the ISM (e.g. Draine 2003 and references therein). Evidence for the presence of interstellar dust is given by its absorption and scattering of stellar radiation. These effects result in the reddening, extinction, and polarization of stellar light at optical and UV wavelengths. Based on the wavelength dependence of interstellar reddening, the size distribution of dust grains can be described as $n(a) \sim a^{-3.5}$, which ranges from ≃3000 Å to ∼5 Å (molecular domain). Interstellar dust is observable

---

[1] `http://www.astro.uni-koeln.de/cdms`

through its thermal emission at infrared wavelengths. Large interstellar dust grains (>100 Å) re-radiate stellar photons as infrared and submillimeter continuum emission. Very small ($\lesssim$100 Å) dust grains emit predominantly at mid-infrared wavelengths (25-60 μm). Interstellar dust consists of four main components: silicates, carbonaceous grains, ice mantles, and polycyclic aromatic hydrocarbon (PAH) materials. PAH bands that are observable at mid-IR wavelengths are produced through the vibrational relaxation process in FUV-pumped PAH species, containing typically 50 C atoms. Figure 1.1 shows the infrared emission spectrum of interstellar dust heated by the interstellar radiation field and the contribution by emission related to different grain sizes and composition (Reach & Boulanger 1998).

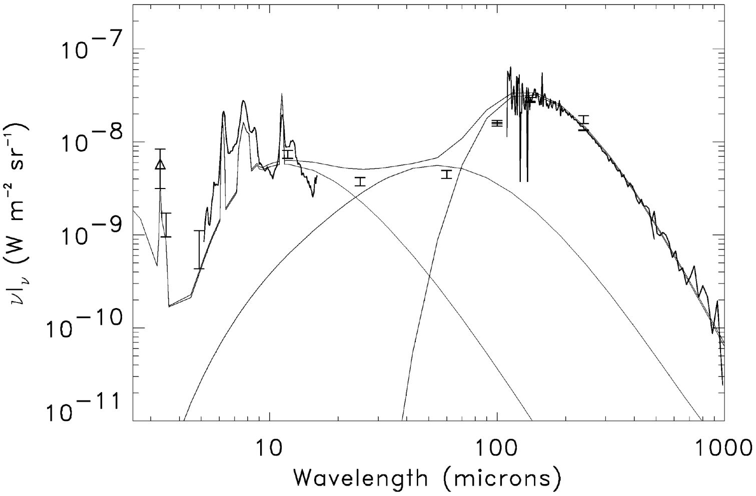

Figure 1.1 — The infrared emission spectrum of interstellar dust heated by the interstellar radiation field as observed by COBE/FIRAS (far-infrared), ISOCAM (mid-infrared), COBE/DIRBE and Arome balloon experiment (points with error bars). The brightness corresponds to an interstellar gas column density of 10^{20} cm^{-2}. The continuous thin curves show a model with three dust components: PAHs and PAHs-clusters (lines and continuum at the shortest wavelengths), (very) small grains (30-80 μm), and large grains (far-infrared emission). Figure from Reach & Boulanger (1998).

Large molecules other than PAHs may be related to the Diffuse Interstellar Bands (DIBs, e.g. Snow & McCall (2006) and references therein) with typical widths of 1-20 Å. More than 400 bands have been discovered (e.g. Hobbs et al. 2008), spanning the wavelength range of the near-UV (4300 Å) to the far-red (∼1 μm), and their relation to specific molecules is not well constrained. A typical gas-to-dust mass ratio in molecular clouds is 100.

1.1.2 Star formation

The formation of stars typically occurs in the densest parts of GMCs clouds and is initiated by a gravitational collapse in the densest parts of molecular clouds, where gravity overcomes the magnetic, turbulent, and thermal pressure of the interstellar medium. The collapse occurs when the minimum mass for which gravity dominates over other forces – Jeans (1928) mass – is reached. In the simplest case gravity has to overcome the gas pressure, which results in a Jeans mass (depending on the gas temperature $T_{\rm gas}$ and density ρ):

$$M_{\rm Jeans} \simeq 1.1 M_\odot \left[\frac{T_{\rm gas}}{10\ \rm K}\right]^{3/2} \left[\frac{\rho}{10^{-19}\ \rm g\ cm^{-3}}\right]^{-1/2} \tag{1.1}$$

Turbulence may exceed gas pressure if motions are supersonic. However, without a continuous source, supersonic turbulence dies out on a dynamical timescale (e.g. Stone et al. 1998; Clark & Bonnell 2005; Kritsuk et al. 2006). Once the Jeans mass is reached in an optically thin gas capable of radiating compressional heat, the gas collapses on a free-fall timescale (Shu et al. 1987):

$$t_{\rm ff} \simeq 2.1 \times 10^5\ {\rm year} \left[\frac{\rho}{10^{-19}\ \rm g\ cm^{-3}}\right]^{-1/2} \tag{1.2}$$

The gas collapses until the densest parts become optically thick. As a result of the conservation of angular momentum, centrifugal forces increase during the collapse, which results in flattened structures. Material flows onto a central, quasi-hydrostatic core, until the hydrogen burning starts. In this phase, the core contracts on the Kelvin-Helmholtz timescale ($t_{\rm KH}$) that is dependent on the mass, radius, and luminosity of the protostellar object ($M_\star$, $R_\star$, and $L_\star$, respectively):

$$t_{\rm KH} \sim \frac{G M_\star^2}{R_\star L_\star} \tag{1.3}$$

The timescale for the accretion phase ($t_{\rm acc}$) is approximately the mass of the protostar ($M_\star$) divided by the accretion rate of matter onto the protostar $\dot{M}$, with a typical value of $\dot{M} \sim 10^{-5}\ M_\odot\ {\rm yr}^{-1}$ (Palla & Stahler 1993). For low-mass stars the accretion phase ends by the time the star enters the hydrogen burning phase, i.e. $t_{\rm acc} < t_{\rm KH}$. For high-mass stars, these two timescales are comparable or $t_{\rm acc} > t_{\rm KH}$. This means that accretion continues for high-mass protostellar objects even after the hydrogen burning starts. The shorter Kelvin-Helmholtz timescale for high-mass stars compared to that of low-mass stars is a result of the luminosity-mass and radius-mass relations predicted for zero-age main-sequence (ZAMS) stars (e.g. Zinnecker & Yorke 2007 and references therein). In the range between $1.5\ M_\odot < M < 120\ M_\odot$, the luminosity-mass relation changes from $L \sim M^{3.7}$ to $L \sim M^{1.6}$, and the radius-mass relation is $R \sim M^{0.5}$.

The formation process of low-mass stars is well characterized observationally and theoretically (e.g. McKee & Ostriker 2007 and references therein). Though massive stars play an important role in the life cycle of galaxies, by enriching the interstellar medium with heavy elements, providing an important source of heating, UV-irradiation, cosmic rays, and turbulence of the interstellar medium, their formation process is less well understood compared to that of low-mass stars (Zinnecker & Yorke 2007 and references therein). The difficulty of studying the formation of massive stars lies in their location at typically large distances ($d \gtrsim 1$ kpc), requiring high spatial resolution to study substructure in the regions. Also, the massive star-formation process has a short timescale including an embedded phase of $\sim 10^5$ years, resulting in statistically fewer candidates to study the embedded phase of massive star-formation. The complexity of the theoretical modeling of high-mass star formation lies in the formation of massive stars in clusters, which introduces the problems of the feedback of newly formed massive stars on their environment, and the impact of protostars on star-formation in their close vicinity.

1.1.3 High-mass star-formation

Possible scenarios for the formation of massive stars

Several scenarios on how massive stars form have been discussed in the literature and include three basic concepts of 1) monolithic collapse and disk accretion, 2) competitive accretion and runaway growth, and 3) stellar collisions and mergers (Fig. 1.2).

Monolithic collapse and disk accretion is an analogue of the low-mass star formation model, assuming an initial collapse that creates a protostar which accretes material through a disk, where the radiation pressure is about 30-times lower than in other directions, allowing high mass infall rates in the equatorial plane (typical rates of $\sim 10^{-5}$ $M_\odot$ year^{-1}, Zinnecker & Yorke 2007). Radiation and stellar wind create polar cavities perpendicular to the disk. The mass of the resulting high-mass star is dependent on the details of the radiative transfer i.e. on the used opacity (Yorke & Sonnhalter 2002). An important question - apart from the collapse and mass accretion - is the issue of fragmentation, as it can limit the mass of the forming stars. It has been shown by hydrodynamical radiative calculations, such as by Krumholz et al. (2007) that, when the radiative transfer is taken into account in the simulations, the gas temperature of the cloud is higher, by factors up to 10, than in the isothermal case. Thus, taking radiation into account results in less fragmentation than when isothermality is used. Apart from the radiative feedback, the magnetic field also affects the fragmentation of the cloud. The fragmentation can be controlled by the magnetic field as the number of objects decreases by a factor of two for the strongest magnetic fields explored (Hennebelle & Commerçon 2011). Therefore, the magnetic field itself cannot suppress the fragmentation of collapsing cores. To suppress the fragmentation, both radiative feedback and the magnetic field are required (Commerçon et al. 2011). See Hennebelle & Commerçon (2012) for a recent review of simulations of the formation of high-mass stars.

Competitive accretion and runaway growth (e.g. Bonnell et al. 1997, 2001) is based on the picture of a forming stellar cluster with its members accreting material from the same molecular cloud. The material that each cluster member can accrete (i.e. the material that enters the accretion domain) is dependent on its environment. For an isolated protostar, the amount of material that enters an accretion domain is proportional to the gas density. A potential corresponding to a protocluster results in material settling to the central part of the cloud. As material flows inwards in the cluster, the accretion domain of an off-center protostar is tidally limited to the outer parts of the cloud, while protostars in the center of the cloud can accrete material from the whole cloud. This will result in the most massive stars to be located in the center of the cloud surrounded by a hierarchy of lower mass objects (Bonnell et al. 2003). The settling of material to the inner parts of clusters also results in higher gas densities toward the center. This is supported by the observations. One example is the W49A high-mass star forming region, where the gas density was found to be above 3×10^5 cm^{-3} within the inner 1 pc and $\sim$$10^4$ cm^{-3} in the outer parts of the cloud (Welch et al. 1987).

Stellar collisions and mergers were proposed to explain the formation of massive stars based on two arguments. In early models, radiation pressure on dust limited the gas accretion, as it was assumed to occur spherically symmetrically. Massive stars form in dense clusters with high stellar densities, therefore a sufficiently large gas reservoir for monolithic collapse may not be available. A threshold for the number density of stars can be derived for which the collisional time-scale is short enough for mergers to occur. Bonnell & Bate (2005) estimated a stellar density threshold of 10^6 stars pc^{-3}. This number depends on the mass ratio of the collision partners (equal mass vs non-equal mass encounters) and on the collisional cross sections, which are larger if a disk is present and if binary components are taken into account (Davies et al. 2006).

Observable stages of massive star formation

Different evolutionary stages of massive star formation co-exist in Giant Molecular Clouds (GMCs) and are detectable at different wavelengths.

- Massive dense clouds represent the earliest phase of massive star formation. Some of them are cold ($T \sim 10$ K) *infrared dark clouds* (IRDCs), that are seen in silhouette against the bright Galactic background in the mid-IR and are observable through their mm/sub-mm emission. Some of these clouds may contain low-mass and intermediate-mass accreting

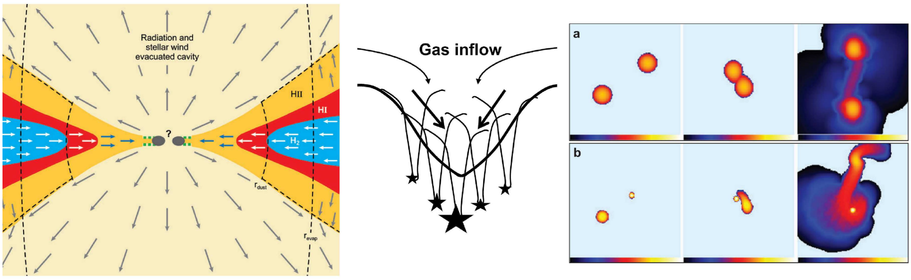

Figure 1.2 — The three proposed models for the formation of massive stars. *Left:* Accretion disk around a massive binary pair with inward radial flow in the equatorial plane and a polar cavity evacuated by a combination of radiation and the stellar wind. Sizes are not to scale. (figure from Zinnecker & Yorke 2007) *Middle:* Potential around a cluster of stars (the concept of the competetive accretion and runaway growth theory). Figure from Bonnell et al. (2007). *Right:* Examples for simulations of stellar mergers (with the density shown in colors): a) Encounter between two 3 $M_\odot$ premain-sequence stars with a periastron distance of the encounter of 25.8 solar radii that results in the formation of a binary. b) detached encounter between a 3 $M_\odot$ and a 10 $M_\odot$ star with radii of 12.9 and 3.92 solar radii, respectively, resulting in the disruption of the 3 $M_\odot$ star, forming a disk around the massive star (Figure from Zinnecker & Yorke 2007, adapted from Zinnecker & Bate 2002, Davies et al. 2006.)

protostars and outflows (Beuther et al. 2005, Van der Wiel & Shipman 2008).

- Once the densest, gravitationally unstable parts of GMCs start to collapse, embedded *high mass protostellar objects* heat the surrounding molecular gas. This phase is observable through its mm/sub-mm emission.

- In the *hot core* stage, the excess angular momentum of the protostars forms jets and outflows, and therefore heats the envelope to 100-300 K. The gas is mainly molecular and emits in the mm/sub-mm and far-infrared. Hot cores also show large abundances of complex organic molecules observable at mm/sub-mm wavelengths (Herbst & Van Dishoeck 2009), which have been evaporated off the grains.

- *Hypercompact and Ultracompact HII regions* (sizes between 0.01 and 0.1 pc) are created around the newly formed stars, that ionize their surroundings and destroy complex molecules. Hypercompact HII regions are probably created around individual photoevaporating disks (Keto 2007); and ultracompact HII regions probably contain a disk-less star photoionizing its massive envelope. This phase is observable through cm radio emission (ionised gas component at $T \sim 10000$ K) and at mm, sub-mm, and far infrared wavelengths ($T \sim 100 - 300$ K molecular gas).

- *Compact and classical H*II *regions* form around massive O- and B-stars that ionize their surroundings and disrupt the parent molecular cloud, revealing the embedded OB stars for optical and near infrared observations, for example in He I and He II lines (e.g. Bik et al. 2012).

Photon-Dominated Regions

Photon-Dominated Regions or Photodissociation Regions (PDRs) are regions around massive young stars where the mainly ionized medium changes to mainly molecular. The chemistry in this region is largely affected by the FUV irradiation (6 eV $< h\nu <$ 13.6 eV) of the nearby young stars. Different chemical layers form as the FUV radiation penetrates into the molecular cloud (e.g. Fig. 1.3). The stratification (chemical layering) in PDRs can be best studied for an edge-on orientation, such as the prototypical dense, high UV-illumination Orion Bar (e.g. Van der Wiel et al. 2009 and references therein). In addition to the different chemical layers, observations and theoretical studies found evidence for the non-homogeneous structure of PDRs (clumpiness).

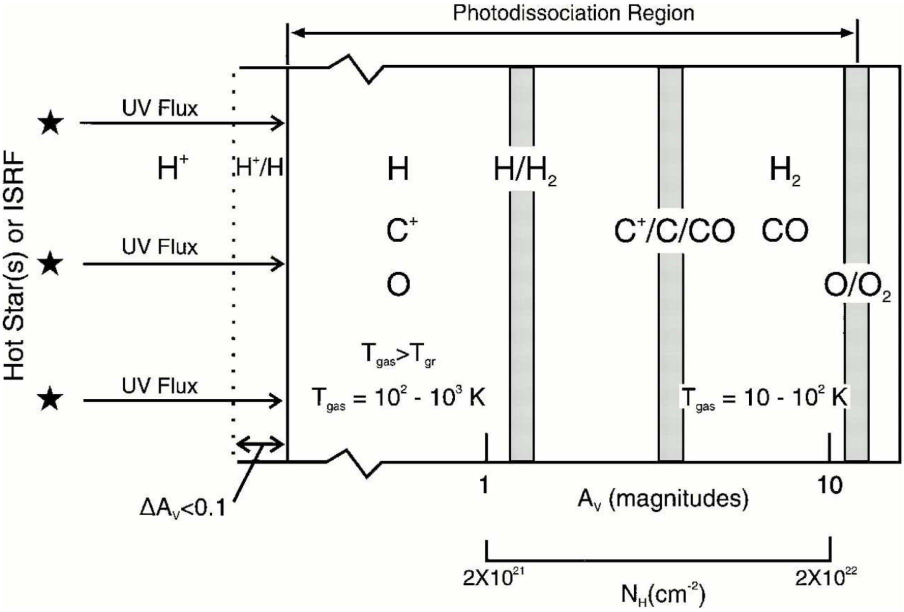

Figure 1.3 — Schematic structure of a PDR illuminated by a strong radiation field (such as the Orion Bar) from the left side (figure from Hollenbach & Tielens 1997), including the main chemical regions. For a standard radiation field the H/H_2 transition occurs at lower A_V.

Many processes contribute to the energy balance of PDRs.
One of the most important heating processes is the *photoelectric effect* on grains and on Polycyclic Aromatic Hydrocarbons (PAHs). By absorbing an FUV photon, the grain creates an energetic electron. If the energy of the electron is enough that it can leave the grain (i.e. can overcome the work function of the grain and the Coulomb potential), it is injected into the gas with an excess kinetic energy, and heats the gas through collisions.
Another important heating process is the *collisional de-excitation of FUV-pumped H_2 molecules.* During this process, the absorption of an FUV photon pumps H_2 molecules to a bound excited electronic state. Collisional de-excitation from this state leads to gas heating.
Another source of heating of the gas is the *ionization of C atoms.* After photoionization, the electron is injected in the gas phase with a kinetic energy excess, heating the gas through collisions. This process is the main resource of electrons in PDRs.
Gas-grain collisions are important for the heating of the gas in regions where the dust temperature is higher than the gas temperature. Gas-grain heating is important at depths equivalent to a visual extinction of $A_{\rm V} > 4$, where penetrating red and near-infrared photons keep the dust warm. Goldsmith & Langer (1978) find that gas and dust temperatures are closely coupled above an H_2 volume density of $\sim 10^5$ cm^{-3}.
Cosmic rays ionize the gas by energetic protons, leading to injecting energetic electrons in the gas. The amount of heat deposited in a molecular gas is ∼8 keV per primary ionisation (Cravens & Dalgarno 1978, Glassgold & Langer 1973). This heating process can be important at large depths in molecular clouds (equivalent to visual extinctions of up to $A_{\rm V} \sim 100$ mag) as unlike FUV photons, cosmic rays can penetrate deeper into molecular clouds.

The cooling of the gas is dominated by species that are radiatively de-excited after collisional excitation. In the outer, warm layers of the PDR the cooling is dominated by H_2 rotational and vibrational lines and FIR fine structure lines (e.g. [CII] 158 μm, [OI] 63, 146 μm, [CI] 609, 370 μm)). Deeper in the cloud molecular rotational lines of CO are the most important coolants.

The mechanisms mentioned above are the main heating and cooling mechanisms that are taken into account in PDR models while solving the energy balance (see Sect. 1.2.2). The exact heating and cooling rates are summarized in e.g. (Meijerink & Spaans 2005).

High-mass star forming regions near and far

The Orion region including the Orion Molecular Cloud 1 ($d \sim 420$ pc, Menten et al. 2007, Hirota et al. 2007) is one of the nearest massive star forming regions. The center of the Orion nebula is marked by the Trapezium cluster of four massive stars, including the most massive θ^1Ori C (O7 spectral type), which ionized its surroundings and created an HII region (Figure 9.1).

Parts of the OMC-1 region are irradiated by the Trapezium cluster, including the well studied Orion Bar PDR. As it is a nearby PDR with a nearly edge-on geometry allowing to directly study the stratification (chemical layering), it is used as a template for other PDRs. The FUV radiation field at the ionization front is $\sim 1-4\times10^4\ \chi_0$ the average interstellar radiation field in Draine (1978) units, with $\chi_0 = 2.7\times10^{-3}$ erg s^{-1} cm^{-2}. It has an average kinetic temperature of 85 K and H_2 volume density of $\sim10^5$ cm^{-3} (Hogerheijde et al. 1995). The standard model of the region consists of an interclump medium with a density of 10^4-2×10^5 cm^{-3} (Simon et al. 1997) and large dense clumps detected in dense gas tracers such as HCN, with a volume density of $1.5-6\times10^6$ cm^{-3} (Lis & Schilke 2003).

Other main regions of the OMC-1 cloud include the Becklin-Neugebauer object and the Kleinmann-Low nebula (Orion BN/KL). The Orion BN/KL region is located about $1'$ Northwest of the Trapezium cluster and has a total luminosity of $\sim10^5\ L_\odot$ (Gezari et al. 1998). It is a complex region including outflows, masers, young stellar objects, and the warm and dense Orion hot core region that shows a complex chemistry.

The Orion S (OMC1-S, S6) molecular condensation is located $1'$ southwest of the Trapezium and $90''$ south of the BN-KL complex. It has been argued based on observational evidence that Orion S is located within the ionized nebula, in front of the OMC-1 cloud (e.g. O'Dell et al. 2009) as shown on Figure 1.5. Its total luminosity is about 10% of that of Orion BN/KL (Mezger et al. 1990). Part of the molecular line emission detected toward this region is related to hot cores and outflows embedded in the Orion S condensation and are characterized by high angular resolution measurements (e.g. Zapata et al. 2005, 2006). Some of the outflows have features detectable at optical wavelengths, such as Herbig-Haro objects (e.g. O'Dell et al. 1997; Bally et al. 2000; Henney et al. 2007; O'Dell & Henney 2008). Due to the irradiation by the nearby Trapezium cluster, the part of the Orion S region facing the Trapezium cluster includes an ionization front and a PDR.

The W49A region is located at a distance about 30× larger than the OMC-1 region ($d \sim 11.4$ kpc, Gwinn et al. 1992). Therefore, it requires interferometric observations to resolve individual objects such as hot cores (Wilner et al. 2001) and UCHII regions. With its luminosity of $\sim10^7\ L_\odot$ (Sievers et al. 1991), equivalent to that of 100 O7 V stars, it is one of the best Galactic analogues of the starburst phenomenon seen in starburst galaxies, where the star-formation rate can be orders of magnitude above that of the Milky Way. However, its luminosity is orders of magnitude below that of external galaxies with a global starburst phenomenon, such as luminous infrared galaxies (LIRGs; $L_{\rm IR} > 10^{11}\ L_\odot$) and ultraluminous infrared galaxies (ULIRGs; $L_{\rm IR} > 10^{12}\ L_\odot$). Therefore, W49A may be a template for starburst galaxies in terms of star-formation efficiency, but not in terms of luminosity. Many studies aimed at explaining the large amount of massive stars currently seen in W49A. The competing

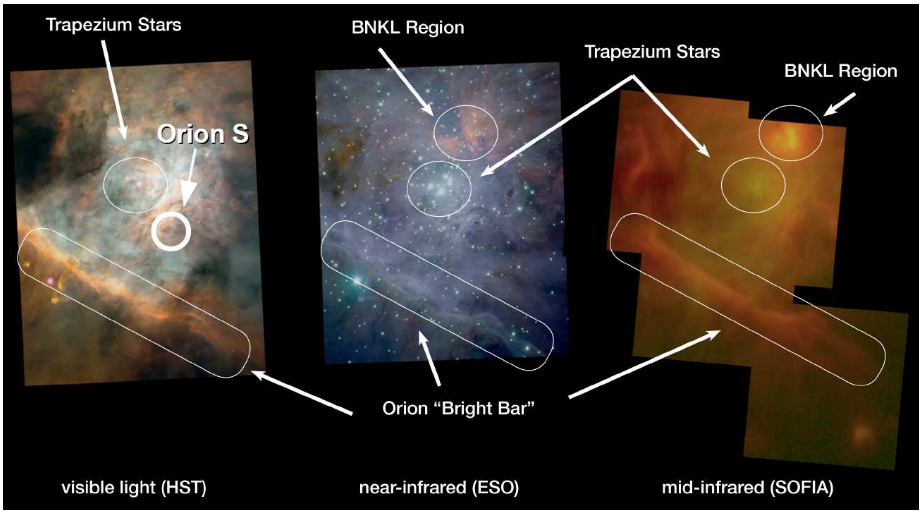

Figure 1.4 — The multiwavelength view of the Orion region around the Trapezium cluster. Credit: Visible-light image: NASA/ESA/HST/AURA/STScI/O'Dell & Wong; Near-IR image: ESO/McCaughrean et al.; Mid-IR image: NASA/DLR/SOFIA/USRA/DSI/FORCAST Team

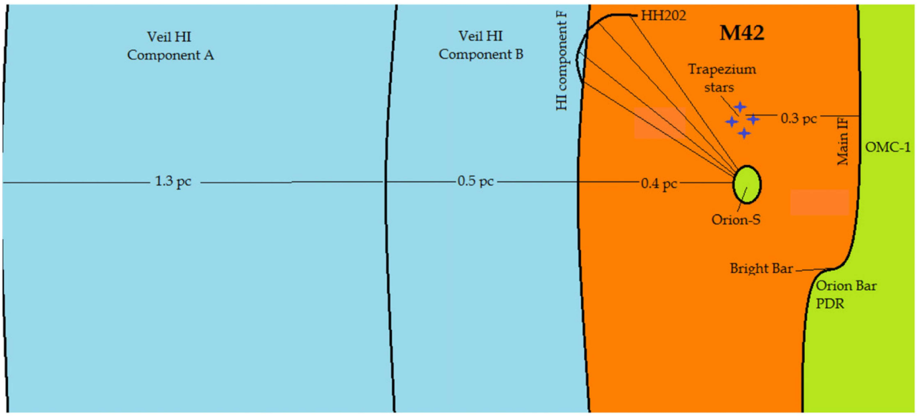

Figure 1.5 — Schematic geometry of the Orion region around the Trapezium cluster, including neutral foreground clouds ('Veil'). Ionized gas is shown in orange, molecular gas in green, and atomic gas in blue. While the Orion Bar is part of the OMC-1 cloud itself, the Orion S region is an individual dense cloud located in the HII region cavity around the Trapezium cluster. The largest outflow is also shown for Orion S. Figure from Van der Werf et al. (2013).

explanations include a large-scale inside-out gravitational collapse (Welch et al. 1987) and a collision of two clouds (Serabyn et al. 1993). Both of these explanations are consistent with the observations of double-peaked lines of different molecules, including infall signatures. Therefore, it is not yet clear which of the above mentioned explanations describes the origin of high star-formation efficiency in the W49A region.

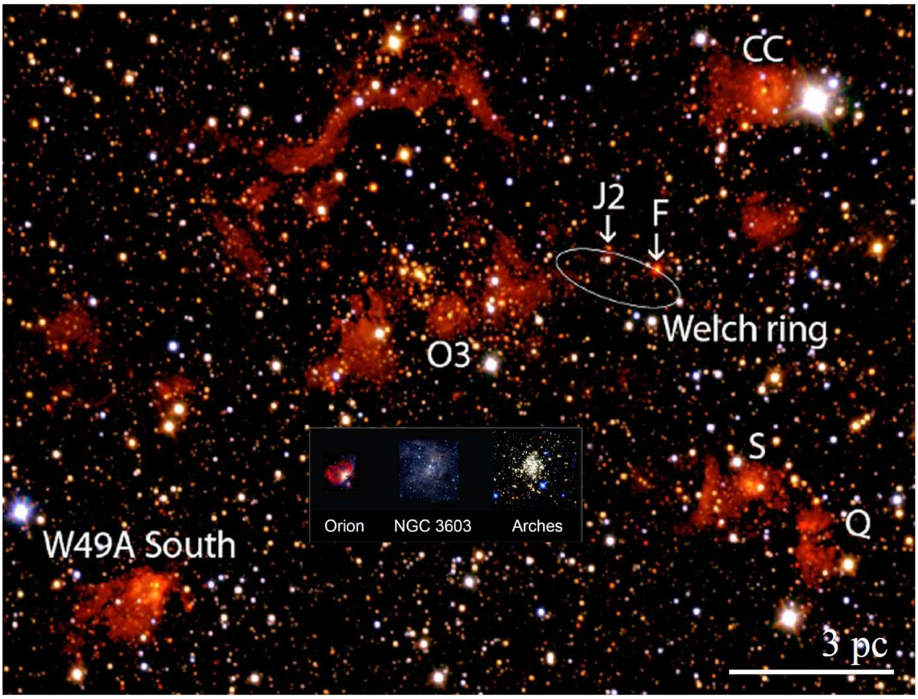

Figure 1.6 — A size comparison between the W49A region and other Galactic massive star-forming regions. The background is a JHK_S composite image of W49A from Alves & Homeier (2003a). The labels show the known continuum sources (De Pree et al. 1997). The figure is based on Alves & Homeier (2003b).

1.2 Interpretation of molecular line observations

1.2.1 Radiative transfer models

Estimating the physical properties of star-forming regions requires continuum and molecular line observations at sub-mm and infrared wavelengths. The observed continuum emission can help to constrain the dust temperature and dust mass. In this section we focus on the analysis of molecular lines. For a discussion of continuum radiative transfer see Pascucci et al. (2004). For a recent review on line radiative transfer and molecular data see Van der Tak (2011). Comparing molecular line observations to radiative transfer models, abundances/column densities can be derived for the detected molecular species and physical parameters such as temperatures and densities of the emitting regions can be constrained.

Radiative transfer models describe the propagation of radiation taking into account emission and absorption processes and scattering by gas and dust. Here we discuss the propagation of radiation in the ISM. The basic form of the radiative transfer equation:

$$\frac{\mathrm{d}I_\nu}{\mathrm{d}s} = -\alpha_\nu I_\nu + j_\nu \tag{1.4}$$

with the specific intensity I_ν, defined as the amount of energy passing through a surface normal to the path, per unit time, surface, bandwidth, and solid angle. In Eqn. 1.4 j_ν and α_ν are the local emission and absorption coefficients. The source function S_ν is defined as $S_\nu \equiv j_\nu/\alpha_\nu$, which for line radiation can be expressed as:

$$S_\nu = \frac{A_{ji}}{B_{ji}} \frac{1}{\frac{n_i g_j}{g_i n_j} - 1} \tag{1.5}$$

with n_i the number density of molecules in level i, g_i the statistical weight of level i, and A_{ji} and B_{ji} Einstein coefficients for spontaneous- and stimulated emission, respectively. The excitation temperature T_{ex} is defined through the Boltzmann equation

$$\frac{n_j}{n_i} = \frac{g_j}{g_i} \exp\left(-\frac{h\nu}{kT_{\mathrm{ex}}}\right) \tag{1.6}$$

With this definition the source function becomes the black body radiation field at a temperature T_{ex}. In the simplest case, when the density of the medium is large enough that collisions determine the excitation, Local Thermodynamic Equilibrium (LTE) applies, with an excitation temperature equal to the kinetic temperature in the region.

Another commonly used method is the *rotational diagram method* (e.g. Turner 1991) which is based on multi-line observations covering a sufficient range in upper level energies. The rotational diagram method assumes the level populations of a molecule to be characterized by a single excitation temperature according to the Boltzmann equation. This method also assumes that the lines are optically thin and that the emission is homogeneous and fills the telescope beam. The excitation ('rotational') temperature T_{rot} in this case can be derived using a linear fit to the logarithm of upper level column densities (N_u) as a function of the upper level energies of the transitions. The observed line intensities can be directly converted to N_u. Once the rotational temperature is known, the total column density $N_{\rm tot}$ can be calculated from

$$\ln\left(\frac{N_u}{g_u}\right) = \ln\left(\frac{N_{\rm tot}}{Q_{\rm rot}}\right) - \frac{E_u}{kT_{\rm rot}} \tag{1.7}$$

where $Q_{\rm rot}$ is the rotational partition function and is obtained as

$$Q_{\rm rot} = \sum_i g_i \exp\left(-\frac{E_i}{kT}\right).$$

When the above mentioned assumptions hold, this method gives a reliable estimate of column densities. In general, optical depth effects and non-uniform beam filling affect the column density estimate from multi-line observations and requires a correction for these effects such as using the *population diagram method* (e.g. Goldsmith & Langer 1999).

At low densities, the contribution of radiative decay exceeds that of collisional de-excitation, and leads to an excitation temperature below the kinetic temperature. Non-LTE models (e.g. RADEX, Van der Tak et al. 2007) take collisional and radiative processes into account to calculate level populations of molecules. In these models, the statistical equilibrium is a commonly used approach:

$$\frac{dn_i}{dt} = \sum_{j\neq i}^{N} n_j P_{ji} - n_i \sum_{j\neq i}^{N} P_{ij} + \mathcal{F}_i - n_i \mathcal{D}_i = 0$$

where

$$\begin{aligned} P_{ij} &= A_{ij} + B_{ij}\bar{J} + C_{ij} \quad (i > j) \\ &= B_{ij}\bar{J} + C_{ij} \quad (i < j) \end{aligned}$$

and A_{ij} and B_{ij} are the Einstein coefficients, $\bar{J}$ is the mean intensity at the frequency of transition $i \to j$, C_{ij} is the sum over all collision partners of the rates of inelastic, collision-induced transitions $i \to j$, n_i is the number density (cm^{-3}) of molecules in level i. In most non-LTE radiative transfer codes it is assumed that the state-specific rates of formation ($\mathcal{F}_i$, cm^3 s^{-1}) and destruction ($\mathcal{D}_i$, s^{-1}) are zero so that the radiative transfer is solved independently of assumptions about chemical processes. In most cases this is a reasonable assumption. For some species such as reactive ions like CH$^+$ and CO$^+$, this assumption does not hold, therefore the formation and destruction of these species need to be taken into account for realistic column density estimates of these species (e.g. Black 1998). This effect is taken into account in the chemical models in this thesis (see Sect. 1.2.2). A limitation of the use of non-LTE methods is that it requires collisional excitation rates, that are only available for a limited number of molecules, and in some cases only for a limited number of collision partners, or for a limited temperature range (e.g. Schöier et al. 2005). Databases containing collisional excitation rates include the Leiden Atomic and Molecular Database (LAMDA[2]) and BASECOL[3] (Dubernet et al. 2012).

One practical use of non-LTE models is the comparison of a grid of models to observed line intensity ratios of tracers of either the kinetic temperature or the gas density. One commonly used temperature and density tracer is H_2CO, where lines from different J-states are density tracers, while ratios of lines from the same J-state but different K-states[4] are mostly probes of the temperature.

Simple non-LTE programs like RADEX assume average conditions - temperatures, densities, and column densities - for the observed region, and do not take variations of these properties into account as a function of position in the cloud. Non-local radiative transfer codes, such as RATRAN (Hogerheijde & van der Tak 2000) solve for the molecular excitation as a function of position, allowing to assume geometries in one or two dimension. Non-local models also include the treatment of temperature and density gradients. These models estimate the local radiation field at all line frequencies taking into account the radiation field from every other position in the cloud using two different methods. One of the methods is the Accelerated Lambda Iteration method, where the local radiation field and excitation are solved on a grid of points, separately from the overall radiative transfer problem. Monte Carlo methods divide the cloud into grid cells and send photon packages in random directions from each cell. The random nature of the Monte Carlo method makes the solution independent to the angular, spatial, and frequency sampling of the radiation field. For a comparison of the two types of models, see Van Zadelhoff et al. (2002).

1.2.2 Chemical models

Chemical models are available for many different environments including shocks (e.g. Flower & Pineau des Forêts 2003), turbulent dissipation regions (e.g. Godard et al. 2009), X-ray dominated regions (XDRs, e.g. Meijerink & Spaans 2005), and PDRs (e.g. Röllig et al. 2007, Hollenbach & Tielens 1997). In this section we restrict ourselves to PDR models as several chapters of this thesis are based on them.

The simplest PDR models assume *steady-state stationary* clouds, where the chemical reactions have much shorter timescales compared to the dynamical time scales or the time scales for significant change in the FUV flux. This is not the case for *time-dependent and nonstationary* PDR models where the chemical abundances and temperatures change as a function of time. Time-dependent

---

[2] `http://home.strw.leidenuniv.nl/~moldata/`

[3] `http://basecol.obspm.fr/`

[4] In case of non-linear molecules the rotational motion is characterized by two quantum numbers: the total angular momentum J, and its projection on the symmetry axis, K. In case of asymmetric top molecules each K-level is split into two.

effects become important when the radiation field or the density change on a time-scale shorter than the time-scale of the chemical reactions. Examples of time-dependent effects include expanding shells around stars or in a planetary nebula, or shadowing effects due to clumps moving in the PDR. Time dependent effects are also important when the freeze-out of molecules is taken into account in the model (e.g. Hollenbach et al. 2009). The freeze-out of molecules typically occurs on time-scales comparable to the lifetime of interstellar clouds, and is inversely proportional to the cloud density. Nonstationary representation is needed when neutral gas flows through the ionization front, that results in a different structure compared to that in stationary PDRs.

Another key difference between PDR models is the assumed geometry. Several models assume a *plane-parallel* cloud illuminated from one or both sides (e.g. the Meudon code; Le Petit et al. 2006, Goicoechea & Le Bourlot 2007). The other class of PDR models includes a *spherical* geometry with an isotropic radiation field (e.g. KOSMA-τ, Röllig et al. 2006). In particular cases, a more complex geometry is required, such as in the case of massive protostellar objects, where the FUV photons directly irradiate the outflow walls, represented by an axisymmetric geometry (Bruderer et al. 2009).

For the assumed geometry and chemical network, PDR codes typically 1) calculate the structure of irradiated regions by solving the chemical balance to determine the abundances of species; 2) solve the energy balance to estimate the physical properties (temperatures, pressures, and level populations, commonly using the escape probability approximation[5]) at each position of the cloud (details of the important processes affecting the energy balance of PDRs were discussed in Sect. 1.1.3); and 3) solve the radiative transfer (as discussed in 1.4) to calculate the emergent spectrum for comparison with observations.

Solving the chemical balance includes all the species in the chemical network including their formation and destruction processes in the form of a non-linear system of equations:

$$\begin{aligned}\frac{\mathrm{d}n_i}{\mathrm{d}t} &= \sum_j \sum_k n_j n_k R_{jki} + \sum_l n_l \zeta_{li} \\ &\quad - n_i \left(\sum_l \zeta_{il} + \sum_l \sum_j n_j R_{ijl} \right) \qquad (1.8)\end{aligned}$$

The first two terms represent the formation, the second two the destruction processes of the species. n_i is the density of species i, R_{jki} and R_{ijl} are the reaction rate coefficients between two atoms, molecules, or ions; and ζ_{li} and ζ_{ij} are the reaction rates in the case of photo-reactions (reactions between an atom, molecule, or ion and an FUV photon or cosmic ray). In stationary models,

---

[5] A treatment of optical depth effects in which the chance for photons to leave the cloud is based on the current local estimate for the optical depth and an assumed geometry.

$\mathrm{d}n_i/\mathrm{d}t = 0$. A number of databases of rate coefficients is available including the UMIST database for astrochemistry 2006 (Woodall et al. 2007), that is used in this thesis (Chapters 4, 5, and 6). A detailed comparison between different types of PDR models, e.g. stationary homogeneous and clumpy models, is given in Röllig et al. (2007).

The most important chemical reactions in PDRs include *photodissociation* ($\mathrm{XY} + \mathrm{h}\nu \rightarrow \mathrm{X} + \mathrm{Y}$) and *photoionization* ($\mathrm{XY} + \mathrm{h}\nu \rightarrow \mathrm{XY}^+ + \mathrm{e}^-$). The rates of such reactions are dependent on the penetration of the FUV radiation in the PDR and are proportional to $\exp(-kA_\mathrm{V})$ with the scaling factor k and the visual extinction A_V. The penetration of the FUV field is largely dependent on the observational fact that interstellar clouds have an inhomogeneous, clumpy structure on all scales (e.g. Stutzki et al. 1998). This effect is taken into account in the KOSMA-τ PDR model (Röllig et al. 2006) which represents irradiated clouds with an ensemble of clumps with a fixed size-spectrum. Apart from the cloud structure, the penetration of radiation in the cloud is affected by the properties of dust grains. Dust properties can vary as a function of depth into the cloud due to, for instance, the growth of ice mantles. Goicoechea & Le Bourlot (2007) demonstrated, that the penetration depth of the FUV radiation is larger when dust scattering is more efficient (as dust grains grow toward bigger grains). Other important chemical reactions in PDRs are highly endothermic *reactions with FUV-pumped, vibrationally excited H_2 molecules.* These reactions are responsible for the formation of OH and some reactive ions such as CH^+ and SH^+. An overview of these reactions is presented in Agúndez et al. (2010).

At low temperatures, other processes also become important (e.g. Bergin et al. 1995, Hollenbach et al. 2009 and references therein).
Photodesorption of a molecule on a grain surface may follow the absorption of a UV-photon by the molecule. In this case, an electron will be put in an excited state. As a result of the interaction between the excited state with the binding to the surface, the excited molecule may be ejected from the surface of the grain.
Direct *thermal desorption* is dependent on the binding energy of the molecular species to the grain and on the dust temperature. The time-scale for thermal desorption is greater than cloud lifetimes for typical dust temperatures of the dense interstellar medium ($T_\mathrm{dust} \sim 10 - 30$ K). This effect becomes important at high dust temperatures or for low binding energies.
Deep in the cloud *cosmic-ray desorption* is important in maintaining O- and C-based species in the gas phase. The time-scale of this process is mainly determined by the abundance of the species on the grain, and by the cosmic-ray desorption rate per surface atom or molecule. Under certain conditions, cosmic-ray desorption can increase the abundance of gas-phase CO, which can then serve as a source of gas-phase $\mathrm{H_2O}$ and $\mathrm{O_2}$.
As mentioned above, the *freeze-out* of molecules can be important for certain physical conditions, especially at high densities. The freeze-out of oxygen

controls the abundance of species such as H_3O^+ (discussed in Chapter 5) in the mainly molecular region of the PDR.

Figure 1.7 shows important reactions involved in the PDR chemistry of oxygen-and carbon-bearing species. The ions analysed in Chapters 4, 5, and 6 are shown in green. Other reactions not included in Fig. 1.7 are discussed in (Hollenbach et al. 2009). The chemistry in PDRs is discussed in Sternberg & Dalgarno (1995) and Hollenbach & Tielens (1997) and references therein.

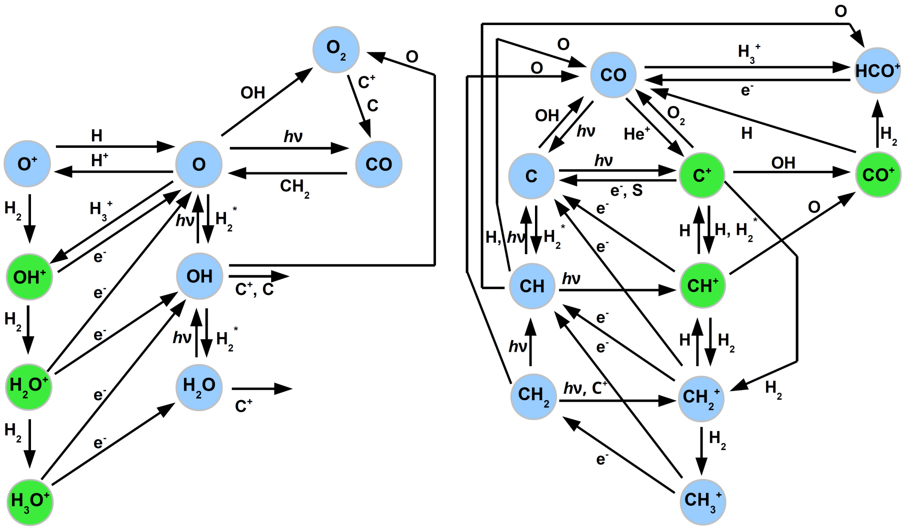

Figure 1.7 — The most important reactions involved in PDR chemistry of oxygen-bearing (left) and carbon-bearing (right) species. The ions shown with green colors are subjects of Chapters 4, 5, and 6. Based on Figure 5 in Hollenbach & Tielens (1997).

1.3 Summary of the thesis

This thesis is based on single-dish sub-mm and FIR line surveys toward two high-mass star forming regions, the nearby Orion region and the luminous and distant W49A, that were introduced in Section 1.1.3. These data allow us to study the radiation and mechanical feedback of young massive stars on the surrounding molecular material. The main goals of this work are the following.

- To study the physical and chemical structure of the Galactic starburst analogue W49A in key molecular line tracers and probe how it compares to starburst galaxies.
- To study the feedback effect of young massive stellar clusters and forming massive stars (hot cores, UCHII regions) on their environment.

- To probe the radiation feedback in a more nearby environment, the Orion region, using molecular ion lines that trace the warm surface of PDRs.

The physical and chemical structure of the Galactic starburst template W49A

Chapters 2 and **3** focus on a $2' \times 2'$ (6.6×6.6 pc) region centered on W49A and use data from the James Clerk Maxwell Telescope (JCMT) Spectral Legacy Survey (SLS, Plume et al. 2007). The SLS and its high-frequency extension cover the 330-373 GHz frequency range and correspond to an angular resolution of $\sim$15$''$ ($\sim$0.8 pc). This frequency range includes key molecular line tracers to probe the physical and chemical structure of W49A and the excitation of species with multiple detected transitions.

Chapter 2 provides a general description of the data, an inventory of column densities for the detected species, and an analysis of their spatial extent and observed line profiles. 260 lines were detected in the SLS survey range toward the central position of the field (that corresponds to the center of the largest stellar cluster in W49A, and to the highest excitation region). These 260 detected lines correspond to 59 molecular species. Excitation conditions can be probed for 19 molecules, including the complex organic molecules CH_3CCH, CH_3CN, and CH_3OH. The detected species suggest the importance of shock-, PDR-, and hot core chemistry. Many molecular lines show a significant spatial extent accross the maps including CO and its isotopes, high density tracers (e.g. HCN, HNC, CS, HCO^+) and tracers of UV-irradiation (e.g. CN and C_2H).

Chapter 3 focuses on the temperature and density structure of W49A using H_2CO and HCN line ratios detected over a large region within the $2' \times 2'$ (6.6×6.6 pc) SLS field. We also analyze the excitation of molecules with multiple transitions with corrections for optical depth and beam dilution, and estimate excitation temperatures and column densities. Comparing the observed line intensity ratios with non-LTE radiative transfer models, our data reveal an extended region (about $1' \times 1'$, equivalent to $\sim$3×3 pc at the distance of W49A) of warm (>100 K) and dense ($>10^5$ cm^{-3}) molecular gas, with a mass of $2\times10^4-2\times10^5\ M_\odot$ (by applying abundances derived for other regions of massive star-formation). These temperatures and densities in W49A are comparable to those found in clouds near the center of the Milky Way and in starburst galaxies. The highly excited gas is likely to be heated via shocks from the stellar winds of embedded, O-type stars or alternatively due to UV irradiation, or possibly a combination of these two processes. Cosmic rays, X-ray irradiation and gas-grain collisional heating are less likely to be the source of the heating in the case of W49A.

The chemistry of ions with high activation barriers

Chapters 4 and **6** focus on the CH^+ and SH^+ ions that have highly endothermic formation channels. Several mechanisms have been proposed to overcome the high activation barriers, including shocks, turbulence, and H_2 vibrational excitation. Both of these chapters use data from the HEXOS (Herschel/HIFI Observations of EXtraOrdinary Sources, PI: E. Bergin) key program. High resolution HIFI and low resolution PACS spectra provide information on the chemistry and excitation of CH^+ and SH^+ ions. The PACS footprint observations also trace the spatial distribution of CH^+. Our observations are pointed toward the CO^+ peak of the high UV-illumination warm and dense Orion Bar PDR (Chapter 4) and toward the massive dense core Orion S (Chapter 6). We interpret the observed line intensities by a comparison to radiative transfer and photo-chemical models.

CH^+ $J = 1-0$ and $2-1$ were detected in the HIFI data, and the $J = 3-2, ..., 6-5$ in the PACS footprint observations toward the Orion Bar (**Chapter 4**). In addition, three hyperfine components of SH^+ $1_2 - 0_1$ were detected (with one of them a tentative detection). A comparison to PDR models for physical conditions that are expected for the Orion Bar confirms a formation via a reaction with vibrationally excited H_2 for CH^+. This is the most likely formation mechanism for SH^+ as well, though the lack of state-to-state formation rates make our results for SH^+ less accurate. The PDR models predict CH^+ and SH^+ formation at the surface ($A_V \lesssim 1.5$) of the PDR at temperatures between 500-1000 K. The physical conditions predicted by the PDR models are well reproduced by non-LTE radiative transfer models with a correction for the formation and destruction of ions in excited levels. Inelastic collisions by electrons mostly affect the lowest$-J$ transitions of CH^+.

The Orion S (**Chapter 6**) massive dense core, similar to the Orion Bar, is illuminated by the Trapezium cluster, resulting in PDR-stratification on the side facing the Trapezium. Due to its smaller distance to the illuminating source, the radiation field at the position in Orion S is about 10-times above that of the Orion Bar. CH^+ 1-0 was detected there with an intensity similar to that of the same transition detected in the Orion Bar. Two hyperfine components of SH^+ $1_2 - 0_1$ were detected toward Orion S. A key difference is the non-detection of the CH^+ 2-1 transition in Orion S. Another difference is the detection of CO^+ $N = 5-4$ toward Orion S, but not toward the Bar, where lower$-N$ CO^+ transitions were previously detected. The observed CH^+, SH^+, and [CII] line intensities are consistent with a PDR model illuminated by a radiation field derived by earlier studies toward the Orion S position ($\sim 10^5$ χ_0) and a pressure of $\sim 10^8$ K cm^{-3}. This pressure is similar to what was found for the Orion Bar required to explain the origin of CH^+ and SH^+ emission. The models also indicate that the previously poorly constrained inclination of the PDR at the Orion S position is around 45° rather than face-on.

The chemistry of ions which react rapidly with H_2

In **Chapter 5** we study the reactive H_nO^+ ions (OH^+, H_2O^+, and H_3O^+), that are widespread in the interstellar medium and act as precursors to the H_2O molecule. Their lines are commonly detected in Galactic diffuse clouds in absorption against strong continuum sources. Their appearance in emission has so far only been reported for some active galactic nuclei. We show the first example of a Galactic source of H_nO^+ line emission toward the Orion Bar in our HEXOS line survey (used in Chapters 4 and 6). An additional HIFI map of a $115'' \times 65''$ region centered on the position of the HIFI line survey (the CO^+ peak) shows that OH^+ line emission extends over $\sim 1'$ tracing the Bar itself as well as a perpendicular feature identified as the Southern tip of the Orion Ridge, which borders the Orion Nebula on its Western side. While OH^+ is seen in emission and with a significant spatial extent, H_2O^+ and H_3O^+ are not detected in our line survey. Using the non-LTE radiative transfer code RADEX we derive an OH^+ column density of $\sim 1.5 \times 10^{14}$ cm^{-2}, that is similar to that in previous absorption line studies, as are our limits on the H_2O^+/OH^+ and H_3O^+/OH^+ ratios. PDR models suggest that the OH^+/H_2O^+ ratio of $\gtrsim 2$ is naturally explained by the high UV radiation field and electron density in the Orion region. However, a pressure of 10^8 K cm^{-3} and a radiation field of $10^4 \chi_0$ that explains CH^+ excitation (Chapter 4) underpredicts the observed column densities by a factor of 2.5, which is within the uncertainty of the model through the gas pressure and the spectral shape of the radiation field. Photodissociation and electron recombination are more effective destroyers of OH^+ than the reaction with H_2, which limits the production of H_2O^+. The appearance of the OH^+ lines in emission is the result of the high electron density in the Orion Bar, since unlike for H_2, inelastic e-OH^+ collisions are faster than reactive ones. In addition, chemical pumping, far-infrared pumping by local dust, and near-UV pumping by Trapezium starlight contribute to the OH^+ excitation. Similar conditions may apply to extragalactic nuclei where H_nO^+ lines are seen in emission.

2

Physical and chemical differentiation of the luminous star-forming region W49A
Results from the JCMT Spectral Legacy Survey

Nagy, Z., Van der Tak, F. F. S., Fuller, G. A., & Plume, R. [1]

---

[1] In preparation, to be submitted to Astronomy & Astrophysics

Abstract

The massive and luminous star-forming region W49A is a well known Galactic candidate to probe the physical conditions and chemistry similar to those expected in external starburst galaxies.

We aim to probe the physical and chemical structure of W49A on a spatial scale of ∼0.8 pc based on the JCMT Spectral Legacy Survey, which covers the frequency range between 330 and 373 GHz.

The wide 2 × 2 arcminutes field and the high spectral resolution of the HARP instrument on JCMT provides information on the spatial structure and kinematics of the cloud traced by the observed molecular lines. For species where multiple transitions are available, we estimate excitation temperatures and column densities using a population diagram method, that takes beam dilution and optical depth corrections into account.

We detected 260 transitions corresponding to 60 species in the 330-373 GHz range at the central position. Excitation conditions can be probed for 16 molecules, including the complex organic molecules CH_3CCH, CH_3CN, and CH_3OH. The chemical composition suggests the importance of shock-, PDR-, and hot core chemistry. Many molecular lines show a significant spatial extent across the maps including CO and its isotopologues, high density tracers (e.g. HCN, HNC, CS, HCO^+), and tracers of UV-irradiation (e.g. CN and C_2H). The spatially extended species reveal a complex velocity-structure of W49A with possible infall and outflow motions. Large variations are seen between the sub-regions with mostly blue-shifted emission toward the Eastern tail, mostly red-shifted emission toward the Northern clump, and emission peaking around the expected source velocity toward the South-west clump.

A comparison of column density ratios of characteristic species observed toward W49A to Galactic PDRs suggests that while the chemistry toward the W49A center is driven by a combination of UV-irradiation and shocks, UV-irradiation dominates for the Northern Clump, Eastern tail, and South-west clump regions. A preliminary comparison to a starburst galaxy and an AGN suggests similar C_2H, CN, and H_2CO abundances between the ∼0.8 pc scale probed for W49A and the >1 kpc regions in external galaxies with global star-formation.

2.1 Introduction

W49A is one of the most massive ($M \sim 10^6$ $M_\odot$, Sievers et al. 1991) and luminous ($>10^7$ $L_\odot$, Ward-Thompson & Robson 1990) star-forming regions in the Galaxy. Even though its luminosity is lower than that of starburst galaxies (such as Luminous and Ultra-luminous Infrared Galaxies with $L_{\rm IR} > 10^{11}$ $L_\odot$ and 10^{12} $L_\odot$, respectively), W49A may be used as a template to probe physical processes and the chemistry of those regions. As it is located at a distance of 11.4 kpc (Gwinn et al. 1992), its small-scale structure including hot cores, outflows, and Ultracompact HII regions cannot be fully resolved with single-dish telescopes. However, previous studies using single-dish telescopes have already provided information on the chemical complexity of W49A, and the physical and chemical properties of the region.

HCO^+ 1-0 lines with red-shifted absorption and blue-shifted emission were observed by Welch et al. (1987) and interpreted as an evidence of a collapse toward the central ∼2 pc region of W49A. An alternative explanation for the large number of O-stars contributing to the luminosity of W49A was proposed by Serabyn et al. (1993), who suggest a cloud-cloud collision based on multiple transitions of CS and $C^{34}S$ (from J=3-2 to J=10-9). Peng et al. (2010) have identified two expanding shells in Spitzer mid-IR images and in position-velocity diagrams based on ^{13}CO $J = 2-1$ and $C^{18}O$ $J = 2-1$ data. Though the origin of these shells is not clear, they may give an indication of the origin of the high star-formation activity.

Vastel et al. (2001) have studied the physical conditions in the PDR component of W49A using the FIR lines of [OI] and [CII] observed with the Long Wavelength Spectrometer of the Infrared Space Observatory as well as rotational lines of CO (CO 1-0, $C^{18}O$ 2-1) observed with the 15-m SEST telescope, and derived a radiation field of $G_0 = 3\times10^5$ and an average gas density of 10^4 cm^{-3}.

A recent study based on data from the JCMT Spectral Legacy Survey (SLS, Plume et al. 2007) focused on an extended warm and dense gas component toward W49A seen in H_2CO (Nagy et al. 2012, Chapter 3), and characterized the physical properties and excitation of the region using CH_3OH, SO_2, H_2CO, and HCN transitions. Another study that makes use of the SLS line survey data focuses on dense gas tracers (Roberts et al. 2011), such as HCN, HNC, DCN, HCO^+, and their isotopologues, and by a comparison to line ratios measured toward starburst galaxies and Active Galactic Nuclei (AGN), as well as to chemical models, finds that W49A is a template for starburst galaxies rather than for AGN.

In this chapter, we present results on the chemical inventory of W49A based on the SLS, carried out with the James Clerk Maxwell Telescope (JCMT) at a resolution of $\sim15''$. This line survey provides the largest frequency coverage data toward W49A up to date, and as such, it provides a useful starting point for future higher resolution studies with instruments such as ALMA.

2.2 Observations and data reduction

The SLS observations have been carried out using the 16-receptor (spatial pixel) Heterodyne Array Receiver Programme B (HARP-B, 325-375 GHz) and the Auto-Correlation Spectral Imaging System (ACSIS) correlator (Buckle et al. 2009) at the James Clerk Maxwell Telescope[2] (JCMT) on Mauna Kea, Hawai'i. The observations were carried out in jiggle position switch mode, sampled every $7.5''$ for a 2×2 arcminutes field centered on RA(J2000) = $19^{\rm h}10^{\rm m}13.^{\rm s}4$; Dec(J2000) = $09^\circ06'14''$. The spectra were calibrated using an off-position $14'$ to the northeast of the source center. The pointing was checked every hour and is estimated to be accurate to $1.5''$. The angular resolution of the JCMT is $\sim15''$ at 345 GHz, equivalent to $\sim$0.8 pc at the distance of W49. The spectral resolution at the observed frequencies is $\sim$0.8 km s^{-1} and the beam efficiency is 0.63 (Buckle et al. 2009). The original line survey was carried out in the 330-360 GHz frequency range and was later extended to 373 GHz. This paper summarizes the results from the whole 330-373 GHz line survey.

The data reduction was done using a combination of tasks from the Starlink package and the ORAC Data Reduction pipeline (ORAC-DR). We reduced the observed time-series cubes using the ORAC-DR pipeline, which creates three-dimensional cubes after checking for consistency between the calculated $T_{\rm sys}$ and observed rms noise in the data; checking for variations in the rms noise measured by each receptor across the map, removes baselines from every spectrum and co-adds spectra that corresponds to the same position and frequency. The results of the pipeline were checked and were corrected for remaining bad data, such as spectra with high rms noise level, bad baselines, and spectral ranges affected by spikes, using a combination of Starlink tasks.

Figure 2.1 shows the typical rms noise levels as a function of frequency in the 330-373 GHz frequency range measured at every 2 GHz. Typical noise levels in $T_{\rm A}^*$ units are in the range between 0.02 and 0.12 K. The highest noise level measured at $\sim$368 GHz is due to the poor atmospheric transmission as shown in the top panel of Fig. 2.1. Atmospheric transmissions are shown for typical precipitable water vapor (PWV) levels of 1 mm and 3.75 mm on Mauna Kea.

2.3 Results

2.3.1 Line identification

We have identified the lines detected toward the center of W49A (RA(J2000) = $19^{\rm h}10^{\rm m}13.^{\rm s}4$; Dec(J2000) = $09^\circ06'14''$) in the frequency range between 360 and 373 GHz, in the SLS and in its high frequency extension. Anal-

---

[2] The James Clerk Maxwell Telescope is operated by the Joint Astronomy Centre on behalf of the Science and Technology Facilities Council of the United Kingdom, the Netherlands Organisation for Scientific Research, and the National Research Council of Canada.

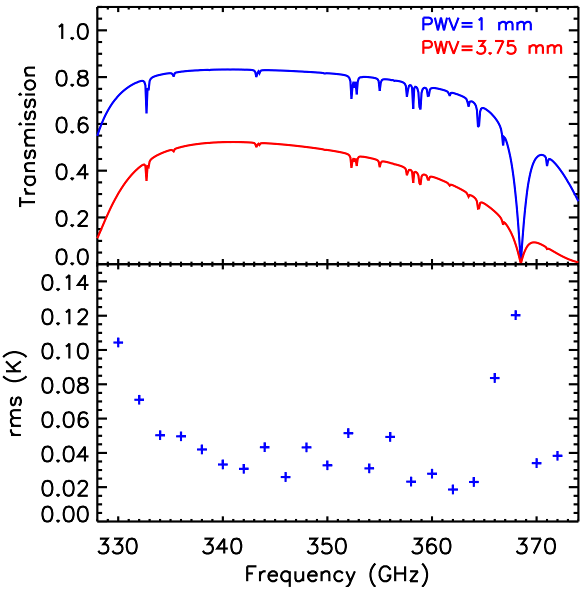

Figure 2.1 — The typical rms noise levels in T_{A}^{*} units measured in the SLS survey as a function of the frequency (bottom panel) and the corresponding atmospheric transmission for typical levels of water vapor at Mauna Kea (top panel).

ysed positions other then the center include the eastern tail (RA(J2000) = $19^{\mathrm{h}}10^{\mathrm{m}}16.^{\mathrm{s}}6$; Dec(J2000) = $09°05'48''$), northern clump (RA(J2000) = $19^{\mathrm{h}}10^{\mathrm{m}}13.^{\mathrm{s}}6$; Dec(J2000) = $09°06'48''$) and southwest clump (RA(J2000) = $19^{\mathrm{h}}10^{\mathrm{m}}10.^{\mathrm{s}}6$; Dec(J2000) = $09°05'18''$). These positions were selected based on different kinematical signatures traced by dense gas tracers such as HCO^{+}, HCN, and HNC (Roberts et al. 2011) and are shown for example on Fig. 2.3. Appendix 2.6 shows details on the detected species in the frequency range between 360 and 373 GHz, in the SLS and in its high frequency extension toward the center of W49A. We added a comment when the lines were detected in the high-mass protostar AFGL 2591, another source of the JCMT SLS, based on Van der Wiel (2011). The spectroscopic data are based on the Cologne Database for Molecular Spectroscopy (CDMS, Müller et al. 2005)[3] and the Jet Propulsion Laboratory (JPL, Pickett et al. 1998)[4] molecular databases. The identification is based on an initial search range of transitions with an upper level energy of 400 K, and was extended in particular cases such as vibrationally excited lines of HCN and HNC. In the case of weak ($\lesssim 3\sigma$ detections) lines, an additional check of the spatial distribution and a cross-check of the detection

---

[3] `http://www.astro.uni-koeln.de/cdms/catalog`

[4] `http://spec.jpl.nasa.gov`

in data corresponding to different rest frequencies was applied to avoid possible artifacts e.g. spurs or baseline errors.

Toward the center we detected 260 lines in the 360-373 GHz frequency range, that belong to 60 molecular species summarized in Table 2.1. Most of the detected molecules are sulphur-bearing species, such as SO_2 and its isotopologues. Various species are detected that indicate the possible importance of shock- and hot core chemistry and UV irradiation (see Sect. 6.4). The detected transitions cover a large energy range up to ~1067 K corresponding to vibrationally excited HCN (Fuller et al, in prep.). However, most transitions have upper level energies below 400 K (Fig. 2.2). Excitation conditions can be probed for 16 species (Table 2.2) based on multiple detected transitions with a sufficient energy range.

To measure the spatial extent of the detected species, we apply a 2-dimensional Gaussian fit to the integrated line intensities, using the BEAMFIT task in Starlink. The values shown in Table 2.1 correspond to the FWHM (full width at half maximum) values of the fit. For molecules with multiple detected transitions we include their largest spatial extent. In addition to CO and its isotopologues, high density tracers (e.g. HCN, HNC, CS, HCO^+) and tracers of UV-irradiation (e.g. CN and C_2H) show the largest spatial extent (Table 2.1). The measured position angles cover a large range indicating a complex source structure. Section 2.3.2 includes a summary of the detected molecules. We discuss the excitation conditions and column densities of the species with multiple detected transitions in Section 2.3.4.

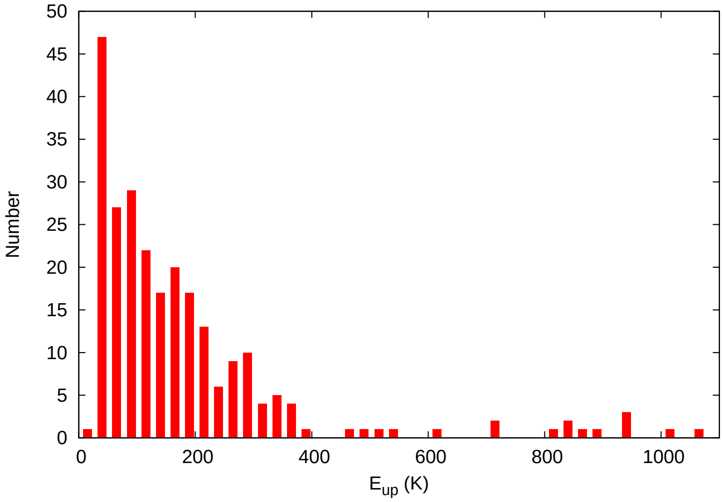

Figure 2.2 — The number of lines corresponding to a range of upper level energies in 25 K bins.

Table 2.1: The spatial extent of the species detected toward the center of W49A. The position angle is measured from North through East.

Species	Number of transitions	E_{up} (K)	Spatial extent		
			Major axis (″)	Minor axis (″)	Pos. angle (deg)
SO_2	39	31−612	13.6±0.4	12.2±0.4	105.2±0.2
$^{33}SO_2$	18	35 – 338	16.4±0.5	15.1±0.5	82.4±0.3
$^{34}SO_2$	33	35 – 547	15.5±0.4	14.4±0.4	170.4±0.3
$SO^{18}O$	4	117 – 326	14.5±0.2	13.3±0.2	100.0±0.1
$SO^{17}O$	6	58 – 180	12.8±10.1	5.1±12.2	56.8±11.4
SO_2, v_2=1	8	805 – 998	13.9±2.8	11.9±2.4	125.6±25.1
SO	6	26 – 143	18.6±0.2	16.5±0.2	74.1±0.1
^{34}SO	5	25 – 85	15.5±0.2	15.1±0.2	112.1±0.4
OCS	3	237 – 271	25.1±1.1	15.4±0.7	50.8±0.1
HNCO	7	127 – 204	15.2±0.9	12.1±0.7	134.6±0.2
CH_3OH	24	17 – 372	29.9±0.9	20.5±0.6	63.8±0.1
CH_3CN	5	151 – 215	23.1±0.9	13.9±0.5	57.4±0.1
H_2CO	7	52 – 241	28.6±0.7	21.2±0.5	64.1±0.1
H_2CS	6	91 – 209	30.0±1.4	17.3±0.8	141.5±0.1
CH_3CCH	4	172 – 254	20.3±4.1	13.0±2.6	118.1±23.6
HC_3N	3	307 – 376	12.1±2.4	10.1±2.0	160.0±32.0
NO	3	36 – 209	29.1±0.7	22.9±0.5	62.4±0.1
^{33}SO	3	78 – 87	32.8±6.5	12.7±2.5	111.5±22.3
$S^{18}O$	3	91 – 99	17.5±0.9	16.3±0.8	141.9±0.6
CN	3	33	54.4±1.6	38.8±1.1	76.9±0.1
C_2H	3	42	60.9±1.9	46.4±1.4	78.8±0.1
H_2S	2	135 – 263	18.9±0.3	15.3±0.2	70.2±0.1
$H_2^{13}CO$	2	61 – 65	19.7±1.5	15.4±1.2	42.2±0.2
HNC, v_2=1	2	709 – 710	17.2±0.9	12.9±0.7	139.5±0.1
CO	1	33	97.6±3.8	60.3±1.5	89.7±0.1
^{13}CO	1	32	71.6±1.9	54.0±1.2	86.9±0.1
$C^{17}O$	1	32	38.7±1.0	27.8±0.7	68.6±0.1
HCN	1	43	37.2±0.8	27.1±0.6	75.6±0.1
HNC	1	43	31.1±0.8	23.1±0.6	67.4±0.1
HCO^+	1	43	32.3±0.7	26.4±0.5	179.0±0.1
CS	1	66	38.9±0.8	24.3±0.5	69.8±0.1
N_2H^+	1	45	23.4±0.7	17.3±0.5	15.7±0.1

Continued on next page

Table 2.1: The spatial extent of the species detected toward the center of W49A. The position angle is measured from North through East.

Species	Number of transitions	E_{up} (K)	Spatial extent Major axis (″)	 Minor axis (″)	 Pos. angle (deg)
^{13}CS	1	80	20.8±1.3	15.0±0.9	146.9±0.1
H_3O^+	1	140	17.0±0.7	15.9±0.7	75.3±0.5
SiO	1	75	18.0±0.3	16.0±0.3	1.7±0.1
$C^{34}S$	1	65	27.5±1.1	18.1±0.7	68.5±0.1
$^{13}CH_3OH$	1	45	14.1±0.4	13.1±0.4	20.8±0.3
HCS^+	1	74	21.1±7.1	10.7±3.4	155.4±0.3
$H^{13}CN$	1	41	17.5±0.3	15.1±0.3	111.3±0.1
SO^+	1	70	15.6±0.6	13.4±0.6	88.2±0.2
$O^{13}C^{34}S$	1	247	13.6±2.7	13.0±2.6	132.5±6.5
$HC^{15}N$	1	41	21.2±0.8	15.8±0.6	62.1±0.1
NS	1	70	29.2±14.2	21.8±11.2	9.4±7.1
$H^{13}CO^+$	1	42	22.6±0.4	20.1±0.4	81.1±0.1
$HN^{13}C$	1	42	20.2±1.0	15.8±0.8	162.3±0.1
HCN, v_2=1	1	1067	15.9±0.4	14.7±0.3	151.5±0.2
t-HCOOH	1	144	16.4±1.0	15.0±1.0	6.0±0.6
DCN	1	52	36.3±51.7	12.6±53.5	145.8±29.2
HCO	1	74	16.3±0.6	14.1±0.5	22.6±0.2
CO^+	1	34	14.9±3.0	11.2±2.2	83.1±16.6
H_2CN	3	53 – 100	$\lesssim 15''$	$\lesssim 15''$	——
CH_3OCH_3	2	48 – 49	$\lesssim 15''$	$\lesssim 15''$	——
$S^{17}O$	2	76 – 103	$\lesssim 15''$	$\lesssim 15''$	——
CH_3CHO	2	155 – 250	$\lesssim 15''$	$\lesssim 15''$	——
$H^{15}NC$	1	43	$\lesssim 15''$	$\lesssim 15''$	——
$HC^{17}O^+$	1	42	$\lesssim 15''$	$\lesssim 15''$	——
C_2H_5CN	1	153	$\lesssim 15''$	$\lesssim 15''$	——
$HO^{13}C^+$	1	41	$\lesssim 15''$	$\lesssim 15''$	——
$HC^{18}O^+$	1	41	$\lesssim 15''$	$\lesssim 15''$	——
$H_2C^{34}S$	1	118	$\lesssim 15''$	$\lesssim 15''$	——
CH_3COCH_3	1	282	$\lesssim 15''$	$\lesssim 15''$	——
$H_2^{33}S$	1	154	$\lesssim 15''$	$\lesssim 15''$	——
$H_2^{34}S$	1	154	$\lesssim 15''$	$\lesssim 15''$	——

2.3.2 The detected species

The detected species summarized in Table 2.1 can be related to various processes including shocks, UV-irradiation by the embedded OB stars, and to hot core chemistry that includes complex organic molecules that are released from the grains into the gas-phase at temperatures of 100-300 K and are shielded from the dissociative UV-radiation.

Shock tracers

A large number of the detected molecules can be related to shock chemistry (Fig. 2.3). All of these molecules are observed toward a $\lesssim 20'' \times 20''$ field around the center, but not detected toward the other subregions analysed in this paper.

- SiO was detected in hot and shocked regions, such as molecular outflows (e.g. Nisini et al. 2007) and supernova remnants (e.g. Ziurys et al. 1989). The observations suggest that silicon is released from grain mantles in these regions. A process that can release silicon into the gas phase is the sputtering of (charged) grains by heavy neutral particles in C-shocks (Schilke et al. 1997, Gusdorf et al. 2008). SiO is detected toward W49A with a spatial extent of $\sim 18'' \times 16''$ covering the positions corresponding to the central stellar cluster in its $J = 8 - 7$ transition. Its $J = 2 - 1$ transition has previously been detected toward W49A by Lucas & Liszt (2000).

- Most of the detected species are sulphur-bearing molecules, such as SO and SO_2 and their isotopologues $^{34}SO_2$, $^{33}SO_2$, $SO^{17}O$, $SO^{18}O$, ^{34}SO, ^{33}SO, $S^{17}O$, and $S^{18}O$. Sulphur is frozen onto grain mantles and can be evaporated by shocks, leading to the formation of the species mentioned above (e.g. Scalo & Slavsky 1980, Millar & Herbst 1990). We also detected 8 transitions of vibrationally excited SO_2. These molecules are only detected toward the center of W49A and spatially confined to a region of $\lesssim 20'' \times 20''$, similar to SiO.

- Other detected sulphur-bearing species include H_2S, OCS (and its isotopologue $O^{13}C^{34}S$). H_2S and OCS show spatial extents similar to that of SO_2, SO, and their isotopologues; and to SiO.

- We also detected SO^+, which has been reported to be a diagnostic of dissociative shock chemistry (Turner 1992), but has also been detected toward various PDRs (see Sect. 2.3.2).

- We detected 6 transitions of HNCO, which has also been reported to trace shocks toward the Galactic Center and in molecular outflows, such as L1157 (Rodríguez-Fernández et al. 2010).

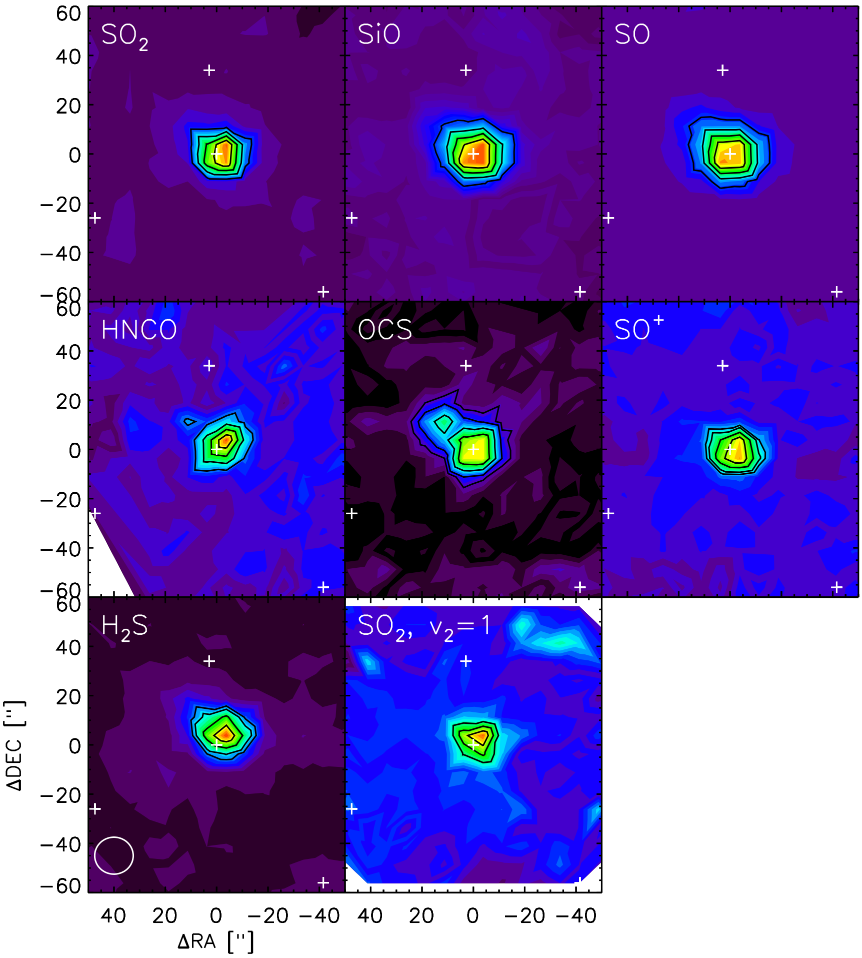

Figure 2.3 — The spatial distribution of species that can be related to shock chemistry. The crosses correspond to the subregions discussed in this chapter: source center, eastern tail, northern clump, and south-west clump. The contours correspond to the 20%, 40%, 60%, and 80% of the maximum line intensity.

Tracers of UV-irradiation

The embedded clusters of O and B stars in the W49 region are expected to create PDRs. Several species that can be related to PDR chemistry are detected in the SLS frequency range (Fig. 2.4), some of them with a significant spatial extent.

- We detected CN with a large extent (∼54″×39″), including all subregions. It suggests the possible importance of PDR chemistry in W49A and may be tested using the ratio of CN/HCN, which is a well-known tracer of PDRs (e.g. Fuente et al. 1996). The spatial distribution of HCN and its isotopomer HNC based on SLS data were analysed in Roberts et al. (2011).

- C_2H (ethynyl) is a commonly observed molecule in the interstellar medium, including PDRs. In star-forming regions it was proposed to be related to the earliest stages of massive star-formation (Beuther et al., 2008). We detected three transitions toward W49A, with a very large spatial extent (∼61″ × 46″).

- HCO (formyl radical) is also detected in a ∼16″ × 14″ region around the center. HCO was found to be a tracer of illuminated cloud interfaces as it was detected in several PDRs including the Orion Bar, NGC 2023, NGC 7023, and S140 (Schilke et al. 2001) and the Horsehead PDR (Gerin et al. 2009).

- The SO^+ and CO^+ reactive ions have been detected in various PDRs, such as the Orion Bar (Fuente et al. 2003), and in other regions of high FUV- and X-ray irradiation. We detected both CO^+ and SO^+ toward the center of W49A with a spatial extent of $\lesssim$15″ × 15″.

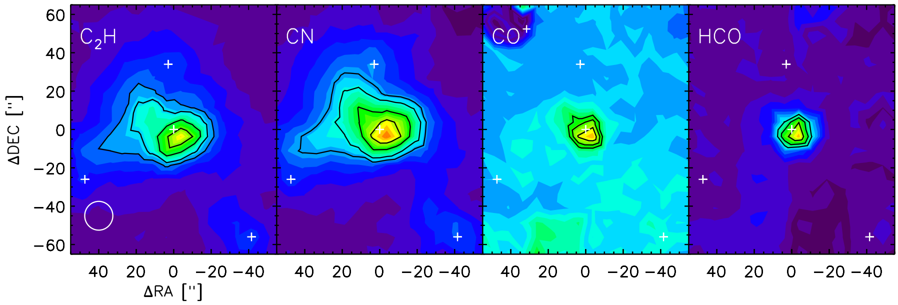

Figure 2.4 — The spatial distribution of species that can be related to PDR chemistry. The crosses correspond to the subregions discussed in this chapter: source center, eastern tail, northern clump, and south-west clump. For C_2H and CN the contours correspond to the 30%, 40%, 60%, and 80% of the maximum line intensity. For CO^+ and HCO the contours correspond to the 45%, 60%, and 80% of the maximum line intensity.

Complex organic molecules

We have detected a number of complex organic molecules (e.g. Herbst & Van Dishoeck 2009), that are most likely related to hot cores.

- H_2CO (formaldehyde) is a commonly used temperature and density tracer in Galactic star-forming regions (e.g. Mangum & Wootten 1993) and in external galaxies (e.g. Mangum et al. 2008) as well. Previous results from this line survey focused on this molecule, which revealed a large ~3×3 pc region around the W49A center with kinetic temperatures of >100 K and densities of $>10^5$ cm^{-3} (Nagy et al. 2012, Chapter 3). Its isotopologue $H_2^{13}CO$ is also detected toward the center.

- Similar to H_2CO, H_2CS (thio-formaldehyde) is a near-prolate rotor, which allows estimation of both kinetic temperature and density. Though its spatial extent ($30'' \times 17''$) given by a 2D Gaussian fit toward the center is similar to that of H_2CO, H_2CS was not detected toward the other main regions (Eastern tail, Northern clump, and Southwest clump). Its isotopologue $H_2C^{34}S$ is also detected.

- CH_3OH is detected over a $30'' \times 20''$ region around the center. Its spatial distribution is shown in Chapter 3 (Nagy et al. 2012). Its $^{13}CH_3OH$ isotopologue is also detected.

- We detected 5 transitions of CH_3CN (methyl cyanide), that has been detected in a number of hot cores, including Orion KL. The $J = 12 - 11$ transition of CH_3CN was previously detected toward W49 using the BIMA array and is likely connected to hot cores and also follows the compact dust concentrations (Wilner et al. 2001).

- We detected four transitions of HC_3N (cyanoacetylene), that has been detected toward various Galactic star forming regions. It has also been detected in a number of obscured galaxies (Lindberg et al. 2011). As it is destroyed by UV radiation and in reactions with the C^+ ion, it is expected to trace warm, dense, and shielded regions. This may explain the fact that H_3CN is seen to be confined toward the central $<15'' \times 15''$ region.

- Two transitions of CH_3CHO (acetaldehyde) are detected toward the W49A center. A previous survey by Ikeda et al. (2001) detected this molecule toward various hot molecular clouds.

- Four transitions of CH_3CCH (propyne) are detected in our line survey at a few central pixels with a spatial extent of $\sim 20'' \times 13''$. This molecule has been detected in a number of starburst galaxies, such as M82 (Aladro et al. 2011a).

- We detected HCOOH (formic acid) toward a ∼16″ × 14″ region around the W49A center. The effect of outflow shocks on its abundance is probable, as it has been detected toward the L1157 molecular outflow (Arce et al. 2008).

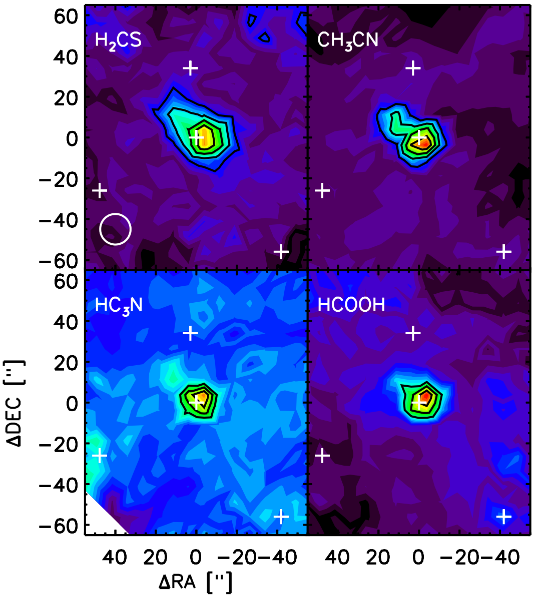

Figure 2.5 — The spatial distribution of the detected most spatially extended complex organic molecules. The crosses correspond to the subregions discussed in this chapter: source center, eastern tail, northern clump, and south-west clump. For H_2CS and CH_3CN the contours correspond to the 20%, 40%, 60%, and 80% of the maximum line intensity. For HC_3N and HCOOH the contours correspond to the 40%, 60%, and 80% of the maximum line intensity.

Other detected species

- CO, ^{13}CO, and $C^{17}O$ are covered by the SLS survey, and are detected at each position of the SLS field (Figue 2.7), allowing us to probe the gas kinematics and column density.

- The only deuterated species we detected toward W49A is DCN (Roberts et al. 2011). An upper limit for the covered but not detected DCO^+ J=5-4 transition was also reported by Roberts et al. (2011). A low abundance of deuterated ions is expected as deuterated molecular ions are destroyed rapidly at gas temperatures above 30 K (e.g. Roberts & Millar 2007).

- We detected a few ions, including HCO^+ and its isotopologues $HC^{18}O^+$, $H^{13}CO^+$, and $HC^{17}O^+$. As a dense gas tracer, HCO^+ data in the SLS survey were analysed by Roberts et al. (2011). Other detected ions not mentioned in the sections above include H_3O^+ and N_2H^+. N_2H^+ shows a larger spatial extent than H_3O^+ covering the Eastern tail and Northern clump regions. H_3O^+ is an important chemical ingredient of molecular clouds as it can be related to the formation of water in the gas phase and is formed via OH^+ and H_2O^+ ions, that have recently been found to be important tracers of the cosmic-ray ionization rate in the diffuse interstellar medium (e.g. Neufeld et al. 2010, Gerin et al. 2010, Hollenbach et al. 2012). Strong emission lines of OH^+, H_2O^+, and H_3O^+ ions are also found in AGNs (e.g. Van der Werf et al. 2010).

- CS is a well-known tracer of dense gas that has been analysed both in Galactic star-forming regions (e.g. Helmich & van Dishoeck 1997) and in external galaxies, including starburst galaxies (e.g. Aladro et al. 2011b). Multiple rotational transitions of CS have previously been studied in W49A by Serabyn et al. (1993), leading to the idea that the large star-formation activity in W49A has been triggered by a cloud-cloud collision. CS J=7-6 has been detected toward W49A with a spatial extent of $\sim 40'' \times 24''$. Its isotopologues ^{13}CS and $C^{34}S$ have also been detected in the SLS survey.

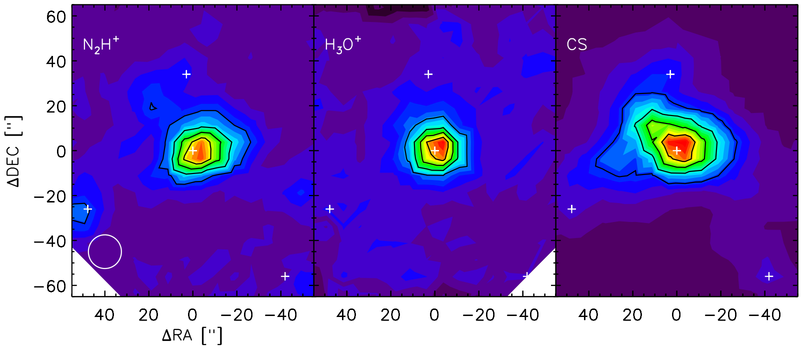

Figure 2.6 — The spatial distribution of N_2H^+ and H_3O^+ ions and CS. The crosses correspond to the subregions discussed in this chapter: source center, eastern tail, northern clump, and south-west clump. The contours correspond to the 20%, 40%, 60%, and 80% of the maximum line intensity.

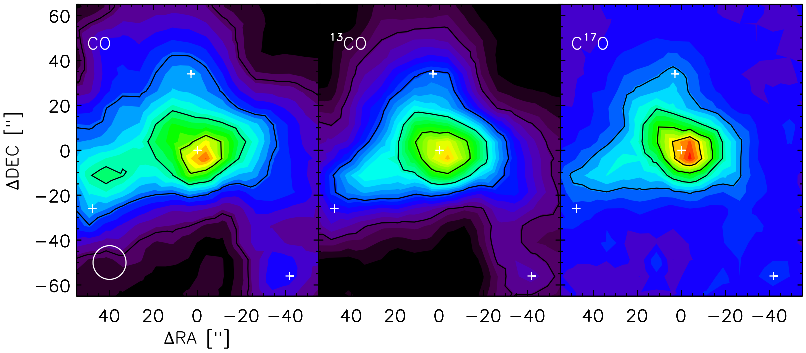

Figure 2.7 — The spatial distribution of CO, ^{13}CO, and C^{17}O line emission. The crosses correspond to the subregions discussed in this chapter: source center, eastern tail, northern clump, and south-west clump. The contours correspond to the 20%, 40%, 60%, and 80% of the maximum line intensity.

2.3.3 Line profiles and velocity structure

Figure 2.8 shows typical line profiles observed toward the various subregions of W49A for the most spatially extended molecular lines, with the exception of HCN, HNC, and HCO$^+$ that were analysed in Roberts et al. (2011). Most of the detected lines are double-peaked or asymmetric. While lines observed toward the center and the South-West clump peak around the source velocity of ∼7-8 km s^{-1} (e.g. Roberts et al. 2011 and references therein), line emission is seen mainly blue-shifted toward the Eastern tail, and red-shifted toward the Northern clump, similar to what is seen for HNC, HCN, and HCO$^+$, and their isotopologues (Roberts et al. 2011). Infall signatures have been observed toward the source center in HCO$^+$ 1-0 (Welch et al. 1987, Serabyn et al. 1993) and in the SLS survey traced by HCN 4-3 and 3-2, HNC 4-3, and HCO$^+$ 4-3 (Roberts et al. 2011). Though most observed lines show an excess emission in the blue-shifted wing of the line profile toward the source center, typical infall profiles are best probed by HCN 4-3 and 3-2, HNC 4-3, and HCO$^+$ 4-3.

To investigate the velocity distribution of the observed line emission, we obtained channel maps for the species shown on Fig. 2.8. CO 3-2 shows emission in a large range of velocities between -25 and 35 km s^{-1} (Fig. 2.9). The most extended line emission is seen around the expected source velocity, in the range between +5 and +10 km s^{-1}. Toward the Eastern tail, significant blue-shifted line emission is seen at velocities between -5 and 0 km s^{-1}. The Northern clump is more prominent at velocities of ∼20 km s^{-1}, but also shows significant emission around the source velocity. The South-west clump is only seen around the expected source velocity (between 5 and 10 km s^{-1}). Significant line emission is seen at a velocity of +15 km s^{-1} that does not correspond to any of the analysed subregions, including the center. The ^{13}CO 3-2 line shows a very similar structure (Fig 2.10) to that traced by CO 3-2 with the main difference at a velocity of +15 km s^{-1}, likely related to a self-absorption of the optically thick CO 3-2 lines around the center.

Lines that show spatially extended emission other than CO and ^{13}CO are distributed over the velocity range between -5 and +20 km s^{-1} (Fig. 2.11). The strongest emission is seen in CN, especially the redshifted wings of the CN lines. While other molecules show emission toward the center and the Northern clump at a velocity of +15 km s^{-1}, CN emission at this velocity is also detected toward the South-west clump.

2.3.4 Excitation and column densities

Table 2.2 includes a number of species with at least three detected transitions covering a sufficient energy range to probe excitation conditions. We estimate the excitation conditions of these molecules using the population diagram method introduced by Goldsmith & Langer (1999). Column densities ($N_{\rm tot,1}$) and excitation temperatures ($T_{\rm ex}$) can be estimated based on

$$\ln\left(\frac{N_u}{g_u}\right) = \ln\left(\frac{N_{\rm tot,1}}{Q_{\rm rot}}\right) - \frac{E_u}{kT_{\rm ex}} + \ln\left(\frac{\Omega_s}{\Omega_a}\right) - \ln\left(C_\tau\right), \tag{2.1}$$

where N_u is the observed upper state column density of the molecule including line opacity and beam-source coupling effects; g_u is the degeneracy of the upper state; $Q_{\rm rot}$ is the rotational partition function; k is the Boltzmann constant; E_u is the upper level energy; $f = \Omega_s/\Omega_a$ is the source filling factor with $\Omega_a \sim 15''$ the beam solid angle and Ω_s the solid angle of the source; and $C_\tau = \tau/(1 - e^{-\tau})$ where τ is the optical depth. For a uniform beam filling ($\Omega_a \sim \Omega_s$) and low optical depth, Eqn. 3.2 reduces to a rotational diagram with a rotational temperature $T_{\rm rot}$ and total column density $N_{\rm tot}$. We evaluate Eqn. 3.2 for a set of $N_{\rm tot,1}$, $T_{\rm ex}$, f and C_τ ($N_{\rm tot,1}$, $T_{\rm ex}$). We apply Ω_s in the range between $1''$ and $15''$ (uniform beam filling) and a column density in the range between 10^{12} cm^{-2} and 10^{18} cm^{-2}. For molecules with just three detected transitions we use $T_{\rm rot} = T_{\rm ex}$ to derive a best fit source size and column density.

The results are summarized in Table 2.2. The rotation- and population diagrams are shown on Fig. 2.12 and 2.13. Most molecular lines have excitation temperatures between ~100 and ~200 K with H_2CO, H_2CS, and SO^{18}O showing the highest excitation. The population diagrams suggest a non-uniform beam filling in several cases and result in emission originating in regions of ~1-4$''$, that are consistent with the sizes of hot cores and UCHII regions revealed by high resolution studies (e.g. Wilner et al. 2001). Together with the spatially extended emission seen in the maps, this is evidence that the gas in W49A has a clumpy structure.

CH_3CCH has a very low excitation temperature toward the center (~32 K) suggesting an origin from a colder material around the central cluster of UC

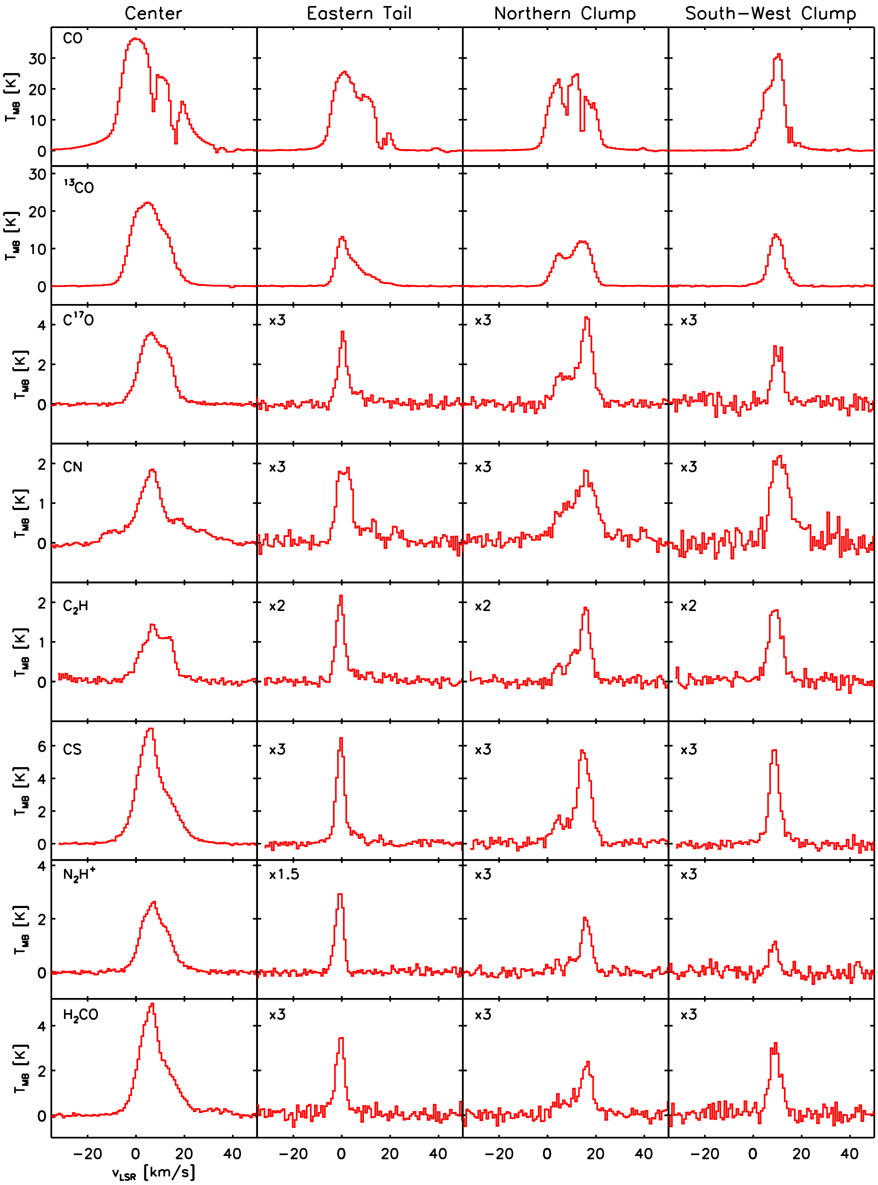

Figure 2.8 — Line profiles of molecules observed toward the various subregions of W49A.

HII regions and hot cores. CH_3CCH was also found to originate in a lower excitation component toward Sgr B2, Orion and DR 21 (Churchwell & Hollis

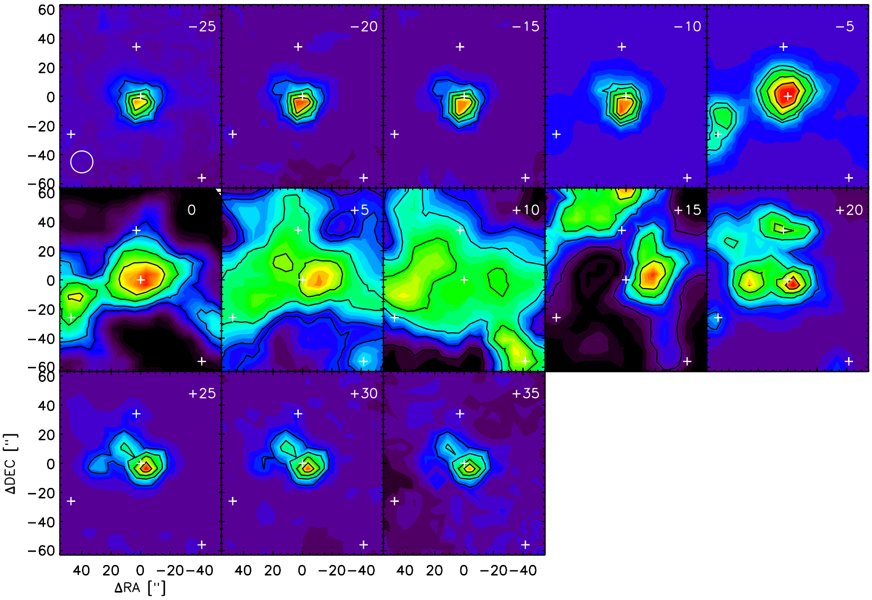

Figure 2.9 — Channel maps of CO 3-2 obtained with the JCMT at a resolution of ∼15″ at the overplotted velocities (in km s^{-1}).

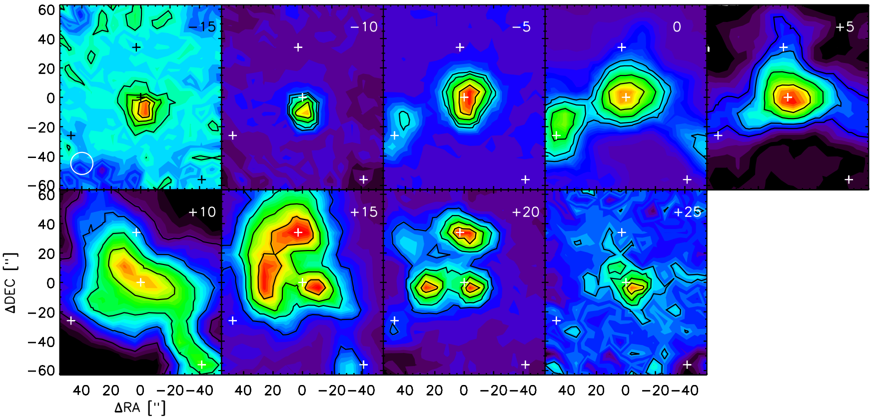

Figure 2.10 — Channel maps of ^{13}CO 3-2 obtained with the JCMT at a resolution of ∼15″ at the overplotted velocities (in km s^{-1}).

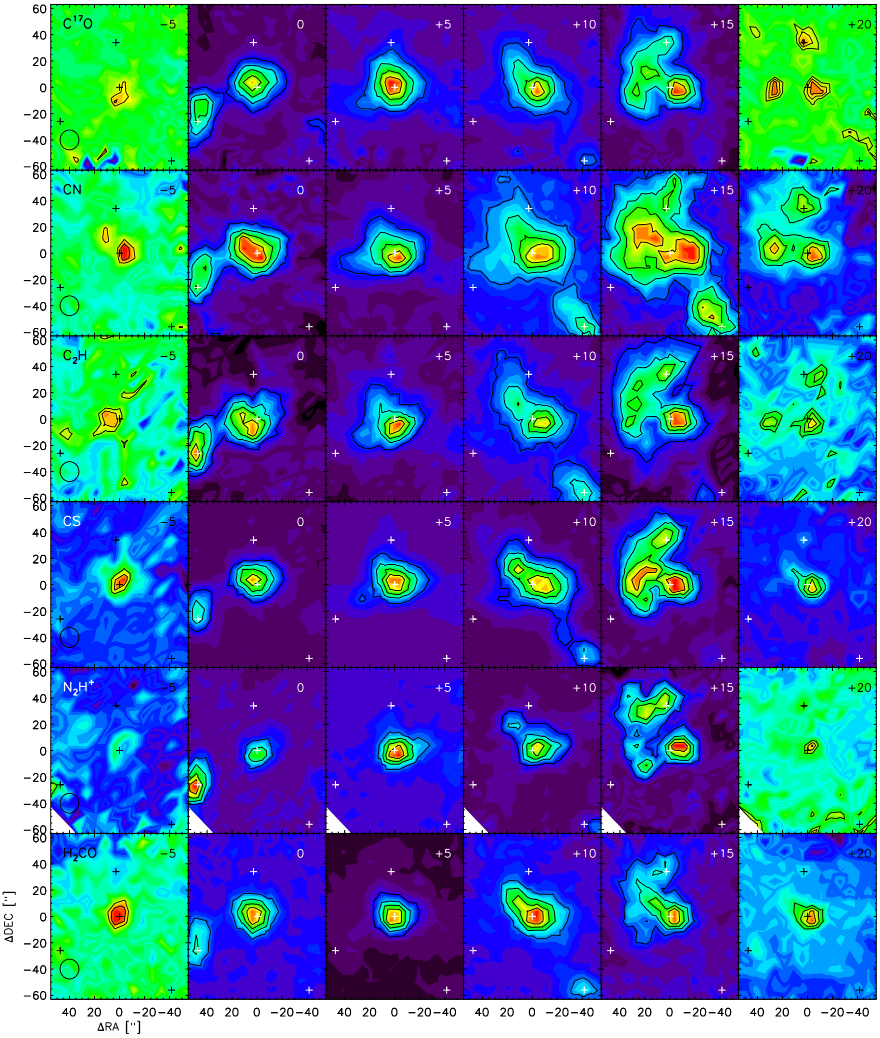

Figure 2.11 — Channel maps of the most spatially extended species in the SLS obtained with the JCMT at a resolution of ∼15″ at the overplotted velocities (in km s^{-1}).

1983). The other species that shows a very low excitation temperature is ^{34}SO ($T_{\rm ex}$ ∼ 32.6 K). Results for SO are not listed in Table 2.2 as the detected SO transitions are not consistent with a single excitation temperature. This may suggest that some of the detected SO lines originate in the low excitation component suggested by the ^{34}SO lines, and the others from the high-excitation

($\gtrsim$100 K) component that most detected molecular lines originate in. Apart from different excitation conditions, gas components with different source sizes (beam-filling factors) may contribute to the observed line emission, as suggested by the large range of source sizes corresponding to the different sulphur-bearing molecules. Distinguishing between these explanations requires observations of more SO transitions.

Differences in the excitation of the subregions (Northern clump, Eastern tail, and South-west clump) are well traced by H_2CO, as more of its transitions were detected with a spatial extent large enough to include the discussed subregions. More details are shown in Nagy et al. (2012) (Chapter 3).

For molecules with no information available on their excitation we derive a column density in the LTE approximation, assuming rotation temperatures in the range between 75 K and 150 K, as most molecules with multiple detected transitions have rotation temperatures that fall into this range. Then we derive column densities using:

$$N_{\rm tot} = \frac{8\pi k\nu^2}{hc^3}\frac{Q(T_{\rm rot})}{g_u A_{\rm ul}} e^{E_u/kT_{\rm rot}} \int T_{\rm mb} d{\rm v} \tag{2.2}$$

Table 2.3 includes a selection of molecules that have been detected in AGNs, starburst galaxies, and in Galactic star-forming regions. The line intensities were obtained using a Gaussian fit for nearly Gaussian line profiles. For double-peaked or asymmetric line profiles, the velocity-integrated intensity is used to calculate column densities. The error of these column densities is about a factor of 2, dominated by the uncertainty in $T_{\rm ex}$. The optically thin approximation results in an under-estimate of the column densities for some of the species detected toward the center, such as for CS or CN. The CS column density is under-estimated by a factor of $\sim$3, by applying the observed $N(\mathrm{C}^{34}\mathrm{S})$ and an isotopic ratio of $^{32}\mathrm{S}/^{34}\mathrm{S}$ of 22 (Frerking et al. 1980). The column density of CN cannot be constrained as no isotopologue of CN has been detected in the SLS survey. Therefore, the value derived from CN is a lower limit of the CN column density. We discuss these column densities in more details in Sect. 6.4.

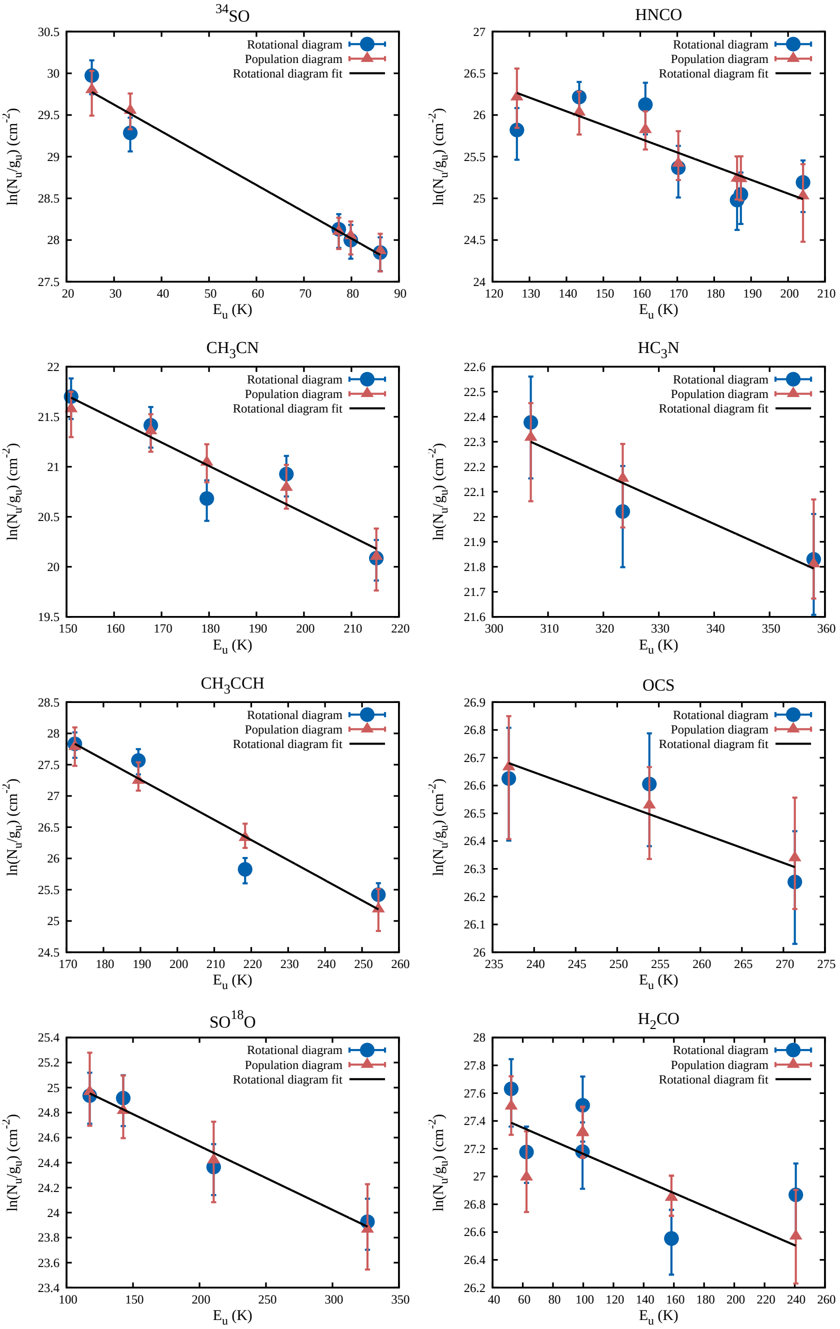

Figure 2.12 — Rotation and population diagram plots toward the center. For CH$_3$OH, H$_2$CO, and SO$_2$ the transitions from the high-frequency extension of the SLS (between 360-373 GHz) were originally analyzed in Nagy et al. (2012).

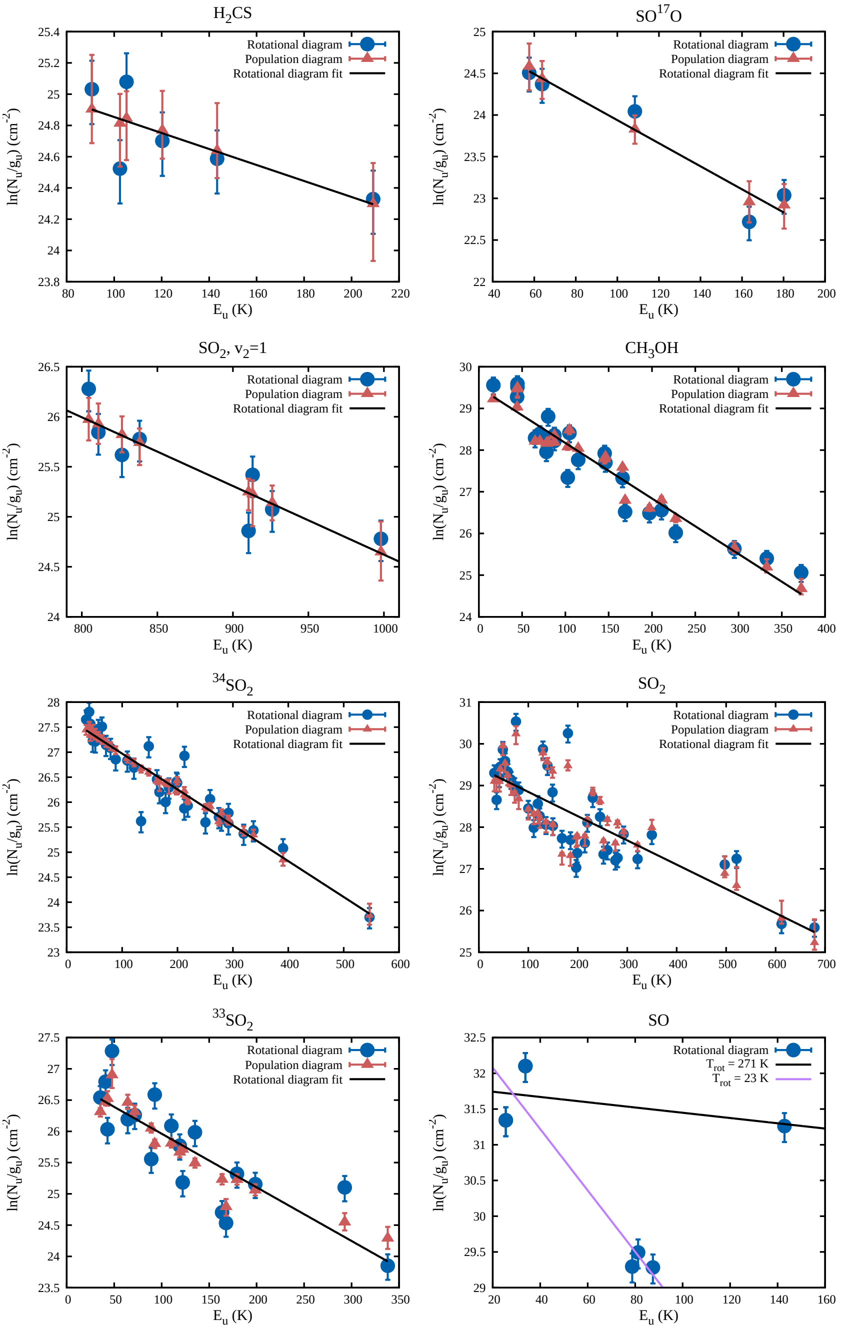

Figure 2.13 — Figure 2.12 continued.

Table 2.2 — Results of the rotation and population diagram analysis for molecules with multiple transitions.

Species	T_{rot} (K)	N_{tot} (cm^{-2})	T_{ex} (K)	$N_{\mathrm{tot,1}}$ (cm^{-2})	Source size ($''$)	Optical depth
SO_2[b]	172±21	$(3.1 \pm 0.02) \times 10^{16}$	122^{+24}_{-9}	$2.1^{+1.1}_{-0.0} \times 10^{18}$	$2.9^{+0.0}_{-0.5}$	0.03-8.9
$^{34}SO_2$	140±9	$(4.0 \pm 0.02) \times 10^{15}$	133±11	$4.8^{+11.8}_{-4.3} \times 10^{16}$	$4.3^{+9.3}_{-1.9}$	0.01-0.2
CH_3OH[b]	75±5	$(7.7 \pm 0.04) \times 10^{15}$	65^{+7}_{-2}	$5.0^{+0.0}_{-0.6} \times 10^{17}$	2.4^{+0}_{-0}	0.14-2.69
$^{33}SO_2$	117±20	$(1.3 \pm 0.01) \times 10^{15}$	108±16	$5.0^{+1.6}_{-0.6} \times 10^{17}$	1.0±0.0	0.5-3.2
SO_2, v_2=1	146±28	$(1.9 \pm 0.07) \times 10^{17}$	146^{+61}_{-34}	$1.9^{+500}_{-1.3} \times 10^{17}$	$14.5^{+0.5}_{-13.5}$	0.001-0.005
H_2CO[b]	213±96	$(8.6 \pm 0.09) \times 10^{14}$	159^{+90}_{-51}	$1.4^{+2.0}_{-1.2} \times 10^{16}$	$3.3^{+4.9}_{-0.7}$	0.10-1.50
HNCO	61±20	$(4.9 \pm 0.2) \times 10^{14}$	54^{+43}_{-34}	$7.6^{+6599}_{-3.8} \times 10^{14}$	$12.7^{+2.3}_{-9.8}$	0.01-0.05
$SO^{17}O$[c]	72±13	$(1.4 \pm 0.02) \times 10^{14}$	97^{+45}_{-73}	$6.31^{+87}_{-6.29} \times 10^{16}$	1^{+14}_{-0}	1.0-2.2
H_2CS	196±85	$(1.6 \pm 0.02) \times 10^{14}$	195^{+104}_{-97}	$1.7^{+723}_{-0.5} \times 10^{14}$	$14.5^{+0.7}_{-13.5}$	0.001-0.005
CH_3CN	70±30	$(1.1 \pm 0.1) \times 10^{13}$	69^{+94}_{-27}	$3.1^{+16.9}_{-1.1} \times 10^{14}$	$3.0^{+0.0}_{-1.6}$	0.16-0.27
^{34}SO	31±3	$(5.9 \pm 0.04) \times 10^{14}$	33^{+8}_{-6}	$6.2^{+16.7}_{-1.2} \times 10^{14}$	$15.0^{+0.0}_{-7.5}$	0.01-0.22
$SO^{18}O$	196±26	$(8.4 \pm 0.05) \times 10^{14}$	173^{+126}_{-105}	$1.91^{+7.4}_{-1.89} \times 10^{17}$	$1.0^{+14.0}_{-0.0}$	0.20-0.70
CH_3CCH	31±7	$(2.8 \pm 0.1) \times 10^{16}$	32 ± 7	$2.6^{+91}_{-1.4} \times 10^{16}$	$15.0^{+0.0}_{-12.1}$	0.01-0.03
HC_3N	101±39	$(4.7 \pm 0.2) \times 10^{13}$	101[a]	$4.8^{+737}_{-0.6} \times 10^{13}$	$15.0^{+0.0}_{-13.5}$	0.004-0.006
OCS	92±46	$(1.6 \pm 0.08) \times 10^{15}$	92[a]	$1.7^{+953}_{-0.3} \times 10^{15}$	$14.4^{+0.6}_{-13.2}$	0.008-0.010

---

[a] Fixed parameter in the fit

[b] Transitions in the frequency range between 360 and 373 GHz were included in Nagy et al. (2012).

[c] The $SO^{17}O$ $15_{2,14}$-$14_{1,13}$ (358986.2 MHz) transition is not included as it is probably blended with $^{34}SO_2$ $15_{2,14}$-$14_{1,13}$ (358988 MHz)

Table 2.3 — Column densities toward the four analysed subregions of W49A (in case of detections) derived in the LTE approximation. The two values correspond to adopted temperatures of 75 K and 150 K, respectively. The error of these column densities is about a factor of 2 dominated by the uncertainty in T_{ex}.

Species	Column density (cm^{-2})			
	Center	Eastern tail	Northern clump	South-west clump
C_2H	$(1.73 - 2.75) \times 10^{15}$	$(3.81 - 6.04) \times 10^{14}$	$(5.67 - 9.01) \times 10^{14}$	$(5.23 - 8.31) \times 10^{14}$
NO	$(0.99 - 1.82) \times 10^{17}$	$(0.76 - 1.41) \times 10^{16}$	$(1.03 - 1.90) \times 10^{16}$	$(4.76 - 8.78) \times 10^{15}$
$H^{13}CN$	$(0.95 - 1.44) \times 10^{14}$	$(6.48 - 9.81) \times 10^{11}$	$(2.00 - 3.03) \times 10^{12}$	$(1.62 - 2.45) \times 10^{12}$
$H^{13}CO^+$	$(2.53 - 3.82) \times 10^{13}$	$(0.84 - 1.27) \times 10^{12}$	$(1.31 - 1.98) \times 10^{12}$	$(1.25 - 1.88) \times 10^{12}$
CN	$(1.40 - 2.24) \times 10^{15}$	$(3.02 - 4.83) \times 10^{14}$	$(4.29 - 6.86) \times 10^{14}$	$(3.68 - 5.89) \times 10^{14}$
N_2H^+	$(3.00 - 4.44) \times 10^{13}$	$(0.74 - 1.09) \times 10^{13}$	$(4.06 - 6.01) \times 10^{12}$	$(1.36 - 2.02) \times 10^{12}$
CS	$(4.37 - 5.62) \times 10^{14}$	$(4.74 - 6.09) \times 10^{13}$	$(7.47 - 9.60) \times 10^{13}$	$(4.84 - 6.22) \times 10^{13}$
$C^{34}S$	$(6.15 - 8.77) \times 10^{13}$	$(2.15 - 2.77) \times 10^{12\mathrm{a}}$	$(4.24 - 6.06) \times 10^{12}$	$(5.79 - 8.27) \times 10^{11}$
H_2S	$(4.91 - 4.89) \times 10^{15}$			
HCO	$(1.37 - 2.36) \times 10^{15}$			
CO^+	$(1.36 - 2.15) \times 10^{13}$			
HCS^+	$(1.78 - 2.17) \times 10^{13}$			
SO^+	$(4.41 - 5.65) \times 10^{14}$			
H_3O^+	$(4.79 - 5.25) \times 10^{14}$			
SiO	$(0.84 - 1.02) \times 10^{14}$			

---

[a] Based on $N(\mathrm{CS})$ and an isotopic ratio of $^{32}S/^{34}S$ of 22 (Frerking et al. 1980).

2.4 Discussion

We presented results from the SLS sub-mm line survey of a 2 × 2 arcminutes region of the Galactic starburst template W49A carried out with the JCMT at a resolution of $\sim 15''$ in the frequency range between 330 and 373 GHz. The data reveal a complex structure both in terms of kinematics and chemical composition. Molecular line tracers detected in the SLS frequency range can be related to various physical components including shocked regions and PDRs. Some of the detected molecules can be used for a comparison between the local starburst seen in W49A and global starburst phenomenon seen for some external galaxies.

2.4.1 The importance of UV irradiation

We probe the importance of UV-irradiation in the chemistry of W49A by a comparison of the observed column density ratios to values observed toward well-known Galactic PDRs, and by a comparison to predictions of PDR models.

For the comparison of column density ratios to those observed toward PDRs we select a sample of lines that have been observed both in the SLS survey and in multiple PDRs (Table 2.4). One of the most commonly used tracers of PDRs is the [CN]/[HCN] abundance ratio, which was found to be larger than unity in NGC 7023 (Fuente et al. 1993). An increase in the abundance ratio of [CN]/[HCN] in PDRs is a result of the production of CN via the photodissociation of HCN. Using the HCN column densities presented in (Nagy et al. 2012, Chapter 3) derived in a non-LTE approximation and CN column densities from Table 2.2, we estimate a [CN]/[HCN] abundance ratio of ~2.0-4.6 toward the Northern clump, ~3.8-6.9 toward the Eastern tail, and ~0.4-0.95 toward the South-West clump. The [CN]/[HCN]=0.04-0.07 toward the Center is underestimated due to optical depth effects not taken into account for the CN column density estimate. A non-LTE estimate (RADEX, Van der Tak et al. 2007) of the CN column density toward the center results in $N(\mathrm{CN}) = 4 \times 10^{15}$ cm^{-2}, indicating [CN]/[HCN]=0.55. The [CN]/[HCN] ratio of 0.55 indicates that the chemistry toward the center is only partially affected by UV-irradiation.

Though SiO is a tracer of shocks, it has been detected toward several PDRs as well (e.g. Schilke et al. 2001, Rizzo et al. 2005). Typical [SiO]/[H^{13}CO^{+}] abundance ratios of 0.03-0.37 were found toward Mon R2 (Rizzo et al. 2005), 0.54 toward NGC 7023 (Schilke et al. 2001), and 3-14 toward the Orion Bar (Schilke et al. 2001), based on detections toward multiple positions. We measure an [SiO]/[H^{13}CO^{+}] abundance ratio of 2.7-3.3 toward the W49A center. The HCO abundance with respect to the SiO abundance was found to be 50-720 in Mon R2 (Rizzo et al. 2005), while is in the range between 16 and 23 toward the W49A center. The [HCO]/[SiO] abundance ratio of >4.6-10 measured toward NGC 7023 (Schilke et al. 2001) is based on an upper limit for the SiO column density. The [HCO]/[SiO] abundance ratio toward the Orion Bar was measured to be 2-9, based on detections toward multiple positions. Though the large ($\sim$17 $\mathrm{km\,s^{-1}}$) line width of SiO detected toward the W49A center (Table 2.7) suggests its origin related to shocks rather than PDRs, the [HCO]/[SiO] and [SiO]/[$H^{13}CO^+$] abundance ratios do not confirm it.

The CO^+ ion is a tracer of warm ($T_{\mathrm{gas}} \gtrsim 500$ K) PDR surfaces, corresponding to the region of $A_V < 2$ mag (Fuente et al. 2003, Rizzo et al. 2003). We measure an abundance ratio of [CO^+]/[$H^{13}CO^+$] of 0.54-0.56. This is an upper limit on the [CO^+]/[$H^{13}CO^+$] ratio as the CO^+ line may be blended with $SO^{17}O$. Ginard et al. (2012) measure [CO^+]/[$H^{13}CO^+$]=0.53 in Mon R2, similar to that in the Orion Bar (0.52, based on Fuente et al. 1996 and Fuente et al. 2003) and to that in NGC 7023 (0.6, based on Fuente et al. 1993 and Fuente et al. 2003). The detection of CO^+ at several positions toward the center suggests the existence of a hot gas component directly exposed to UV-irradiation by a radiation field of $G_0 \sim 3 \times 10^5$ (Vastel et al. 2001).

HCS^+ was found to be abundant in PDRs (Ginard et al. 2012). We measure a CS abundance with respect to that of HCS^+ of $\sim$76-89. This is between the lower ratios of 11 and 25 found toward the ionization front and MP2 positions in Mon R2 (Ginard et al. 2012) and the higher [CS]/[HCS^+] ratio of 175 measured toward the Horsehead nebula (Goicoechea et al. 2006).

The sulphur-bearing species SO^+ and SO_2 can be related to shock chemistry, but have also been detected in several PDRs. In PDRs SO^+ is formed near the PDR surface (at $A_{\mathrm{V}} < 2$) through the reaction $S^+ + OH \rightarrow SO^+ + H$ and destroyed by dissociative recombination into S and O. SO and SO_2 form in the more shielded regions in the PDR. The [SO^+]/[SO_2] abundance ratio of <0.02 that we measured toward the center of W49A (based on the beam-averaged estimate for SO_2 in Table 2.2) is at least an order of magnitude below the value measured in several PDRs, such as in the Orion Bar ([SO^+]/[SO_2]$\sim$0.4-1, Fuente et al. 2003). This difference may also be interpreted as the effect of shocks on the SO_2 and SO^+ the abundances toward the W49 center.

The importance of FUV-irradiation in the chemistry of W49A can be probed by comparing the observed column density ratios to predictions of PDR models. Vastel et al. (2001) derive a radiation field toward the W49A center that is equivalent to $\chi = 3.5 \times 10^5 \chi_0$ in Draine (1978) units, with $\chi_0 = 2.7 \times 10^{-3}$ erg $\mathrm{s^{-1}\ cm^{-2}}$. We use the 1.4.4 version of the Meudon code (Le Petit et al. 2006, Goicoechea & Le Bourlot 2007, Le Bourlot et al. 2012) to calculate column densities for the radiation field derived by Vastel et al. (2001) for expected densities of 10^5 $\mathrm{cm^{-3}}$ and 10^6 $\mathrm{cm^{-3}}$ and temperatures of order 100 K derived by previous studies, corresponding to isobaric models with pressures of 10^7 $\mathrm{cm^{-3}}$ K and 10^8 $\mathrm{cm^{-3}}$ K. We apply a cosmic ray ionization rate of 2×10^{-16} $\mathrm{s^{-1}}$ / H_2 molecule. Predictions of column density ratios of selected species are summarized in Table 2.5. The [HCO]/[$H^{13}CO^+$] and [CO^+]/[$H^{13}CO^+$] line ratios may be consistent with the 10^7 $\mathrm{cm^{-3}}$ K pressure PDR model, showing that the abundance of some species may be described by PDR chemistry. However,

Table 2.4 — Summary of observed column density ratios in W49A (Center, Eastern Tail, Northern Clump and South-west clump, when available) and in Galactic PDRs. References: (a) Fuente et al. (1996); (b) Fuente et al. (1993); (c) Ginard et al. (2012); (d) Schilke et al. (2001); (e) Rizzo et al. (2005); (f) Fuente et al. (2003); (g) Goicoechea et al. (2006)

Ratio	W49A	Orion Bar	NGC 7023	Mon R2	Horse-head
CN/HCN center	0.55	3.0[(a)]	4.5[(b)]	2-12[(c)]	
CN/HCN ET	3.8-6.9				
CN/HCN NC	2-4.6				
CN/HCN SWC	0.4-0.95				
SiO/$H^{13}CO^+$	2.7-3.3	3-14[(d)]	0.54[(d)]	0.03-0.37[(e)]	
HCO/SiO	16-23	2-9[(d)]	>4.6-10[(d)]	50-720[(e)]	
CO^+/$H^{13}CO^+$	<0.56	0.52[(a,f)]	0.6[(b,f)]	0.53[(c)]	
CS/HCS^+	76-108			11-25[(c)]	175[(g)]
SO^+/SO_2	<0.02	0.4-1[(f)]	>0.4[(f)]	0.2-0.7[(c)]	

Table 2.5 — Comparison of the column density ratios measured toward the center of W49A to PDR models with pressures of 10^7 cm^{-3} K and 10^8 cm^{-3} K illuminated by a radiation field of $\chi = 3.5 \times 10^5 \chi_0$.

		Models	
Ratio	W49A center	$P = 10^7$ cm^{-3} K	$P = 10^8$ cm^{-3} K
CN/HCN	0.55	42.4	7.1
HCO/$H^{13}CO^+$	43.2-75.9	31.5	5.0
CO^+/$H^{13}CO^+$	<0.56	0.81	0.86
CS/HCS^+	76-108	7151	5696
SO^+/SO_2	<0.02	6564	4892

the [CN]/[HCN], [CS]/[HCS^+], and [SO^+]/[SO_2] column density ratios clearly show, that the chemistry of the W49A center cannot be explained by a PDR component only. The orders of magnitude difference seen in the [CS]/[HCS^+] and [SO^+]/[SO_2] column density ratios may suggest the importance of shock chemistry.

2.4.2 Comparison to regions with shock chemistry

As we have shown above, the chemistry toward the W49A center is mostly related to effects other than FUV-irradiation. Another possible effect that has an impact on the chemistry in the W49 center is shocks related to outflows and winds of the young massive stars and protostars in the central stellar cluster. The importance of shocks in W49A has previously been studied by Peng et al.

(2010) through their relation to expanding shells identified in ^{13}CO data, and by Nagy et al. (2012) (Chapter 3) as a possible contribution to the gas heating. Here we select a sample of regions with shock chemistry for a comparison to the observed column density ratios (Table 2.6).

The Orion KL is a well studied high-mass star-forming region at a distance of ~414 pc (Menten et al. 2007). Spectral line surveys toward Orion KL show a component (Plateau) related to outflows and shocks (e.g. Tercero et al. 2010 and references therein). We use the OCS/CS, CS/HCS$^+$, CS/HCO$^+$, CS/H$_2$CO, HCO$^+$/HCS$^+$, and H$_2$CO/H$_2$CS column density ratios measured for the Orion KL plateau by Tercero et al. (2010). The SiO/H$_2$CO and SO$_2$/H$_2$CO ratios correspond to the low velocity flow component reported by Persson et al. (2007).

The low-mass Class 0 protostar L1157 drives a strong molecular outflow (e.g. Bachiller & Pérez Gutiérrez 1997 and references therein). Its blue lobe has a heating rate related to shocks comparable to that in the shocked region of Orion KL. The column density ratios shown in Table 2.6 correspond to the B1 position of the blue lobe measured by Bachiller & Pérez Gutiérrez (1997).

W3 IRS5 is a bright infra-red source located in the W3 star-forming region at a distance of 2.0 kpc (e.g. Chavarría et al. 2010 and references therein). The embedded young massive stars drive several outflows, which affect the chemistry of the region. In Table 2.6 we show the column density ratios measured by Helmich & van Dishoeck (1997).

The NGC 1333 star forming region is located at a distance of 253 pc (Hirota et al. 2008) and contains several low-mass protostars including IRAS 4A, which is also a source of outflows. The column density ratios toward this source in Table 2.6 are from Blake et al. (1995).

The column density ratios observed toward the W49A center are closest to those measured toward the W3 IRS5 source, and match within a factor of 3. The lower limit that we derive for the CS/HCS$^+$ column density ratio is also close to those toward the Orion KL Plateau and the L1157 regions. While the CS/HCS$^+$ column density is not explained by any of the PDR models shown above, they match those observed toward regions with shock chemistry reasonably well. The CS/H$_2$CO column density ratios are also consistent with those measured toward L1157 (within a factor of 2) and NGC 1333 IRAS 4A (within a factor of 3). The SiO/H$_2$CO and H$_2$CO/H$_2$CS column density ratios are very similar to that measured toward L1157. The largest differences between the regions compared in Table 2.6 is seen in the SO$_2$/H$_2$CO line ratios. As we have shown in the population diagram analysis, the SO$_2$ lines probably originate in clumps smaller than the beam-size. Therefore, the large differences in the SO$_2$/H$_2$CO column density ratio between the regions may be related to the combination of the different spatial scales that correspond to the observations and to the clumpy structure of SO$_2$.

Even this simple comparison of observed column density ratios shows the importance of shocks in the chemistry of the center of W49A. Further

Table 2.6 — Comparison of the column density ratios measured toward the center of W49A to values measured toward regions with shock chemistry. References: Orion KL Plateau SiO/H_2CO and SO_2/H_2CO (Persson et al. 2007), Orion KL Plateau other column density ratios (Tercero et al. 2010); L1157 position B1 (Bachiller & Pérez Gutiérrez 1997); W3 IRS5 (Helmich & van Dishoeck 1997); NGC 1333 IRAS 4A outflow (Blake et al. 1995).

Ratio	W49A center	Orion KL Plateau	L1157	W3 IRS5	NGC 1333 IRAS 4A
OCS/CS	0.9-1.3	5	0.2	0.4	
CS/HCS^+	76-108	50	63	321	
CS/HCO^+	0.5-1.0	5.6	3.7	1.1	19.5
CS/H_2CO	1.6-2.3	0.1	0.3-0.9	2.4	0.6
HCO^+/HCS^+	90-165	9	17	304	
H_2CO/H_2CS	5.0-5.1	18	2-5.3	6.2	
SiO/H_2CO	0.1	0.8	0.1-0.3	0.06	0.04
SO_2/H_2CO	35.4-36.7	140	0.4-1	64.5	<0.55

evidence could be given by a comparison to shock models and by smaller scale observations of sulphur-bearing molecules in particular.

2.4.3 Comparison to starburst galaxies and AGNs

Several molecules seen in our line survey have been detected in starburst galaxies and AGNs. A preliminary comparison between these regions and W49A is shown on Fig. 2.14, based on line surveys toward the starburst galaxy M82 (Aladro et al. 2011b, carried out using the IRAM-30m with beam sizes of $14'' - 19''$ at ~2 mm and $9'' - 10''$ at ~1.3 mm) and the AGN NGC 1068 (Aladro et al. 2013, carried out using the IRAM-30m with a $\sim 21'' - 29''$ beam). For the column density ratios toward the center the beam-averaged column densities are used in the case of species with multiple detected transitions (see Sect. 2.3.4). Though a comparison of Galactic scales to those probed in external galaxies, such as a scale of ~0.8 pc for W49A to the 1.5-2 kpc for NGC 1068 (Aladro et al. 2013) and 158-333 pc for M82 (Aladro et al. 2011b) is an over-simplification, a few conclusions can be drawn.

The most similar abundances w.r.t. that of $C^{34}S$ between W49A and the AGN and starburst environments are seen for C_2H, CN, and H_2CO. In the case of H_2CO, the Northern clump region also shows a very similar abundance w.r.t. $C^{34}S$ as M82 and the W49A center. These three species (C_2H, CN, and H_2CO) are detected with a large spatial extent in W49A. The similarity of the fractional abundance of these species to that in W49A suggests that they are good tracers to compare physical and chemical properties of in Galactic star-forming regions at scales of <1 pc and global star-formation seen in external galaxies on scales of >1 kpc.

Among the four subregions of W49A, the largest differences compared to the other regions in the observed fractional abundances w.r.t. $C^{34}S$ are seen for the South-west clump. As $C^{34}S$ is a dense-gas tracer, the explanation is possibly related to the lower average H_2 volume density of the South-west clump compared to the other regions, which is traced by HCN 3-2 and 4-3 line intensity ratios (Chapter 3, Nagy et al. 2012).

The largest difference compared both to the AGN and starburst examples is seen in the SO_2 fractional abundance. This is probably related to the difference between the spatial scales of the observations. SO_2 and most sulphur-bearing species in W49A are detected in a $\sim 20'' \times 20''$ region around the center and therefore are least likely to trace 'global' properties of >kpc regions such as C_2H, CN, and H_2CO.

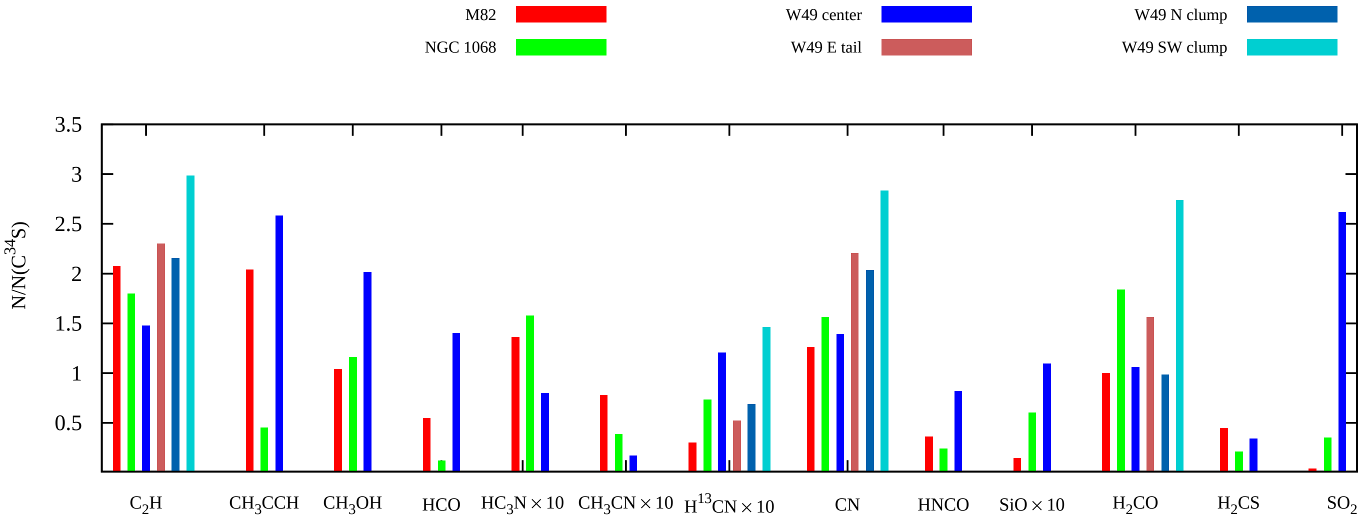

Figure 2.14 — Comparison of column density ratios (with respect to that of C^{34}S) estimated in W49A and its subregions to those measured in the starburst galaxy M82 (Aladro et al. 2011b) and in the AGN NGC 1068 (Aladro et al. 2013).

2.5 Summary

We presented results from the SLS survey carried out using the JCMT at an angular resolution of ∼15″ in the 330-373 GHz frequency range toward the luminous and massive star-forming region W49A.

- The detected 260 transitions correspond to 60 species including shock-, and PDR-tracers, and complex organic molecules. Excitation conditions can be probed using multiple detected transitions for 16 species.
- The species detected with the largest spatial extent include CO (and its ^{13}CO and C^{17}O isotopologues), N_2H^+, and H_2CO; the dense gas tracers including CS, HCN, HNC, and HCO^+; PDR tracers such as CN and C_2H.
- The most spatially extended species reveal a complex spatial and kinematic structure, covering the velocity range of [-5, +20] km s^{-1}. Most observed lines toward the center are double-peaked or asymmetric, with signatures of infall and outflow motions. Mostly blue-shifted emission is detected toward the Eastern tail region, mostly red-shifted emission toward the Northern clump region, while emission toward the South-west clump is detected around the source velocity.
- Based on column density ratios of characteristic species, a combination of shock and PDR chemistry affects the physical and chemical structure of the central 20″ × 20″ region, while UV-irradiation dominates outside of this region including the Northern clump, Eastern tail, and South-west clump regions. A preliminary comparison to a starburst galaxy and to an AGN suggests similar C_2H, CN, and H_2CO abundances between the ∼0.8 pc scale probed for W49A and the >1 kpc regions in external galaxies with global star-formation, suggesting them to be best tracers for such a comparison of physical and chemical properties of star-formation seen on different scales.

In the future, a detailed comparison to PDR- and shock models will be used to probe the contribution of UV-irradiation and shocks to the chemistry of W49A and its subregions.

Acknowledgements We thank Kuo-Song Wang for providing his population diagram code.

2.6 Appendix: The detected lines toward the center of W49A

Table 2.7: The detected species toward the central position of the SLS field. The transitions marked with * have been detected toward AFGL 2591 in the SLS survey (Van der Wiel 2011). The transitions marked with ♦ are non-gaussian. Their intensity is obtained by integrating over the whole line profile. Their $V_{\rm LSR}$ is the velocity at $T_{\rm peak}$. The parameters without error bars are fixed parameters in the fit.

Molecule	Transition	Freq. (MHz)	$E_{\rm up}$ (K)	$A_{\rm ij}$ (s^{-1})	$\int T_{\rm mb} dv$ (K km s^{-1})	$V_{\rm LSR}$ (km s^{-1})	FWHM (km s^{-1})	$T_{\rm peak}$ (K)
HNCO	$15_{0,15}$-$14_{0,14}$	329664.4	126.6	5.04×10^{-4}	12.09±0.95	9.68±0.64	16.57±1.50	0.69±0.14
^{34}SO$_2$	$8_{2,6}$-$7_{1,7}$	330191.1	42.8	1.19×10^{-4}	8.90±0.58	10.70±0.42	13.31±1.02	0.63±0.12
^{13}CO*	3-2	330588.0	31.7	2.19×10^{-6}	616.28±1.01	5.31±0.01	15.88±0.03	36.46±1.80
^{34}SO$_2$	$21_{2,20}$-$21_{1,21}$	330667.6	218.9	1.45×10^{-4}	5.35±0.62	10.78±0.89	14.72±1.69	0.34±0.07
CH$_3$OH*	8_{-3}-9_{-2} E	330793.9	146.3	5.39×10^{-5}	4.62±0.45	9.85±0.86	17.44±1.80	0.25±0.09
HNCO	$15_{1,14}$-$14_{1,13}$	330848.6	170.3	5.01×10^{-4}	7.59±0.51	11.33±0.49	14.47±1.07	0.49±0.10
CH$_3$CN*	18_3-17_3	331014.3	215.2	3.07×10^{-3}	9.00±0.55	9.16±0.45	15.18±1.08	0.56±0.10
CH$_3$CN*	18_2-17_2	331046.1	179.5	3.12×10^{-3}	4.15±0.99	12.22±1.49	13.66±3.19	0.29±0.10
CH$_3$CN	18_0-17_0	331071.5	151.0	3.16×10^{-3}	11.64±0.11	12.35±0.51	19.02±0.78	0.57±0.10
CH$_3$OH*	11_1-11_0 $E^\mp$	331502.4	169.0	3.93×10^{-4}	13.91±0.56	7.85±0.28	13.88±0.62	0.94±0.13
SO$_2$	$11_{6,6}$-$12_{5,7}$	331580.2	149.0	4.35×10^{-5}	15.67±0.49	10.87±0.21	13.46±0.50	1.09±0.12
SO$_2$ *	$21_{2,20}$-$21_{1,21}$	332091.4	219.5	1.51×10^{-4}	48.98±0.57	10.11±0.09	15.58±0.21	2.95±0.16
^{34}SO$_2$	$23_{3,21}$-$23_{2,22}$	332173.6	275.1	2.54×10^{-4}	8.06±0.63	12.07±0.49	12.91±1.24	0.59±0.12
^{33}SO$_2$	$8_{2,6}$-$7_{1,7}$	332352.3	43.6	2.71×10^{-6}	2.28±0.50	13.53±1.40	11.49±2.25	0.19±0.08
SO$_2$ *	$4_{3,1}$-$3_{2,2}$	332505.2	31.3	3.29×10^{-4}	73.18±0.61	9.11±0.06	15.71±0.15	4.38±0.14
^{34}SO$_2$	$16_{4,12}$-$16_{3,13}$	332836.2	163.1	3.02×10^{-4}	14.32±0.63	12.26±0.31	14.02±0.72	0.96±0.11
S^{17}O	8_9-7_8	333121.6	75.9	4.50×10^{-4}	3.31±0.78	12.52±1.63	15.19±4.83	0.20±0.07
^{34}SO*	7_8-6_7	333901.0	79.9	4.69×10^{-4}	46.94±0.36	9.61±0.05	13.99±0.12	3.15±0.11
U-line								
SO$_2$ *	$8_{2,6}$-$7_{1,7}$	334673.4	43.1	1.27×10^{-4}	61.05±0.60	9.09±0.07	14.98±0.17	3.83±0.11
CH$_3$OH*	2_2-3_1 A$^-$	335133.7	44.7	2.69×10^{-5}	4.05±0.24	11.78±0.58	18.62±1.07	0.20±0.06
U-line								
CH$_3$CHO	$18_{0,18,2}$-$17_{0,17,2}$	335318.1	154.9	1.30×10^{-3}	6.53±0.41	11.02±0.61	20.02±1.44	0.31±0.06

Continued on next page

Table 2.7: The detected species toward the central position of the SLS field. The transitions marked with * have been detected toward AFGL 2591 in the SLS survey (Van der Wiel 2011). The transitions marked with ♦ are non-gaussian. Their intensity is obtained by integrating over the whole line profile. Their $V_{\rm LSR}$ is the velocity at $T_{\rm peak}$. The parameters without error bars are fixed parameters in the fit.

Molecule	Transition	Freq. (MHz)	$E_{\rm up}$ (K)	$A_{\rm ij}$ ($\rm s^{-1}$)	$\int T_{\rm mb}{\rm d}v$ (K km $\rm s^{-1}$)	$V_{\rm LSR}$ (km $\rm s^{-1}$)	FWHM (km $\rm s^{-1}$)	$T_{\rm peak}$ (K)
$CH_3OH^\star$	7_1-6_1 A$^+$	335582.0	79.0	1.63×10^{-4}	20.67±0.32	7.68±0.11	14.28±0.24	1.36±0.11
SO_2 *	$23_{3,21}$-$23_{2,22}$	336089.2	276.0	2.67×10^{-4}	37.35±0.41	10.02±0.08	14.77±0.20	2.38±0.10
HC_3N	37-36	336520.1	306.9	3.05×10^{-3}	5.43±2.51	11.15±2.74	11.83±6.53	0.43±0.08
SO	11_{10}-10_{10}	336553.8	142.9	6.12×10^{-6}	22.03±1.01	9.40±0.31	13.57±0.69	1.52±0.08
SO_2	$16_{7,9}$-$17_{6,12}$	336669.6	245.1	5.84×10^{-5}	16.22±0.11	11.05±0.17	11.46±0.34	1.33±0.14
$CH_3OH^\star$	12_1-12_0 A$^\mp$	336865.1	197.1	4.07×10^{-4}	14.71±0.44	7.69±0.22	15.21±0.53	0.91±0.10
$C^{17}O^\star$	3-2	337062.0	32.4	4.30×10^{-7}	84.53±0.39	7.39±0.03	13.62±0.07	5.83±0.32
^{33}SO	7_8-6_7	337199.4	80.5	4.65×10^{-4}	19.13±0.64	10.11±0.24	14.68±0.59	1.22±0.10
$SO^{17}O$	$19_{1,19}$-$18_{0,18}$	337337.7	168.9	4.79×10^{-4}	3.67±0.56	7.60±0.92	12.89±2.41	0.27±0.09
$C^{34}S^\star$	7-6	337396.5	50.2	8.00×10^{-4}	24.98±0.56	8.02±0.15	13.79±0.35	1.70±0.15
$^{34}SO^\star$	8_8-7_7	337580.1	86.1	4.89×10^{-4}	46.74±0.43	9.08±0.06	13.66±0.14	3.21±0.10
CH_3OH, v_t=1	$7_{7,1}-6_{6,1}$ A$^+$	337643.9	365.4	1.69×10^{-4}	3.54±0.50	9.49±1.20	15.61±2.04	0.21±0.06
CH_3OCH_3	$7_{4,3,0}-6_{3,4,0}$	337787.2	48.0	1.94×10^{-4}	1.80±0.53	11.72±1.38	10.13±3.81	0.17±0.04
^{34}SO	3_3-2_3	337892.2	25.3	1.40×10^{-5}	4.59±0.54	10.81±0.70	12.32±1.81	0.35±0.08
H_2CS	$10_{1,10}$-$9_{1,9}$	338083.2	102.4	5.77×10^{-4}	7.31±0.57	7.36±0.54	13.65±1.17	0.50±0.07
$CH_3OH^\star$	7_0-6_0 E	338124.5	78.1	1.70×10^{-4}	15.87±0.88	6.64±0.37	13.31±0.85	1.12±0.10
SO_2 *	$18_{4,14}$-$18_{3,15}$	338306	196.8	3.27×10^{-4}	29.82±0.39	7.47±0.11	18.52±0.28	1.51±0.10
$CH_3OH^\star$	7_{-1}-6_{-1} E	338344.6	70.6	1.67×10^{-4}	23.99±0.31	6.59±0.09	13.53±0.21	1.67±0.10
$CH_3OH^\star$	7_0-6_0 A$^+$	338408.7	65.0	1.70×10^{-4}	22.13±0.30	6.62±0.08	12.26±0.19	1.70±0.10
$CH_3OH^\star$	$7_{4,4}-6_{4,3}$ A$^-$	338512.6	145.3	1.15×10^{-4}	10.32±0.48	7.35±0.32	13.83±0.72	0.70±0.09
CH_3OH	$7_{3,4}-6_{3,3}$ A$^-$	338543.2	114.8	1.39×10^{-4}	10.68±0.50	7.97±0.33	13.87±0.75	0.72±0.09
SO_2 *	$20_{1,19}$-$19_{2,18}$	338611.8	198.9	2.87×10^{-4}	40.93±0.50	6.95±0.09	15.73±0.22	2.44±0.10
CH_3OH	7_2-6_2 A^+	338639.9	102.7	1.57×10^{-4}	7.93±0.90	6.75±1.00	11.79±1.00	0.63±0.10

Continued on next page

Table 2.7: The detected species toward the central position of the SLS field. The transitions marked with * have been detected toward AFGL 2591 in the SLS survey (Van der Wiel 2011). The transitions marked with ♦ are non-gaussian. Their intensity is obtained by integrating over the whole line profile. Their $V_{\rm LSR}$ is the velocity at $T_{\rm peak}$. The parameters without error bars are fixed parameters in the fit.

Molecule	Transition	Freq. (MHz)	$E_{\rm up}$ (K)	$A_{\rm ij}$ ($\rm s^{-1}$)	$\int T_{\rm mb} dv$ (K km $\rm s^{-1}$)	$V_{\rm LSR}$ (km $\rm s^{-1}$)	FWHM (km $\rm s^{-1}$)	$T_{\rm peak}$ (K)
$\mathbf{CH_3OH}^\star$	7_2-6_2 E	338721.6	87.3	1.55×10^{-4}	21.52±0.27	5.92±0.09	13.16±0.20	1.54±0.17
$^{34}\mathbf{SO_2}$	$14_{4,10}$-$14_{3,11}$	338785.7	134.5	3.08×10^{-4}	5.35±0.32	11.23±0.38	12.57±0.83	0.40±0.04
$\mathbf{SO}^\star$	3_3-3_2	339341.5	25.5	1.45×10^{-5}	18.61±0.34	8.02±0.12	13.74±0.28	1.27±0.08
$^{33}\mathbf{SO_2}$	$16_{4,12}$-$16_{3,13}$	339482.3	166.1	3.18×10^{-4}	2.72±0.31	10.53±0.71	12.33±1.53	0.21±0.05
$\mathbf{CN}^\star$	N=3-2, J=5/2-5/2	339516.6	32.6	2.54×10^{-5}	3.15±0.50	7.46±1.40	17.27±3.49	0.17±0.07
$^{34}\mathbf{SO}^\star$	9_8-8_7	339857.3	77.3	5.08×10^{-4}	70.69±0.33	9.15±0.03	14.43±0.08	4.60±0.15
$\mathbf{CN}^{\star}$♦	N=3-2, J=5/2-3/2	340035.4	32.6	2.89×10^{-4}	51.50±1.01	6.98±1.0		3.07±0.06
$\mathbf{CH_3OH}^\star$	2_2-3_1 A$^+$	340141.2	44.7	2.78×10^{-5}	4.38±0.35	8.03±0.60	14.91±1.39	0.28±0.05
$\mathbf{CN}^{\star}$♦	N=3-2, J=7/2-5/2	340248.5	32.7	3.67×10^{-4}	51.14±0.99	5.44±1.0		3.61±0.07
$^{13}\mathbf{CH_3OH}$	$2_{2,1}-3_{1,2}$ A$^-$	340313.9	44.6	2.82×10^{-5}	31.79±0.32	8.21±0.07	14.43±0.17	2.07±0.08
$\mathbf{OCS}^\star$	28-27	340449.3	237.0	1.15×10^{-4}	10.68±0.41	10.38±0.29	14.55±0.58	0.69±0.08
$^{33}\mathbf{SO_2}$	$20_{1,19}$-$19_{2,18}$	340526.1	201.5	2.96×10^{-4}	4.61±0.32	11.27±0.40	11.24±0.86	0.39±0.06
$\mathbf{HC^{18}O^+}$	4-3	340630.7	40.9	3.11×10^{-3}	6.98±0.36	7.58±0.29	11.26±0.68	0.58±0.07
$\mathbf{SO}^\star$	7_8-6_7	340714.2	81.2	4.99×10^{-4}	213.26±1.09	7.49±0.04	15.61±0.10	12.83±0.52
$^{33}\mathbf{SO}$	8_8-7_7	340839.6	86.8	5.03×10^{-4}	22.64±0.26	10.49±0.08	13.84±0.18	1.54±0.09
$\mathbf{SO_2}$	$21_{8,14}-22_{7,15}$	341275.5	369.1	6.86×10^{-5}	14.77±0.36	11.60±0.15	12.69±0.37	1.09±0.10
$\mathbf{HCS^+}$	8-7	341350.2	73.7	8.35×10^{-4}	5.68±0.37	9.40±0.46	13.38±0.87	0.40±0.08
$\mathbf{CH_3OH}^\star$	7_1-6_1 A$^-$	341415.6	80.1	1.71×10^{-4}	36.71±0.48	10.62±0.14	20.43±0.31	1.69±0.19
$\mathbf{HCO}$	$4_{1,4}-3_{1,3}$	341671.6	73.8	3.46×10^{-4}	18.60±0.31	7.78±0.14	16.70±0.33	1.05±0.09
$^{33}\mathbf{SO_2}$	$13_{2,12}-12_{1,11}$	341721.7	94.1	2.30×10^{-4}	10.70±1.45	10.51±0.95	17.67±2.28	0.57±0.09
$\mathbf{CH_3CCH}$	$20-19$	341741.0	172.2	1.39×10^{-4}	9.38±1.43	9.82±0.86	14.53±1.58	0.61±0.09
$^{34}\mathbf{SO_2}$	$5_{3,3}-4_{2,2}$	342208.9	35.1	3.10×10^{-4}	15.29±0.51	11.77±0.19	11.83±0.46	1.21±0.10
$^{34}\mathbf{SO_2}$	$20_{1,19}-19_{2,18}$	342231.6	198.5	3.06×10^{-4}	16.20±0.52	11.60±0.21	14.02±0.55	1.09±0.10

Continued on next page

Table 2.7: The detected species toward the central position of the SLS field. The transitions marked with * have been detected toward AFGL 2591 in the SLS survey (Van der Wiel 2011). The transitions marked with ♦ are non-gaussian. Their intensity is obtained by integrating over the whole line profile. Their $V_{\rm LSR}$ is the velocity at $T_{\rm peak}$. The parameters without error bars are fixed parameters in the fit.

Molecule	Transition	Freq. (MHz)	$E_{\rm up}$ (K)	$A_{\rm ij}$ ($\rm s^{-1}$)	$\int T_{\rm mb}{\rm d}v$ (K km $\rm s^{-1}$)	$V_{\rm LSR}$ (km $\rm s^{-1}$)	FWHM (km $\rm s^{-1}$)	$T_{\rm peak}$ (K)
$^{34}\mathbf{SO_2}$	$12_{4,8}-12_{3,9}$	342332.0	109.7	3.06×10^{-4}	15.07±0.47	11.57±0.20	12.77±0.46	1.11±0.10
$\mathbf{CH_3OH}^\star$	13_1-13_0 A$^\mp$	342729.8	227.5	4.23×10^{-4}	9.95±0.38	9.06±0.26	13.71±0.57	0.68±0.09
$\mathbf{O^{13}C^{34}S}$	29-28	342759.8	246.8	1.18×10^{-4}	17.47±0.35	9.66±0.14	13.45±0.34	1.22±0.09
$\mathbf{CS}^\star$	$7-6$	342882.9	65.8	8.40×10^{-4}	155.79±0.66	6.35±0.03	14.21±0.08	10.30±0.80
$\mathbf{H_2CS}$	$10_{0,10}-9_{0,9}$	342946.4	90.6	6.08×10^{-4}	4.15±0.35	9.11±0.52	11.58±0.99	0.34±0.06
$\mathbf{HO^{13}C^+}$	$4-3$	342983.3	41.2	3.34×10^{-3}	2.49±0.35	10.83±0.82	11.91±2.29	0.20±0.07
$^{33}\mathbf{SO}$	9_8-8_7, $F=\frac{17}{2}-\frac{15}{2}$	343087.3	78.0	5.09×10^{-4}	30.65±0.53	9.66±0.12	14.21±0.29	2.03±0.10
$\mathbf{H_2^{13}CO}$	5_{15}-4_{14}	343325.7	61.3	1.12×10^{-3}	8.76±0.58	10.88±0.60	18.27±1.50	0.45±0.07
$\mathbf{H_2CS}$	$10_{3,7}-9_{3,6}$	343414.1	209.1	5.56×10^{-4}	5.62±0.33	12.12±0.48	15.75±0.89	0.33±0.09
$\mathbf{H_2CS}$	$10_{2,8}-9_{2,7}$	343813.2	143.4	5.88×10^{-4}	2.56±0.41	10.25±0.83	11.91±2.68	0.20±0.10
$\mathbf{HC^{15}N}^\star$	4-3	344200.1	41.3	1.88×10^{-3}	13.85±0.46	8.49±0.24	14.51±0.56	0.90±0.09
$^{34}\mathbf{SO_2}$	$10_{4,6}-10_{3,7}$	344245.3	88.5	2.96×10^{-4}	12.41±0.36	10.85±0.17	11.56±0.39	1.01±0.07
$\mathbf{SO}^\star$	8_8-7_7	344310.6	87.5	5.19×10^{-4}	199.46±1.96	7.39±0.07	15.37±0.17	12.19±0.50
$^{34}\mathbf{SO_2}$ *	$19_{1,19}$-$18_{0,18}$	344581.0	167.7	5.16×10^{-4}	20.86±0.43	11.35±0.12	12.20±0.30	1.61±0.15
$^{34}\mathbf{SO_2}$ *	$13_{4,10}$-$13_{3,11}$	344807.9	121.6	3.17×10^{-4}	14.45±0.54	11.54±0.25	13.69±0.64	0.99±0.12
$^{34}\mathbf{SO_2}$	$15_{4,12}$-$15_{3,13}$	344987.6	148.3	3.27×10^{-4}	26.22±0.64	6.18±0.22	17.92±0.49	1.37±0.14
$^{33}\mathbf{SO_2}$	$14_{4,10}-4_{3,11}$	345134.4	137.1	3.19×10^{-6}	7.92±1.14	12.86±0.93	15.36±2.61	0.48±0.12
$\mathbf{SO_2}$	$5_{5,1}$-$6_{4,2}$	345149.0	75.1	9.81×10^{-6}	8.51±1.20	11.36±0.41	9.70±1.13	0.82±0.12
$^{34}\mathbf{SO_2}$	$8_{4,4}$-$8_{3,5}$	345168.7	71.0	2.75×10^{-4}	12.42±0.68	12.25±0.28	11.39±0.83	1.02±0.12
$^{34}\mathbf{SO_2}$	$9_{4,6}$-$9_{3,7}$	345285.6	79.3	2.88×10^{-4}	13.67±0.66	11.93±0.25	10.22±0.56	1.26±0.17
$\mathbf{H^{13}CN}^\star$	4-3	345339.8	41.4	1.90×10^{-3}	110.90±0.72	8.59±0.05	15.70±0.12	6.64±0.46
$\mathbf{SO_2}$	$26_{9,17}-27_{8,20}$	345449.0	521.0	7.63×10^{-5}	11.82±0.65	11.12±0.35	13.25±0.90	0.84±0.17
$^{34}\mathbf{SO_2}$ *	$7_{4,4}$-$7_{3,5}$	345519.7	63.7	2.59×10^{-4}	14.84±0.63	11.70±0.24	11.80±0.62	1.18±0.13

Continued on next page

Table 2.7: The detected species toward the central position of the SLS field. The transitions marked with * have been detected toward AFGL 2591 in the SLS survey (Van der Wiel 2011). The transitions marked with $^{\blacklozenge}$ are non-gaussian. Their intensity is obtained by integrating over the whole line profile. Their V_{LSR} is the velocity at T_{peak}. The parameters without error bars are fixed parameters in the fit.

Molecule	Transition	Freq. (MHz)	E_{up} (K)	A_{ij} (s^{-1})	$\int T_{\mathrm{mb}}dv$ (K km s^{-1})	V_{LSR} (km s^{-1})	FWHM (km s^{-1})	T_{peak} (K)
^{34}SO$_2$	$6_{4,2}$-$6_{3,3}$	345553.1	57.3	2.35×10^{-4}	11.10±2.13	12.08±0.96	10.04±2.15	1.04±0.13
^{33}SO$_2$	$19_{1,19}-18_{0,18}$	345584.7	170.2	5.19×10^{-4}	4.22±0.60	12.85±0.53	7.71±1.28	0.51±0.11
HC$_3$N	38-37	345609.0	323.5	3.30×10^{-3}	4.01±0.65	11.45±0.61	7.20±1.41	0.52±0.10
^{34}SO$_2$	$5_{4,2}$-$5_{3,3}$	345651.3	51.8	1.96×10^{-4}	6.12±0.78	11.99±0.51	7.46±0.98	0.77±0.11
^{34}SO$_2$	$4_{4,0}-4_{3,1}$	345678.8	47.2	1.31×10^{-4}	3.38±0.39	11.30±0.61	10.38±1.30	0.31±0.09
CO*	3-2	345796.0	33.2	2.50×10^{-6}	1161.6±4.43	2.77±0.001	21.22±0.10	51.42±7.3
^{34}SO$_2$	$17_{4,14}$-$17_{3,15}$	345929.3	178.8	3.37×10^{-4}	9.96±0.53	12.02±0.32	12.24±0.77	0.76±0.09
NS*	15/2-13/2	346220.1	71.0	7.38×10^{-4}	7.35±0.50	10.84±0.68	20.31±1.54	0.34±0.06
SO$_2$, v$_2$=1	$19_{1,19}-18_{0,18}$	346379.2	930.6	5.16×10^{-4}	9.82±0.41	9.03±0.38	18.64±0.91	0.49±0.09
CH$_3$CHO	$7_{3,4,3}-6_{2,5,3}$	346451.9	250.4	1.03×10^{-4}	2.48±0.37	10.85±0.88	11.96±2.23	0.19±0.04
SO*	9_8-8_7	346528.5	78.8	5.38×10^{-4}	231.50±0.69	7.63±0.02	16.69±0.06	13.03±0.68
^{33}SO$_2$	$5_{3,3}$-$4_{2,2}$	346589.8	36.0	1.76×10^{-5}	6.41±0.33	10.91±0.30	11.76±0.71	0.51±0.06
SO$_2$ *	$19_{1,19}$-$18_{0,18}$	346652.2	168.1	5.22×10^{-4}	96.43±0.32	9.42±0.03	15.47±0.06	5.85±0.14
C$_2$H$_5$CN	$19_{8,11}$-$19_{7,12}$	346945.7	152.8	1.61×10^{-4}	2.41±0.32	8.82±1.00	13.17±2.02	0.17±0.10
H^{13}CO$^+$ *	4-3	346998.3	41.6	3.29×10^{-3}	50.66±0.41	6.58±0.05	11.86±0.12	4.01±0.19
SiO	8-7	347330.6	75.0	2.20×10^{-3}	68.67±0.66	7.91±0.08	16.98±0.20	3.80±0.16
^{34}SO$_2$	$28_{2,26}$-$28_{1,27}$	347483.1	391.2	2.65×10^{-4}	5.01±0.37	11.48±0.45	11.89±1.03	0.40±0.07
SO$^+$	8-7	347740	70.1	2.28×10^{-4}	19.44±0.41	8.83±0.15	13.87±0.33	1.32±0.09
SO$_2$, v$_2$=1	$13_{2,12}-12_{1,11}$	347991.8	854.3	2.41×10^{-4}	4.48±0.47	9.98±0.88	16.43±1.81	0.26±0.08
^{34}SO$_2$	$19_{4,16}$-$19_{3,17}$	348117.5	212.9	3.50×10^{-4}	28.62±0.38	11.22±0.09	14.24±0.22	1.89±0.10
HC^{17}O$^+$	4-3	348211.2	41.8	3.32×10^{-3}	1.64±0.33	8.75±1.12	10.73±2.59	0.14±0.05
HN^{13}C	4-3	348340.8	41.8	2.03×10^{-3}	5.66±1.05	11.00±1.00	11.88±1.00	0.45±0.11
SO$_2$ *	$24_{2,22}$-$23_{3,21}$	348387.8	292.7	1.91×10^{-4}	48.45±1.14	10.12±1.00	13.99±1.00	3.25±0.10

Continued on next page

Table 2.7: The detected species toward the central position of the SLS field. The transitions marked with * have been detected toward AFGL 2591 in the SLS survey (Van der Wiel 2011). The transitions marked with ♦ are non-gaussian. Their intensity is obtained by integrating over the whole line profile. Their $V_{\rm LSR}$ is the velocity at $T_{\rm peak}$. The parameters without error bars are fixed parameters in the fit.

Molecule	Transition	Freq. (MHz)	$E_{\rm up}$ (K)	$A_{\rm ij}$ ($\rm s^{-1}$)	$\int T_{\rm mb}{\rm d}v$ (K km $\rm s^{-1}$)	$V_{\rm LSR}$ (km $\rm s^{-1}$)	FWHM (km $\rm s^{-1}$)	$T_{\rm peak}$ (K)
^{33}SO$_2$	$12_{4,8}$-$12_{3,9}$	348490.9	111.9	2.96×10^{-6}	6.28±0.78	8.90±1.17	18.08±3.31	0.33±0.10
o-H$_2$CS*	$10_{1,9}$-$9_{1,8}$	348534.4	105.2	6.32×10^{-4}	13.13±0.62	9.32±0.36	15.55±0.86	0.79±0.10
C$_2$H*	$4_{9/2}$-$3_{5/2}$, F=4-3	349108.5	41.9	5.76×10^{-8}	9.05±0.46	9.59±0.37	14.35±0.80	0.59±0.08
SO^{18}O	$15_{4,12}$-$15_{3,13}$	349209.6	149.8	3.37×10^{-4}	2.84±0.62	10.65±1.58	12.26±3.04	0.22±0.09
SO^{18}O	$13_{4,10}$-$13_{3,11}$	349224.9	123.3	3.27×10^{-4}	2.44±0.53	11.95±0.28	4.76±1.27	0.48±0.09
C$_2$H*	$4_{9/2}$-$3_{7/2}$	349338.3	41.9	1.28×10^{-4}	33.15±0.46	8.49±0.10	13.97±0.22	2.23±0.17
C$_2$H*	$4_{7/2}$-$3_{5/2}$	349400.7	41.9	1.20×10^{-4}	28.34±1.14	10.32±0.24	14.04±0.46	1.90±0.10
CH$_3$CN*	19_2-18_2	349426.8	196.3	3.68×10^{-3}	5.91±3.13	10.57±2.57	19.45±12.17	0.29±0.10
CH$_3$CN*	19_0-18_0	349453.7	167.7	3.72×10^{-3}	9.74±1.63	12.05±1.12	15.03±1.74	0.61±0.10
U-line								
^{33}SO$_2$	$10_{4,6}$-$10_{3,7}$	350302.4	90.4	4.02×10^{-6}	2.87±0.34	10.39±0.73	11.41±1.29	0.24±0.08
HNCO*	$16_{1,16}$-$15_{1,15}$	350333.1	186.2	5.97×10^{-4}	5.82±0.32	12.30±0.26	9.89±0.64	0.55±0.08
NO*	$7/2$-$5/2^+$	350694.8	36.1	4.81×10^{-6}	35.27±0.44	12.03±0.09	14.78±0.21	2.24±0.06
^{33}SO$_2$	$13_{4,10}$-$13_{3,11}$	350787.0	124.0	2.64×10^{-6}	2.84±0.36	11.42±0.89	14.02±2.08	0.19±0.08
SO$_2$ *	$10_{6,4}$-$11_{5,7}$	350862.8	138.8	4.40×10^{-5}	24.44±0.51	11.46±0.13	12.58±0.30	1.83±0.12
CH$_3$OH*	1_1-0_0 A^+	350905.1	16.8	3.31×10^{-4}	28.53±0.52	5.82±0.11	12.22±0.28	2.19±0.24
SO^{17}O	$12_{4,8}$-$12_{3,9}$	350993.2	112.1	3.27×10^{-4}	5.55±0.54	11.15±0.46	9.97±1.17	0.52±0.12
NO*	$7/2$-$5/2^-$	351049.0	36.1	4.99×10^{-6}	35.03±0.61	9.79±0.14	16.80±0.34	1.96±0.13
^{33}SO$_2$	$8_{4,4}$-$8_{3,5}$	351177.4	72.7	5.65×10^{-6}	4.14±0.43	12.48±0.38	8.01±1.05	0.49±0.09
SO$_2$ *	$5_{3,3}$-$4_{2,2}$	351257.2	35.9	3.36×10^{-4}	42.96±0.59	9.27±0.11	16.27±0.28	2.48±0.13
^{33}SO$_2$	$7_{4,4}$-$7_{3,5}$	351508.5	65.2	6.76×10^{-6}	3.09±0.34	11.35±0.47	8.20±0.96	0.35±0.09
^{33}SO$_2$	$6_{4,2}$-$6_{3,3}$	351542.1	58.7	8.06×10^{-6}	8.37±0.55	13.22±0.61	18.63±1.30	0.42±0.09
HNCO	$16_{0,16}-15_{0,15}$	351633.3	143.5	6.13×10^{-4}	20.41±0.79	12.36±0.24	12.78±0.57	1.50±0.12

Continued on next page

Table 2.7: The detected species toward the central position of the SLS field. The transitions marked with * have been detected toward AFGL 2591 in the SLS survey (Van der Wiel 2011). The transitions marked with ♦ are non-gaussian. Their intensity is obtained by integrating over the whole line profile. Their V_{LSR} is the velocity at T_{peak}. The parameters without error bars are fixed parameters in the fit.

Molecule	Transition	Freq. (MHz)	E_{up} (K)	A_{ij} (s^{-1})	$\int T_{\mathrm{mb}}\mathrm{d}v$ (K km s^{-1})	V_{LSR} (km s^{-1})	FWHM (km s^{-1})	T_{peak} (K)
^{33}SO$_2$	$4_{4,0}$-$4_{3,1}$	351661.8	48.5	1.18×10^{-5}	3.39±0.53	9.73±0.85	10.67±1.90	0.30±0.11
^{33}SO$_2$	$17_{4,14}$-$17_{3,15}$	351743.7	181.9	1.78×10^{-6}	5.17±0.53	13.39±0.56	11.22±1.08	0.43±0.18
o-H$_2$CO*	$5_{1,5}$-$4_{1,4}$	351768.6	62.5	1.20×10^{-3}	104.71±1.35	6.54±0.08	13.75±0.22	7.15±0.65
SO$_2$ *	$14_{4,10}$-$14_{3,11}$	351873.9	135.9	3.43×10^{-4}	63.49±0.71	10.17±0.08	14.94±0.19	3.99±0.17
^{34}SO$_2$	$21_{4,18}$-$21_{3,19}$	352082.9	250.8	3.65×10^{-4}	8.53±0.59	11.65±0.37	11.33±0.96	0.71±0.07
OCS*	29-28	352599.6	253.9	1.28×10^{-4}	11.23±0.33	10.91±0.20	13.54±0.44	0.78±0.08
HNCO*	$16_{1,15}$-$15_{1,14}$	352897.6	187.2	6.10×10^{-4}	6.28±0.33	11.71±0.27	10.12±0.63	0.58±0.07
^{34}SO$_2$	$14_{7,7}$-$15_{6,10}$	353002.4	212.6	5.70×10^{-5}	1.18±0.20	11.24±0.98	10.59±1.51	0.11±0.05
SO^{18}O	$26_{3,24}$-$26_{2,25}$	353195.8	342.7	2.94×10^{-4}	1.59±0.25	12.54±0.89	11.07±1.87	0.13±0.03
SO^{17}O$^{\mathrm{blend/1}}$	$7_{4,4}-7_{3,5}$	353597.1	65.9	2.77×10^{-4}	5.97±0.48	9.27±1.05	14.0	0.40±0.09
SO^{17}O$^{\mathrm{blend/2}}$	$20_{1,20}-19_{0,19}$	353625.3	186.3	5.59×10^{-4}	9.48±0.56	15.06±0.89	14.0	0.64±0.09
SO^{17}O$^{\mathrm{blend/3}}$	$6_{4,2}-6_{3,3}$	353629.6	59.5	2.51×10^{-4}	6.51±0.59	3.14±1.23	14.0	0.44±0.09
CO$^+$[5]	N=3-2, F=$\frac{5}{2}$-$\frac{3}{2}$	353741.3	33.9	2.06×10^{-4}	5.55±0.45	12.11±0.82	21.09±2.06	0.25±0.06
HCN,v$_2$=1$^{\mathrm{blend/1}}$ ♦	4-3	354460.4	1066.9	1.87×10^{-3}	9.78±0.95	12.50±1.0		0.62±0.06
HCN$^{\mathrm{blend/2}}$ *♦	4-3	354505.5	42.5	2.05×10^{-3}	184.9±1.30	1.32±1.0		8.55±0.06
SO$_2$, v$_2$=1	$16_{4,12}-16_{3,13}$	354800	927.8	3.60×10^{-4}	3.16±0.32	10.73±0.91	15.39±1.89	0.19±0.08
SO$_2$ *	$12_{4,8}-12_{3,9}$	355045.5	111.0	3.40×10^{-4}	49.46±0.32	9.74±0.05	15.04±0.12	3.09±0.09
SO$_2$	$17_{4,14}-18_{1,17}$	355186.5	180.1	2.62×10^{-6}	5.16±0.36	9.08±0.57	16.41±1.47	0.30±0.05
H^{15}NC	$4-3$	355439.5	42.6	1.69×10^{-3}	1.25±0.23	10.68±0.83	8.36±1.71	0.14±0.05
S^{18}O	8_9-7_8	355571.1	93.1	5.74×10^{-4}	8.35±0.26	11.21±0.24	16.00±0.58	0.49±0.06
CH$_3$OH*	$13_{0,13}$-$12_{1,12}$ A$^+$	355603.1	211.0	2.53×10^{-4}	9.52±0.27	9.61±0.22	15.04±0.47	0.59±0.06

Continued on next page

---

[5] May be blended with SO^{17}O

Table 2.7: The detected species toward the central position of the SLS field. The transitions marked with * have been detected toward AFGL 2591 in the SLS survey (Van der Wiel 2011). The transitions marked with $^\blacklozenge$ are non-gaussian. Their intensity is obtained by integrating over the whole line profile. Their $V_{\rm LSR}$ is the velocity at $T_{\rm peak}$. The parameters without error bars are fixed parameters in the fit.

Molecule	Transition	Freq. (MHz)	$E_{\rm up}$ (K)	$A_{\rm ij}$ ($\rm s^{-1}$)	$\int T_{\rm mb}{\rm d}v$ (K km $\rm s^{-1}$)	$V_{\rm LSR}$ (km $\rm s^{-1}$)	FWHM (km $\rm s^{-1}$)	$T_{\rm peak}$ (K)
$\mathbf{CH_3OH}^\star$	$15_{1,14}$-$15_{0,15}$ A$^+$	356007.2	295.3	4.60×10^{-4}	7.87±0.62	8.70±0.58	14.19±1.13	0.52±0.10
$\mathbf{SO_2}$	$15_{7,9}-16_{6,10}$	356040.6	230.4	6.40×10^{-5}	23.58±0.67	10.51±0.19	13.27±0.45	1.67±0.10
$^{34}\mathbf{SO_2}$	$25_{3,23}-25_{2,24}$	356222.2	320.0	2.97×10^{-4}	6.39±0.51	10.72±0.45	10.87±0.92	0.55±0.08
$\mathbf{t\text{-}HCOOH}^\star$	$16_{1,16}-15_{0,15}$	356254.5	143.6	8.63×10^{-6}	11.47±0.77	11.03±0.60	20.43±1.81	0.53±0.08
$\mathbf{HCO^+}$ *	4-3	356734.2	42.8	3.57×10^{-3}	503.55±0.55	3.10±0.01	27.35±0.03	17.30±1.30
$^{34}\mathbf{SO_2}$ *	$20_{0,20}-19_{1,19}$	357102.2	184.8	5.81×10^{-4}	25.19±0.53	11.25±0.14	13.36±0.33	1.77±0.14
$\mathbf{SO_2}$ *	$13_{4,10}-13_{3,11}$	357165.4	123.0	3.51×10^{-4}	72.28±0.41	9.24±0.04	15.20±0.10	4.47±0.15
$\mathbf{SO_2}$ *	$15_{4,12}-15_{3,13}$	357241.2	149.7	3.62×10^{-4}	67.49±0.68	9.24±0.07	14.70±0.17	4.31±0.14
$\mathbf{SO_2}$ *	$11_{4,8}-11_{3,9}$	357387.6	100.0	3.38×10^{-4}	71.00±0.84	9.85±0.09	15.00±0.21	4.45±0.13
$^{34}\mathbf{SO_2}$	$32_{5,27}-32_{4,28}$	357497.8	547.5	4.55×10^{-4}	2.34±0.24	12.21±0.47	9.23±1.22	0.24±0.05
$\mathbf{SO_2}$ *	$8_{4,4}-8_{3,5}$	357581.4	72.4	3.06×10^{-4}	81.60±0.61	9.32±0.06	17.96±0.16	4.27±0.24
$\mathbf{SO_2}$ *	$9_{4,6}-9_{3,7}$	357671.8	80.6	3.20×10^{-4}	86.02±0.30	9.88±0.03	16.93±0.07	4.77±0.23
$\mathbf{SO_2}^{\rm blend/1\ \star}$	$7_{4,4}-7_{3,5}$	357892.4	65.0	2.87×10^{-4}	78.52±2.36	9.36±1.00	15.65±1.00	4.71±0.15
$\mathbf{SO_2}^{\rm blend/2\ \star}$	$6_{4,2}-6_{3,3}$	357925.8	58.6	2.60×10^{-4}	74.40±0.36	9.47±0.04	15.64±0.09	4.47±0.14
$\mathbf{SO_2}^{\rm blend/3}$	$17_{4,14}-17_{3,15}$	357962.9	180.1	3.73×10^{-4}	69.61±0.38	10.06±0.04	15.86±0.10	4.12±0.14
$\mathbf{SO_2}^{\rm blend/4\ \star}$	$5_{4,2}-5_{3,3}$	358013.2	53.1	2.18×10^{-4}	68.11±0.36	9.71±0.01	15.47±0.10	4.14±0.14
$\mathbf{SO_2}^{\rm blend/5\ \star}$	$4_{4,0}-4_{3,1}$	358037.9	48.5	1.45×10^{-4}	48.82±2.39	9.68±1.00	13.32±1.00	3.44±0.14
$\mathbf{SO_2}$ *	$20_{0,20}-19_{1,19}$	358215.6	185.3	5.83×10^{-4}	102.21±0.56	9.29±0.04	15.47±0.10	6.21±0.17
$^{34}\mathbf{SO_2}$	$23_{4,20}-23_{3,21}$	358347.3	292.4	3.86×10^{-4}	9.32±0.30	11.67±0.20	12.70±0.48	0.69±0.08
$\mathbf{CH_3OCH_3}$	$5_{5,1,1}-4_{4,1,1}$	358454.0	48.8	2.94×10^{-4}	3.32±0.30	8.56±0.68	14.95±1.40	0.21±0.05
$\mathbf{CH_3OH}^\star$	4_1-3_0 E	358605.8	44.3	1.32×10^{-4}	24.58±1.35	7.66±0.38	13.84±0.83	1.67±0.14
$\mathbf{S^{18}O}$	9_9-8_8	358645.7	99.3	5.92×10^{-4}	9.23±3.28	9.38±2.27	12.81±5.15	0.68±0.05
$\mathbf{CH_3CCH}^{\rm blend/1}$	21_3-20_3	358756.5	254.5	1.58×10^{-4}	3.63±0.18	9.34±0.30	12.03±0.66	0.28±0.04

Continued on next page

Table 2.7: The detected species toward the central position of the SLS field. The transitions marked with * have been detected toward AFGL 2591 in the SLS survey (Van der Wiel 2011). The transitions marked with ♦ are non-gaussian. Their intensity is obtained by integrating over the whole line profile. Their $V_{\rm LSR}$ is the velocity at $T_{\rm peak}$. The parameters without error bars are fixed parameters in the fit.

Molecule	Transition	Freq. (MHz)	$E_{\rm up}$ (K)	$A_{\rm ij}$ (s^{-1})	$\int T_{\rm mb}{\rm d}v$ (K km s^{-1})	$V_{\rm LSR}$ (km s^{-1})	FWHM (km s^{-1})	$T_{\rm peak}$ (K)
CH$_3$CCH$^{\rm blend/2}$	21_2-20_2	358790.6	218.3	1.60×10^{-4}	2.75±0.28	8.37±0.67	12.40±1.45	0.21±0.06
CH$_3$CCH$^{\rm blend/3}$	21_0-20_0	358817.9	189.5	1.61×10^{-4}	7.92±0.43	10.53±0.36	14.48±0.93	0.51±0.06
SO^{17}O[6]	$15_{2,14}$-$14_{1,13}$	358986.2	119.9	2.84×10^{-4}	20.64±0.25	9.95±0.08	13.18±0.19	1.47±0.10
SO$_2$ *	$25_{3,23}-25_{2,24}$	359151.2	320.9	3.10×10^{-4}	42.63±0.21	10.57±0.04	14.47±0.09	2.77±0.08
^{34}SO$_2$	$24_{2,22}-23_{3,21}$	359651.7	292.4	2.20×10^{-4}	6.76±0.34	12.02±0.26	11.01±0.71	0.58±0.07
SO$_2$ *	$19_{4,16}-19_{3,17}$	359770.7	214.3	3.85×10^{-4}	58.89±0.28	10.13±0.03	15.16±0.08	3.65±0.10
SO$_2$, $v_2=1$	$14_{4,10}-14_{3,11}$	360133.2	898.7	1.43×10^{-4}	4.42±0.37	11.53±0.58	13.44±1.23	0.31±0.06
SO$_2$	$34_{5,29}-34_{4,30}$	360290.4	612.0	4.80×10^{-4}	18.63±0.32	11.14±0.11	13.93±0.28	1.26±0.06
S^{18}O	10_9-9_8	360637.9	90.6	6.10×10^{-4}	11.30±0.52	9.65±0.32	13.98±0.71	0.76±0.09
SO$_2$ *	$20_{8,12}-21_{7,15}$	360721.8	349.8	7.72×10^{-5}	15.07±0.55	11.51±0.22	12.59±0.56	1.12±0.12
CH$_3$OH*	$11_{0,11}$-$10_{1,9}$ E	360848.9	166.0	1.21×10^{-4}	8.12±0.44	8.42±0.42	15.26±0.87	0.50±0.08
NO	J=7/2-5/2	360948.3	209.4	4.52×10^{-6}	15.30±0.55	11.31±0.52	29.18±1.19	0.49±0.06
CH$_3$OH*	8_1-7_2 E	361852.3	104.6	7.70×10^{-5}	11.25±0.38	6.58±0.27	16.60±0.68	0.64±0.07
DCN*	5-4	362045.8	52.1	2.25×10^{-3}	2.26±0.33	6.99±0.75	9.17±1.22	0.23±0.09
^{34}SO$_2$ *	$6_{3,3}-5_{2,4}$	362158.2	40.7	3.29×10^{-4}	19.93±0.27	11.17±0.08	12.88±0.21	1.45±0.09
^{33}SO$_2$	$15_{2,14}-14_{1,13}$	362487.6	120.8	2.98×10^{-4}	6.11±0.25	10.16±0.26	13.16±0.61	0.44±0.04
HNC, v$_2$=1	4-3	362554.4	709.3	2.15×10^{-3}	4.20±0.29	12.65±0.35	11.39±1.06	0.35±0.05
HNC*	4-3	362630.3	43.5	2.30×10^{-3}	52.96±0.56	5.72±0.06	12.93±0.18	3.85±0.42
p-H$_2$CO*	$5_{0,5}-4_{0,4}$	362736	52.3	1.37×10^{-3}	60.08±0.26	6.91±0.03	12.45±0.06	4.53±0.25
^{34}SO$_2$	$23_{2,22}-23_{1,23}$	362834.1	259.2	1.77×10^{-4}	6.75±0.31	11.91±0.26	11.59±0.65	0.55±0.06
SO$_2$ *	$21_{4,18}-21_{3,19}$	363159.3	252.1	4.00×10^{-4}	50.66±0.33	10.33±0.05	15.12±0.12	3.15±0.10

Continued on next page

---

[6] Probably blended with ^{34}SO$_2$ $15_{2,14}-14_{1,13}$ at 358988 MHz

Table 2.7: The detected species toward the central position of the SLS field. The transitions marked with * have been detected toward AFGL 2591 in the SLS survey (Van der Wiel 2011). The transitions marked with ♦ are non-gaussian. Their intensity is obtained by integrating over the whole line profile. Their $V_{\rm LSR}$ is the velocity at $T_{\rm peak}$. The parameters without error bars are fixed parameters in the fit.

Molecule	Transition	Freq. (MHz)	$E_{\rm up}$ (K)	$A_{\rm ij}$ ($\rm s^{-1}$)	$\int T_{\rm mb}{\rm d}v$ (K km $\rm s^{-1}$)	$V_{\rm LSR}$ (km $\rm s^{-1}$)	FWHM (km $\rm s^{-1}$)	$T_{\rm peak}$ (K)
^{33}SO$_2$	$23_{4,20}-23_{3,21}$	363286.4	297.1	4.01×10^{-4}	6.25±0.35	9.08±0.35	13.79±1.02	0.43±0.07
CH$_3$OH*	$16_1-16_0\ A^{\mp}$	363440.4	332.6	2.40×10^{-4}	6.63±0.39	9.74±0.46	15.26±0.94	0.41±0.06
U-line								
CH$_3$OH*	$7_2-6_1\ E$	363739.8	87.3	1.70×10^{-4}	17.91±0.26	8.36±0.10	13.80±0.22	1.22±0.07
HC$_3$N	40-39	363785.4	358.0	3.85×10^{-3}	3.67±0.22	12.39±0.28	9.71±0.70	0.35±0.05
SO$_2$	$24_{1,23}-24_{0,24}$	363890.9	280.5	1.78×10^{-4}	23.45±0.24	10.42±0.07	14.59±0.18	1.51±0.07
SO$_2$ *	$23_{2,22}-23_{1,23}$	363925.8	259.9	1.83×10^{-4}	27.90±0.34	10.33±0.08	15.27±0.22	1.72±0.07
p-H$_2$CO*	$5_{2,4}-4_{2,3}$	363945.9	99.5	1.16×10^{-3}	25.65±0.28	7.73±0.07	12.59±0.15	1.91±0.07
p-H$_2$CO	$5_{4,2}-4_{4,1}$	364103.2	240.7	4.99×10^{-4}	11.15±0.28	8.12±0.17	13.31±0.39	0.79±0.06
o-H$_2$CO*	$5_{3,3}-4_{3,2}$	364275.1	158.4	8.88×10^{-4}	39.52±0.32	7.79±0.07	12.00	3.09±0.14
o-H$_2$CO*	$5_{3,2}-4_{3,1}$	364288.9	158.4	8.88×10^{-4}	39.70±0.38	7.22±0.08	12.00	3.11±0.14
Atmospheric								
OCS*	$30-29$	364749	271.4	1.42×10^{-4}	8.45±0.31	9.89±0.27	14.07±0.56	0.56±0.07
H$_3$O$^+$	$3_{2,1}-2_{2,0}$	364797.4	139.7	2.78×10^{-4}	17.88±0.35	8.58±0.14	14.41±0.30	1.17±0.09
SO$_2$	$25_{9,17}-26_{8,18}$	364950.1	497.1	8.70×10^{-5}	10.11±0.26	12.12±0.14	11.08±0.34	0.86±0.08
CH$_3$OH, v_t=1	$5_3-5_2\ E$	364986.8	452.1	3.76×10^{-5}	3.59±0.24	6.02±0.36	10.52±0.80	0.32±0.06
HNC, v$_2$=1	4-3	365147.5	709.6	2.20×10^{-3}	4.32±0.44	3.50±0.43	9.01±1.18	0.45±0.09
p-H$_2$CO*	$5_{2,3}-4_{2,2}$	365363.4	99.7	1.18×10^{-3}	44.27±0.74	7.73±0.12	14.23±0.28	2.92±0.16
H$_2$CN	$5_{0,5}-4_{0,4}$	365443.6	52.7	4.15×10^{-5}	2.98±0.31	10.05±0.49	9.13±1.07	0.31±0.06
H$_2$C^{34}S	$11_{1,11}-10_{1,10}$	365613.4	118.5	7.33×10^{-4}	4.32±0.37	9.25±0.51	11.83±1.25	0.34±0.07
CH$_3$COCH$_3$	$27_{11,16,0}$-$26_{12,15,1}$	365696.2	281.7	1.20×10^{-3}	2.97±0.41	9.46±0.91	13.63±2.40	0.20±0.06
^{34}SO$_2$	$24_{1,23}-24_{0,24}$	365794.6	279.9	1.75×10^{-4}	4.56±0.45	13.44±0.26	7.54±0.68	0.57±0.07
U-line								

Continued on next page

Table 2.7: The detected species toward the central position of the SLS field. The transitions marked with * have been detected toward AFGL 2591 in the SLS survey (Van der Wiel 2011). The transitions marked with $^\blacklozenge$ are non-gaussian. Their intensity is obtained by integrating over the whole line profile. Their $V_{\rm LSR}$ is the velocity at $T_{\rm peak}$. The parameters without error bars are fixed parameters in the fit.

Molecule	Transition	Freq. (MHz)	$E_{\rm up}$ (K)	$A_{\rm ij}$ (s^{-1})	$\int T_{\rm mb} {\rm d}v$ (K km s^{-1})	$V_{\rm LSR}$ (km s^{-1})	FWHM (km s^{-1})	$T_{\rm peak}$ (K)
SO$_2$, v$_2$=1	$9_{4,6}-9_{3,7}$	365904.5	842.5	3.39×10^{-4}	3.42±0.53	11.84±0.91	11.60±2.68	0.28±0.06
SO$_2$, v$_2$=1	$7_{4,4}-7_{3,5}$	366125.8	826.6	3.05×10^{-4}	3.04±0.36	12.82±0.71	10.00	0.29±0.07
SO$_2$, v$_2$=1	$17_{4,14}-17_{3,15}$	366145.1	943.8	3.95×10^{-4}	4.28±0.32	14.10±0.50	10.00	0.40±0.07
SO$_2$, v$_2$=1	$6_{4,2}-6_{3,3}$	366159.5	820.0	2.76×10^{-4}	3.68±0.34	13.16±0.67	10.00	0.35±0.07
SO$_2$ *	$15_{2,14}-14_{1,13}$	366214.5	119.3	3.04×10^{-4}	91.77±1.56	9.43±0.13	15.80±0.32	5.46±0.15
H$_2^{13}$CO	$5_{1,4}-4_{1,3}$	366270.2	64.6	1.36×10^{-3}	6.96±0.77	10.14±1.06	14.00	0.47±0.08
^{33}SO$_2$	$6_{3,3}-5_{2,4}$	366521.9	41.6	1.31×10^{-5}	7.52±0.33	11.61±0.25	11.79±0.64	0.60±0.07
H$_2$CN	$5_{2,4}-4_{2,3}$	366637	100.4	9.42×10^{-5}	2.19±0.32	9.06±1.04	10.00	0.21±0.06
H$_2$CN	$5_{2,4}-4_{2,3}$	366655.4	100.4	7.69×10^{-5}	2.96±0.33	8.36±0.80	10.00	0.28±0.06
Atmospheric								
^{34}SO$_2$	$25_{4,22}-25_{3,23}$	367369.3	337.6	4.14×10^{-4}	8.97±0.37	11.97±0.26	12.69±0.60	0.66±0.09
o-H$_2$S$^{\rm blend/1}$ *	$3_{2,1}-3_{1,2}$	369101.4	154.5	1.90×10^{-4}	145.64±0.92	8.54±0.04	15.67±0.12	8.73±0.43
p-H$_2$S$^{\rm blend/2}$	$4_{3,1}-4_{2,2}$	369126.9	262.8	2.20×10^{-4}	15.23±0.76	9.69±0.24	10.45±0.56	1.37±0.43
H$_2^{33}$S	$3_{2,1}-3_{1,2}$	369170.4	154.4	2.55×10^{-5}	7.31±1.32	11.26±1.40	16.12±3.71	0.43±0.13
H$_2^{34}$S	$3_{2,1}-3_{1,2}$	369246.1	154.3	1.91×10^{-4}	8.92±0.63	11.15±0.42	11.54±1.13	0.73±0.15
^{13}CS*	$8-7$	369908.6	79.9	1.06×10^{-3}	11.87±0.45	10.00±0.26	14.02±0.59	0.80±0.10
SO$_2$ *	$9_{6,4}-10_{5,5}$	370108.6	129.7	4.19×10^{-5}	28.15±0.43	11.41±0.09	12.53±0.23	2.11±0.12
U-line								
^{34}SO	4_4-3_4	370931.7	33.4	1.45×10^{-5}	2.55±0.39	9.63±1.24	13.90±2.46	0.17±0.08
SO$_2$ *	$6_{3,3}-5_{2,4}$	371172.5	41.4	3.55×10^{-4}	81.33±0.57	9.89±0.05	15.66±0.13	4.88±0.13
SO$_2$, v$_2$=1	$21_{4,18}-21_{3,19}$	371264.8	1017.1	4.24×10^{-4}	4.11±0.71	11.59±1.25	13.72±3.49	0.28±0.08
CH$_3$OH*	17_1-17_0 A$^\mp$	371415.7	372.4	2.52×10^{-4}	5.04±0.41	9.57±0.62	14.45±1.14	0.33±0.09
^{33}SO$_2$	$25_{4,22}-25_{3,23}$	371804.6	343.0	1.35×10^{-6}	1.89±0.34	10.69±0.85	8.79±1.51	0.20±0.08

Continued on next page

Table 2.7: The detected species toward the central position of the SLS field. The transitions marked with * have been detected toward AFGL 2591 in the SLS survey (Van der Wiel 2011). The transitions marked with $^\blacklozenge$ are non-gaussian. Their intensity is obtained by integrating over the whole line profile. Their $V_{\rm LSR}$ is the velocity at $T_{\rm peak}$. The parameters without error bars are fixed parameters in the fit.

Molecule	Transition	Freq. (MHz)	$E_{\rm up}$ (K)	$A_{\rm ij}$ (s^{-1})	$\int T_{\rm mb}{\rm d}v$ (K km s^{-1})	$V_{\rm LSR}$ (km s^{-1})	FWHM (km s^{-1})	$T_{\rm peak}$ (K)
o-H$_2$CS*	$11_{1,11}-10_{1,10}$	371847.4	120.3	7.72×10^{-4}	10.58±0.28	9.06±0.18	13.18±0.36	0.75±0.09
S^{17}O	9_9-8_8	372113.6	102.5	6.33×10^{-4}	3.06±0.48	9.84±0.95	11.42±1.78	0.25±0.09
HNCO	$17_{1,17}-16_{1,16}$	372221.0	204.1	7.46×10^{-4}	8.13±0.64	11.96±0.35	9.23±0.83	0.83±0.08
^{34}**SO$_2$**	$13_{7,7}-14_{6,8}$	372279.8	199.7	6.00×10^{-5}	1.73±0.37	11.74±0.50	6.30±2.23	0.26±0.05
N$_2$H$^+$ *	4-3	372672.5	44.7	3.33×10^{-3}	54.14±0.33	7.44±0.04	12.82±0.09	3.97±0.20
U-line[7]								
SO^{18}O	$22_{0,22}-21_{1,21}$	373110.1	221.2	6.69×10^{-4}	4.18±0.70	13.21±0.90	10.93±2.26	0.36±0.09
SO*	4_4-3_4	373344.2	33.8	1.51×10^{-5}	43.76±1.28	9.78±0.20	14.32±0.51	2.87±0.27
HNCO	$17_{0,17}-16_{0,16}$	373600.7	161.4	7.54×10^{-4}	21.05±0.55	10.73±0.15	11.84±0.35	1.67±0.13

---

[7] HC$_3$N 41-40 is probable, but the line intensity is not consistent with its other three detected transitions.

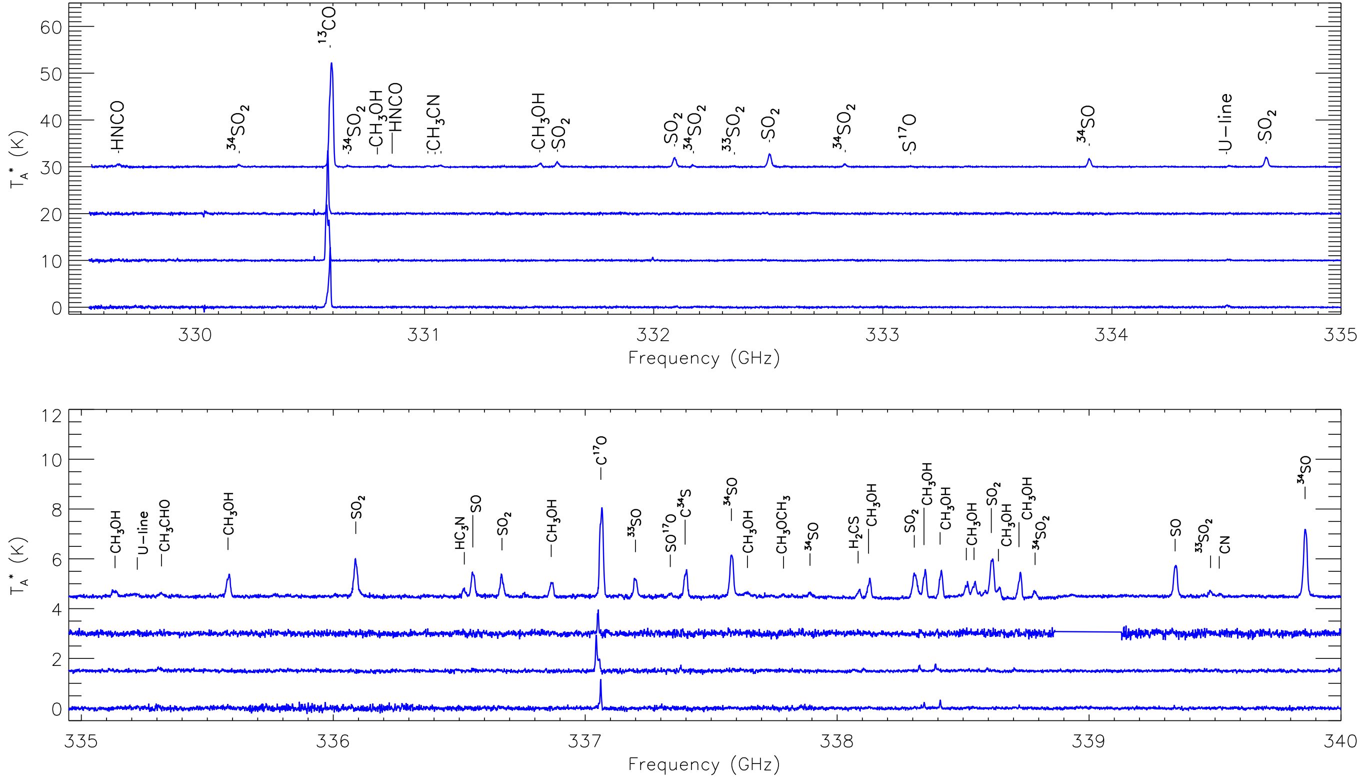

Figure 2.15 — The identified lines toward the (from bottom to top) Eastern tail, Northern clump, South-west clump regions, and the center of W49A in the frequency range between 330 and 335 GHz and 335 and 340 GHz.

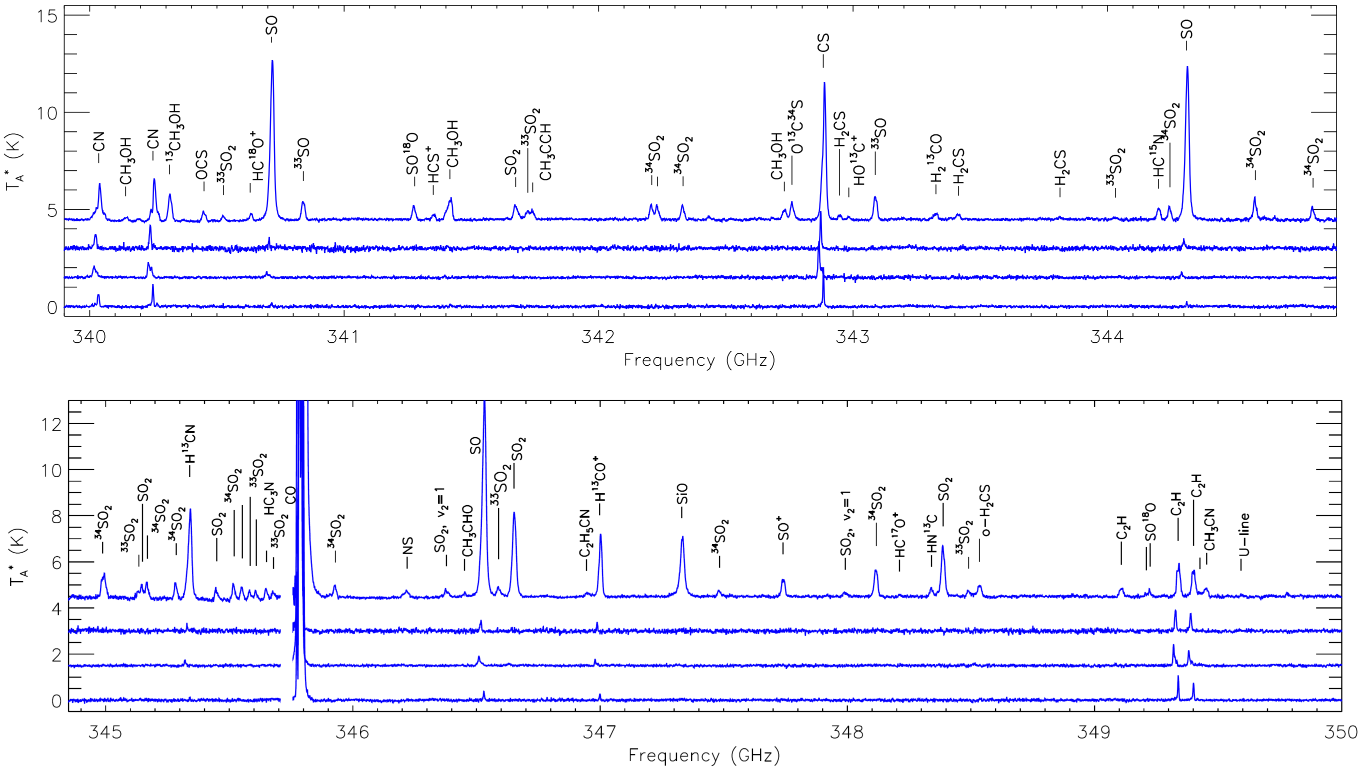

Figure 2.16 — The identified lines toward the (from bottom to top) Eastern tail, Northern clump, South-west clump regions, and the center of W49A in the frequency range between 340 and 345 GHz and 345 and 350 GHz.

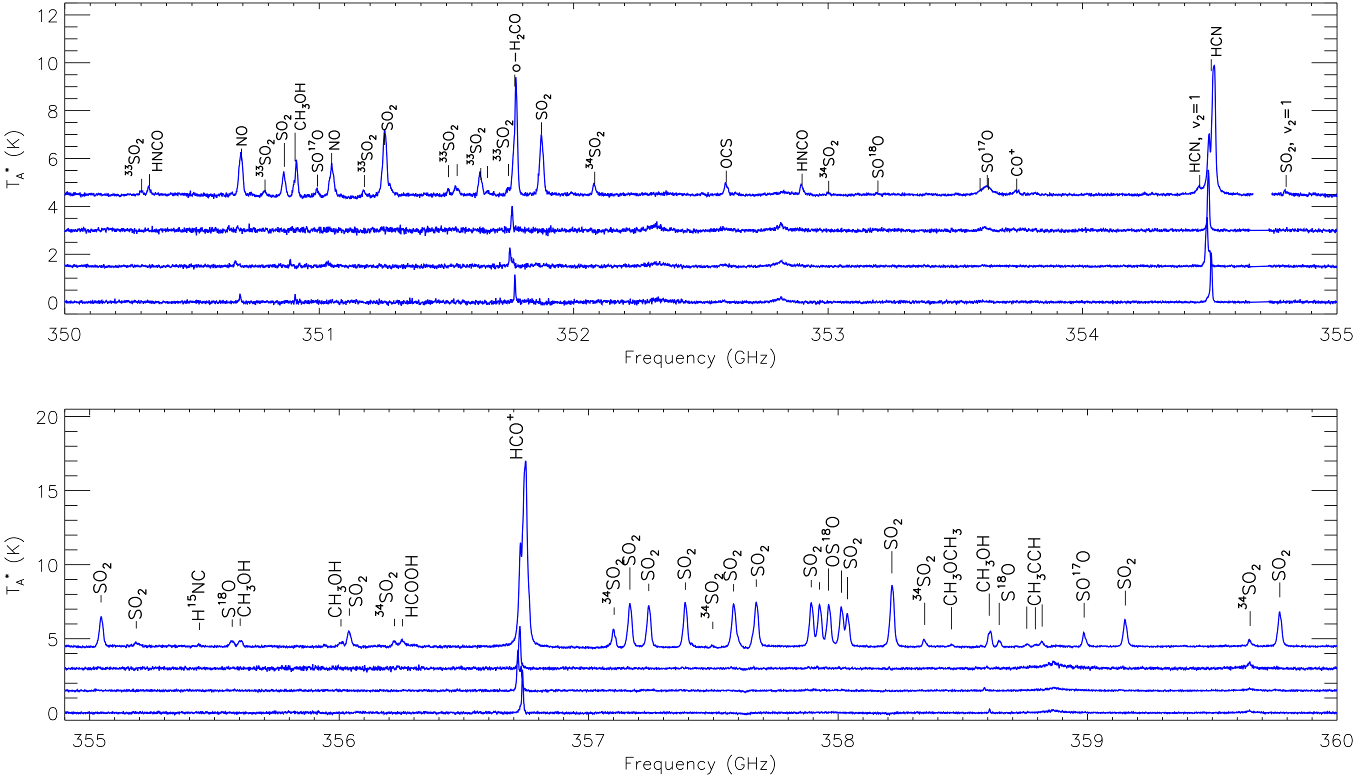

Figure 2.17 — The identified lines toward the (from bottom to top) Eastern tail, Northern clump, South-west clump regions, and the center of W49A in the frequency range between 350 and 355 GHz and 355 and 360 GHz.

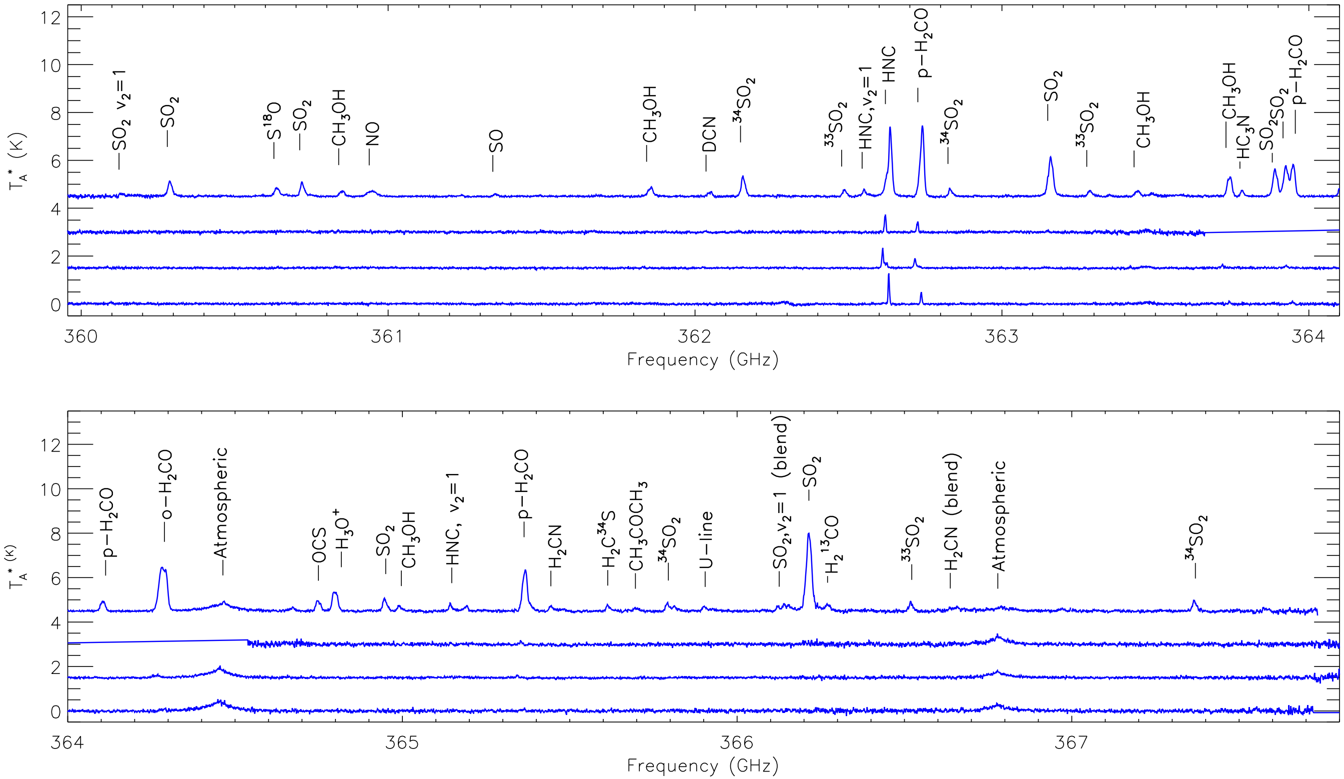

Figure 2.18 — The identified lines toward the (from bottom to top) Eastern tail, Northern clump, South-west clump regions, and the center of W49A in the frequency range between 360 and 364 GHz and 364 and 368 GHz.

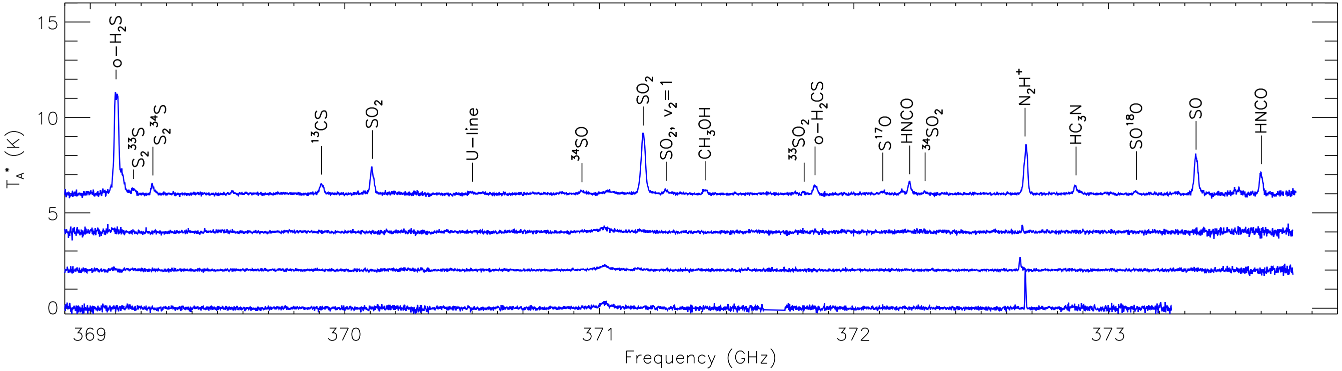

Figure 2.19 — The identified lines toward the (from bottom to top) Eastern tail, Northern clump, South-west clump regions, and the center of of W49A in the frequency range between 369 GHz and 374 GHz.

3

Extended warm and dense gas towards W49A: starburst conditions in our Galaxy?

Nagy, Z., Van der Tak, F. F. S., Fuller, G. A., Spaans, M. & Plume, R. [1]

---

[1] Published as: *"Extended warm and dense gas towards W49A: starburst conditions in our Galaxy?"* Astronomy & Astrophysics 542, 6

Abstract

The star formation rates in starburst galaxies are orders of magnitude higher than in local star-forming regions, and the origin of this difference is not well understood. We use sub-mm spectral line maps to characterize the physical conditions of the molecular gas in the luminous Galactic star-forming region W49A and compare them with the conditions in starburst galaxies. We probe the temperature and density structure of W49A using H_2CO and HCN line ratios over a $2' \times 2'$ (6.6×6.6 pc) field with an angular resolution of $15''$ ($\sim$0.8 pc) provided by the JCMT Spectral Legacy Survey. We analyze the rotation diagrams of lines with multiple transitions with corrections for optical depth and beam dilution, and estimate excitation temperatures and column densities. Comparing the observed line intensity ratios with non-LTE radiative transfer models, our results reveal an extended region (about $1' \times 1'$, equivalent to $\sim 3 \times 3$ pc at the distance of W49A) of warm ($>$100 K) and dense ($>10^5$ cm^{-3}) molecular gas, with a mass of $2 \times 10^4 - 2 \times 10^5$ $M_\odot$ (by applying abundances derived for other regions of massive star-formation). These temperatures and densities in W49A are comparable to those found in clouds near the center of the Milky Way and in starburst galaxies. The highly excited gas is likely to be heated via shocks from the stellar winds of embedded, O-type stars or alternatively due to UV irradiation, or possibly a combination of these two processes. Cosmic rays, X-ray irradiation and gas-grain collisional heating are less likely to be the source of the heating in the case of W49A.

3.1 Introduction

The formation of stars proceeds on scales ranging from 1000 AU-sized isolated low-mass cores to ~10 pc-sized GMCs with embedded massive clusters. The observed levels of star-formation activity also vary greatly: from ~10^{-4} $M_\odot$/yr in dwarf galaxies like I Zw 18 (Aloisi et al. 1999) to ~3 $M_\odot$/yr in the Milky Way to ~10^3 $M_\odot$/yr in starburst galaxies (e.g. Solomon & Vanden Bout 2005). The origin of this large spread in star formation rate may lie in different physical conditions with the gas forming the stars, the nature and role of feedback effects or other mechanisms. As one of the the most active star-forming regions in the Galactic disk, W49A provides a relatively nearby laboratory in which to study intense star formation activity and may provide insights into explaining the large observed range in star-formation activity in galaxies.

W49A is a luminous (>10^7 $L_\odot$) and massive (~10^6 $M_\odot$) star-forming region (Sievers et al. 1991) at a distance of 11.4 kpc (Gwinn et al. 1992). W49A contains several signatures of high star-formation activity, in particular, strong H_2O maser emission (Genzel et al. 1978). Line ratios of HNC, HCN and HCO^+ and their isotopologues suggest similar conditions to starburst galaxies (Roberts et al. 2011). Several ideas have been proposed to explain the high star-formation activity of W49A.

Welch et al. (1987) propose a large-scale inside-out gravitational collapse by interpreting two velocity components of HCO^+ J=1−0 spectra measured toward the ring-like configuration of UC Hii regions in terms of an infall profile. Serabyn et al. (1993) interpret the two-components of the double-peak line profile seen in CS (J=10−9, 7−6, 5−4, 3−2) and $C^{34}S$ (J=10−9, 7−6, 5−4) transitions as coming from different clouds, and suggest that massive star formation in W49A is triggered by a large-scale cloud merger. Williams et al. (2004) argue that one cannot distinguish between a global collapse model of a large cloud and a multiple-cloud model, based on HCO^+ (J=3−2 and 1−0) and $C^{18}O$ (J=2−1) data. Roberts et al. (2011) observe single-peaked $HC^{18}O^+$ (J=4−3) line profiles, which supports the large-scale infall hypothesis. In ^{13}CO and $C^{18}O$ J=2−1 maps of the W49A region Peng et al. (2010) find evidence of expanding shells with the dense clumps in the region lying peripherally along the shells. These expanding shells could provide a natural explanation of the observed molecular line profiles, and triggered massive star formation in W49A.

This paper reports new kinetic temperature and density estimates for a $2' \times 2'$ region of W49A based on single dish, JCMT images with $15''$ resolution. These indicate the presence of extended warm and dense gas towards the central region of the source. We use these results to compare W49A to starburst galaxies where similar results have been reported.

3.2 Observations and Data reduction

This paper presents results from data obtained as part of the JCMT Spectral Legacy Survey (SLS, Plume et al. 2007) covering between 330 and 373 GHz which has been carried out at the James Clerk Maxwell Telescope (JCMT)[2] on Mauna Kea, Hawai'i. The data were taken using the HARP-B receiver and the ACSIS correlator (Buckle et al. 2009). HARP-B consists of 16 pixels or receptors separated by 30 arcsec with a foot print of 2 arcmin.

The observations were carried out using jiggle - position switch mode. Each map covers a $2' \times 2'$ field sampled every $7.5''$, half of the JCMT beam width at the relevant frequencies ($15''$ at 345 GHz). The spectral resolution at these frequencies is $\sim$0.8 km s^{-1}and the beam efficiency is 0.63 (Buckle et al. 2009). The spectra were taken using an off-position $14'$ to the northeast of the source.

Data reduction was done manually using the tools in the `Starlink` software package. The raw time series files are processed in 1 GHz wide chunks. These files were inspected for bad receptors, baselines and frequency spikes. Bad receptors, bad baselines and spikes were masked in the time series files before they have been converted to three-dimensional data cubes (RA$\times$Dec$\times$frequency). These 3D cubes then were baseline corrected by fitting and removing a linear or second-order polynomial baseline. The baseline corrected cubes are then mosaicked to a larger cube covering an area of $2' \times 2'$ and the frequency range of interest. Single sideband system temperatures for these observations are in the range between 255 K (at 360 GHz) and 700 K (at 373 GHz). The analysis here primarily focuses on a number of spectral lines in the 360−373 GHz range plus a few selected lines from the 330−360 GHz part of the survey. The whole, systematic data analysis of the full SLS frequency range is the focus of a future paper.

We also use ancillary observations of the HCN $J = 3{-}2$ transition made using JCMT raster maps with half-beamwidth spacing using the Receiver A (211−276 GHz; beamwidth $20''$; main beam efficiency: 0.69). The HCN 3−2 map covers approximately the same field that of the SLS HARP maps. The HCN 3−2 data were reduced and calibrated with standard Starlink procedures. Linear baselines were removed and the data were Hanning smoothed. The map is a grid of 15 pixel × 15 pixels, where each pixel covers $8''\times 8''$.

Table 3.1 — Summary of the molecular lines used in this paper

Molecule	Transition	Frequency (MHz)	$E_{\rm up}$ (K)	rms ($T_{\rm mb}$) [a] (K)
HCN	$J = 3$–2	265886.2	25.5	0.90
HCN	$J = 4$–3	354505.5	42.5	0.05
H_2CO	$5_{1,5} - 4_{1,4}$	351768.6	62.5	0.12
H_2CO	$5_{0,5} - 4_{0,4}$	362736.1	52.3	0.05
H_2CO	$5_{2,4} - 4_{2,3}$	363945.9	99.5	0.06
H_2CO	$5_{4,1} - 4_{4,0}$	364103.3	240.7	0.06
H_2CO	$5_{3,3} - 4_{3,2}$	364275.1	158.4	0.08
H_2CO	$5_{3,2} - 4_{3,1}$	364288.9	158.4	0.08
H_2CO	$5_{2,3} - 4_{2,2}$	365363.4	99.7	0.06
CH_3OH	$11_{0,11} - 10_{1,9}$	360848.9	166.0	0.04
CH_3OH	$8_{1,7} - 7_{2,5}$	361852.3	104.6	0.05
CH_3OH	$16_{1,15} - 16_{0,16}$	363440.3	332.6	0.06
CH_3OH	$7_{2,5} - 6_{1,5}$	363739.8	87.3	0.06
CH_3OH	$17_{1,16} - 17_{0,17}$	371415.5	372.4	0.09
SO_2	$34_{5,29} - 34_{4,30}$	360290.4	611.9	0.06
SO_2	$20_{8,12} - 21_{7,15}$	360721.8	349.8	0.04
SO_2	$21_{4,18} - 21_{3,19}$	363159.3	252.1	0.05
SO_2	$24_{1,23} - 24_{0,24}$	363890.9	280.5	0.06
SO_2	$23_{2,22} - 23_{1,23}$	363925.8	259.9	0.06
SO_2	$25_{9,17} - 26_{8,18}$	364950.1	497.1	0.06
SO_2	$15_{2,14} - 14_{1,13}$	366214.5	119.3	0.09
SO_2	$9_{6,4} - 10_{5,5}$	370108.6	129.7	0.11
SO_2	$6_{3,3} - 5_{2,4}$	371172.5	41.4	0.09

[a] noise level measured over the central $1' \times 1.5'$, for 1 km s^{-1} channels.

3.3 Results

3.3.1 Line selection

Figure 3.1 shows the 360–373 GHz spectrum towards the central position (RA(J2000)=19:10:13.4; Dec(J2000)=09:06:14). More than 80 lines have been identified in this spectrum.

---

[2] The James Clerk Maxwell Telescope is operated by The Joint Astronomy Centre on behalf of the Science and Technology Facilities Council of the United Kingdom, the Netherlands Organisation for Scientific Research, and the National Research Council of Canada.

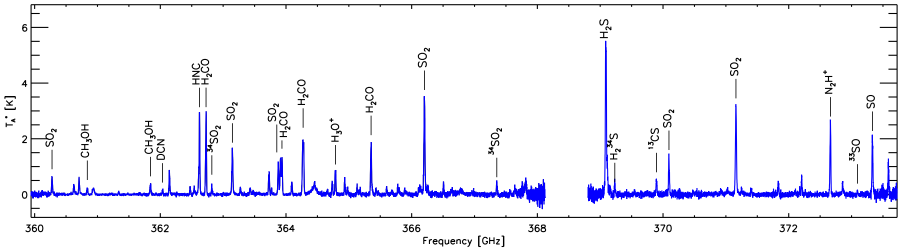

Figure 3.1 — The spectrum towards the source center (RA(J2000)=19:10:13.4; Dec(J2000)=09:06:14) in the 360−373 GHz frequency range of the SLS. The main detected lines are labeled. The gap in the spectrum around 368.5 GHz is a region of high atmospheric extinction and was not observed.

Our initial selection of lines for the analysis here is based on molecules that show multiple transitions in the high-frequency range (360−373 GHz) of the SLS, which include six H_2CO, five CH_3OH and nine SO_2 transitions (Table 3.1). These are used to trace the excitation conditions. One more H_2CO transition from the lower frequency part of the survey (H_2CO $5_{15} - 4_{14}$) was added to be used as a tracer of kinetic temperatures, together with the $5_{33} - 4_{32}$ transition from the high-frequency part of the SLS. The HCN 4−3 transition was selected from the lower frequency range, to trace the density structure, together with the HCN 3−2 transition.

In this paper, we restrict our analysis to our line selection summarized above and in Table 3.1. A subsequent paper (Chapter 2) will give more details on the chemical inventory including the full SLS frequency range (330−373 GHz) and on kinematics traced by various species with significant spatial extension. Figure 3.2 shows the main regions around the center of W49A overplotted on the integrated intensity maps in the HCN 4−3, SO_2 $15_{2,14}-14_{1,13}$, CH_3OH $7_{2,5}-6_{1,5}$ and H_2CO $5_{15}-4_{14}$ lines. The integrated intensities of the HCN and H_2CO lines show a similar distribution, indicating that their emission originates in the same volume. This is also supported by the line profiles of these two species (Nagy et al, in prep). In the following sections, we will refer to these regions with the coordinates indicated in the figure: source center (RA(J2000) = 19:10:13.4; Dec(J2000) = 09:06:14), Eastern tail (RA(J2000) = 19:10:16.6; Dec(J2000) = 09:05:48), Northern clump (RA(J2000) = 19:10:13.6; Dec(J2000) = 09:06:48) and South-West clump (RA(J2000)=19:10:10.6; Dec(J2000) = 09:05:18).

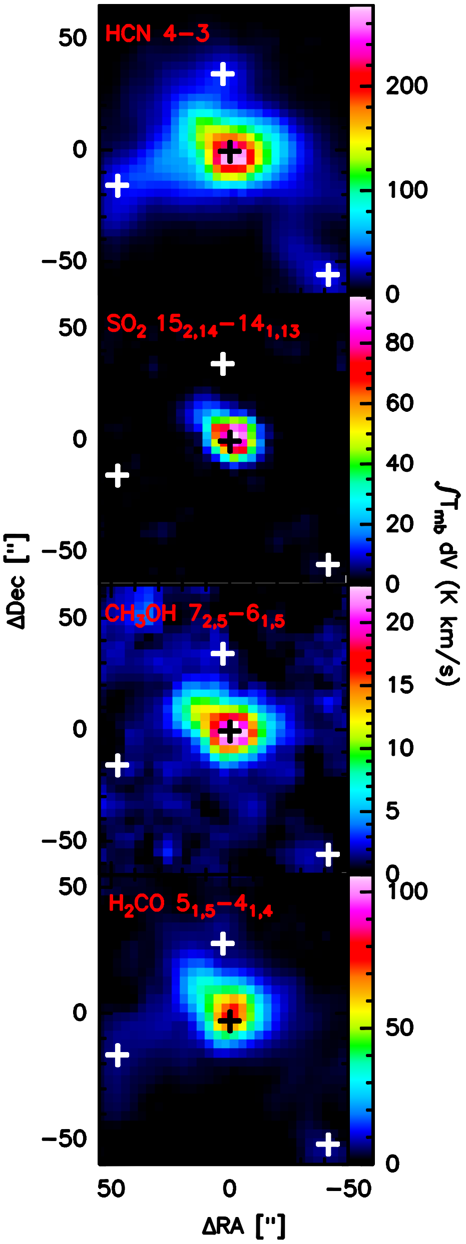

Figure 3.2 — The integrated intensity distribution of HCN 4–3, SO_2 $15_{2,14} - 14_{1,13}$, CH_3OH $7_{2,5} - 6_{1,5}$ and H_2CO $5_{15} - 4_{14}$. The central position is shown with black plus signs, the off-center regions (Northern clump, Eastern tail and South-west clump) are also shown with white plus signs.

3.3.2 Excitation conditions

A well known method for the estimation of excitation temperatures and column densities is the rotational diagram method (e.g. Turner 1991). It can be applied to molecules with multiple observed transitions using three assumptions: 1) the lines are optically thin, 2) the level populations can be characterized by a single excitation temperature ('rotational temperature', $T_{\rm rot}$) and 3) the emission is homogeneous and fills the telescope beam. Then the measured integrated main-beam temperatures of lines ($\int T_{\rm MB}{\rm d}V$ K km s^{-1}) is related to the column densities of the molecules in the upper level ($N_{\rm u}$) by:

$$\frac{N_{\rm u}}{g_{\rm u}} = \frac{N_{\rm tot}}{Q(T_{\rm rot})} \exp\left(-\frac{E_{\rm u}}{T_{\rm rot}}\right) = \frac{1.67 \cdot 10^{14}}{\nu \mu^2 S} \int T_{\rm MB}{\rm d}V, \tag{3.1}$$

with $g_{\rm u}$ the statistical weight of level u, $N_{\rm tot}$ the total column density in cm^{-2}, $Q(T_{\rm rot})$ the partition function for $T_{\rm rot}$, $E_{\rm u}$ the upper level energy in K, ν the frequency in GHz, μ the permanent dipole moment in Debye and S the line strength value. A linear fit to ln($N_{\rm u}/g_{\rm u}$) - $E_{\rm u}$ gives $T_{\rm rot}$ as the inverse of the slope, and $N_{\rm tot}$, the column density can be derived. The rotational temperature would be expected to be equal to the kinetic temperatures if all levels were thermalized.

In the case of non-LTE excitation, a different excitation temperature may characterize the population of each level relative to that of the ground state or relative to that of any other level. In this case, the three assumptions mentioned for the rotation diagram method do not apply. Equation 3.1 can be modified to include the effect of optical depth τ through the factor $C_\tau = \tau/(1-e^{-\tau})$ and beam dilution f ($= \Omega_s/\Omega_a$) (Goldsmith & Langer 1999), with Ω_s the size of the emission region and Ω_a the size of the telescope beam.

$$\ln\left(\frac{N_{\rm u}}{g_{\rm u}}\right) = \ln\left(\frac{N_{\rm tot,1}}{Q(T_{\rm rot})}\right) - \frac{E_{\rm u}}{kT_{\rm ex}} + \ln(f) - \ln(C_\tau). \tag{3.2}$$

According to equation 3.2, for a given upper level, $N_{\rm u}^{\rm obs}$ can be evaluated from a set of $N_{\rm tot,1}$, $T_{\rm ex}$, f and C_τ. Since C_τ is a function of $N_{\rm tot,1}$ and $T_{\rm ex}$, the independent parameters are therefore $N_{\rm tot,1}$, $T_{\rm ex}$ and f. Solving the equation for a 'source size' between $1''$ and $15''$ (which is equivalent with a beam dilution factor between $(1/15)^2$ and uniform beam filling), χ^2 minimization gives $N_{\rm tot,1}$ and $T_{\rm ex}$. Figure 3.3 shows the rotation diagrams for CH_3OH, H_2CO & SO_2 toward the central position with (green symbols) and without (red symbols) taking into account the optical depth and beam dilution. Table 3.2 includes the parameters of the rotation diagram fit toward the central position.

The CH_3OH lines are found to be optically thin ($\tau = 0.004 - 0.02$), so the rotation diagram fit is a good approximation to the column densities and excitation temperatures. The derived rotation temperature is 83±7 K. The H_2CO and SO_2 lines are mostly optically thick with optical depths in the range of 0.2−2.35 for H_2CO and 0.1−5.4 for SO_2. The best fit excitation temperatures are 138 K for H_2CO and 115 K for SO_2. The best fit total column densities are 4.3×10^{16} cm^{-2} for H_2CO and 1.4×10^{18} cm^{-2} for SO_2. The χ^2 minimization for H_2CO and SO_2 results in a best fit 'source size' of ∼2−3″, which is equivalent with 0.11−0.17 pc for W49A. This is consistent with the sizes of hot cores and UC HII regions resolved by sub-arcsecond resolution measurements, such as Wilner et al. (2001), De Pree et al. (1997, 2004).

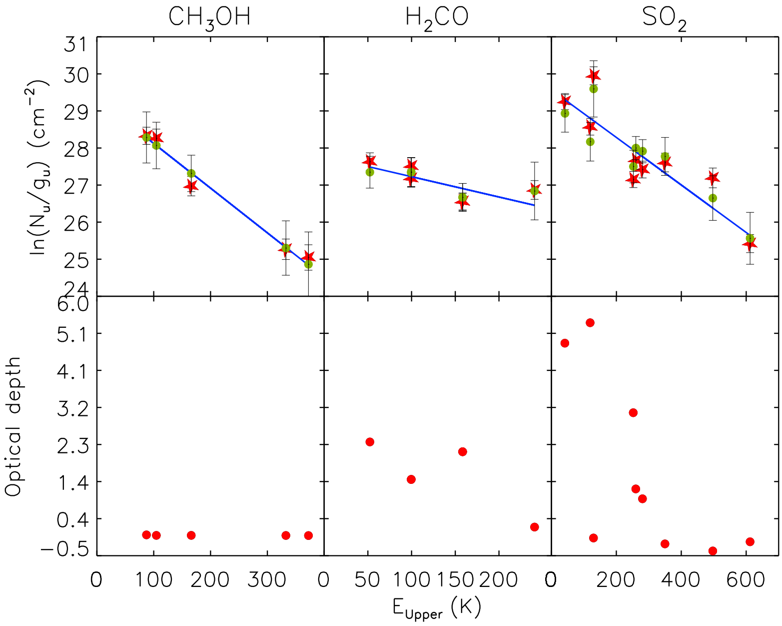

Figure 3.3 — The results of the rotation diagram analysis for H_2CO toward the center. *Top panels*: The results of the rotation diagram analysis before (red symbols) and after (green symbols) corrections for optical depth and beam dilution. The overplotted blue line corresponds to a linear fit to the rotational diagram without corrections. *Bottom panels*: The corresponding best fit optical depths from the χ^2 minimization.

Figure 3.4 shows the rotation diagrams for H_2CO toward the three main regions outside the center. The rotation diagram with corrections for optical depth and beam dilution (Figure 3.4. and Table 3.3.) gives similar excitation conditions toward the three main sub-regions (excitation temperatures: 67 K for the Northern clump, 56 K for the Eastern tail and 61 K for the South-west clump). These excitation temperatures are about half of the excitation temperature towards the central position (138 K). Since the lines are optically thin, the rotation temperatures are good estimates for the excitation temperatures. The best fit column densities are also similar between the off-center positions, about 1.7–2.2×10^{13} cm^{-3}, almost three orders of magnitude less than the best fit column density towards the center. The data at these positions are consistent with optically thin emission and uniform beam filling.

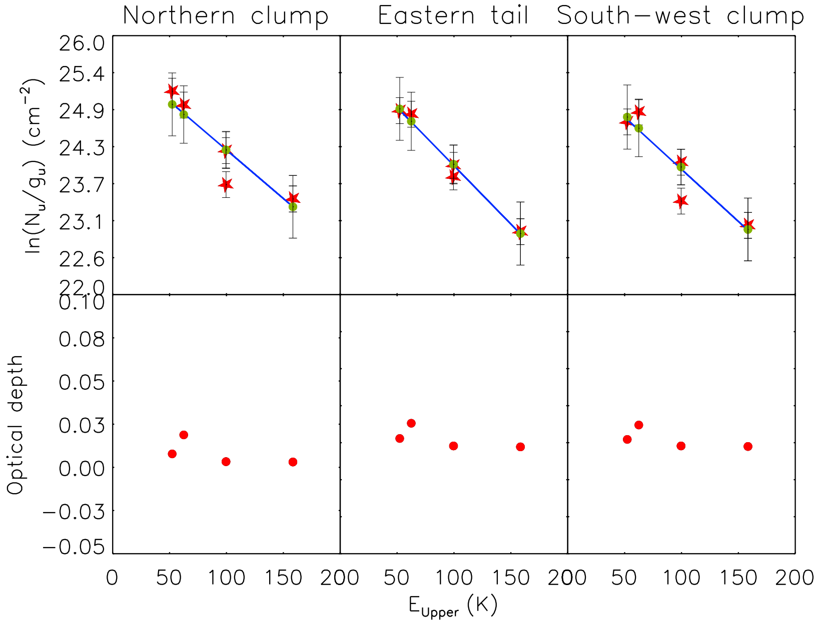

Figure 3.4 — The results of the rotation diagram analysis for H_2CO at off-center positions. *Top panels*: The results of the rotation diagram analysis before (red symbols) and after (green symbols) corrections for optical depth and beam dilution. The overplotted blue line corresponds to a linear fit to the rotational diagram without corrections. *Bottom panels*: The corresponding best fit optical depths from the χ^2 minimization.

3.3.3 Kinetic temperature estimates

To estimate the local physical conditions in W49A, we use ratios of lines from the same molecular species. The kinetic temperature can be probed by the line ratios of H_2CO lines from the same J-state but different K-states. In this case, we use the o−H_2CO $5_{15} - 4_{14}$ (351.769 GHz) and o−H_2CO $5_{33} - 4_{32}$ (364.275 GHz) transitions, since they have been detected in a large part of the SLS field and have been found to be excellent tracers of kinetic temperature (Figure 3.8). Our calculations use the non-LTE radiative transfer program Radex (Van der Tak et al. 2007), molecular data file from the LAMDA database (Schöier et al. 2005) and H_2CO collision data from Green (1991), which have been scaled by 1.37 to make a first order approximation for collisions with H_2. Uncertainties introduced by using these rates may be up to 50% for the column densities, but less affect the densities and temperatures, since those are derived from line intensity ratios. More recent calculations by Troscompt et al. (2009) are more accurate, however, include a more limited range of temperatures and transitions, therefore, were not used in our calculations.

Figure 3.8 shows the calculated line ratios as a function of kinetic temperature and H_2 density. In the central $40'' \times 40''$ region, FWHM=12 km s^{-1} was used as an initial parameter for Radex, while outside of this region we used FWHM=6 km s^{-1}, based on the observed values. However, there is no strong dependence on the FWHM of the lines. We apply a molecular column density of $N(H_2CO)=5 \times 10^{14}$ cm^{-2} as an 'average' value for all the positions over the SLS field. This is slightly below the value that can reproduce the optical depths derived from rotation diagram method for the central position, assuming uniform beam filling.

The results are shown in Figure 3.5 with the main regions highlighted. We derive a kinetic temperature of 300 K toward the center, 98 K toward the Northern clump, 85 K toward the South-west clump and 68 K toward the Eastern tail, with an uncertainty of ~30%. In fact, there is a large, about $1' \times 1'$ ($\sim 3 \times 3$ pc) region around the center, with kinetic temperatures $\gtrsim$100 K.

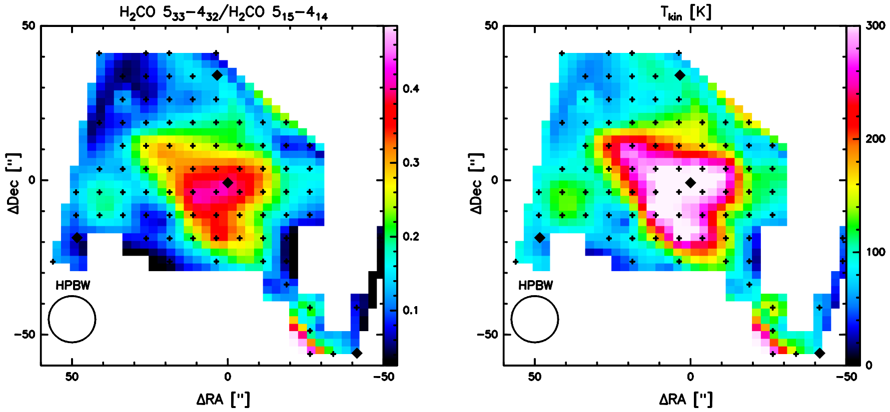

Figure 3.5 — Left panel: Ratio of $5_{33}-4_{32}$ to the $5_{15}-4_{14}$ H_2CO transition. Right panel: Kinetic temperature map of W49A determined from line ratio shown in the left panel. The black diamonds show the positions of the four main regions: center, Northern clump, Eastern tail and South-west clump.

3.3.4 Volume- and column density estimates

To estimate H_2 volume densities of the high temperature gas that the H_2CO line ratios trace, we use the ratio of the HCN 3−2 (265.886 GHz) to the HCN 4−3 (354.505 GHz) transition. Our calculations are based on collisional rates from Dumouchel et al. (2010), which have been scaled by a factor 1.37 to represent collisions with H_2. The HCN 4−3 map has been convolved to the resolution of the HCN 3−2 map (20″). Since the line ratios depend on the kinetic temperature (Figure 3.8), we use the kinetic temperatures determined from the H_2CO line ratios to convert the measured HCN line ratios (Figure 3.6) to volume densities. Therefore, even though HCN was detected towards almost the entire SLS field, our calculations only take into account the positions where both of the H_2CO transitions were detected. The uncertainty of these density estimates is about a factor of two. Figure 3.7 shows the estimated volume densities. Note that not all the positions with kinetic temperature estimates are included in the density map: this is due to the uncertainty of our method below 100 K, where the HCN 3−2 / 4−3 line ratios are temperature rather than density tracers. With a search range in the densities between 10^3 and 10^8 cm^{-3}, an extended area towards the center (approximately corresponding to the high-excitation area revealed by the H_2CO line ratios) corresponds to densities as higher than 10^5 cm^{-3} or higher, with a maximum of 6.9×10^6 cm^{-3}. The maximum density is measured toward an offset position compared to the position we refer to as 'center'. The densities toward the central part show a little less than an order of magnitude variation.

The average H_2 volume density corresponding to the central 1×1 arcminute region is 1.6×10^6 cm^{-3}. The lowest densities, toward the edges of the cloud area covered by our estimates, is a few times 10^4 cm^{-3}. However, our density estimates are more accurate for densities between 10^5 and 10^8 cm^{-3} (Figure 3.8). In addition to the uncertainty of the method below $\sim 10^5$ cm^{-3}, the H_2CO $5_{15} - 4_{14}$ and $5_{33} - 4_{32}$ transitions are detected over a less extended region, compared to the HCN 3−2 and 4−3 transitions. Estimating the physical conditions outside the area covered by our kinetic temperature and volume density maps requires molecular line tracers with a larger spatial extent.

Based on the kinetic temperatures and volume densities presented above, we estimate the column densities of the two main molecular tracers used in this paper, HCN and H_2CO. These estimates use H_2 volume densities of 1.8×10^6 cm^{-3} for the center, 1.2×10^6 cm^{-3} for the Eastern tail, 5.6×10^5 cm^{-3} for the Northern clump and 1.3×10^5 cm^{-3} for the South-west clump. The kinetic temperatures used for each position are listed in section 3.3.3. To calculate the HCN column density toward the center, we use the $H^{13}CN$ 4−3 (345.3 GHz) transition, and $^{12}C/^{13}C=77$ (Wilson & Rood 1994). HCN peaks toward the center, with a column density of 7.3×10^{15} cm^{-2}. The HCN column densities of the Eastern tail and Northern clump regions are comparable: $N(\mathrm{HCN}) = 7-8 \times 10^{13}$ cm^{-2} toward the Eastern tail and $N(\mathrm{HCN}) = 1.5-2 \times 10^{14}$ cm^{-2} toward the Northern clump. N(HCN) toward the South-west clump is a factor of 4−5 above

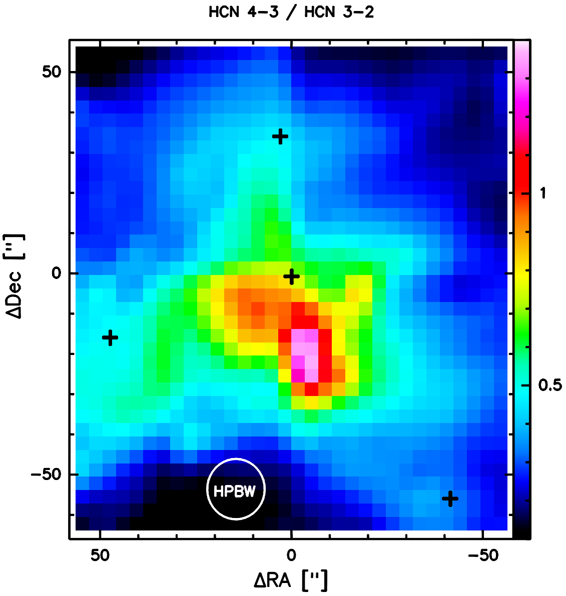

Figure 3.6 — Map of the line ratio of HCN J = 4–3 to HCN J = 3–2. The black crosses show the positions of the four main regions: center, Northern clump, Eastern tail and South-west clump.

the column density of the Northern clump: N(HCN) = $6.2 - 9.6 \times 10^{14}$ cm^{-2}. $N(H_2CO)$ is $\sim 3.2 \times 10^{14} - 4.5 \times 10^{14}$ cm^{-2} toward the center as well as the South-west clump. The Northern clump has $N(H_2CO)$ slightly below the center and South-west clump, $7.0 \times 10^{13} - 1.1 \times 10^{14}$ cm^{-2}, while toward the Eastern tail, we measure a column density of $4.9 \times 10^{13} - 5.0 \times 10^{13}$ cm^{-2}. The two orders of magnitude difference in the H_2CO column density toward the center compared to the best fit column density derived from the rotation diagrams can be accounted for the simple assumption used in the rotation diagram method, that the level populations can be described by a single excitation temperature.

The mass of the warm and dense gas can be estimated based on the H_2CO column density, by assuming an H_2CO abundance. Van der Tak et al. (2000) derive H_2CO abundances in the range of $10^{-9} - 10^{-10}$ for thirteen regions of massive star formation. For an 'average' column density of 10^{14} cm^{-2} and an abundance of 10^{-9}, the mass of the central $1' \times 1'$ region with warm and dense gas is $\sim 2 \times 10^4$ $M_\odot$, which becomes $\sim 2 \times 10^5$ $M_\odot$ for an H_2CO abundance of 10^{-10}. These are comparable to the mass estimates based on dust continuum measurements. Ward-Thompson & Robson (1990) estimate a mass of $\sim 2.4 \times 10^5$ $M_\odot$ corresponding to the central $\sim$2 pc. Buckley & Ward-Thompson (1996)

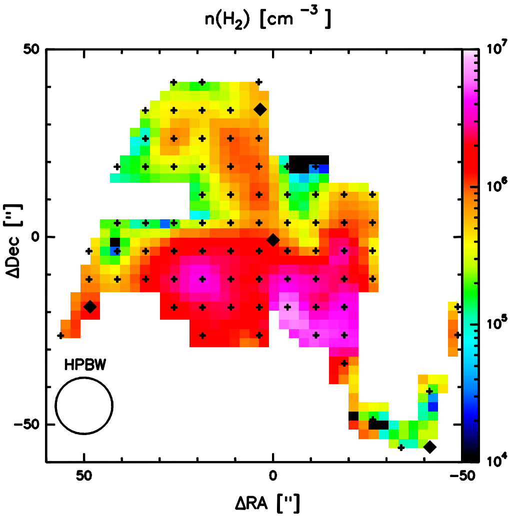

Figure 3.7 — Volume density estimates from the HCN 3−2 and HCN 4−3 lines. The black diamonds show the positions of the four main regions: center, Northern clump, Eastern tail and South-west clump.

adopt a value of $\sim 10^5\ M_\odot$ as a best fit based on dust continuum as well as on CS data published by Serabyn et al. (1993).

A second estimate of the mass of dense gas can be obtained from the HCN analysis. Adopting an average number density of 1.6×10^6 cm^{-3} over the central $1' \times 1'$ region and assuming an approximately spherical region would imply a mass of $\sim 2\times10^6\ M_\odot$. This is a factor of 10−100 larger than the H_2CO suggests indicating that the dense HCN material fills a fraction between 1% and 10% of the volume of this extended region.

Further evidence for a small volume filling factor is given by the best fit source sizes from the rotation diagrams toward the central position. The column densities derived from Radex are beam-averaged, while the best fit column densities from the rotation diagram correspond to clumps with sizes indicated by the best fit source size. Comparing the HCN column densities to the H_2 volume densities gives another indication of the volume filling factor. While the volume densities change between 10^5 and a few times 10^6 cm^{-3} and show a rather uniform distribution, N(HCN) shows a 2 orders of magnitude variation (7×10^{13}–7×10^{15} cm^{-2}) and peaks toward the center. The emission may originate in warm and dense gas in a number of unresolved clumps. Such a behavior was found before, by Snell et al. (1984) and Mundy et al. (1986) for M17, S140 and NGC 2024.

Table 3.2 — Results of the excitation analysis toward the center of W49A

	I. Rotation diagrams		
	SO_2	**CH_3OH**	**H_2CO**
$T_{\rm rot}$ [K]	156±11	83±7	182±84
$N_{\rm tot}{}^a$ [10^{15} cm^{-2}]	14.56±2.99	6.58±1.38	0.78±0.17
Source size[″]	$3.1^{+0.0}_{-0.7}$	$12.5^{+2.5}_{-10.7}$	$2.4^{+4.2}_{-0.3}$
$T_{\rm ex}$ [K]	115^{+40}_{-15}	$82.1^{+16.1}_{-16.1}$	$138.2^{+111.3}_{-115.0}$
$N_{\rm tot,1}{}^b$ [10^{15} cm^{-2}]	$1400.0^{+400.0}_{-430.0}$	$9.5^{+860.5}_{-3.2}$	43^{+1857}_{-25}
	II. Non-LTE calculation		
$T_{\rm kin}$ [K]^c	300		
N[H_2CO] [cm^{-2}]	3.2–4.5×10^{14}		
N[HCN] [cm^{-2}]	7.3×10^{15}		
n [cm^{-3}]^d	1.8×10^6		

---

[a] Total beam-averaged column density calculated using the assumption that the lines are optically thin, the level populations can be characterized by a single excitation temperature and the emission fills the telescope beam.

[b] Total source-averaged column density given by the χ^2 minimization, including a correction for the optical depth and a beam dilution factor. The errors show the 1-σ upper and lower limits of the best fit.

[c] The uncertainty of the kinetic temperatures is ∼30%.

[d] The uncertainty of the density estimates is a factor of 2.

3.4 Discussion

We have detected warm ($\gtrsim$100 K) and dense ($\gtrsim 10^5$ cm^{-3}) gas extended over a $1' \times 1'$ (∼3×3 pc) field towards W49A. Based on a rotation diagram analysis with corrections for optical depth and beam dilution, we derive excitation temperatures of 115 K (for SO_2), 82 K (for CH_3OH), 138 K (for H_2CO) towards the center. From H_2CO line ratios with the same J and different K-states, we derive kinetic temperatures of ∼300 K toward the center, 68 K toward the Eastern tail, 98 K toward the Northern clump and 85 K toward the South-West clump. Our kinetic temperature estimates are consistent with the excitation temperatures derived from the rotation diagram method, given that non-LTE conditions are expected, with excitation temperatures below the kinetic temperatures. Ratios of HCN 3−2 / HCN 4−3 line intensities, using our kinetic temperature estimates, result in H_2 volume densities of 1.8×10^6 cm^{-3} for the center, 1.2×10^6 cm^{-3} for the Eastern tail, 5.6×10^5 cm^{-3} for the Northern clump and 1.3×10^5 cm^{-3} for the South-west clump.

Our kinetic temperature estimates are significantly higher than previously reported values. Based on Planck brightness temperatures derived from the CO

Table 3.3 — Results of the excitation analysis toward the off-center regions of W49A

	I. Rotation diagrams		
	Northern clump	**Eastern tail**	**South-west clump**
$T_{\rm rot}$ [K]	67±13	56±3	62±11
$N_{\rm tot}{}^{a}$ [10^{13} cm^{-2}]	2.26±0.48	1.82±0.46	1.68±0.36
Source size[″]	$14.44^{+0.56}_{-11.2}$	$14.44^{+0.56}_{-11.2}$	$14.44^{+0.56}_{-10.64}$
$T_{\rm ex}$ [K]	67^{+21}_{-13}	55^{+14}_{-9}	61^{+19}_{-10}
$N_{\rm tot,1}{}^{b}$ [10^{13} cm^{-2}]	$2.2^{+44.8}_{-0.2}$	$1.9^{+39.1}_{-0.3}$	$1.7^{+22.3}_{-0.2}$
	II. Non-LTE calculation		
	Northern clump	**Eastern tail**	**South-west clump**
$T_{\rm kin}$ [K]^{c}	98	68	85
N[H$_2$CO] [cm^{-2}]	0.7−1.1×10^{14}	4.9−5.0×10^{13}	3.2−4.5×10^{14}
N[HCN] [cm^{-2}]	1.5−2×10^{14}	7−8×10^{13}	6.2−9.6×10^{14}
n [cm^{-3}]^{d}	5.6×10^{5}	1.2×10^{6}	1.3×10^{5}

---

[a] Total beam-averaged column density calculated using the assumption that the lines are optically thin, the level populations can be characterized by a single excitation temperature and the emission fills the telescope beam.

[b] Total source-averaged column density given by the χ^2 minimization, including a correction for the optical depth and a beam dilution factor. The errors show the 1-σ upper and lower limits of the best fit.

[c] The uncertainty of the kinetic temperatures is ∼30%.

[d] The uncertainty of the density estimates is a factor of 2.

$J = 7{-}6$ transition, Jaffe et al. (1987) estimate kinetic temperatures of >70 K in the centre, falling below 50 K in the outer parts of the cloud. However, these observations have a beam size of 32″, which suggests higher kinetic temperatures on a smaller scale, and as such, may be consistent with our results. Roberts et al. (2011) use HCN/HNC line ratios compared to chemical models to estimate kinetic temperatures and derive temperatures of 100 K toward the center, 40 K toward the South-west clump, 40 K toward the Eastern tail and 75 K toward the Northern clump. One possible reason of the difference between the kinetic temperatures presented in this paper and the values estimated by Roberts et al. (2011) is that Roberts et al. (2011) adopted the HCN collision rates for HNC, which can result in an uncertainty, due to the fact that HCN and HNC have slightly different dipole moments (3.0 vs. 3.3 D).

Our density estimates are consistent with the estimates by Welch et al. (1987), who estimate the cloud density to be >3×10^5 cm^{-3} within the inner 1 pc and ∼10^4 cm^{-3} in the outer parts of the cloud. Our estimates are also consistent with (Plume et al. 1997), who find - based on CS 2−1, 3−2, 5−4, 14−13, 10−9 transitions - that n(H$_2$) toward W49A varies between 5.2×10^5 and

$1.8{\times}10^6$ cm^{-3}. Serabyn et al. (1993) estimate densities between $2{-}6{\times}10^6$ cm^{-3} for three clumps using CS (3−2, 5−4, 7−6, 10−9) and $C^{34}S$ (5−4, 7−6, 10−9) transitions. Our mass, volume- and column density estimates also indicate a low filling factor for the dense gas. Plume et al. (1997) probe masses and densities for a number of massive star-forming regions, and find, that filling factor for the dense gas is <25%.

3.4.1 Possible heating sources

The most probable mechanisms that contribute to the heating of the warm and dense molecular gas seen toward W49A are mechanical heating (shocks produced by stellar winds), and UV or X-ray irradiation. Another possible mechanism, that has been suggested for starburst galaxies, is heating by cosmic rays (Bradford et al. 2003). In the case of W49A, the only possible source of cosmic-rays above the Galactic background is the supernova remnant W49B, however, due to the high uncertainty in the distance of W49B (Brogan & Troland 2001), this remains an open question. Therefore, we focus on quantifying the effect of mechanical heating and irradiation by UV and X-rays for the warm and dense region revealed by our H_2CO and HCN data.

Mechanical heating The luminosity corresponding to the *mechanical heating* produced by stellar winds of embedded O-type stars can be estimated from:

$$L_{\rm w} = 1.3 \times 10^{36} \left(\frac{\dot{M}}{10^{-6} M_\odot \ {\rm year}^{-1}}\right) \left(\frac{v_{\rm w}}{2 \times 10^3 \ {\rm kms}^{-1}}\right)^2 {\rm erg \ s}^{-1} \tag{3.3}$$

where $v_{\rm w} = 2000$ km s^{-1} can be applied as the velocity of the stellar wind (Tielens 2005). Peng et al. (2010) found evidence for two expanding shells with a size of ∼2.9 pc, comparable to the size of the extended high excitation region we have found. They found that a constant mass-loss rate of $\sim 1.2{\times}10^{-6}\ M_\odot$ yr^{-1} can sustain a wind-driven bubble with a size of ∼2.9 pc, which corresponds to the mass loss rate of one O-type star. Using these values, the mechanical luminosity is $L_{\rm w} = 1.56 \times 10^{36}$ erg s^{-1} or about 405 $L_\odot$. Assuming an efficiency of 1−10 % (Loenen et al. 2008), the mechanical heating rate is ∼4−40.5 $L_\odot$. However, this is only a lower limit of the luminosity corresponding to the mechanical heating. Alves & Homeier (2003a) estimate that ∼30 O-type stars belong to the central stellar cluster, which has a diameter of ∼6 pc. Taking this into account, the mass-loss rate, as well as the luminosity is about an order of magnitude larger than the value we derive by taking a mass-loss rate that belongs to one O-type star. This gives 40.5−405 $L_\odot$ as a mechanical heating luminosity.

In addition to the effect of stellar winds, protostellar outflows give a contribution to the mechanical heating. The largest outflow is connected to the most luminous water-maser emission in the Milky Way (Gwinn et al. 1992).

It has been characterized by Scoville et al. (1986) and recently by Smith et al. (2009). Adopting an outflow dynamical time-scale of 10^4 yr, that corresponds to an average ~25 km s^{-1} outflow speed (Smith et al. 2009), an energy of $4.4{\times}10^{47}$ erg (Scoville et al. 1986, scaled to a distance of 11.4 kpc), the mechanical luminosity is $L_{\rm mech} = 1.4{\times}10^{36}$ erg s^{-1} or about ~400 $L_{\odot}$. Assuming the same efficiency as for the mechanical luminosity produced by the stellar wind, only the most powerful outflow produces a mechanical luminosity that is 10 % of the mechanical luminosity produced by the stellar winds of an embedded cluster of ~30 O-type stars. This estimate gives a lower limit on the mechanical luminosity produced by outflows. Additional kinetic energy injection may have been resulted by past outflows of the current O-type stars. These flows may still be dissipating energy. The existence of these flows may be probed using ALMA.

An additional source of the mechanical heating may exist in the form of shocks driven by the expansion of the (UC)Hɪɪ regions into the molecular cloud. The corresponding heating rate is proportional to the kinetic energy injection rate and is given by:

$$G = \frac{1}{2}A\frac{{\rm d}\rho}{{\rm d}t}V^2 = \frac{1}{2}\rho A V^3 \tag{3.4}$$

where A is the surface area of the shocks, ρ is the density of the medium into which the shock is moving, and V is the velocity of the shock. The surface area of the shocks can be estimated based on De Pree et al. (1997), who measure the sizes of the (UC)Hɪɪ regions, based on high-resolution ($0\farcs8$) 3.6 cm data. We use an average radius of 0.05 pc to calculate the surface area of the shocks. Based on $n({\rm H_2}) = 10^6$ cm^{-3}, a shock velocity of 10 km/s results in a heating rate of 1.6×10^{37} for a cluster of 30 O-type stars. For a shock velocity of 5 km/s, the mechanical heating rate of the expanding (UC)Hɪɪ regions corresponding to the cluster of 30 O-type stars is $\sim 2 \times 10^{36}$ erg/s - in the same order of magnitude as the mechanical heating produced by the stellar winds of the 30 O-type stars.

Radiative heating by the embedded stellar cluster The importance of *heating by UV radiation* from young massive stars, in the form of photo-electric emission by dust grains and PAHs, can be estimated from the far-infrared luminosity. Vastel et al. (2001) estimates a total FIR flux of 1.54×10^{-6} erg s^{-1} cm^{-2}, which, at the distance of W49A, is equivalent to a total IR luminosity of 6.3×10^6 $L_{\odot}$. Adopting an efficiency of $10^{-3} - 10^{-2}$ (Meijerink & Spaans 2005), the heating rate by UV irradiation is on the same order of magnitude as the luminosity that can be expected from the mechanical heating.

X-ray heating Hard X-ray emission has been detected (Tsujimoto et al. 2006) toward the center of W49A, associated with two Hɪɪ regions. They measure an X-ray luminosity of 3×10^{33} erg s^{-1} in the 3−8 keV band. Assuming an efficiency of 10% (Meijerink & Spaans 2005), the X-ray heating luminosity is on the order of 0.1 $L_\odot$, about three orders of magnitudes below the luminosity of the mechanical and UV heating. In addition, since X-ray emission is due to point-sources, rather than an extended region, X-rays mostly act locally and seem less likely to be responsible for the extended emission region what we detected.

Gas-grain collisional heating At the densities estimated using HCN transitions (10^5 -10^6 cm^{-3}), gas-grain collisions may give a significant contribution to the heating of the gas. Based on a greybody fit to the dust emission, Ward-Thompson & Robson (1990) derive a dust temperature of 50 K. They also find evidence, that a population of small, hot dust grains with $T \sim$350 K also exists, based on an excess in the near-infrared. The heating rate of the gas per unit volume can be estimated using (Hollenbach & McKee 1979, 1989):

$$\begin{aligned} \Gamma_{\rm coll.} = & \quad 1.2 \quad \times 10^{-31} n^2 \left(\frac{T_{\rm kin}}{1000}\right)^{1/2} \left(\frac{100~\mathring{A}}{a_{\rm min}}\right)^{1/2} \\ \times & \quad [1 - 0.8 \exp\left(-75/T_{\rm kin}\right)](T_{\rm d} - T_{\rm kin})(\text{erg cm}^{-3}~\text{s}^{-1}) \end{aligned} \tag{3.5}$$

where the minimum grain size is set at $a_{\rm min} = 10~\mathring{A}$. Using T$\sim$150 K and n=10^6 cm^{-3}, assuming a volume filling factor of 1-10% for the hot gas, a gas-to-dust ratio of 100, and that the fraction of the warm ($T \sim$350 K) dust is up to 1% of the total dust, gas-grain heating for a 3×3 pc region toward the center of W49A is expected to be $\sim 10^{34}$-10^{35} erg s^{-1}, equivalent to $\sim$3-30 $L_\odot$.

Based on these estimates, mechanical heating and UV heating seem to be the most probable heating mechanisms, while irradiation by X-rays and gas-grain collisions are less probable. The contribution of radiation to the excitation of W49A has been investigated earlier by Roberts et al. (2011), based on HCN, HNC and HCO$^+$ transitions from the SLS. By comparing the observed line intensity ratios to PDR (Photon-dominated Region) and XDR (X-ray Dominated Region) models of Meijerink et al. (2007), they find, that HCN/HCO$^+$ line ratios are consistent with PDR models, while HCN/HNC line ratios are consistent with XDR models. They interpret this result as evidence that irradiation by UV and X-ray photons plays a minor role in the excitation of W49A. However, as seen above, based on the UV heating luminosity, UV radiation cannot be ruled out to contribute significantly to the heating of W49A.

3.4.2 Comparison to the cooling rate

One of the main contributions to the total cooling in W49A is expected to occur via CO lines, therefore we derive a lower limit on the total cooling rate from the ^{12}CO 3−2 (345.8 GHz) line luminosity based on data from the SLS. The CO line luminosity can be calculated from the CO 3−2 line intensities (Solomon &

Vanden Bout 2005), as

$$L_{\mathrm{CO}}\ [\mathrm{K\ kms^{-1}\ pc^2}] = 23.5\Omega[\mathrm{arcsec}^2](d[\mathrm{Mpc}])^2 I_{\mathrm{CO}}[\mathrm{Kkms^{-1}}] \tag{3.6}$$

or alternatively, in units of $L_\odot$:

$$L_{\mathrm{CO}}\ [L_\odot] = 1.04 \times 10^{-3} S_{\mathrm{CO}}[\mathrm{Jy}]\Delta \mathrm{V}[\mathrm{kms^{-1}}]\nu[\mathrm{GHz}](d[\mathrm{Mpc}])^2 \tag{3.7}$$

where I_{CO} = 593.4 K km/s, T_{B} = 34.5 K, $S_{\mathrm{CO}} = 1.2 \times 10^4$ Jy (using the Rayleigh-Jeans law to convert the brightness temperature to flux density) and ΔV = 17.2 km/s is the average line width. These numbers correspond to a spectrum smoothed to a FWHM = $1'$ beam, which covers the high-excitation region around the center. Using these numbers, $L_{\mathrm{CO(3-2)}} = 6.5 \times 10^3$ K kms^{-1} pc^2 = 9.65 $L_\odot$ for the highly excited central square arcminute region. The fraction of the flux of the CO 3-2 transition to the total CO line flux can be estimated using Radex, adopting an H_2 volume density of 10^6 cm^{-3} and a CO column density of 10^{19} cm^{-2}. The CO column density estimate is based on the C^{17}O 3−2 transition (at ∼337 GHz) and a ratio of ^{16}O/^{17}O∼1800 (Wilson & Rood 1994). For T_{kin} = 100 K, the 3−2 transition is expected to be 9%, and for T_{kin} = 300 K, 5 % of the total CO line flux. Using our Radex estimates of the total CO line flux:

$$\begin{aligned} L_{\mathrm{CO}} &= 7.2 \times 10^4 - 1.3 \times 10^5\ \mathrm{K\ kms^{-1}\ pc^2} \\ &= 107.2 - 192.9\ L_\odot \\ &= 4.1 \times 10^{35} - 7.4 \times 10^{35}\ \mathrm{erg\ s^{-1}}, \end{aligned}$$

gives a lower limit on the cooling, with an accuracy of ∼20%, mainly as a contribution from the typical calibration error in deriving the CO 3−2 line intensity.

Based on Neufeld et al. (2005), for kinetic temperatures >100 K and H_2 volume densities ∼10^6 cm^{-3}, the total cooling is up to an order of magnitude above the CO cooling, ∼10^3 $L_\odot$.

Our estimates of the heating rate indicate that the two most important mechanisms to consider for W49A, are mechanical heating by the winds of O-type stars and UV-irradiation. These two mechanisms give a heating rate equivalent with 1000 $L_\odot$, depending on the heating efficiency. This is of a same order of magnitude as the expected total cooling, assuming that the total cooling rate is a factor of 10 higher than the CO cooling rate. This result supports that the effect of embedded O-type stars in the form of stellar winds and UV-irradiation can explain the high-excitation region around the center of W49A.

3.4.3 Comparison to other warm and dense regions

Galactic Center In our Galaxy, a similar level of excitation to what we found toward W49A was reported for clouds near the center. Hüttemeister et al.

(1993) measured kinetic temperatures in 36 clouds near the Galactic center and based on NH_3 transitions, they have found a temperature component of $\sim$200 K, together with a cold gas and dust component. This sample, however, include no embedded stars, which could explain the highly excited gas component, and therefore, cannot be used as an analogue for W49A. De Vicente et al. (1997) have detected hot molecular gas toward the Sagittarius B2 molecular cloud. The highest temperatures measured toward Sagittarius B2 are in the range between 200−400 K, with typical densities of $10^6 - 10^7$ cm^{-3}, similar to what we find for the center of W49A. However, these conditions correspond to hot cores with sizes in the range of 0.5−0.7 pc, much smaller than the region with similar physical properties in W49A. De Vicente et al. (1997) have also found a more extended component of warm (100−120 K) gas as a ring surrounding Sgr B2M and Sgr B2N with a radius of 2 pc and a thickness of 1.4 pc, with a density of about 2×10^5 cm^{-3}. Ferrière et al. (2007) study physical conditions in the innermost 3 kpc of the Galaxy, and find a high-temperature gas component ($T \sim 150$ K), however, it corresponds to a low-density environment ($n_{\mathrm{H}_2} \sim 10^{2.5}$ cm^{-3}), unlike what we find for W49A. On Galactic scales, W49A shows a uniquely extended region of high ($T \gtrsim 100$ K) temperature which appears to be tracing the feedback from the young and forming stars in the region on their surrounding gas.

Starbursts and active galaxies In even nearby galaxies sensitivity and angular resolution mean that the physical conditions of the molecular gas can only be estimated on $\sim$100 pc scales with uncertain filling factors. Nevertheless there are regions where temperatures similar to those in W49A are measured. In particular, extended warm molecular gas (>100 K) has been detected in a number of starburst- and Seyfert galaxies (e.g. Rigopoulou et al. (2002)). Mühle et al. (2007) have detected a warm, $T_{\mathrm{kin}} \sim 200$ K gas component with moderate density ($n(\mathrm{H}_2) = 7 \times 10^3$ cm^{-3}) in the starburst galaxy M82, using p-H_2CO line ratios, probing scales of $\sim$320 pc. Ott et al. (2005) derived kinetic temperatures of 140 K and 200 K toward two positions of the starburst galaxy NGC 253, using NH_3(3,3) ATCA data on a scale of 65 pc. Mauersberger et al. (2003) have detected a warm (100−140 K) gas component toward the center of three nearby starburst galaxies (NGC 253, IC 342 and Maffei 2) for regions of 300−660 pc, based on NH_3 (1,1)-(6,6) transitions. An even warmer component (T>400 K) was detected toward IC 342. Papadopoulos et al. (2011), based on a sample of 70 (Ultra-)Luminous Infrared Galaxies, most of them dominated by a warm ($T_{\mathrm{kin}} > 100$ K) and dense ($n > 10^4$ cm^{-3}) gas phase with masses of $\sim 10^9\ M_\odot$, come to the conclusion that the main heating mechanism is rather cosmic-rays and highly supersonic turbulence than far-UV radiation or shocks related to star-formation. This might be one of the key differences between the extended, but compared to scales of entire galaxies, still local phenomenon seen for W49A, and starburst galaxies. However, in the context of the Milky

Way, W49A is a close analogue in terms of physical parameters to regions in starburst- and active galaxies.

Another key comparison with warm ($\gtrsim$100 K) and dense ($\gtrsim 10^5$ cm^{-3}) regions, such as starburst galaxies, is the initial mass function (IMF). Klessen et al. (2007) have found, based on hydrodynamical numerical calculations, that for regions of warm ($\sim$100 K) and dense ($\gtrsim 10^5$ cm^{-3}) gas, the slope of the IMF is in the range of -1.0 and -1.3, with a turn-over mass of 7 $M_{\odot}$. Homeier & Alves (2005) derived an IMF in W49A with a slope of -1.70 ± 0.30 and -1.6 ± 0.3 down to masses of $\sim$10 $M_{\odot}$. This result may be consistent with the calculations of Klessen et al. (2007), and if so, supports that W49A is a Galactic template for starburst galaxies. However, incompleteness at low luminosities and masses might explain the observed cut-off at masses of $\sim$10 $M_{\odot}$.

Pressure as a diagnostic of starburst environments Environments with increased star-formation activity, such as starburst galaxies, massive star-forming regions and clouds near the Galactic center can be characterized with their pressures, $P/k \sim nT$. Typical pressures that can be expected in the Galaxy and in the midplane of ordinary spirals are in the order of 10^4 K cm^{-3} (Papadopoulos et al. 2011). Table 3.4 shows the measured values of n, T and P/k for W49A, Sgr B2 and starburst galaxies. P/k values show more than an order of magnitude variation. Based on our derived densities and temperatures, the gas pressure in W49A is up to 5.4×10^8 K cm^{-3}, similar to those measured toward SgrB2 and Arp 220. Other galactic nuclei appear to have lower pressures, which seems to be mainly the effect of a lower gas density. Beam dilution seems not to play a major role for the density estimates, given the high densities measured toward Arp 220 as well as the sensitivity, which makes measurements in external galaxies biased toward the warm and dense gas. However, the estimated densities significantly depend on the tracer used, as was shown by Greve et al. (2009), who find a 10$-$100 factor difference between densities estimated from HCN compared to densities estimated from HCO$^+$. Therefore, the uncertainty in P/k is about an order of magnitude.
Pressures measured toward W49A and Sgr B2 are not entirely unique in our Galaxy. Dense gas has been detected toward a number of massive star forming regions, such as reported by Plume et al. (1997), Wu et al. (2010) and McCauley et al. (2011). However, the temperatures of those regions are only comparable to what we measure toward W49A 'locally', on sub-parsec scales, corresponding to hot cores, such as toward Orion KL (Mangum & Wootten 1993). Considering the spatial extent, pressures measured toward W49A provide a Galactic analogue of starburst galaxies.

Table 3.4 — Comparison of physical parameters in W49A to Galactic center clouds and starburst galaxies

Source	**n** (cm^{-3})	**T** (K)	**P/k** ($K\ cm^{-3}$)
W49A center	1.8×10^6	300	5.4×10^8
W49A N clump	5.6×10^5	98	5.5×10^7
W49A E tail	1.2×10^6	68	8.2×10^7
W49A SW clump	1.3×10^5	85	1.1×10^7
Sgr B2[a]	2×10^5	100–120	$2\times10^7 - 2.4\times10^7$
Henize 2-10[b]	$\gtrsim1\times10^4$	50–100	$5\times10^5 - 10^6$
M82[c]	$10^{4.2} - 10^{4.4}$	130–160	$10^{6.4} - 10^{6.6}$
Arp 220[d]	$(0.3–1)\times10^6$	45–120	$1.4\times10^7 - 1.2\times10^8$
Antennae[e]	10^5	90	9×10^6

---

[a] De Vicente et al. (1997) based on CH_3CN J = 5–4, 8–7, 12–11 lines.

[b] Bayet et al. (2004), based on ^{12}CO(J = 3–2, 4–3, 6–5, 7–6) and ^{13}CO(J = 3–2)

[c] Median values based on three different positions (Naylor et al. 2010b). Obtained from multiple species radiative transfer modeling of the lines of CS, HCO^+, HCN, HNC, and $C^{34}S$.

[d] Greve et al. (2009), based on HCN and CS lines.

[e] Zhu et al. (2003), based on CO and ^{13}CO 2–1 and 3–2 lines.

3.5 Summary and conclusions

We have analyzed the physical conditions towards the central 2 × 2 arcminutes region of W49A using JCMT maps with 15″ resolution. We have reported a detection of warm (>100 K) and dense ($>10^5\ cm^{-3}$) gas toward the center, extending up to a few parsecs.

- We have characterized the excitation toward four main regions of W49A (center, Northern clump, South-West clump and Eastern tail) based on rotational diagrams of SO_2, CH_3OH and H_2CO, taking account the optical depth and beam dilution. High excitation and column densities, as well as significant beam dilution is seen towards the center, likely to trace embedded hot cores. The off-center positions show excitation temperatures corresponding to about half of those derived for the center, and no significant beam dilution.
- Based on H_2CO line ratios, we estimate kinetic temperatures of the main regions of W49A. Toward the center, we derive a kinetic temperature of 250–300 K, 60–100 K toward the Northern clump, 80–150 K toward the South-west clump and 70–130 K toward the Eastern tail. Our estimates show an approximately $1' \times 1'$ (∼3.3 × 3.3 pc) region with extended warm

(>100 K) gas towards the center of W49A. Based on HCN 3−2 / HCN 4−3 line ratios, the high-temperature central $1' \times 1'$ region has H_2 volume densities of $>10^5$ cm^{-3}. The high excitation of W49A is comparable to clouds near the center of our Galaxy and to starburst galaxies with estimates on scales of ∼100 pc.

- The most important heating mechanisms for W49A are mechanical heating due to stellar winds of embedded, O-type stars and UV irradiation. X-ray irradiation and gas-grain collisional heating are less probable than other two mechanisms, while the effect of cosmic-rays remains an open question. However, the two main mechanisms corresponding to embedded young stellar populations provide a heating so that no other mechanism is needed to contribute significantly in the heating of W49A. Based on earlier studies of starburst galaxies and their proposed heating mechanisms, W49A is a Galactic starburst analogue, in terms of excitation and physical conditions, but not in terms of the heating mechanism which yields the high excitation. In starburst- and active galaxies additional heating mechanisms compared to those expected in W49A have been proposed to explain the excitation (such as cosmic rays or supersonic turbulence).

  Our future work includes an analysis of the chemical inventory as well as kinematics of selected species, based on the entire SLS survey including data from the main survey (330−360 GHz, Plume et al. 2007) and will be presented in Nagy et al. (in prep, Chapter 2).

Acknowledgements We thank the referees John Bally and Adam Ginsburg for the careful reading of the manuscript and for the constructive suggestions. We also thank the editor Malcolm Walmsley for additional helpful comments. The authors thank Alexandre Faure for discussion on H_2CO collision rates, Kuo-Song Wang for advice about population diagrams and Paul Goldsmith for discussion about the cooling rates and volume filling factors. Z. N. acknowledges Stefanie Mühle and Chris dePree for their useful comments.

3.6 Appendix - Radex line ratio plots

In sections 3.3.3 and 3.3.4 we compare the observed line ratios to line ratios calculated using the non-LTE code Radex (Van der Tak et al. 2007). Figure 3.8 shows the the o−H_2CO $5_{15} - 4_{14}$ and $5_{33} - 4_{32}$ line intensity ratios for H_2 volume densities between 10^3 cm^{-3} and 10^6 cm^{-3} and temperatures between 20 K and 300 K. Figure 3.8 shows the HCN 3−2 and 4−3 line intensity ratios for H_2 column densities between 10^3 cm^{-3} and 10^8 cm^{-3} and temperatures between 20 K and 300 K. Both of these calculations use a molecular column density of 10^{14} cm^{-2} and a background temperature of 2.73 K. We assume a line width of

FWHM = 12 km s^{-1}for H_2CO , and a line width of 18 km s^{-1}for HCN for the central 40″ × 40″, in consistence with the observed line widths.

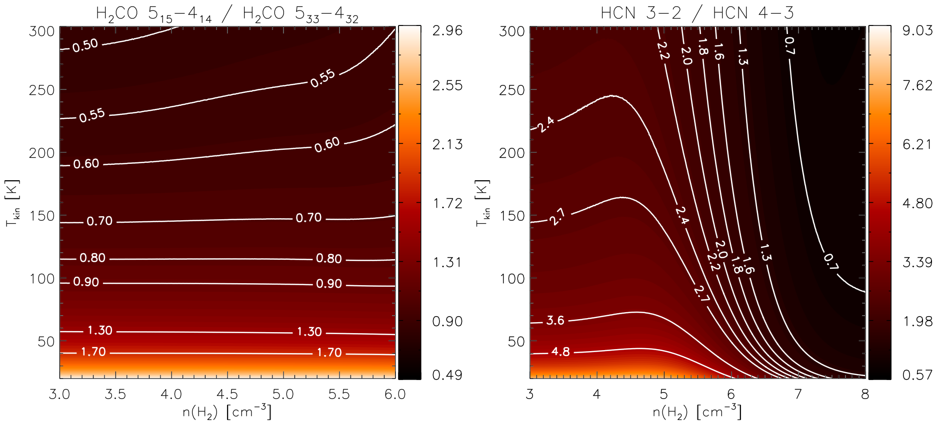

Figure 3.8 — *Left*: Line ratios of o−H_2CO $5_{15} - 4_{14}$ and $5_{33} - 4_{32}$ as a function of kinetic temperature and H_2 density for FWHM=12 km s^{-1}. The intensity scale is logarithmic. *Right*: Line ratios of HCN 3−2 and 4−3 as a function of kinetic temperature and H_2 density for FWHM=18 km s^{-1}.

4

The chemistry of ions in the Orion Bar I. - CH^+, SH^+ and CF^+ - The effect of high electron density and vibrationally excited H_2 in a warm PDR surface

Z. Nagy, F.F.S. Van der Tak, V. Ossenkopf, M. Gerin, F. Le Petit, J. Le Bourlot, J. H. Black, J. R. Goicoechea, C. Joblin, M. Röllig & E. A. Bergin [1]

---

[1] Published as: Z. Nagy, F.F.S. Van der Tak, V. Ossenkopf, M. Gerin, F. Le Petit, J. Le Bourlot, J. H. Black, J. R. Goicoechea, C. Joblin, M. Röllig & E. A. Bergin – *"The chemistry of ions in the Orion Bar I. - CH^+, SH^+ and CF^+ - The effect of high electron density and vibrationally excited H_2 in a warm PDR surface"* 2013, Astronomy & Astrophysics 550, 96

Abstract

The abundances of interstellar CH$^+$ and SH$^+$ are not well understood as their most likely formation channels are highly endothermic. Several mechanisms have been proposed to overcome the high activation barriers, including shocks, turbulence, and H$_2$ vibrational excitation.

Using data from the Herschel Space Observatory, we studied the formation of ions, in particular CH$^+$ and SH$^+$ in a typical high UV-illumination warm and dense photon-dominated region (PDR), the Orion Bar.

The HIFI instrument on board Herschel provides velocity-resolved line profiles of CH$^+$ 1-0 and 2-1 and three hyperfine transitions of SH$^+$ 1_2-0_1. The PACS instrument provides information on the excitation and spatial distribution of CH$^+$ by extending the observed CH$^+$ transitions up to $J = 6-5$. We compared the observed line intensities to the predictions of radiative transfer and PDR codes.

All CH$^+$, SH$^+$, and CF$^+$ lines analyzed in this paper are seen in emission. The widths of the CH$^+$ 2-1 and 1-0 transitions are of $\sim$5 km s^{-1}, significantly broader than the typical width of dense gas tracers in the Orion Bar ($\sim$2-3 km s^{-1}) and are comparable to the width of species that trace the interclump medium such as C$^+$ and HF. The detected SH$^+$ transitions are narrower than the CH$^+$ and have line widths of $\sim$3 km s^{-1}, indicating that SH$^+$ emission mainly originates in denser condensations. Non-LTE radiative transfer models show that electron collisions affect the excitation of CH$^+$ and SH$^+$ and that reactive collisions need to be taken into account to calculate the excitation of CH$^+$. Comparison to PDR models shows that CH$^+$ and SH$^+$ are tracers of the warm surface region (A_V <1.5) of the PDR with temperatures between 500 and 1000 K. We have also detected the 5-4 transition of CF$^+$ with a width of $\sim$1.9 km s^{-1}, consistent with the width of dense gas tracers. The intensity of the CF$^+$ 5-4 transition is consistent with previous observations of its lower$-J$ transitions toward the Orion Bar.

An analytic approximation and a numerical comparison to PDR models indicate that the internal vibrational energy of H$_2$ can explain the formation of CH$^+$ for typical physical conditions in the Orion Bar near the ionization front. The formation of SH$^+$ is also likely to be explained by H$_2$ vibrational excitation. The abundance ratios of CH$^+$ and SH$^+$ trace the destruction paths of these ions, and indirectly, the ratios of H, H$_2$, and electron abundances as a function of depth into the cloud.

4.1 Introduction

The methylidyne cation CH^+ was one of the first molecules to be detected in the interstellar medium (Douglas & Herzberg 1941). Early studies of CH^+ found its abundance to be consistently larger than the predictions of steady-state chemical models in quiescent molecular clouds (e.g. Van Dishoeck & Black 1986). One of the possible formation routes is the endothermic reaction $C^+ + H_2 +$ 0.41 eV $\rightarrow CH^+ + H$. To reproduce the observed CH^+ abundances, several mechanisms have been proposed to overcome the high activation barrier of the formation reaction. For low-density diffuse interstellar clouds, C-shocks (Pineau des Forêts et al. 1986) and turbulent dissipation (Godard et al. 2009) have been proposed and confirmed by Falgarone et al. (2010a,b) and Godard et al. (2012). Alternatively, in denser regions with strong far-ultraviolet (FUV) radiation fields, the internal energy available in the vibrationally excited H_2 molecules has been proposed to help overcome the large activation barrier (Sternberg & Dalgarno 1995, Agúndez et al. 2010).

Sulfanylium (SH^+) has a similar chemistry to CH^+, having a formation route via S^+ and H_2; however, this reaction is twice as endothermic as the CH^+ formation reaction. After non-detections of SH^+ in the UV domain in the spectra of nearby stars (Millar & Hobbs 1988, Magnani & Salzer 1989, 1991), the 526 GHz $N_J = 1_2 - 0_1$ transition of SH^+ has been detected in emission using Herschel toward the high-mass protostar W3 IRS 5 (Benz et al. 2010). The 526 GHz transition has also been detected in absorption in the diffuse interstellar medium towards various distant star-forming regions (Godard et al. 2012). The 683 GHz transition of SH^+ has been detected in absorption towards Sgr B2(M) from the ground with the Carbon Heterodyne Array of the MPIfR (CHAMP+) receiver of the Atacama Pathfinder EXperiment 12 m telescope (APEX) (Menten et al. 2011).

In this paper, we study the formation and excitation of CH^+ and SH^+ in a prototypical photon-dominated region (PDR), the Orion Bar. The Orion Bar is located at a distance of 414 pc (Menten et al. 2007). Its stratified structure has been the subject of many previous studies (such as Van der Wiel et al. 2009 and references therein). The mean density of the Orion Bar is about $\gtrsim 10^5$ $\mathrm{cm^{-3}}$, the mean molecular gas temperature 85 K (Hogerheijde et al. 1995), and the impinging radiation field is $(1-4) \times 10^4$ in Draine units (Draine field: $\chi = 2.7 \times 10^{-3}$erg $\mathrm{s^{-1}}$ $\mathrm{cm^{-2}}$ for the energy range $6 < h\nu < 13.6$ eV; Draine 1978). Most of the low-J molecular line emission originates in an interclump medium with a density between a few 10^4 and 2×10^5 $\mathrm{cm^{-3}}$ (Simon et al. 1997). High-density tracers such as HCN and $H^{13}CN$ originate in dense clumps, as confirmed by interferometric observations (Young Owl et al. 2000). The density of the clumps is in the range between 1.5×10^6 and 6×10^6 $\mathrm{cm^{-3}}$ (Lis & Schilke 2003). Apart from the large clumps detected in $H^{13}CN$ deep inside the Bar, small, warm ($T_{\mathrm{kin}} \sim 160-220$ K), and dense ($n_{\mathrm{H}} \sim 10^{6-7}$ $\mathrm{cm^{-3}}$) condensations have been suggested to explain the excited OH emission at the PDR surface (Goicoechea et al. 2011).

This paper aims to characterize the medium where ions such as CH^+ and SH^+ form and to distinguish between the mechanisms that can overcome the high activation barriers of the formation reaction in a warm and dense PDR. We also report the detection of the CF^+ 5-4 transition. We will address another ion, OH^+ in a separate paper (Van der Tak & Nagy et al., in preparation).

4.2 Observations and Data reduction

The CO^+ peak ($\alpha_{\rm J2000} = 05^{\rm h}35^{\rm m}20.6^{\rm s}$, $\delta_{\rm J2000} = -05°25'14''$) in the Orion Bar (Störzer et al. 1995) has been observed as part of the Herschel observations of EXtra-Ordinary Sources (HEXOS) guaranteed-time key program (Bergin et al. 2010) for the Heterodyne Instrument for the Far-Infrared (HIFI, De Graauw et al. 2010) of the Herschel Space Observatory (Pilbratt et al. 2010) in every HIFI band as a spectral scan. The data were reduced using the *Herschel* Interactive Processing Environment (HIPE, Ott 2010) pipeline version 6.0. The velocity calibration of HIFI data is accurate to $\sim$0.5 kms^{-1} or better. The sideband deconvolution was done using the *doDeconvolution* task in HIPE. In this paper we use the HIFI bands 1a, 1b, 2a and 3a from the HEXOS spectral line survey. These observations were carried out in March and April 2011 in load chop mode with a redundancy of 4 and had total integration times of 2.4 h, 2.2 h, 3.1 h, and 1.3 h, respectively. The Wide-Band Spectrometer (WBS) backend was used which covers 4 GHz bandwidth in four 1140 MHz subbands at 1.1 MHz resolution.

In addition to HIFI spectral scans observed as a part of the HEXOS key program, the CH^+ 2-1 transition was observed as a deep integration in a spectral scan in band 6b, with a total integration time of 11.7 h and a redundancy 4 in dual-beam-switch (DBS) mode. Both WBS and the High Resolution Spectrometer (HRS) backends were used. It was reduced using HIPE pipeline version 8.0.

Besides the HIFI data, we used observations of the CH^+ 3-2, 4-3, 5-4, and 6-5 transitions from the Photodetector Array Camera and Spectrometer (PACS, Poglitsch et al. 2010) onboard Herschel. The PACS observations were carried out in September 2010 and consist of two spectral scans in Range Spectroscopy mode with 5 range repetitions each (Joblin et al. 2012, in preparation). The PACS spectrometer provides 25 spectra over a $47'' \times 47''$ field-of-view resolved in 5×5 spatial pixels ("spaxels"), each with a size of $\sim$9.4″ in the sky. The measured width of the spectrometer point spread function (PSF) is relatively constant at $\lambda \lesssim 100\,\mu$m, but it significantly increases above the spaxel size for longer wavelengths. The resolving power varies between $\lambda/\Delta\lambda \sim$1000 (R1 grating order) and $\sim$5000 (B3A grating order). The central spaxel was centered at the same HIFI survey position. Observations were carried out in the "chopnodded" mode with the largest chopper throw of 6 arcmin. The total integration time was 3.2 h for the 1342204117 observation (B2B and R1) and 2.7 h for the 1342204118 observation (B3A). PACS data were processed using HIPE 6.0.3.

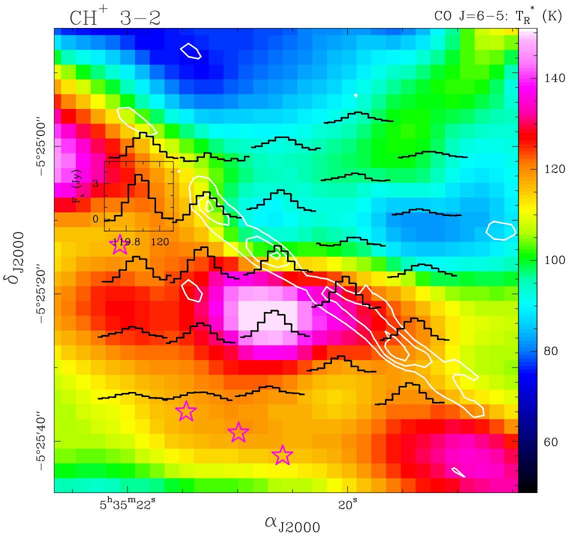

Figure 4.1 — PACS CH$^+$ 3-2 lines (black, centered on the CO$^+$ peak) overlaid on the distribution of the CO $J = 6-5$ peak brightness temperature (color image) observed with the CSO telescope at ∼11″ resolution (Lis et al. 1998). The PACS line intensity distributions are shown in units of Jy/spaxel as a function of wavelength in μm and are not velocity resolved. White contours show the brightest regions of H_2^* $v = 1-0$ S (1) emission (Walmsley et al. 2000). Lower-intensity H_2^* extended emission is present in the entire field (Van der Werf et al. 1996). Violet stars show the position of the $H^{13}CN$ $J = 1-0$ clumps deeper inside the Bar (Lis & Schilke 2003).

Table 4.1 shows the spectroscopic and observational parameters of the transitions used in this paper. The rest frequencies are based on the Cologne Database for Molecular Spectroscopy (CDMS database, Müller et al. 2005). In particular, the frequencies of the CH$^+$ 1-0 and 2-1 and ^{13}CH$^+$ 1-0 transitions are based on Müller (2010).

Table 4.2 includes the observed line parameters for our line sample observed with HIFI, which have been corrected for main beam efficiencies based on Roelfsema et al. (2012). In the case of the detected HIFI transitions we use the average of H- and V-polarizations. The detected lines show similar line profiles in both polarizations. The intensity difference between the polarizations is 12% for CH$^+$ $J = 1-0$, 8% for CH$^+$ $J = 2-1$, ∼20% for SH$^+$ $N_J = 1_2 - 0_1$, and

~30% for CF$^+$ 5-4. To compare the line intensities of the transitions detected with HIFI with different beam sizes, we convert all the observed line intensities to a common ~47″ resolution. We derive conversion factors between the original beam sizes and ~47″ based on the integrated intensity map of the HCN 4−3 transition from the James Clerk Maxwell Telescope (JCMT) Spectral Legacy Survey (Van der Wiel et al. 2009). For this, we assume the intensity distribution of the HCN 4−3 transition to trace the spatial structure of the Orion Bar. For the PACS data (Table 4.2), because of uncertainties in the PSF-correction, we use the mean value of the intensity measured at the central spaxel ($I_{\rm central}$) and that corresponding to the value integrated over 3×3 spaxels around the center ($I_{3\times3}$). The corresponding error bars are the difference between $I_{\rm central}$ and $I_{3\times3}$. This method provides the correct agreement between Spectral and Photometric Imaging Receiver (SPIRE, Griffin et al. 2010) and HIFI data for CO lines (Joblin et al. 2012, in preparation). The large (40%) error bar corresponding to the intensity of the 5-4 transition is caused by the presence of oscillations (fringes) in this range. Owing to a lower band intensity and a significant noise level, only $I_{3\times3}$ was measured for the intensity of the 6-5 transition; $I_{\rm central}$ was then estimated using a standard error value.

4.3 Results

4.3.1 The detected CH$^+$, SH$^+$, and CF$^+$ transitions

Figure 4.2 shows the velocity-resolved CH$^+$ transitions that were detected with significantly broad lines (~5 km s^{-1}) compared to the line width of dense gas tracers in the Orion Bar (~2-3 km s^{-1}, Hogerheijde et al. 1995 and an example of the CO 16-15 transition in Fig. 4.2). The line width of the CH$^+$ 2-1 and 1-0 transitions is not only significantly larger than the width of dense gas tracers, but also of species that trace a similar region to CH$^+$, such as CO$^+$ (Störzer et al. 1995, Fuente et al. 2003). The 5 km s^{-1} is comparable to the width of tracers of the interclump medium, such as C$^+$ ($\Delta v \sim 3.8$ km s^{-1}, also shown in Fig. 4.2) and HF ($\Delta v \sim 4.9$ km s^{-1}, Van der Tak et al. 2012).

Other non velocity-resolved transitions from PACS, such as the J=3-2 transition (Fig. 4.1), show extended emission detected over all PACS spaxels, decreasing with distance from the ionization front. The maximum CH$^+$ 3-2 emission is seen farther into the nearly edge-on PDR compared to the peak H$_2$ v=1-0 emission (Figure 4.1). As CH$^+$ forms via a reaction between C$^+$ and H$_2^*$, we compare the CH$^+$ 3-2 intensity distribution to C$^+$ emission from Figure 4 in Ossenkopf et al. (2013). The C$^+$ peak matches the CH$^+$ peak within the HIFI beam. This indicates that CH$^+$ formation is limited by the C$^+$ abundance rather than by the H$_2$ excitation that is traced by the H$_2$ $v = 1-0$ S(1) emission observed by Walmsley et al. (2000).

Figure 4.3 shows a tentative detection of the ^{13}CH$^+$ $J = 1-0$ in V-polarization. If it were a real detection, the observed ^{12}CH$^+$/^{13}CH$^+$ line ratio of ∼40 would indicate an optical depth of the ^{12}CH$^+$ line of ∼unity, assuming that the ^{13}CH$^+$ emission is optically thin. However, this seems unlikely since a ^{12}CH$^+$ optical depth of ∼1 at a temperature >100 K (see Sect. 6.3.2) is inconsistent with the observed ^{12}CH$^+$ line intensity. Deeper observations are needed to confirm the detection of ^{13}CH$^+$.

Figure 4.4 shows three hyperfine components of the $N_J = 1_2 - 0_1$ transition of SH$^+$ ($F = 3/2-1/2$, $F = 5/2-3/2$, and $F = 3/2-3/2$). The SH$^+$ F=3/2-3/2 transition is only detected in V-polarization. The line width of the detected SH$^+$ transitions (3.0 km s^{-1}) is narrower than those of CH$^+$ and are consistent with the width of dense gas tracers in the Orion Bar, suggesting that it does not originate in the same gas component as CH$^+$.

We have also detected the CF$^+$ 5-4 transition for the first time, with a line width of ∼2 km s^{-1}(Fig. 4.5). The 3-2, 2-1, and 1-0 transitions of CF$^+$ were previously detected toward the Orion Bar from the ground by Neufeld et al. (2006) with beam sizes of HPBW=24″, 12″, and 21″, respectively. The velocity and the width of the $5-4$ transition is consistent with the parameters reported for the other detected transitions by Neufeld et al. (2006). One of the positions covered by Neufeld et al. (2006), $05^{\rm h}35^{\rm m}22.8^{\rm s}$, $-5°25'01''$, is close (ΔRA ∼ 30″, ΔDec∼ 13″) to our observed position which is within the beam of HIFI at the frequency of the 5-4 transition (∼44.2″). Assuming uniform beam-filling, a single excitation temperature of all four levels and optically thin lines, the measured line intensity is consistent with those detected by Neufeld et al. (2006) (Fig. 4.6) and implies a column density of ∼2.1×10^{12} cm^{-2} and a rotation temperature of ∼32 K.

We derived upper limits for other non-detected CF$^+$ and SH$^+$ transitions. We estimated rms noise levels in the averaged spectrum of H- and V-polarizations; 3σ upper limits on the integrated line intensities are estimated using (e.g. Coutens et al. 2012)

$$I(3\sigma)\ [\mathrm{K\ km\ s^{-1}}] = 3\ \mathrm{rms}\sqrt{2\ \mathrm{d}v\ FWHM},$$

where dv is the channel width in km s^{-1}and the rms noise level is derived in a velocity range of ±5 km s^{-1}around the expected velocity. We use a full width at half maximum (FWHM) of 1.9 km s^{-1}for the ^{13}CF$^+$ 5-4 (488664.3 MHz) and the CF$^+$ 6-5 (615365.6 MHz) upper limits, and FWHM=3 km s^{-1}for SH$^+$ $N_J = 1_1 - 0_1$ (∼683 GHz). The derived 3σ upper limits are listed in Table 4.2.

4.3.2 Physical conditions traced by CH$^+$ and SH$^+$

To estimate molecular column densities, we use the non-LTE radiative transfer code RADEX (Van der Tak et al. 2007). We use H$_2$ as a collision partner for the excitation of CH$^+$, as we expect a significant fraction of hydrogen to

Table 4.1 — Spectroscopic and observational parameters of the transitions used in this paper.

Transition	Frequency (MHz)	E_{up} (K)	A (s^{-1})	instrument /band	beam -size (″)	η_{mb}
CH^+ 1–0	835137.5	40.1	6.36×10^{-3}	HIFI, band 3a	26.5	0.75
CH^+ 2–1	1669281.3	120.2	6.10×10^{-2}	HIFI, band 6b	15.0	0.72
CH^+ 3–2	2501440.5	240.2	2.20×10^{-1}	PACS	9.4[1]	
CH^+ 4–3	3330629.7	400.1	5.38×10^{-1}	PACS	9.4[1]	
CH^+ 5–4	4155872.0	599.5	1.07	PACS	9.4[1]	
CH^+ 6–5	4976201.4	838.3	1.86	PACS	9.4[1]	
$^{13}CH^+$ 1–0	830216.1	39.9	5.83×10^{-3}	HIFI, band 3a	26.5	0.75
SH^+ $N_J = 1_2 - 0_1$, $F = 3/2 - 1/2$	526038.7	25.3	7.99×10^{-4}	HIFI, band 1a	44.2	0.76
SH^+ $N_J = 1_2 - 0_1$, $F = 5/2 - 3/2$	526047.9	25.3	9.59×10^{-4}	HIFI, band 1a	44.2	0.76
SH^+ $N_J = 1_2 - 0_1$, $F = 3/2 - 3/2$	526124.9	25.3	1.60×10^{-4}	HIFI, band 1a	44.2	0.76
SH^+ $N_J = 1_1 - 0_1$, $F = 3/2 - 1/2$	683336.1	32.8	2.90×10^{-4}	HIFI, band 2a	33.2	0.75
SH^+ $N_J = 1_1 - 0_1$, $F = 1/2 - 1/2$	683362.0	32.8	1.16×10^{-3}	HIFI, band 2a	33.2	0.75
SH^+ $N_J = 1_1 - 0_1$, $F = 3/2 - 3/2$	683422.3	32.8	1.45×10^{-3}	HIFI, band 2a	33.2	0.75
SH^+ $N_J = 1_1 - 0_1$, $F = 1/2 - 3/2$	683448.2	32.8	5.79×10^{-4}	HIFI, band 2a	33.2	0.75
CF^+ 5-4	512846.5	73.8	8.21×10^{-4}	HIFI, band 1a	44.2	0.76
CF^+ 6-5	615365.6	103.4	1.44×10^{-3}	HIFI, band 1b	44.2	0.76
$^{13}CF^+$ 5-4	488664.3	70.0	7.10×10^{-4}	HIFI, band 1a	44.2	0.76

[1] The size of one PACS spaxel.

be in a molecular form at the observed position. Rates for inelastic collisions between CH^+ and H are not available, but are expected to be of the same order of magnitude as the rates for inelastic collisions between CH^+ and H_2. If most H is in an atomic state, the density used as an input parameter is then the sum of $n(\mathrm{H})$ and $n(\mathrm{H_2})$. We also include excitation via inelastic collisions between CH^+ and electrons, as the importance of excitation by electrons for HF has been recently demonstrated by Van der Tak et al. (2012). We apply an electron density of $\sim$10 $\mathrm{cm^{-3}}$. This is justified, if we assume that the electron abundance is determined by the abundance of C^+. The column density of C^+ is approximately 10^{18} $\mathrm{cm^{-2}}$ (Ossenkopf et al. 2013) and the H_2 column density is approximately 10^{22} $\mathrm{cm^{-2}}$ (e.g. Habart et al. 2010, Van der Wiel et al. 2009). This implies an electron abundance of 10^{-4} and using $n(\mathrm{H_2}) = 10^5$ $\mathrm{cm^{-3}}$, an electron density of 10 $\mathrm{cm^{-3}}$. In the following we consider both H_2 and electron collisions to probe the excitation of CH^+ and SH^+.

For CH^+ our calculations are based on collision rates from Turpin et al. (2010), for temperatures in the range between 10 K and 200 K, covering transitions up to the 5-4 transition ($E_{\mathrm{up}} = 599.5$ K). These rates have been scaled from CH^+ $-$He to $CH^+$$-$$H_2$ based on Schöier et al. (2005). For electron collisions, we use collision rates from Lim et al. (1999) that are available for temperatures between 100 and 15000 K.

Collisions of H_2 and electrons are not always inelastic, but may lead to a chemical reaction. In the case of CH^+ this is important since the collision rates with H_2 and electrons are comparable to the chemical reaction rates for CH^+

Table 4.2 — The detected CH$^+$, SH$^+$, and CF$^+$ transitions; the Gaussian fit parameters for the velocity-resolved transitions observed with HIFI and PACS; and upper limits for non-detections of other CF$^+$ and SH$^+$ transitions. The CH$^+$ $J = 3-2, 4-3, 5-4$, and $6-5$ transitions are spectrally unresolved from PACS. The parameters from HIFI are based on the average spectrum of H- and V-polarizations, unless otherwise specified.

Line	$\int T_{\rm MB}{\rm d}V$ (K km s^{-1})	$V_{\rm LSR}$ (km s^{-1})	ΔV (km s^{-1})	$T_{\rm peak}$ (K)	rms($T_{\rm MB}$) (K)
CH$^+$ 1–0	24.9±0.20	10.5±0.02	5.46±0.04	4.28±0.15	0.12
CH$^+$ 2–1	10.6±0.20	10.4±0.05	4.57±0.11	2.18±0.22	0.23
CH$^+$ 3–2	2.19±0.31				
CH$^+$ 4–3	1.01±0.19				
CH$^+$ 5–4	0.42±0.15				
CH$^+$ 6–5	0.17±0.06				
^{13}CH$^+$ 1–0[1]	0.46±0.11	11.39±0.15	1.30±0.34	0.34±0.10	0.15
SH$^+$ $N_J = 1_2 - 0_1$ $F = 3/2 - 1/2$	0.34±0.02	10.92±0.09	3.00[2]	0.11±0.02	0.02
SH$^+$ $N_J = 1_2 - 0_1$ $F = 5/2 - 3/2$	0.57±0.02	10.84±0.06	3.00[2]	0.18±0.02	0.02
SH$^+$ $N_J = 1_2 - 0_1$ $F = 3/2 - 3/2$	0.14±0.02	10.34±0.24	3.00[2]	0.04±0.01	0.02
SH$^+$ $N_J = 1_1 - 0_1$ $F = 3/2 - 1/2$	≤0.18			≤0.15[3]	
SH$^+$ $N_J = 1_1 - 0_1$ $F = 1/2 - 1/2$	≤0.11			≤0.09[3]	
SH$^+$ $N_J = 1_1 - 0_1$ $F = 3/2 - 3/2$	≤0.13			≤0.12[3]	
SH$^+$ $N_J = 1_1 - 0_1$ $F = 1/2 - 3/2$	≤0.11			≤0.09[3]	
CF$^+$ 5-4	0.20±0.02	11.13±0.11	1.96±0.21	0.10±0.01	0.02
CF$^+$ 6-5	≤0.08			≤0.08[3]	
^{13}CF$^+$ 5-4	≤0.05			≤0.05[3]	

[1] Based on V-polarization data only.
[2] Fixed parameter in the fit.
[3] 3×rms noise level.

with H$_2$ and electrons. For example, for CH$^+$-e$^-$ the chemical reaction rate is 9×10^{-8} cm^3 s^{-1} for the destruction (Woodall et al. 2007) and is 6.4×10^{-7} cm^3 s^{-1} for the excitation of the $J = 1 - 0$ transition at 1000 K. For CH$^+$-H$_2$ the destruction rate is 1.2×10^{-9} cm^3 s^{-1} (Woodall et al. 2007) and an excitation rate is 1.1×10^{-10} cm^3 s^{-1} for the $J = 1 - 0$ transition at 100 K. Therefore, we consider the chemical formation and destruction rates in the statistical equilibrium calculation (e.g. Van der Tak et al. 2007). The statistical equilibrium for states $i = 1$ - N of energy E_i that is solved using the RADEX code is given by the time-independent rate equations

$$\frac{dn_i}{dt} = \sum_{j\neq i}^{N} n_j P_{ji} - n_i \sum_{j\neq i}^{N} P_{ij} + \mathcal{F}_i - n_i \mathcal{D}_i \quad {\rm cm}^{-3}\ {\rm s}^{-1},$$

where

$$\begin{aligned} P_{ij} &= A_{ij} + B_{ij}\bar{J} + C_{ij} \quad (E_i > E_j) \\ &= B_{ij}\bar{J} + C_{ij} \quad (E_i < E_j) \end{aligned}$$

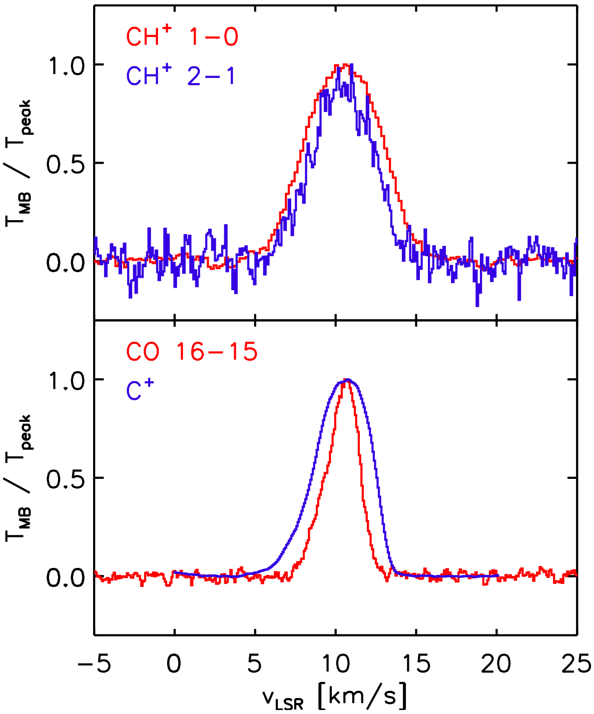

Figure 4.2 — *Top panel:* Line profiles of CH$^+$ 2–1 and 1–0 transitions corresponding to the average of H- and V-polarizations observed with Herschel/HIFI toward the CO$^+$ peak in the Orion Bar. *Bottom panel:* Line profiles of C$^+$ and CO 16-15, for comparison, observed with Herschel/HIFI toward the CO$^+$ peak in the Orion Bar.

and A_{ij} and B_{ij} are the Einstein coefficients, $\bar{J}$ is the mean intensity at the frequency of transition $i \to j$, C_{ij} is the sum over all collision partners of the rates of inelastic, collision-induced transitions $i \to j$, n_i is the number density (cm^{-3}) of molecules in level i, and $\mathcal{D}_i$ is the rate of destruction of the molecule in level i. When detailed knowledge of the state-specific formation process is lacking, the formation rate into level i is expressed as a Boltzmann distribution over all states at an effective formation temperature T_f

$$\mathcal{F}_i \propto g_i \exp(-E_i/kT_f),$$

where g_i is the statistical weight of level i. When the destruction rate can be estimated, as for CH$^+$ here, then the total formation rate is normalized so that the total number density of molecules is consistent with its column density and the density of hydrogen in steady state.

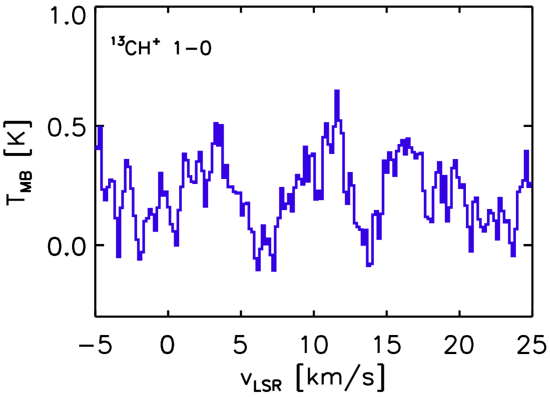

Figure 4.3 — Line profile of $^{13}CH^+$ 1−0 transition observed with Herschel/HIFI in V-polarization toward the CO^+ peak in the Orion Bar.

We assume that there is a balance between the formation and destruction of CH^+. To simulate the chemical pumping effect described above, i.e. the effect of destruction and subsequent formation of CH^+ in excited levels, we add an artificial level to the CH^+ level system, representing the dissociated state, that is populated with a rate equivalent to the reaction rate of CH^+-H_2 and CH^+-e^- (Woodall et al. 2007). On the formation of CH^+ through the reaction of C^+ with vibrationally excited H_2, the re-population from the dissociated level follows a Boltzmann distribution with a formation temperature of $T_f = 9920\,\mathrm{K} - 4560\,\mathrm{K} = 5360\,\mathrm{K}$, where 4560 K is the required energy input for the endothermic CH^+ production and 9920 K is the average energy of the vibrationally excited H_2 levels following the 2-level approximation introduced by Röllig et al. (2006) where the full 15-level system was replaced by the energetically equivalent 2-level system that provides the same total vibrational heating.

Figure 4.7 shows the intensity predictions of two RADEX models with parameters in the range that can be expected for the Orion Bar. The error bars correspond to a 10% calibration error and a 10% error from obtaining integrated intensities by Gaussian fitting for the transitions observed with HIFI. The error bars corresponding to the PACS data are dominated by uncertainty in the PSF correction and are estimated as explained in Sect. 4.2. Both electron collisions and H_2 collisions suggest a kinetic temperature well above the average value (85 K) inferred for the interclump medium in the Orion Bar. Taking the formation pumping and collisional excitation described above into account, we find reasonable fits to the observed line-intensity distribution up to the 5-4 transition (the energy range for which the collision rates are available) with $N(CH^+) = 9 \times 10^{14}$ cm^{-2}, $T_{\mathrm{kin}} = 500$ K, and $n(H_2) = 10^5$ cm^{-3}. The intensity

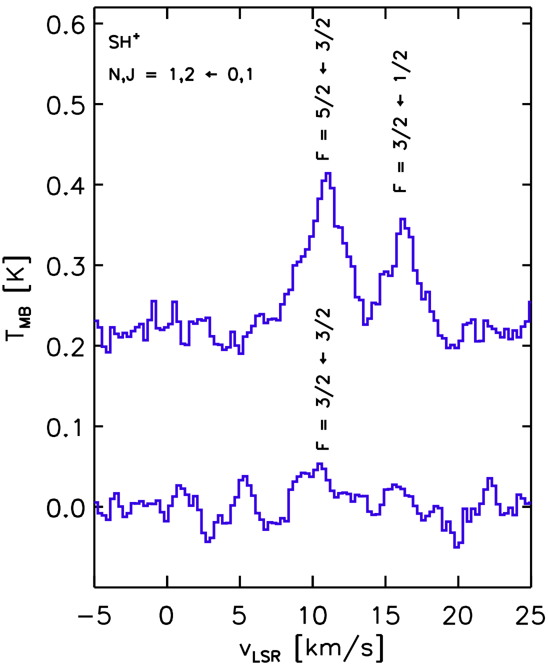

Figure 4.4 — Line profiles of the three hyperfine transitions of SH$^+$ $N_J = 1_2 - 0_1$ observed with Herschel/HIFI corresponding to the average of H and V polarizations toward the CO$^+$ peak in the Orion Bar.

of the 5-4 transition can be better reproduced with a kinetic temperature of $T_{\rm kin} = 1000$ K. Temperatures between 500 K and 1000 K are expected near the edge of the cloud where the observations used in this paper have been taken. Assuming an electron density of $n_{\rm e} = 10$ cm^{-3}, electron collisions mostly affect the two lowest$-J$ transitions for $T_{\rm kin} = 500$ K with an 10-13% increase in the intensities.

In the case of SH$^+$, calculations for collisions with H$_2$ do not exist, so we use scaled radiative rates (J. Black, private communication) for a temperature range of 10-5000 K. We also use collision rates for electron-impact collisions calculated in the Coulomb-Born approximation (J. Black, private communication), for a temperature range of 10-1000 K. Figure 4.8 shows the best fit models overplotted on the observed line intensities. The error bars correspond to 20% of the observed line intensities, including calibration error and the error introduced by the estimation of the integrated intensities using a Gaussian fit. We consider lower kinetic temperatures and higher volume densities than in the case of

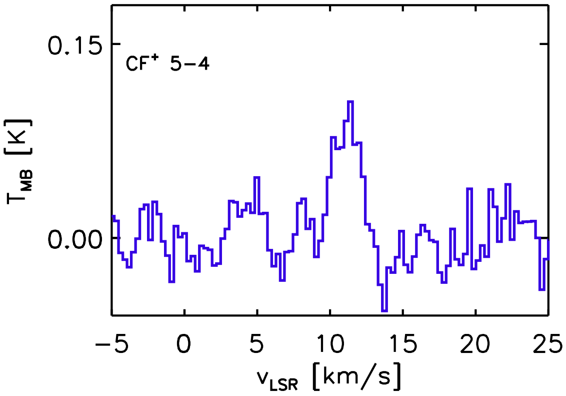

Figure 4.5 — Line profile of CF$^+$ 5-4 transition corresponding to the average of H and V polarizations observed with Herschel/HIFI toward the CO$^+$ peak in the Orion Bar.

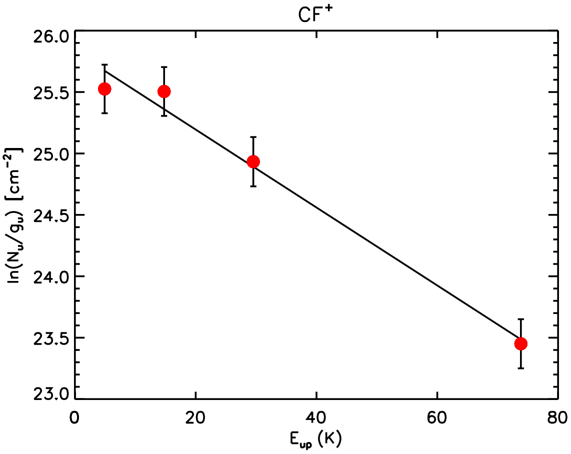

Figure 4.6 — Rotation diagram of CF$^+$ including the transitions detected by Neufeld et al. (2006).

CH$^+$, given that the line width suggests an origin from denser material. At the position of the CO$^+$ peak, warm ($T_{\rm kin} \sim 160-220$ K) and dense (10^{6-7} cm^{-3}) condensations have been suggested to explain the OH emission. Using SH$^+$-H$_2$ collisions, a model with 10^6 cm^{-3}, $T_{\rm kin} = 200$ K, and N(SH$^+$)=10^{13} cm^{-2} gives a reasonable fit to the observed line intensities (Fig. 4.8). On Fig. 4.8

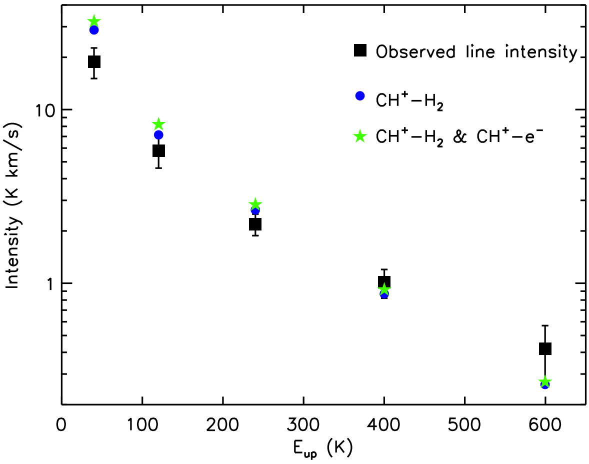

Figure 4.7 — Output of the RADEX models corresponding to a model with $N(CH^+)= 9 \times 10^{14}$ cm^{-2}, $n(H_2)= 10^5$ cm^{-3}, $n(e^-)= 10$ cm^{-3}, $T_{kin} = 500$ K. The blue symbols correspond to a model with excitation via collisions with H_2, the green symbols to a model with excitation via H_2 and electron collisions.

we show a model with the same parameters, which includes electron collisions, assuming an electron density of $n_e = 10$ cm^{-3}. In both of these models the excitation temperatures are low (8.3-10.4 K) and the lines are optically thin ($\tau \sim 0.02 - 0.2$).

4.4 The formation of CH^+ and SH^+ via H_2 vibrational excitation

In this section we investigate the role of H_2 vibrational excitation for the formation of CH^+ and SH^+. We discuss alternative explanations in Sect. 6.4.

4.4.1 Estimate based on an analytic approximation

Testing if H_2 vibrational excitation can drive CH^+ and SH^+ formation in an environment with a given radiation field and physical parameters requires a detailed modeling with a PDR code, with information on the chemical network and physical processes that affect the level populations of vibrationally excited H_2. A first indication can also be given using a simple analytic method to describe H_2 vibrational heating with a two level approximation (Röllig et al. 2006). The H_2 vibrational heating rate can be computed among all 15

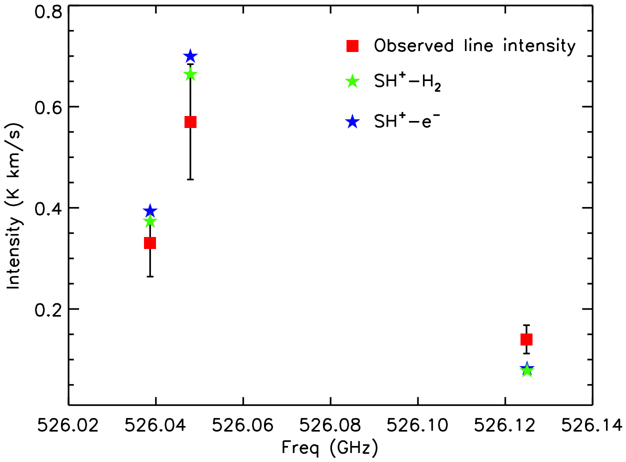

Figure 4.8 — Output of the RADEX models for H$_2$ and electron collisions compared to the observed line intensities of SH$^+$ for a model with $N(\mathrm{SH}^+) = 10^{13}$ cm^{-2}, $n(\mathrm{H}_2) = 10^6$ cm^{-3}, $n(\mathrm{e}^-) = 10$ cm^{-3}, and $T_{\mathrm{kin}} = 200$ K.

vibrational levels in the ground electronic state, but neglecting the rotational structure, based on Equation C.2 in Röllig et al. (2006). A two-level system can be defined that results in the same vibrational heating rate as the full, 15-level system (Equation C.3, Röllig et al. 2006). The vibrationally excited 'virtual' level has an upper level energy of ΔE_{eff}=9920 K. The total rate for populating this vibrationally excited level is $k_{0,1} = P_1 \ \chi$, where χ is the radiation field in Draine units (Draine 1978) and $P_1 = 6.9 \times 10^{-10}$ s^{-1} is the formation rate of vibrationally excited H$_2$ for the defined level of a radiation field of $\chi = 1$. The de-excitation of this vibrationally excited level is via spontaneous emission, dissociation by the UV radiation field and by collisional de-excitation. The coefficient for spontaneous decay is $A_{\mathrm{eff}} = 1.9 \times 10^{-6}$ s^{-1}. The collisional de-excitation scales as $n_{\mathrm{gas}}\gamma_{\mathrm{eff}}$ with a rate coefficient of $\gamma_{\mathrm{eff}} = 5.4 \times 10^{-13}\sqrt{T}$ s^{-1} cm^{-3}. The dissociation rate is $\chi \times D_{\mathrm{eff}}$, where $D_{\mathrm{eff}} = 4.7\,10^{-10}$s^{-1}. These effective coefficients A_{eff}, γ_{eff}, and D_{eff} for the defined 2-level system as well as the energy of the defined vibrationally excited level ΔE_{eff} are obtained by considering different asymptotic values of the density n and the radiation field χ. By neglecting dissociation, the population of the vibrationally excited level is dependent on the formation rate of vibrationally excited H$_2$ as well as on the spontaneous decay and collisional de-excitation rates. Calculating with $n_{\mathrm{gas}} = 10^5$ cm^{-3} and $T = 500$ K for the collisional de-excitation rate, there is a balance between these processes for a radiation field of $\chi \sim 5 \times 10^3$, which gives an expected lower limit on the radiation field, above which H_2 vibrational excitation is expected to be efficient enough to drive the formation of CH^+ and SH^+. Even though neglecting dissociation introduces an additional ∼10% error, this calculation shows that for the radiation field in the Orion Bar ($1-4\times10^4$ in Draine units), there is a large percentage of vibrationally excited H_2 to react with C^+ and form CH^+. This has been observed by Van der Werf et al. (1996) and Walmsley et al. (2000) and has already been noted for the formation of OH through the $O + H_2 \rightarrow OH + H$ reaction by Goicoechea et al. (2011). In the following section we test this idea with a more accurate approach, using PDR models.

4.4.2 CH^+ formation

We use the 1.4.4 version of the Meudon PDR code (Le Petit et al. 2006, Goicoechea & Le Bourlot 2007, Le Bourlot et al. 2012) to model the observed CH^+ line intensities. This version includes the Langmuir Hinshelwood and Eley-Rideal mechanisms to describe the formation of H_2 on grain surfaces. The chemical pumping effect of destruction and formation on CH^+ level populations is taken into account in addition to collisional excitation and de-excitation in the Meudon code (e.g. Gonzalez Garcia et al. 2008). The Meudon code treats CH^+ formation as described in Agúndez et al. (2010)

$$\mathrm{H_2(j = 0 - 7) + C^+ \xrightarrow{k_1} CH^+ + H} \tag{4.1}$$

$$\mathrm{H_2(v = 1) + C^+ \xrightarrow{k_2} CH^+ + H} \tag{4.2}$$

In reaction 4.1, H_2 rotational levels up to J=7 are used, which has an energy, E_7=4586.4 K which is close to the activation barrier of the $H_2 + C^+ \rightarrow CH^+ + H$ reaction. We take into account the $v = 1$ vibrational level only because its energy (∼5987 K) is enough to overcome the activation barrier of the CH^+ formation reaction. The formation rates are $k_1 = 1.58 \times 10^{-10} \exp(-[4827 - E_j/k]/T)$ based on Gerlich et al. (1987) and $k_2 = 1.6 \times 10^{-9}$ (Hierl et al. 1997).

We use isobaric models for typical conditions for the Orion Bar with pressures in the range between 5×10^7 cm^{-3} K and 2×10^8 cm^{-3} K, corresponding to $T_{\rm kin} \sim 500$ K (RADEX models) and n∼10^5 cm^{-3}; and $T_{\rm kin} \sim 1000$ K (RADEX models) and n∼2×10^5 cm^{-3} (typical interclump medium density, e.g. Simon et al. 1997); respectively. We apply a radiation field on the side where the cloud is illuminated from in the range between $\chi_{\rm front}=10^4$ and 3×10^4 in Draine units (Draine 1978). We run the models up to a depth equivalent to a visual extinction of $A_{\rm V} \sim 10$ mag. At the back side of the cloud (at $A_{\rm V} \sim 10$ mag), we use a radiation field 1000 times below that on the front $\chi_{\rm back} = \chi_{\rm front}/1000$. We adopt a cosmic-ray primary ionization rate of $\zeta = 2 \times 10^{-16}$ s^{-1} per H_2 molecule suitable for the dense ISM (Hollenbach et al. 2012).

Figure 4.9 shows the results of a model for a pressure of 10^8 cm^{-3} K and a radiation field of $\chi_{\rm front}=1\times10^4$, consistent with the radiation field near the ionization front of the Orion Bar. An inclination of 60° was used to extract the line intensities, because of uncertainties in the computation of the line intensities in a 1D model above this value (Gonzalez Garcia et al. 2008). This is reasonably close to the model with 75° inclination suggested to explain the geometry of the Bar (e.g. Melnick et al. 2012). The model with an inclination of 60° reproduces the observed CH$^+$ line intensities within a factor of 2 for the J=1-0 transition, and with an accuracy of 20% for the other transitions. Our RADEX calculations show the possible importance of electron collisions in the excitation of CH$^+$. Therefore, to probe the effect of electron collisions on the excitation of CH$^+$, we implemented CH$^+$-e$^-$ collisions in the Meudon code. The models for P=10^8 cm^{-3} K and $\chi = 10^4$ are shown in Fig. 4.9. Including electrons in the excitation of CH$^+$, the model reproduces the observed line intensities with an accuracy of $\sim 30\%$. Including electron collisions affects mostly the two lowest$-J$ transitions. The predicted intensity of the $J = 1 - 0$ transition increases by $\sim$22%, and the intensity of the $J = 2 - 1$ transition increases by $\sim$18% after including electron collisions.

The CH$^+$ abundance profile corresponding to this model is shown in Fig. 4.10 together with the gas temperature in the region where CH$^+$ abundances peak. The model predicts that CH$^+$ forms near the surface of the PDR ($A_{\rm V} < 1$) at high temperatures ($T \sim 500 - 1000$ K), consistent with the predictions by Agúndez et al. (2010) and with our RADEX calculations. Though the best fitting models predict abundances to peak near the surface of the cloud at low $A_{\rm V}$, the PACS observations of excited CH$^+$ used in this paper show a spatial extension along the area covered by PACS ($47'' \times 47''$), as shown in Fig. 4.1. SPIRE observations of the $J = 1 - 0$ transition (Naylor et al. 2010a, Habart et al. 2010) show extended CH$^+$ emission over a $\sim 200'' \times 200''$ region centered on the $\alpha_{\rm J2000} = 05^{\rm h}35^{\rm m}22.83^{\rm s}$, $\delta_{\rm J2000} = -05°24'57.67''$ position. The CH$^+$ $J = 1 - 0$ emission mapped with HIFI was found to extend over a large region covering the OMC-1 cloud (Goicoechea et al., in preparation). One possibility is that the known clumpiness of the Orion Bar extends over a large volume and creates multiple PDR surfaces. Alternative explanation is that the extended CH$^+$ emission seen toward the region is the result of a not completely edge-on PDR that is tilted to the line of sight. Models with lower pressures under-predict the observed line intensities. For example, a model with a pressure of 5×10^7 K cm^{-3} underpredicts the line intensities with a factor of $\sim$4.

4.4.3 SH$^+$ formation

SH$^+$ forms via a similar reaction to CH$^+$, however, with an endothermicity about twice as high, ΔE=9860 K. Since state-to-state formation rates are not available for the $\rm H_2 + S^+ \rightarrow SH^+ + H$ reaction, we use the rates of the $\rm H_2 + C^+ \rightarrow CH^+ + H$ reaction as an approximation, taking into account H$_2$ rotational levels up to $E_{11} = 10261.8$ K and H$_2$ in the v=1 state up to

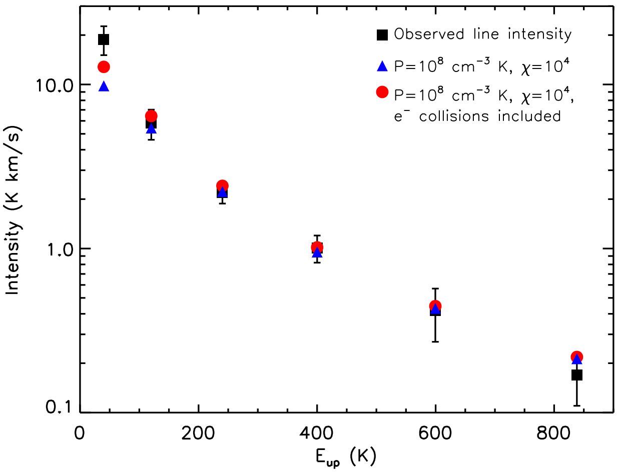

Figure 4.9 — CH^+ line intensities as a function of E_u, comparison between the observed line intensities and the predictions of an isobaric PDR model with a pressure of 10^8 cm^{-3} K for a radiation field of $\chi = 10^4$.

$E = 10341.5$ K. This is a reasonable assumption, since the total rates of the reactions for CH^+ and SH^+ formation via $C^+ + H_2$ and $S^+ + H_2$ are of the same order of magnitude (Woodall et al. 2007). To account for the higher activation barrier, we use $k_{1,\mathrm{mod}} = 1.58 \times 10^{-10} \exp(-[9860 - E_j/k]/T)$. We use the 1.4.4 version of the Meudon code (Le Petit et al. 2006, Goicoechea & Le Bourlot 2007, Le Bourlot et al. 2012), where we introduce the SH^+ formation described above and use scaled radiative rates (J. Black, private communication) and electron-impact collisions calculated in the Coulomb-Born approximation (J. Black, private communication) for the excitation of SH^+.

With these assumptions, our best fit Meudon PDR model for CH^+ ($P = 10^8$ cm^{-3} K, $\chi = 10^4$) underpredicts the absolute intensities of the observed SH^+ transitions by a factor of ~3.5 for the $F = 5/2 \rightarrow 3/2$ and $F = 3/2 \rightarrow 1/2$ transitions, and by a factor of 6.5 for the $F = 3/2 \rightarrow 3/2$ transition. Owing to the uncertainty in the formation rates, this agreement may be reasonable and suggests that like CH^+, SH^+ can also be formed via H_2 vibrational excitation in warm and dense PDRs. It may also suggest that SH^+ originates in a higher-pressure medium compared to CH^+, which would explain the difference in the observed linewidths. The SH^+ abundances corresponding to this model are shown in Fig. 4.10. SH^+ abundances, like CH^+ abundances, peak near the surface of the cloud at $A_V \lesssim 1$ at high temperatures (500-1000 K). The SH^+/CH^+ abundance ratio in this region is between 0.01 and 0.1. This,

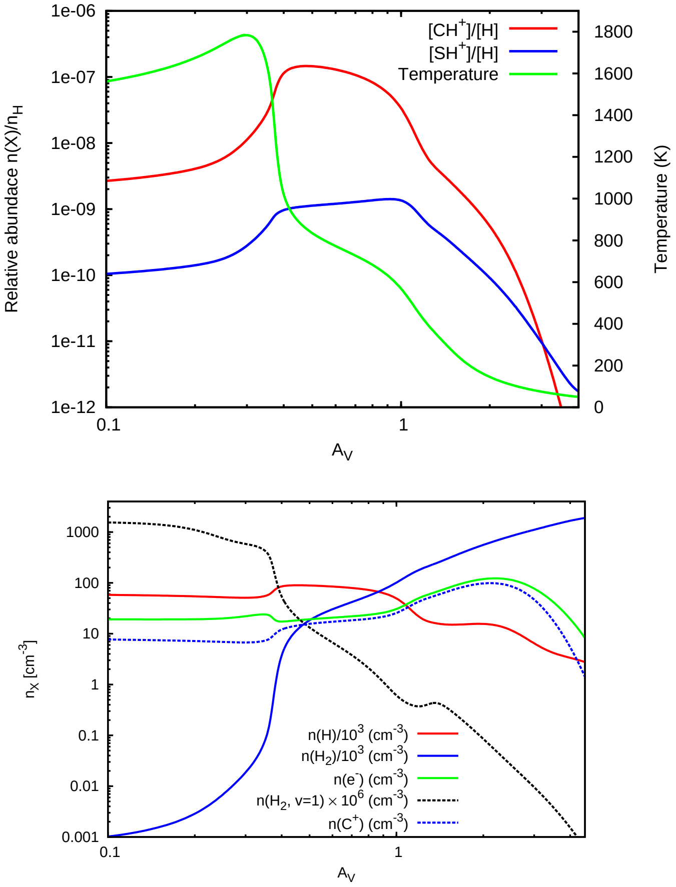

Figure 4.10 — *Top panel*: CH^+ and SH^+ abundances and the gas kinetic temperature as a function of A_V for a pressure of $P = 10^8$ cm^{-3} K and $\chi = 10^4$. *Bottom panel:* H, H_2, H_2 (v=1), e^-, and C^+ densities.

however, is a lower limit on the SH^+/CH^+ abundance ratio, since our model underestimates the SH^+ line intensities.

4.5 The destruction of CH^+ and SH^+

Figure 4.11 shows the abundance ratio of CH^+ to SH^+ predicted by our best-fit model in the region where CH^+ and SH^+ abundances peak. To understand these abundance ratios, it is essential to study the destruction of CH^+ and SH^+. CH^+ destruction can follow four main paths in the probed temperature and density

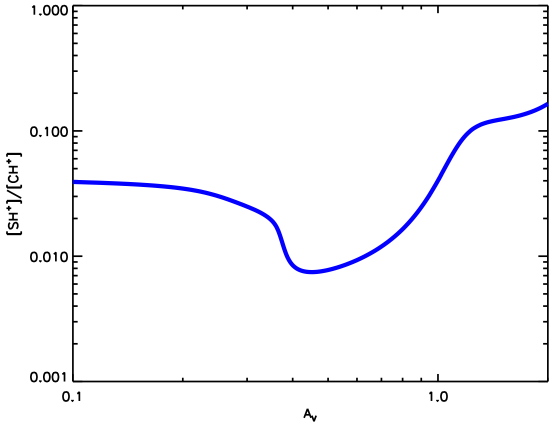

Figure 4.11 — Abundance ratios of CH^+ and SH^+ in our best fit model ($\chi = 10^4$, $P = 10^8$ cm^{-3} K) in the warm surface region ($A_V < 2$) as a function of depth into the cloud.

regime

$$H + CH^+ \xrightarrow{k_{H,CH^+}} H_2 + C^+$$

$$H_2 + CH^+ \xrightarrow{k_{H_2,CH^+}} H + CH_2^+$$

$$e^- + CH^+ \xrightarrow{k_{e^-,CH^+}} H + C$$

$$h\nu + CH^+ \xrightarrow{k_{h\nu,CH^+}} C + H^+$$

Unlike CH^+, SH^+ does not react with H_2 at the given physical conditions, as the reaction rate is orders of magnitude lower than that of reactions with electrons and H. Therefore the most important destruction paths are photodissociation as well as chemical reactions with H and electrons

$$H + SH^+ \xrightarrow{k_{H,SH^+}} H_2 + S^+$$

$$e^- + SH^+ \xrightarrow{k_{e^-,SH^+}} H + S$$

$$h\nu + SH^+ \xrightarrow{k_{h\nu,SH^+}} H + S^+$$

The chemical reaction rates for these reactions are based on Woodall et al. (2007) and are summarized in Table 5.4.

At a depth equivalent to a visual extinction of A_V ~0.5, which is in the region where the CH^+ and SH^+ abundances peak, and at a temperature of ~830 K, most CH^+ (73.2%) is destroyed via collisions with H, while 24.3%

Table 4.3 — Rates corresponding to the main destruction paths of CH^+ and SH^+, based on Woodall et al. (2007).

Reaction	Rate (cm^3 s^{-1})	Temperature regime (K)
k_{H,CH^+}	7.5×10^{-10}	$10 - 41000$
k_{H_2,CH^+}	1.2×10^{-9}	$10 - 41000$
k_{e^-,CH^+}	$1.5 \times 10^{-7} \times (T/300)^{-0.42}$	$10 - 300$
k_{H,SH^+}	1.10×10^{-10}	$10 - 41000$
k_{e^-,SH^+}	$2.0 \times 10^{-7} \times (T/300)^{-0.5}$	$10 - 300$
Reaction	Rate (s^{-1})	Temperature regime (K)
$k_{h\nu,CH^+}$	$2.50 \times 10^{-10} \exp(-2.5A_V)$	$10 - 41000$
$k_{h\nu,SH^+}$	$3.00 \times 10^{-10} \exp(-1.8A_V)$	$10 - 41000$

is destroyed via collisions with H_2 and 2.1% is destroyed via collisions with electrons. Photodissociation is negligible in this regime, since it is responsible for 0.4% of the destructions of CH^+. Deeper in the cloud, at a depth equivalent to $A_V \sim 1$, and at a gas temperature of ~570 K, most CH^+ (74.9%) is destroyed by collisions with H_2, while small percentages of CH^+ are destroyed via collisions with H (22.8%), with electrons (2.2%), and by photodissociation (0.6%).

At a depth of $A_V \sim 0.5$, most SH^+ (~77.2%) is destroyed via reactions with H and a smaller percentage is destroyed via reactions with electrons (~18.2%) and by photodissociation (~4.4%). At a depth corresponding to $A_V \sim 1$, SH^+ is almost equally destroyed by reactions with H (~53.3%) and electrons (~43.7%). A smaller percentage of SH^+ is destroyed via photodissociation (~2.4%).

At $A_V \sim 1$ and deeper, the SH^+ and CH^+ abundance ratio becomes higher than 0.1. Deeper in the cloud than $A_V \sim 1$ CH^+ abundances decrease more rapidly than SH^+ abundances. The $[SH^+]/[CH^+]$ abundance ratio varies in the range between 0.01 (at $A_V \sim 0.2$) and >0.1 (at $A_V \sim 1$) and indicate that the destruction of CH^+ becomes more efficient as a function of the depth into the cloud where H_2 takes over as the most important destruction partner, while with the decrease of atomic hydrogen density SH^+ becomes more abundant because electrons are a less efficient destruction partner. While in diffuse clouds the abundance ratios of $[SH^+]/[CH^+]$ trace the importance of shocks (e.g. Menten et al. 2011) and properties of turbulent dissipation regions (e.g. Godard et al. 2012), in clouds exposed to high UV irradiation these abundances are sensitive to the abundance ratios of H, H_2, and electrons as a function of depth into the cloud, which are determined by the radiation field strength of the irradiation source.

4.6 Discussion

We have analyzed six rotational transitions of CH$^+$ and three transitions of SH$^+$ and reported the first detection of the $J = 5 - 4$ transition of CF$^+$. We have shown that electron collisions affect the excitation of SH$^+$ and CH$^+$, especially the lowest$-J$ transitions. We have also shown the importance of taking reactive collisions into account in the case of CH$^+$ excitation. We have confirmed, both by an analytic approximation and by more detailed PDR modeling, that CH$^+$ formation is driven by H$_2$ vibrational excitation, unlike in the case of diffuse environments with lower UV radiation fields. SH$^+$ is also likely to form via H$_2$ vibrational excitation, although the lack of information on the exact state-to-state formation rates introduces an extra uncertainty in the models.

4.6.1 The formation of CH$^+$ and SH$^+$

Spatially extended vibrationally excited H$_2$ emission was detected in the Orion Bar before the launch of Herschel (Van der Werf et al. (1996), Walmsley et al. (2000)), already indicating an importance in the chemistry of species that react with H$_2$. Using Herschel, CH$^+$ was detected in the Orion Bar by Naylor et al. (2010a) and Habart et al. (2010), based on SPIRE maps of the 1-0 transition. These observations show extended CH$^+$ 1-0 emission in the Orion Bar as well as in the OMC-1 cloud (Naylor et al. 2010a, Morris, P.; priv. comm., Goicoechea, J.; priv. comm.). Naylor et al. (2010a) argue that the large spatial extent of CH$^+$ into regions of low $A_{\rm V}$ suggests the importance of the formation via H$_2$ vibrational excitation. Our observations extend these studies, since the additional observed transitions up to J=6-5 provide additional evidence on the importance of the formation via vibrationally excited H$_2$. An origin of CH$^+$ in the warm surface regions of the PDR is also confirmed by Goicoechea et al. (2011) who found a spatial correlation between excited OH $^2\Pi_{3/2}$ $J = 7/2^- \rightarrow 5/2^+$ ($\sim$84.6 μm, observed with PACS) and CH$^+$ 3-2 emission, and that OH originates in the surface region ($A_{\rm V} < 1$) of a high pressure gas component ($10^8 - 10^9$ K cm^{-3}). The formation and excitation of CH$^+$ in the Orion Bar is similar to that in the envelope of the high-mass protostar AFGL 2591, as its CH$^+$ emission can be explained to originate in the FUV-irradiated outflow-walls (Bruderer et al. 2010). Another region where CH$^+$ formation is driven by the strong FUV radiation field and can be explained by H$_2$ vibrational excitation is the protoplanetary disc HD 100546 (Thi et al. 2011), where CH$^+$ emission mostly originates in the outer disc and the disc surface in warm gas ($T_{\rm gas} > 400$ K).

Other explanations for the formation of CH$^+$ applicable to the diffuse ISM include shocks (e.g. Pineau des Forêts et al. 1986). Tielens et al. (1993) have demonstrated that shocks do not contribute to the chemistry of the Orion Bar; therefore, we consider this scenario unlikely. Another scenario for CH$^+$ formation that has been successful in reproducing CH$^+$ abundances for the diffuse interstellar medium is the dissipation of turbulence (Godard et al. 2009, 2012). Though the CH^+ 1-0 and 2-1 transitions have broader line widths than most dense gas tracers in the Orion Bar, most of the lines detected in the Orion Bar are narrow (2-3 $\mathrm{km\,s^{-1}}$); therefore, we find it unlikely that turbulence plays a role in the chemistry of species detected in the Orion Bar.

Unlike CH^+, SH^+ has not been observed in a large variety of regions since its recent discovery in absorption toward Sagittarius B2 (Menten et al. 2011). A recent study by Godard et al. (2012) probes CH^+ and SH^+ in absorption in the diffuse interstellar medium toward high-mass star-forming regions, suggesting a common origin for the formation and excitation of these ions, based on their observed linewidth-distributions and on comparison with MHD shock models. However, in the diffuse ISM, SH^+ and CH^+ abundances are influenced by the dissipation of turbulence. SH^+ has also been detected in emission in the high-mass star-forming region W3 IRS5 (Benz et al. 2010), which represents a region with physical conditions comparable to the Orion Bar, where the UV-radiation of the embedded protostars drives the chemistry of SH^+.

4.6.2 CH^+ and SH^+ as tracers of the warm PDR surface

Though CH^+ and SH^+ most likely form via the same process and originate in the warm surface region of the PDR, a significant difference between CH^+ and SH^+ emission is suggested by the difference in the observed line widths. While the observed line width of SH^+ ($\Delta v \sim 3$ $\mathrm{km\,s^{-1}}$) is closer to that of dense gas tracers ($\Delta v \sim$ 2-3 $\mathrm{km\,s^{-1}}$), the width of the CH^+ $J = 1-0$ and $2-1$ transitions ($\Delta v \sim 5$ $\mathrm{km\,s^{-1}}$) is similar to that of HF ($\Delta v \sim 4.9$ $\mathrm{km\,s^{-1}}$, Van der Tak et al. 2012) and C^+ ($\Delta v \sim 3.8$ $\mathrm{km\,s^{-1}}$), tracers of the interclump medium. The C91α carbon recombination line was observed with the VLA with a width of 2-2.5 km $\mathrm{s^{-1}}$ (Wyrowski et al. 1997). It was found to match the H_2 [1-0 S(1)] distribution (Van der Werf et al. 1996) and its radial velocity was found to be consistent with that of H_2 pure rotational lines H_2 v=0-0 S(1), S(2), and S(4) (Allers et al. 2005). The $^{13}C^+$ lines have a slightly larger width of 2.5-2.8 km $\mathrm{s^{-1}}$, compared to that of the C91α line. The larger width of the [CII] 158 μm line compared to the $^{13}C^+$ lines can be a result of optical depth broadening of the C^+ line (with an optical depth of 2-3). However, the C^+ line is also broader near the edge of the Bar, where the column density of material is lower, as are the line optical depths. In addition, the recombination line intensity is sensitive to the square of the electron density, while the fine structure line is sensitive to the local density only. Therefore the difference in line profiles of the C91α and [CII] 158 μm lines outside opacity broadening may also be related to gradients in the beam and along the line of sight, with the denser material having a lower velocity dispersion.

This possible difference in the properties of the emitting regions is further indicated by our RADEX models (Sect. 6.3.2). These models reproduce the observed CH^+ line intensities with a temperature of $T = 500 - 1000$ K and a density of $n \sim 10^5$ cm^{-3}, but suggest a higher density component to explain SH^+ emission, $T \sim 200$ K, $n \sim 10^6$ cm^{-3}, which is consistent with the properties of warm and dense condensations suggested to explain the origin of excited OH (Goicoechea et al. 2011) and high-J CO line emission (Joblin et al. 2012, in preparation). In this case, thermal line broadening may contribute to the difference between the widths of the CH^+ and SH^+ lines. The expected contribution of thermal line broadening for CH^+ is $\Delta v = 2\sqrt{2\ln 2}\sqrt{\frac{kT}{m}} = 1.3$ km s^{-1}for $T_{\rm kin}$=500 K, and Δv=1.8 km s^{-1}for $T_{\rm kin}$=1000 K. The contribution of thermal line broadening for SH^+ for $T_{\rm kin}$=200 K is Δv=0.6 km s^{-1}.

As an alternative explanation of the large observed line width of CH^+, formation pumping may play a role in the broadening of CH^+. As explained in Sect. 6.3.2, CH^+ formation results in an excess energy equivalent to 5360 K. This energy may be redistributed and go into kinetic motions. If the 5360 K excess energy goes into excess translational energy of the nascent CH^+, and if this is identified as an ionic kinetic temperature upon formation, then the corresponding FWHM of Doppler motions is 4.4 km s^{-1}.

The difference between the widths of CH^+ and SH^+ may not originate in different excitation conditions, but in the difference in the chemistry of these ions. After its formation, CH^+ rapidly reacts with H and H_2, therefore it is likely that its translational motions never become thermalized. In this case, the large velocity dispersion in CH^+ partially reflects the conditions of its formation. SH^+ on the other hand does not react rapidly with H (and H_2), so that it is destroyed less rapidly by recombination with electrons. Therefore, SH^+ can become thermalized translationally during its chemical lifetime. Therefore, while SH^+ traces the density and the temperature of the emitting region, CH^+ is more sensitive to the details of its formation process.

Another interpretation of the broadening of CH^+ and other molecules could be that they originate in flows created by photoevaporating clumps (e.g. Gorti & Hollenbach 2002, Mackey & Lim 2010). However, our observed data don't completely support this assumption. If the FWHM of ions and other molecules detected at the same position had a contribution by the evaporating flow, we would expect C^+ and CH^+ to have a similar flow velocity, as the momentum transfer from H_2 in the H_2^*+C^+ reaction is small. Based on our HIFI observations of the CO^+ peak, this does not apply, as FWHM(C^+)$\sim$3.8 km s^{-1} and FWHM(CH^+)$\sim$5 km s^{-1}.

The difference in the width of reactive ions tracing the warm surface region of the PDR is a key part of understanding the chemistry of these ions. Future observations of the spatial distribution of SH^+ will help to distinguish between these explanations.

4.6.3 An extension of the ‘CF^+ ladder’ in the Orion Bar

Unlike CH^+ and SH^+, CF^+ does not directly form via collisions with H_2. The reaction between fluorine and H_2 is followed by a reaction between C^+ and HF, where HF is the dominant reservoir of fluorine and was previously been detected in emission in the Orion Bar by Van der Tak et al. (2012)

$$F + H_2 \rightarrow HF + H$$

$$HF + C^+ \rightarrow CF^+ + H.$$

CF^+ is the second most important fluorine reservoir and accounts for ~1% of the gas-phase fluorine abundance. However, CF^+ has so far only been detected in two sources. The 2-1 and 1-0 rotational transitions have been recently detected with a spatially extended emission toward the PDR in the Horsehead nebula (Guzman et al. 2012). The first detection of CF^+ was toward the Orion Bar (Neufeld et al. 2006), showing spatially extended emission in the 1-0, 2-1, and 3-2 rotational transitions. Our observations extend the observed CF^+ transitions toward the Orion Bar up to the 5-4 transition and since the line intensity is consistent with the previously observed transitions, this work gives additional confirmation on the simple CF^+ chemistry tracing the surface layers exposed to UV irradiation.

4.7 Conclusions and outlook

We have analyzed six rotational transitions of CH^+ and three transitions of SH^+ and have reported the first detection of the 5-4 transition of CF^+. Our main conclusions are the following:

- We have detected CH^+ up to the 6-5 transition. The 2-1 and 1-0 transitions are spectrally resolved and show significantly broader lines ($\Delta v \sim 5$ kms^{-1}) than most dense gas tracers in the Orion Bar. SH^+ on the other hand shows significantly narrower lines than CH^+ ($\Delta v \sim 3$ kms^{-1}). Explanations of this difference include their origin in a different density (and temperature) component. Alternatively, because of its reactivity, CH^+ never becomes thermalized therefore, its observed properties trace the formation process rather than the properties of the emitting region, unlike for SH^+. Information on the spatial distribution of SH^+ is needed to resolve this puzzle.

- Inelastic collisions with H_2 and electrons both affect the excitation of CH^+ and SH^+, similar to the case of HF (Van der Tak et al. 2012). Reactive collisions are important in the excitation of CH^+, but have less effect in the case of SH^+.

- Comparing the observed CH$^+$ intensities to predictions of PDR models for typical conditions in the Orion Bar, we confirm that CH$^+$ forms via reactions with vibrationally excited H$_2$, as predicted by Agúndez et al. (2010). Our PDR models also show that CH$^+$ forms in the warm surface region ($T \sim 500 - 1000$ K) of the PDR at high pressures ($\sim 10^8$ cm^{-3} K).
- SH$^+$ is also likely to form via H$_2$ vibrational excitation, assuming that the formation rates are similar to that of CH$^+$. SH$^+$ is also a tracer of the warm surface regions of the PDR.

In the future, higher-resolution follow-up observations of a larger region in the Orion Bar will give more insight into the excitation conditions of SH$^+$. Probing CH$^+$ and SH$^+$ formation in PDRs with a range of parameters, such as different radiation fields would help to deepen our understanding of the chemistry of these ions in regions exposed to UV irradiation.

Acknowledgements We thank the referee for the constructive suggestions that helped to improve the paper. We also thank the editor Malcolm Walmsley for additional comments. We thank Simon Bruderer for useful comments on CH$^+$ and SH$^+$ and Yunhee Choi for the help in the reduction of the HIFI data. J.R.G. is supported by a Ramón y Cajal research contract; he thanks the Spanish MINECO for funding support through grants AYA2009-07304 and CSD2009-00038. Support for this work for E.A.B. was provided by NASA through an award issued by JPL/Caltech. Part of the work was supported by the *Deutsche Forschungsgemeinschaft* through grant SFB 956 C1.
HIFI was designed and built by a consortium of institutes and university departments from across Europe, Canada, and the US under the leadership of SRON Netherlands Institute for Space Research, Groningen, The Netherlands, with major contributions from Germany, France, and the US. Consortium members are Canada: CSA, U.Waterloo; France: IRAP, LAB, LERMA, IRAM; Germany: KOSMA, MPIfR, MPS; Ireland: NUIMaynooth; Italy: ASI, IFSI-INAF, Arcetri-INAF; The Netherlands: SRON, TUD; Poland: CAMK, CBK; Spain: Observatorio Astronomico Nacional (IGN), Centro de Astrobiología (CSIC-INTA); Sweden: Chalmers University of Technology - MC2, RSS & GARD, Onsala Space Observatory, Swedish National Space Board, Stockholm University - Stockholm Observatory; Switzerland: ETH Zürich, FHNW; USA: Caltech, JPL, NHSC. HIPE is a joint development by the Herschel Science Ground Segment Consortium, consisting of ESA, the NASA Herschel Science Center, and the HIFI, PACS, and SPIRE consortia.
PACS was developed by a consortium of institutes led by MPE (Germany) and including UVIE (Austria); KU Leuven, CSL, IMEC (Belgium); CEA, LAM (France); MPIA (Germany); INAFIFSI/OAA/OAP/OAT, LENS, SISSA (Italy); IAC (Spain).

5

Spatially extended OH^+ emission in Orion

F.F.S. van der Tak; Z. Nagy; V. Ossenkopf; Z. Makai; J.H. Black; A. Faure; M. Gerin; & E.A. Bergin [1]

---

[1] Submitted to Astronomy & Astrophysics

Abstract

The reactive H_nO^+ ions (OH^+, H_2O^+ and H_3O^+) are widespread in the interstellar medium and act as precursors to the H_2O molecule. While H_nO^+ absorption is seen on many Galactic lines of sight, active galactic nuclei often show the lines in emission. This paper shows the first example of a Galactic source of H_nO^+ line emission: the Orion Bar, a bright nearby photon-dominated region (PDR). We present line profiles and maps of OH^+ line emission toward the Orion Bar, and upper limits to H_2O^+ and H_3O^+ lines. We analyse these HIFI data with non-LTE radiative transfer and PDR chemical models, using newly calculated inelastic collision data for the e-OH^+ system. Line emission is detected over $\sim 1'$ (0.12 pc), tracing the Bar itself as well as a perpendicular feature identified as the Southern tip of the Orion Ridge, which borders the Orion Nebula on its Western side. The line width of ≈ 4 km s^{-1} suggests an origin of the OH^+ emission close to the PDR surface, at a depth of $A_V \sim 0.3$–0.5 into the cloud. Models with collisional and radiative excitation of OH^+ require unrealistically high column densities to match the observed line strength, indicating that formation and destruction of OH^+ is rapid enough to influence its excitation. Our best-fit OH^+ column density of $\sim 1.5 \times 10^{14}$ cm^{-2} is similar to that in previous absorption line studies, while our limits on the OH^+/H_2O^+ and OH^+/H_3O^+ ratios are somewhat higher than seen before. The column density of OH^+ is consistent with estimates from the Meudon PDR code for parameters applicable to the Orion Bar, given the current uncertainties in the local gas pressure and the spectral shape of the ionizing radiation field. The unusually high OH^+/H_2O^+ and OH^+/H_3O^+ ratios are probably due to the high UV radiation field and electron density in this object. Photodissociation and electron recombination are more effective destroyers of OH^+ than the reaction with H_2, which limits the production of H_2O^+. The appearance of the OH^+ lines in emission is the result of the high electron density in the Orion Bar, since unlike for H_2, inelastic e-OH^+ collisions are faster than reactive ones. In addition, chemical pumping, far-infrared pumping by local dust, and near-UV pumping by Trapezium starlight contribute to the OH^+ excitation. Similar conditions may apply to extragalactic nuclei where H_nO^+ lines are seen in emission.

5.1 Introduction

Although interstellar clouds have ionization fractions of only 10^{-4}–10^{-8}, ionic species are very useful to probe physical conditions in such clouds (Larsson et al. 2012). In diffuse clouds ($A_V < 1$), the main ion source is UV photoionization of carbon, while in dense clouds ($A_V > 1$), cosmic-ray ionization of hydrogen is the dominant ionization mechanism (Bergin & Tafalla 2007). Proton transfer reactions of interstellar H_3^+ with abundant species such as CO and N_2 lead to HCO^+ and N_2H^+, which are widely observed in the interstellar medium. Such stable ionic species are useful as tracers of the interaction of interstellar gas with magnetic fields (Houde et al 2004, Schmid-Burgk et al 2004), whereas ions which react rapidly with H_2 trace other parameters such as the gas density and the ionization rate.

At temperatures $\lesssim 250$ K, the formation of interstellar H_2O in the gas phase proceeds through a series of ion-molecule reactions. After charge transfer of H^+ or H_3^+ to O, repeated reactions of O^+ with H_2 produce OH^+, H_2O^+, and finally H_3O^+, which upon dissociative recombination with a free electron produces H_2O. The OH^+ and H_2O^+ ions are well known from the spectra of comets where they appear as photodissociation products of H_2O (Swings & Page 1950; Herzberg & Lew 1974). In the interstellar medium, H_2O and H_3O^+ have been known for decades (Phillips et al. 1992), but observation of the intermediate products OH^+ and H_2O^+ had to await the launch of ESA's *Herschel* Space Observatory (Pilbratt et al. 2010). Strong absorption in rotational lines of interstellar OH^+ and H_2O^+ is seen with Herschel on many lines of sight in our Galaxy (Gerin et al 2010, Ossenkopf et al 2010) and even some beyond (Weiß et al. 2010). In addition, electronic absorption lines of OH^+ have been reported in sensitive near-UV spectra of several diffuse interstellar clouds (Krełowski et al. 2010).

The Herschel data, as well as the single OH^+ line observed from the ground toward the Galactic Center source SgrB2 (Wyrowski et al. 2010), imply large column densities of OH^+ and H_2O^+. The hydrogen in the absorbing clouds thus cannot be purely in atomic form, because no OH^+ and H_2O^+ would be produced, nor in purely molecular form, because all OH^+ and H_2O^+ would react into H_3O^+ and H_2O. Using models of UV-irradiated interstellar clouds (PDRs), the observed abundances of OH^+ and H_2O^+ can be used to infer the relative fractions of hydrogen in atomic and molecular forms (Neufeld et al. 2010), which itself traces the ionization rates of the clouds (Hollenbach et al. 2012).

While the interpretation of interstellar H_nO^+ absorption is reasonably well understood, lines of OH^+ and H_2O^+ have also been observed in emission from the nuclei of several active galaxies, most famously Mrk 231 (Van der Werf et al. 2010). The large dipole moments and small reduced masses of the H_nO^+ ions imply high line frequencies and large radiative decay rates, so that collisional excitation of their rotational levels requires extremely high densities and line

Table 5.1 — Observed lines.

Molecule	Transition	Frequency GHz	$E_{\rm up}$ K	$A_{\rm ul}$ $\rm s^{-1}$
OH^+	1_0–0_1 F=1/2–3/2	909.159	43.6	0.011
OH^+	1_2–0_1 F=5/2–3/2[a]	971.804	46.7	0.033
OH^+	1_1–0_1 F=3/2–3/2	1033.119	49.6	0.018
p-H_2O^+	1_{10}–1_{01}	607.227	59.2	0.006
o-H_2O^+	1_{11}–0_{00}	1115.186	53.6	0.027
H_3O^+	0_0^-–1_0^+	984.709	54.7	0.023
H_3O^+	1_1^-–1_1^+	1655.831	79.5	0.055

Notes. The strongest hyperfine component is listed, unless otherwise noted.
[a] Blend with the $F = 3/2 - 1/2$ hyperfine component. The frequency and $E_{\rm up}$ are averages, while the $A_{\rm ul}$ is the sum.

emission is not expected to be observable. Understanding this phenomenon benefits from finding a Galactic source of H_nO^+ line emission, which can be studied in more detail than extragalactic nuclei.

This paper presents the first observation of OH^+ line emission toward a source within our Galaxy: the Orion Bar. Due to its brightness and nearly edge-on geometry, this PDR is well-suited to observe physical and chemical changes in the gas as a function of depth into the cloud, as the intensity of UV irradiation by the Trapezium stars decreases (e.g. Van der Wiel et al. 2009). The Orion Bar is also notable as the only known Galactic source of HF line emission (Van der Tak et al. 2012). In this case, the proximity of this region (420 pc: Menten et al 2007, Hirota et al 2007) allows us to resolve the H_nO^+ line emission both spatially and spectrally. We use non-LTE radiative transfer models and PDR thermo-chemical models to interpret our results.

5.2 Observations

The CO^+ peak ($\alpha_{\rm J2000} = 05^{\rm h}35^{\rm m}20.6^{\rm s}$, $\delta_{\rm J2000} = -05°25'14''$) in the Orion Bar (Störzer et al. 1995) has been observed as a spectral scan over the full HIFI range as part of the HEXOS (Herschel observations of EXtra-Ordinary Sources) guaranteed-time key program (Bergin et al. 2010) using the HIFI instrument (De Graauw et al. 2010) of the Herschel Space Observatory (Pilbratt et al. 2010). This paper uses data from HIFI bands 1b (H_2O^+ 1_{10}–1_{01}), 3b (OH^+ 1_0–0_1), 4a (OH^+ 1_2–0_1 and 1_1–0_1) 5a (H_2O^+ 1_{11}–0_{00}), and 6b (H_3O^+ 1_1^-–1_1^+). These observations were carried out in 2011 March and April in load chop mode with a redundancy of 4, except that frequency switching was used in band 5. On-source integration times are ≈50 s for most spectra except OH^+

Table 5.2 — Line parameters measured from the HIFI spectra.

Line	$\int T_A^* \Delta V$ K km s^{-1}	$V_{\rm LSR}$ km s^{-1}	ΔV km s^{-1}	rms mK
OH^+ 1_0–0_1	<0.80	...	...	58
OH^+ 1_2–0_1	2.3(3)	10.9(3)	5.1(6)	133
OH^+ 1_1–0_1	1.2(1)	10.1(3)	4.3(5)	88
H_2O^+ 1_{10}–1_{01}	<0.18	...	...	20
H_2O^+ 1_{11}–0_{00}	<1.90	...	...	112
H_3O^+ 0_0^-–1_0^+	<1.17	...	...	78
H_3O^+ 1_1^-–1_1^+	<2.27	...	...	90

Notes. Numbers in parentheses are error bars in units of the last decimal. Noise levels in the last column are for a channel width of 1 MHz. Upper limits in column 2 are for $\Delta V = 4.3\,{\rm km\,s^{-1}}$.

1_0–0_1 (20 s) and H_2O^+ 1_{11}–0_{00} (190 s). Table 5.1 lists the frequencies of the lines as well as other spectroscopic parameters, which have been taken from the CDMS database (Müller et al. 2001)[2]. The size of the telescope beam for these observations is 19–23″ FWHM, corresponding to 9000 AU or 0.04 pc, except for the H_2O^+ 1_{10}–1_{01} line where it is 35″, and for the H_3O^+ 1_1^-–1_1^+ line where it is 15″. The WBS (Wide-Band Spectrometer) was used as backend, covering 4 GHz bandwidth in four 1140 MHz subbands at 1.1 MHz resolution. The velocity calibration of HIFI data is accurate to ~0.5 kms^{-1} or better. The data were reduced with HIPE (Ott 2010) pipeline version 6.0, using the task *doDeconvolution* for the sideband deconvolution, while further analysis was done in the CLASS package.

In addition to the HIFI spectral scans, a 115″ × 65″ area centered on α = 05:35:20.81, δ = –05:25:17.1 with a position angle of 145° was mapped in the OH^+ $1_2 - 0_1$ transition with HIFI, in On-The-Fly (OTF) mapping mode with position-switch reference, using a total integration time of 20 min. The HIFI map was reduced with HIPE 6.0 and exported to CLASS for further analysis.

5.3 Results

5.3.1 Line profiles

Figure 5.1 presents the line profiles of the OH^+ lines at 971 and 1033 GHz, as observed with HIFI toward the Orion Bar. Although hints of OH^+ and H_2O^+ emission have been seen toward the high-mass protostar W3 IRS5 (Benz et al.

---

[2] `http://www.astro.uni-koeln.de/cdms/`

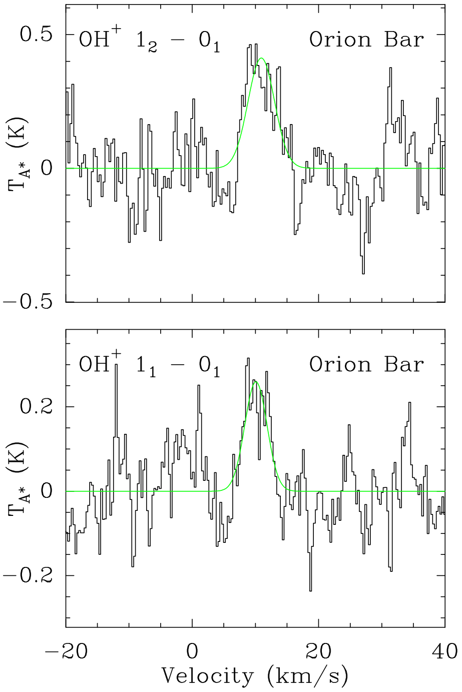

Figure 5.1 — Line profiles of the OH$^+$ 1_2–0_1 (top) and 1_1–0_1 (bottom) transitions, observed with HIFI toward the Orion Bar.

2010), this is the first time that a pure emission profile is seen toward a Galactic source. As the line profiles appear single-peaked at our sensitivity and spectral resolution, we have fitted a Gaussian model to extract the line parameters. Table 5.2 presents the results of these Gaussian fits, and also reports our upper limits to other lines of OH$^+$, H$_2$O$^+$ and H$_3$O$^+$ from our spectral survey of the Orion Bar. We have also searched for the O$^+$ excited fine structure (^{2}D $J = 5/2 \rightarrow 3/2$) line near 593.7 GHz (Blagrave & Martin 2004; Sharpee et al. 2004), leading to an upper limit on T_A^* of 30 mK rms per 0.5 km s^{-1} channel. No continuum emission is detected in the spectra, down to upper limits ranging from $T_{mb}^{SSB} = 0.1$ K at 607 GHz to 0.3 K at 1655 GHz, which is consistent with the SPIRE measurements of Arab et al. (2012).

The difference between the measured central velocities and FWHM widths of the two detected OH$^+$ lines is mostly due to hyperfine blending of the 1_2–0_1 line. We thus adopt the measured parameters of the 1_1–0_1 line as the best estimate of the central velocity and FWHM width of the OH$^+$ emitting gas in the Orion Bar. While the central velocity of this line of 10.1 kms is in good agreement with the value of 10.0±0.2 km s^{-1} from ground-based observations

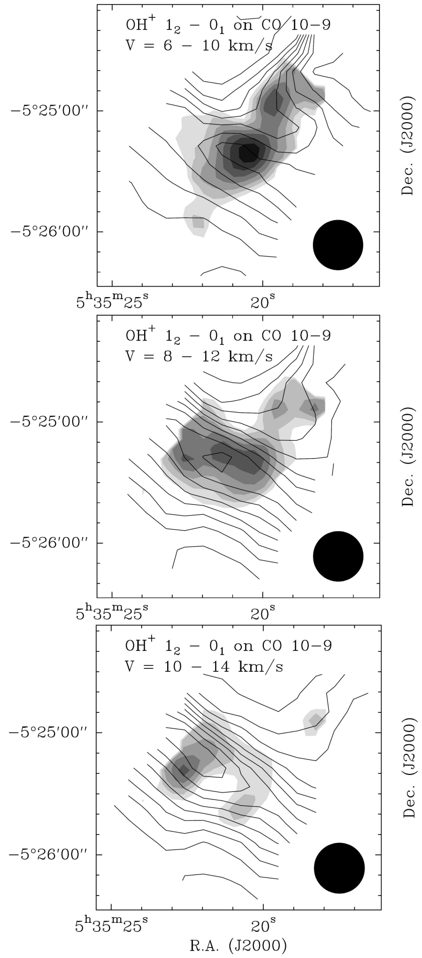

Figure 5.2 — Spatial distribution of the OH$^+$ 1_2–0_1 emission, integrated between $V_{\rm LSR}$ = +6 and +10 km s^{-1} (top), between +8 and +12 km s^{-1} (middle), and between +10 and +14 km s^{-1} (bottom). Greyscale levels start at 0.6 K km s^{-1} and increase by 0.2 K km s^{-1}. Contours of CO 10–9 emission are at 5, 15, ...95% of the peak intensity in the respective velocity channel.

of other molecular species toward this source, its width of 4.3 km s^{-1} is much larger than the value of 1.7±0.3 km s^{-1} measured for the dense gas deep inside ($A_V \gtrsim 1$) the Bar (Hogerheijde et al 1995, Leurini et al 2006). On the other hand, its width is smaller than the value of ≈5 km s^{-1} measured in species such as HF which trace the surface ($A_V \lesssim 0.1$) of the PDR (Van der Tak et al. 2012), and more similar to the width of the [C II] line (Ossenkopf et al. 2013). Based on

Table 5.3 — Optically thin estimates of H_nO^+ column densities, in units of 10^{12} cm^{-2}, as a function of assumed excitation temperature.

T_{ex} (K)	OH^+	H_2O^+	H_3O^+
10	82.1	<2.85	<7.21
20	8.61	<0.21	<0.64
40	4.01	<0.10	<0.27
80	3.90	<0.13	<0.32
160	5.45	<0.25	<0.64

Notes. The limits for H_2O^+ and H_3O^+ are based on the 607 and 985 GHz lines; limits from the other lines are significantly higher.

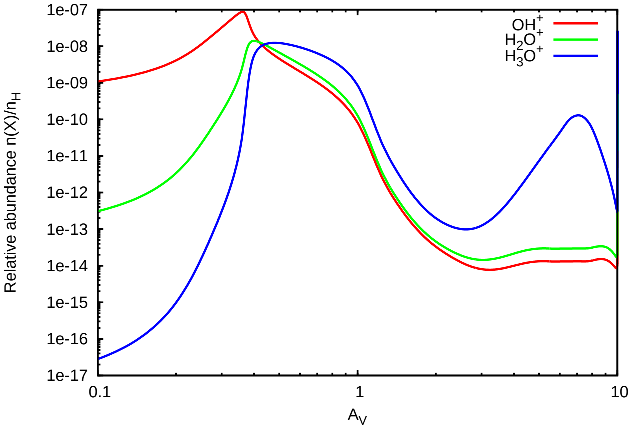

Figure 5.3 — Abundances of OH^+, H_2O^+ and H_3O^+, predicted by the Meudon PDR model as a function of visual extinction for a radiation field of χ=10,000 Draine units and a pressure of P=10^8 K cm^{-3}, as applicable to the Orion Bar.

the line width, the OH^+ emission thus seems to originate from close to the PDR surface ($0.3 < A_V < 0.5$) where CH^+ and SH^+ peak as well in the chemical model of Nagy et al. (2013) (Chapter 4).

5.3.2 Spatial distribution

Figure 5.2 presents our maps of the OH^+ 971 GHz line emission, as observed with HIFI toward the Orion Bar, integrated over three velocity ranges, shown in greyscale. The contours show the CO 10–9 line (ν = 1151.985 GHz; E_{up} = 304 K), also observed within the HEXOS program, integrated over the same velocity ranges. The OH^+ emission around the central velocity (middle panel) is seen to be extended over at least an arc minute (25,000 AU or 0.12 pc) on the sky, and to roughly follow the structure of the Bar seen in CO 10–9 and other molecular tracers (Van der Wiel et al. 2009). The emission from the Bar is concentrated in two clumps: one peaking near the map center at $V_{\rm LSR} \approx 10$ km s^{-1}, and another peaking 20–25$''$ to the East near $V_{\rm LSR} = 12$ km s^{-1}, which is seen most pronounced in the figure's bottom panel.

The map of low-velocity OH^+ in the top panel of Figure 5.2 shows a third clump which lies to the North-West of the Bar, and is connected to it by a bridge of fainter OH^+ emission. This 'perpendicular' emission is also seen in CO 10–9 and other tracers of the Bar surface such as [CII] 158 μm (Ossenkopf et al. 2013), and CH^+ 3–2 (Nagy et al. 2013, Chapter 4). The feature corresponds to the Southern tip of the Orion Ridge facing the Trapezium cluster, which confines the HII region, as visible in large-scale maps of CN line emission (Rodriguez-Franco et al. 1998) and ^{13}CO 3–2 emission (Lis & Schilke 2003; Melnick et al 2012). From multi-line CN observations, Rodríguez-Franco et al. (2001) derive H_2 densities as high as 10^6 cm^{-3} for this ridge, which may be favourable to excite OH^+ line emission. However, this density is probably an overestimate, as collisions of CN with electrons were not taken into account, which are known to be important for CN (Black & van Dishoeck 1991). Furthermore, we note that the OH^+ line is not detected toward the Orion S clump further up the Orion Ridge, possibly because emission and absorption from different layers cancel out each other.

5.3.3 Column densities

The variations in OH^+ emission level by factors of 2–3 across the maps in Figure 5.2 likely correspond to variations in the total column density or the OH^+ abundance with position, although excitation conditions (volume density, kinetic temperature) may also play a role. Since the emission does not appear to be strongly peaked, we focus in the following analysis on the CO^+ peak where we have limits on the other H_nO^+ ions. To estimate the column densities of these ions, we use the line fluxes from Table 5.2 and apply a main beam efficiency of 76% at 607 GHz, 70% at 1655 GHz, and 74% at our other line frequencies (Roelfsema et al. 2012). The column density N depends on the excitation temperature $T_{\rm ex}$ through

$$N_{\rm tot} = \frac{8\pi k\nu^2}{hc^3}\frac{Q(T_{\rm ex})}{g_u A_{\rm ul}} e^{E_u/kT_{\rm ex}} \int T_{\rm mb} dV$$

where ν is the line frequency, Q is the partition function, g_u is the upper state degeneracy, and A_{ul} is the spontaneous decay rate. This equation assumes optically thin emission and negligible background radiation ($T_{\rm bg} << T_{\rm ex}$), but does not assume the Rayleigh-Jeans limit ($h\nu << kT_{\rm ex}$) because our measurements are at high frequency. The optically thin assumption is reasonable given the low expected abundances of the H_nO^+ ions, and neglecting background radiation is justified given the low level of continuum radiation in our observations. Adopting a background brightness temperature of 9 K increases the column density estimates by 5% for $T_{\rm ex}$ = 20 K, and by <1% for higher values of $T_{\rm ex}$.

To evaluate the above expression for the column density, we use the spectroscopic parameters of the lines in Table 5.1. Table 5.3 presents estimates of the column densities of OH^+, H_2O^+ and H_3O^+ for values of $T_{\rm ex}$ between 10 and 160 K, which is the expected range for the Orion Bar. If the excitation of H_nO^+ is close to LTE, $T_{\rm ex}$ would be close to the kinetic temperature of the gas, which ranges from ≈85 K for the dense gas (Hogerheijde et al. 1995) to ≈150 K near the cloud surface (Batrla & Wilson 2003; Goicoechea et al. 2011). If collisional excitation of the lines cannot compete with their radiative decay, $T_{\rm ex}$ will drop below $T_{\rm kin}$, while $T_{\rm ex}$ may exceed $T_{\rm kin}$ if radiative or chemical pumping plays a role. Section 5.5 discusses these processes in more detail. For now, the table shows that the derived column densities of H_nO^+ vary by factors of 2–3 for $T_{\rm ex} \gtrsim 20$ K, but that the estimate increases by an order of magnitude if $T_{\rm ex}$ is as low as 10 K.

The OH^+ column density in Table 5.3 for $T_{\rm ex}$ = 10 K is comparable to the values toward other Galactic sources, while the estimates for $T_{\rm ex} \gtrsim 20$ K are ∼10× lower. Absorption line studies indicate $N(OH^+)$ values between a few 10^{13} and a few 10^{14} cm^{-3}, both for the diffuse foreground clouds toward G10.6, W49N, W51 and OMC-2 (Gerin et al. 2010; Neufeld et al. 2010; Indriolo et al. 2012; López-Sepulcre et al. 2013) and the dense gas around the protostars AFGL 2591, W3 IRS5, and Orion-KL (Bruderer et al. 2010; Benz et al. 2010; Gupta et al. 2010). Our OH^+/H_2O^+ ratio of >40 and OH^+/H_3O^+ ratio of >15 are larger than in previous observations of diffuse clouds, suggesting an origin of the observed emission in very diffuse low-extinction layers of the PDR.

5.4 PDR models

Figure 5.3 shows the abundances of OH^+, H_2O^+ and H_3O^+, predicted by the Meudon PDR model (Le Petit et al. 2006), as a function of visual extinction, for a radiation field of χ=10,000 Draine (1978) units ($\chi_0 = 2.7\times10^{-3}$ erg s^{-1} cm^{-2}) and a pressure of P=10^8 K cm^{-3}. This model successfully reproduces the intensities of the CH^+ $J = 1$–0 to 6–5 transitions observed toward the Orion Bar CO^+ peak with Herschel HIFI and PACS (Nagy et al. 2013, Chapter 4). In this model, the total gas density at the depth where the H_nO^+ abundances peak ($A_{\rm V} \sim 0.3 - 1.0$) is in the range between 5.6×10^4 and 1.8×10^5 cm^{-3}. The column densities of our observed species, integrated up to A_V=1 mag, are $N(OH^+) = 1.6\times10^{13}$ cm^{-2}, $N(H_2O^+) = 4.4\times10^{12}$ cm^{-2}, and $N(H_3O^+) = 7.5\times10^{12}$ cm^{-2}. When integrating up to A_V=10 mag, the values for OH^+

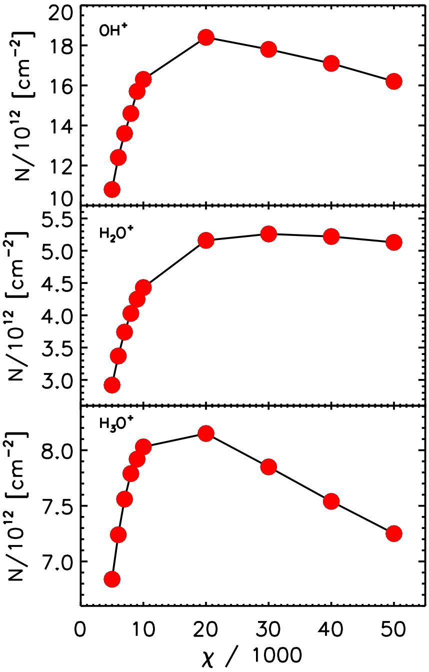

Figure 5.4 — Column densities of OH^+, H_2O^+ and H_3O^+, predicted by the Meudon PDR model as a function of radiation field (in Draine units) for a pressure of P=10^8 K cm^{-3}, as applicable to the Orion Bar.

and H_2O^+ remain the same to 1%, and $N(H_3O^+)$ increases by just 6% which is insignificant. These predictions are consistent with the estimates in Table 5.3 for T_{ex} = 10–20 K, except that the observed OH^+/H_2O^+ ratio is larger than in the models. Note that the predictions correspond to a face-on model; to compare to the observations, they must be multiplied by a factor of $1/\sin i \approx 4$, where $i \approx 15°$ for the Orion Bar.

As shown in Figure 5.3, H_nO^+ abundances in the high UV illumination Orion Bar PDR peak near the cloud surface, at depths of $A_V \sim 0.3 - 0.4$, and decrease rapidly beyond $A_V \sim 1$. Therefore, we study the H_nO^+ chemistry at these depths. The corresponding reaction coefficients and rates are listed in Tables 5.4 and 5.5. At a depth of $A_V \sim 0.3 - 0.4$, the dominant pathways for OH^+ formation are:

$$H_2 + O^+ \xrightarrow{k_1} OH^+ + H \tag{5.1}$$

$$OH + h\nu \xrightarrow{k_2} OH^+ + e^- \tag{5.2}$$

$$\mathrm{OH + H^+ \xrightarrow{k_3} OH^+ + H} \tag{5.3}$$

The dominant OH^+ formation path is via H_2 and O^+, which accounts for 70.2% of the total OH^+ production at $A_V \sim 0.3$ and 85.3% at $A_V \sim 0.4$. Photoionization of OH accounts for ∼18.2% of OH^+ formed at $A_V \sim 0.3$ and ∼11.6% at $A_V \sim 0.4$. Charge exchange between OH and H^+ is mostly significant at $A_V \sim 0.3$, resulting in ∼11.6% of OH^+ production and decreases to ∼3.1% at $A_V \sim 0.4$. This reaction is more important in X-ray dominated regions (XDRs), which is a key difference between such regions and high-illumination PDRs (Van der Werf et al. 2010). At a depth of $A_V \sim 1$, the path via H_2 and O^+ is still the dominant OH^+ formation path (72.1%). However, the role of OH photoionization increases, as it accounts for producing ∼27.3% of OH^+ at this depth.

Once OH^+ is formed, H_2O^+ and H_3O^+ formation rapidly follows via similar reactions with H_2:

$$\mathrm{OH^+ + H_2 \xrightarrow{k_4} H_2O^+ + H} \tag{5.4}$$

$$\mathrm{H_2O^+ + H_2 \xrightarrow{k_5} H_3O^+ + H} \tag{5.5}$$

At a depth of $A_V \sim 0.3$, all H_2O^+ (∼99.8%) forms from OH^+ via a the reaction with H_2. At a depth of $A_V \sim 0.4$, as the H_3O^+ abundance is increased compared to that at $A_V \sim 0.3$, a secondary reaction apart from the reaction from H_2 (∼83%) produces ∼16.6% of the H_2O^+ formed at this depth:

$$\mathrm{H_3O^+ + h\nu \xrightarrow{k_6} H_2O^+ + H} \tag{5.6}$$

At a depth of $A_V \sim 1.0$, the role of H_2O^+ production from H_3O^+ decreases to ∼8.5%, compared to the dominant reaction from H_2 (88.4%). 100% of H_3O^+ is produced from H_2O^+ and H_2 at all of the probed depths in the model ($A_V \sim$ 0.3, 0.4, 1.0).

OH^+ is mainly destroyed via reactions with electrons, photons and H_2. The reaction via H_2 (Eqn. 5.4) is the most important H_2O^+ formation path, as mentioned above. It is also the most important destruction path for OH^+ at depths of $A_V \sim$ 0.4 and beyond. At smaller depths, both dissociative recombination with electrons and UV photodissociation contribute significantly to the OH^+ destruction: at $A_V \sim$ 0.3,

$$\mathrm{OH^+ + e^- \xrightarrow{k_7} H + O} \tag{5.7}$$

contributes 52.4%, and

$$\mathrm{OH^+ + h\nu \xrightarrow{k_8} H + O^+} \tag{5.8}$$

contributes 17.6%. Destruction of H_2O^+ occurs mainly via dissociative recombination with electrons at low depths ($A_V \sim$ 0.3, 0.4):

$$\mathrm{H_2O^+ + e^- \xrightarrow{k_9} H + O + H} \tag{5.9}$$

$$\mathrm{H_2O^+ + e^- \xrightarrow{k_{10}} H + OH} \tag{5.10}$$

Reaction 5.9 accounts for $\sim$ 70.6% of the H_2O^+ destructions at $A_V \sim 0.3$, while reaction 5.10 contributes $\sim$ 19.9%. At a depth of $A_V \sim 0.4$, reactions 5.9 and 5.10 contribute 43.7 and 12.3% (respectively) to the H_2O^+ destruction. Destruction via H_2, which controls H_3O^+ production is only significant at $A_V \sim 1$ ($\sim$87.1%). Therefore, the high electron density and UV radiation field are likely to be the key to explain the H_2O^+ and H_3O^+ non-detections, as a significant fraction of OH^+ and H_2O^+ is directly destroyed by UV photons or by recombination with electrons, limiting the H_2O^+ and H_3O^+ formation. Thus, our non-detections of H_2O^+ and H_3O^+ are consistent with an origin of the OH^+ emission in diffuse gas where C^+ is abundant.

Alternatively, our observed H_2O^+/OH^+ ratio may be due to a low molecular fraction (H_2/H ratio) in the gas probed by our observations. Gerin et al. (2010) derive an analytic expression for the OH^+/H_2O^+ abundance ratio as a function of the gas temperature, electron density, and H_2 volume density:

$$n(\mathrm{OH^+})/n(\mathrm{H_2O^+}) = 0.64 + 430 \times (T/300)^{-0.5} \times [n(\mathrm{e^-})/n(\mathrm{H_2})]$$

As most OH^+ forms in the outermost layers of the PDR ($A_V < 0.4$) at very low molecular fractions (0.01%-0.4% for $A_V = 0.3$ and $A_V = 0.4$, respectively), this formula is consistent with the observed abundance ratio of $N(\mathrm{OH^+})/N(\mathrm{H_2O^+})>2$. This suggests that, apart from the effect of the high electron density mentioned above, the low molecular fraction in the surface of the PDR also contributes to the observed OH^+/H_2O^+ column density ratios. We conclude that most of our observed H_nO^+ emission originates at extinctions below $A_V = 0.4$.

Fig. 3 shows a second peak in the H_3O^+ abundance at a depth of $A_V \sim 7-8$. This second peak is expected in the abundance of H_nO^+ in interstellar clouds with a large range of physical conditions (e.g. Hollenbach et al., 2012) and does not significantly contribute to the total H_3O^+ column density. The sequence of H_nO^+ formation at this depth is initiated by the cosmic-ray ionization of H_2, followed by a reaction of H_2^+ with H_2 producing H_3^+. At this depth, OH^+ is formed from H_3^+, whose abundance is increased due to the lower electron abundance. The second abundance peak disappears toward higher A_V as oxygen freezes out on the grain surfaces as water.

Figure 5.4 shows the effect of changing the radiation field on the H_nO^+ column densities. The model corresponds to $P=10^8$ cm^{-3} K and the figure considers radiation fields between χ=5000 and 50000 Draine units. The

Table 5.4 — Rate coefficients of the main formation and destruction paths of H_nO^+, based on the UMIST database (Woodall et al. 2007).

Reaction	k ($cm^3\,s^{-1}$)	ΔT (K)
k_1	1.70×10^{-9}	10–41000
k_3	2.10×10^{-9}	10–41000
k_4	1.01×10^{-9}	10–41000
k_5	6.40×10^{-10}	10–41000
k_7	$3.75 \times 10^{-8}\ (T/300)^{-0.50}$	10–300
k_9	$3.05 \times 10^{-7}\ (T/300)^{-0.50}$	10–1000
k_{10}	$8.60 \times 10^{-8}\ (T/300)^{-0.50}$	10–1000
Reaction	**k (s^{-1})**	**ΔT (K)**
k_2	$1.60 \times 10^{-12}\ \exp(-3.1A_V)$	10–41000
k_6	$1.00 \times 10^{-9}\ \exp(-1.7A_V)$	10–41000
k_8	$1.10 \times 10^{-11}\ \exp(-3.5A_V)$	10–41000

Notes. The photoreaction rates at the bottom are given for a standard Draine radiation field. The last column gives the temperature range over which the k-values are valid.

predicted column densities of the H_nO^+ species are seen to peak for χ=20,000–30,000 and to drop for higher radiation fields.

5.5 Excitation of OH^+

Our measured column densities of OH^+, H_2O^+ and H_3O^+ are in reasonable agreement with the predictions from the Meudon PDR model, but the appearance of the lines in emission remains a puzzle. To understand this behaviour we perform a non-LTE analysis of the excitation of OH^+, which takes both reactive and inelastic collisions into account, as well as excitation by the background continuum radiation field.

5.5.1 Inelastic collision rates for the OH^+– e^- system

The electronic ground state symmetry of the radical OH^+ is $^3\Sigma^-$. Each rotational level N is therefore split by the spin-rotation coupling between N and the electronic spin $S = 1$ so that each rotational level N has two sublevels given by $j = N \pm 1$. In addition, owing to the non-zero nuclear spin of the hydrogen atom (I=1/2), each fine-structure level is further split into 2 hyperfine levels $F = j \pm 1/2$. The rotational constant of OH^+ is 492.26 GHz. The fine-structure splitting is of the order of 60–90 GHz while the hyperfine

Table 5.5 — Rates (in $\text{cm}^{-3}\ \text{s}^{-1}$) corresponding to the main formation and destruction paths of H_nO^+ in the model at $A_V = 0.3$, 0.4, and 1.0.

A_V	0.3	0.4	1.0
T_{gas}	1783 K	1013 K	569 K
n_{gas}	$5.6\times10^4\ \text{cm}^{-3}$	$9.9\times10^4\ \text{cm}^{-3}$	$1.8\times10^5\ \text{cm}^{-3}$
Reaction		Rate	
k_1	1.31×10^{-10}	6.25×10^{-9}	1.53×10^{-9}
k_2	3.38×10^{-11}	8.46×10^{-10}	5.77×10^{-10}
k_3	2.15×10^{-11}	2.25×10^{-10}	1.22×10^{-11}
k_4	3.11×10^{-11}	7.14×10^{-9}	2.11×10^{-9}
k_5	9.52×10^{-14}	3.29×10^{-9}	2.08×10^{-9}
k_6	4.84×10^{-14}	1.43×10^{-9}	2.03×10^{-10}
k_7	9.75×10^{-11}	1.09×10^{-10}	2.93×10^{-12}
k_8	3.27×10^{-11}	2.50×10^{-11}	-
k_9	2.20×10^{-11}	3.76×10^{-9}	2.18×10^{-10}
k_{10}	6.21×10^{-12}	1.06×10^{-9}	6.15×10^{-11}

splitting is less than 0.3 GHz. The dipole moment of OH^+ is 2.26 D (Werner et al. 1983). For similar information about the H_2O^+ and H_3O^+ molecules, see Gerin et al. (2010) and Ossenkopf et al. (2010).

Electron-impact hyperfine excitation rate coefficients for OH^+ were computed using a three step procedure: *i)* rotational excitation rate coefficients for the dipolar ($\Delta N = 1$) transitions were first computed within the Coulomb-Born approximation; *ii)* fine-structure excitation rate coefficients were then obtained from the Coulomb-Born rotational rates using the (scaled) infinite-order-sudden (IOS) approximation; and *iii)* hyperfine excitation rate coefficients were finally obtained using the so-called "statistical" or "proportional" approach. The Coulomb-Born approximation (Chu & Dalgarno 1974) is expected to be accurate for polar molecules with dipoles in excess of ~ 2 D because the dipolar cross sections are entirely dominated by long-range effects and cross sections for transitions with $\Delta N \geq 2$ are significantly smaller (Faure & Tennyson 2001). In practice, Coulomb-Born cross sections were computed for collision energies below 2 eV and rate coefficients were deduced for temperatures ranging from 10 to 2000 K. The IOS approximation was employed to derive the fine-structure rate coefficients in terms of the rotational rates for excitation out of the lowest rotational level $N = 0$. This IOS formalism was first introduced by Corey & McCourt (1984) for linear molecules with ${}^{2S+1}\Sigma$ symmetry. As the Coulomb-Born rotational rates do not strictly obey the IOS factorization formulae, however, the IOS fine-structure rate coefficients were scaled, as recommended by Faure & Lique (2012) (see their Eqs. (8), (10) and (13), where the quantum number F should be replaced by S). While in principle the IOS approximation should be also applicable to obtain the hyperfine rate coefficients of OH^+, there is to our knowledge no available factorization formula for a $^3\Sigma$ molecule. Hyperfine rate coefficients were therefore obtained from the fine-structure rates by assuming that they are proportional to the degeneracy $(2F+1)$ of the final hyperfine level. We note that this simple statistical approach does not account for the collisional propensity rule $\Delta F = \Delta j$. As shown by Faure & Lique (2012), however, at low total optical depth ($\tau \leq 10$) the statistical approach is applicable because in this regime the relative populations of each hyperfine component are close to the statistical weights.

The above three step procedure was applied to the first 49 levels of OH^+, that is up to the level $(N, j, F) = (8, 8, 17/2)$ which lies 1689 K above the ground state (0, 1, 3/2), resulting in 176 collisional transitions. A typical accuracy of 30% is expected for these rate coefficients, with the largest rate coefficients being of the order of 3×10^{-6} cm^{3}s^{-1}. The rates will be posted on the website of the LAMDA database (Schöier et al. 2005)[3].

5.5.2 Collisional and radiative excitation

The above calculations indicate inelastic collision rates for the OH^+ 971 GHz line of $\approx 6\times10^{-7}$ cm^3 s^{-1}, which is $\sim 10\times$ higher than the dissociative recombination rate at $T \approx 100$ K (Table 5.4). At this temperature, $h\nu/kT \approx 0.5$ for this transition, so that by detailed balance, the upward and downward rates differ by only a few percent. For collisions with H_2, inelastic collision rates are not known, but it may be reasonable to assume that reactive collisions dominate. In contrast, the reaction of OH^+ with H is endothermic, and inelastic collisions with H could influence the excitation of OH^+, but test calculations assuming a collisional rate coefficient of 10^{-10} cm^3 s^{-1} for all radiatively allowed transitions indicate that their effect is negligible compared with electron collisions. We therefore first calculate the excitation of OH^+ assuming that inelastic electron collisions dominate, and consider the effect of reactive collisions with H_2 in §5.5.3.

We have used the non-LTE radiative transfer program RADEX (Van der Tak et al. 2007) to calculate the excitation of OH^+ in the Orion Bar, assuming steady-state conditions and using the inelastic collision rates from §5.5.1. Observations of C recombination lines toward the Orion Bar surface indicate hydrogen densities of 5×10^4–2.5×10^5 cm^{-3} (Wyrowski et al. 1997), which for all carbon in C^+ and C/H = 1.4×10^{-4} translates into an electron density of n(e) ≈ 10 cm^{-3}, as we have used before for HF (Van der Tak et al. 2012). We use an electron temperature of $T_e = 300$ K, but our results are insensitive to variations in T_e between 100 and 1000 K. The adopted line width is the observed 4.3 km s^{-1} and for the background radiation field we adopt a greybody distribution with

---

[3] `http://home.strw.leidenuniv.nl/~moldata/`

a dust temperature of T_d=50 K and a dust emissivity index of β=1.6, as found by Arab et al. (2012) for the interior of the Bar, so that τ_d=0.21 at 971 GHz. The model is insensitive to the details of this radiation field; in particular, the results are unchanged when adopting T_d=70 K and β=1.2 as found by Arab et al for the Bar's surface.

The model predicts an excitation temperature of ≈9.7 K for the OH^+ lines near 1 THz. The excitation is due to the combination of collisions and radiation: a model with only the 2.73 K radiative background results in $T_{\rm ex}$ ≈7 K. The effect on the emerging line intensities is large, since the Planck function at 1 THz increases by a factor of ~4 from $T_{\rm ex}$ = 7 K to 9 K.

The calculated excitation temperature of 9.7 K is above the background radiation temperature of 9.2 K, which explains the appearance of the line in emission, but the models require $N(\mathrm{OH}^+) = 10^{15}$ cm^{-2} to match our observed 971 GHz line intensity. At this high column density, the OH^+ lines become optically thick which drives the three N=1–0 lines to approximately the same peak brightness, in disagreement with our observations. We therefore regard this model as untenable, conclude that the observed line emission is optically thin, and search for a model with a higher excitation temperature in the next section.

5.5.3 Effect of reactive collisions

The above calculation indicates that electron collisions are sufficient to make the OH^+ line appear in emission given the low background intensity of the Orion Bar. A fully self-consistent model should however include formation and destruction terms in the rate equations. We use Equation 12 from Van der Tak et al. (2007), where the number density of OH^+ molecules (in cm^{-3}) is the ratio of its formation rate (in cm^{-3} s^{-1}) and its destruction rate (in s^{-1}). We adopt a destruction rate of OH^+ in the Orion Bar of 10^{-4} s^{-1}, which is due to reactions with H_2, electron recombination, and photodissociation. In contrast, the formation of OH^+ through ion-molecule reactions should proceed at a rate at or below the Langevin rate of ≈10^{-9} cm^3 s^{-1} and is limited by the supply of hydrogen or oxygen ions.

Lacking state-to-state formation rates, we approximate the distribution of the newly-formed OH^+ over its energy levels by a thermal distribution at a temperature T_f. The value of T_f depends on the dominant formation route and is likely to be a significant fraction of its excess energy. The reactions of O^+ with H_2 and of O with H_3^+ have exothermicities of 0.55 and 0.66 eV (Federer et al. 1984; Milligan & McEwan 2000), so T_f should be in the range 2000–3000 K.

For OH^+ formation rates between 10^{-12} and 10^{-9} cm^3 s^{-1} and formation temperatures of 2000–3000 K, the model predicts excitation temperatures of 10.7–11.7 K for the OH^+ lines near 1 THz. Compared to models with a negligible formation rate, the line brightness increases by a factor of ≈5, almost independent of T_f, for the same column density. The observed line intensity is matched for $N(\mathrm{OH}^+) = 1.5\times10^{14}$ cm^{-2}, which is considerably lower than for the steady-state excitation model. The difference with the estimates in Table 5.3 is the presence of background radiation. We conclude that formation pumping plays an important role for OH^+ in the Orion Bar.

5.6 Discussion

5.6.1 Changing the ionization rate

Our derived OH^+ column density is similar to that in diffuse clouds, as observed in absorption toward W49N and other sources (see references in §5.3.3), but $\sim$2.5× higher than the model predictions in §5.4. The calculations in §5.4 assume a cosmic-ray ionization rate of 2×10^{-16} s^{-1}, which is a typical value for diffuse interstellar clouds in the Solar neighbourhood (Indriolo & McCall 2012) and an order of magnitude higher than the value for dense clouds (Van der Tak & van Dishoeck 2000). However, the actual ionization rate of the Orion Bar may be atypically high because of its proximity to the Trapezium stars. The effects of X-rays from these stars on the chemistry are similar to those of cosmic rays (Meijerink et al. 2006). In particular, Gupta et al. (2010) estimate an ionization rate of 3×10^{-15} s^{-1} for the Orion KL region, dominated by X-rays from the star θ^1C Ori. Calculations using the Meudon code with an ionization rate of 2×10^{-15} s^{-1} result in very similar H_nO^+ column densities as before, though, presumably because of the high gas density in the Orion Bar.

5.6.2 Possible ion sources

Regarding the Orion Bar as a molecular cloud under external illumination and heating, the main source of OH^+ may be the reaction of H_3^+ with O, where the H_3^+ is due to cosmic-ray ionization as well as leakage of UV photons from the ionized region. However, interaction of the PDR with the neighbouring photoionized nebula may supply O^+ ions which produce extra OH^+ in their reaction with H_2. The supply of O^+ ions may be due to leakage of hydrogen- and oxygen-ionizing photons, but also to advection of H^+ and O^+ ions from the ionized nebula into the mostly neutral PDR, as in some planetary nebulae (Black 1983). The concentration of H^+ with depth into the PDR is then important, because charge transfer reactions ($H^+ + O \leftrightarrow O^+ + H$) will rapidly couple the O^+/O ratio to the H^+/H ratio. Observations of the [OIII] 88 μm line toward the Orion Bar with Herschel/PACS show that ionized oxygen is widespread in the region (C. Joblin & J. Goicoechea, priv. comm.); the emission extends well into the mostly-neutral gas traced by the [OI] 63 μm line (M. Gerin, priv. comm.), making the $O^+ + H_2$ channel a likely source of OH^+. Detailed comparison of the optical (forbidden and/or permitted) lines of O and O^+ would be a stronger test of this scenario (Mesa-Delgado et al. 2011). In addition, simulations of the full molecular + atomic + ionized gas in the Orion PDR with the Cloudy program (Ferland et al. 2013) would be useful to constrain the role of possible ion sources in the Orion Bar.

5.6.3 Radiative pumping

Besides changing the chemistry of OH^+, the strong infrared and ultraviolet radiation fields in the Orion Bar may change its excitation. Section 5.5.2 already showed that far-infrared continuum radiation raises the OH^+ excitation temperature significantly above the level due to electron collisions alone. In addition, mid-infrared pumping may contribute if the radiative excitation rate of OH^+ in the Bar exceeds the collisional excitation rate by electrons, which is $n(\mathrm{e}) \times C_{\mathrm{lu}} = 10$ cm^{-3} $\times 6\times10^{-7}$ cm^3 s^{-1} $= 6\times10^{-6}$ s^{-1}. The radiative rate is $B_{\mathrm{lu}}U_{\mathrm{rad}}$, the Einstein absorption coefficient times the radiative energy density, which is approximately $A_{\mathrm{vib}}\epsilon f/(e^{(h\nu/(kT_d))}-1)$, where ϵ is the dust emissivity, f the dust filling factor, A_{vib} the spontaneous decay rate of 265 s^{-1}, and T_d the dust temperature. For the Orion Bar, the filling factor should be close to unity, and for the emissivity we assume 1 at the short wavelength (3.38 μm) of the fundamental vibrational band of OH^+. Equating the radiative rate to the electron collision rate indicates a minimum temperature of $\approx$240 K, which is reasonable for the gas at the Bar's surface, but too much for the dust, as the PACS and SPIRE data show (Arab et al. 2012). Only PAHs and small grains would reach such high temperatures, but with very low opacities, even though the OH^+ vibrational fundamental is close to the PAH 3.3 μm and aliphatic 3.4 μm emission features.

Besides continuum radiation from dust in the Bar itself, pumping by infrared starlight from the Trapezium may influence the excitation of OH^+. The brightest of these stars is θ^1C Ori, which is $127''$ away from our observing position (Van Leeuwen 2007). If both objects lie at the same distance from the Sun, the stellar continuum flux at the Orion Bar is 2.96 million times stronger than at the Earth. The stellar temperature of 37,000 K implies a radiative intensity of 0.2 Jy/nsr or 2×10^{-15} erg s^{-1} cm^{-2} Hz^{-1} sr^{-1}. Setting this equal to the Planck function at a radiation temperature T_R, we obtain $T_R = 185$ K at $\lambda = 3.38\,\mu$m. The corresponding pumping rate in the OH^+ vibrational fundamental is of order $A_{\mathrm{vib}}/\{\exp(h\nu/kT_R)-1\} = 5.7\times10^{-8}\,\mathrm{s}^{-1}$, which is much less than the collisional excitation rate by electrons.

While infrared pumping does not seem play a role for OH^+ in the Orion Bar, the absorption rate through electronic transitions in the near ultraviolet is rather higher. The radiative intensity of θ^1C Ori at the wavelength of the $\mathrm{A}^3\Pi_i - \mathrm{X}^3\Sigma^-$ v=0–0 band of OH^+ at 27949 cm^{-1} (3577 Å) is $\approx$1.8 Jy/nsr. The A-value for this band is 8.01×10^5 s^{-1} (de Almeida & Singh 1981), so that the absorption rate in this band alone is $\approx 3.3\times10^{-6}\,s^{-1}$, which is only slightly less than the collisional excitation rate.

5.6.4 Comparison with extragalactic systems

The Orion Bar is the first and so far only position within our Galaxy where lines of OH^+ appear purely in emission. Detections of extragalactic OH^+ and H_2O^+ emission have been made with Herschel-SPIRE by Van der Werf et al. (2010) toward the active nucleus of the galaxy Mrk 231, with Herschel-PACS toward the ultraluminous merger Arp 220 by Rangwala et al. (2011) and with Herschel-SPIRE toward the Seyfert nucleus NGC 1068 by Spinoglio et al. (2012). In addition, detections of extragalactic H_nO^+ absorption exist toward M 82 using HIFI (Weiß et al. 2010) and SPIRE (Kamenetzky et al. 2012). Recently, PACS observations of excited OH^+, H_2O^+ and H_3O^+ toward NGC 4418 and Arp 220 have been discussed by González-Alfonso et al. (2013). We suspect that the nuclei where H_nO^+ lines appear in emission have an enhanced electron density, far-infrared continuum, and/or ionizing (UV/X-ray) continuum.

5.7 Conclusions

We have presented maps and spectra of OH^+ line emission toward the Orion Bar, and limits on lines of H_2O^+ and H_3O^+. The OH^+ line emission is extended over $\sim1'$ (=25,000 AU = 0.12 pc) and traces the Bar itself as well as the Southern tip of the Orion Ridge. The line width suggests an origin of the emission at a depth of A_V=0.3–0.5, similar to CH^+ and SH^+. The OH^+ column density of $\sim1.5\times10^{14}$ cm^{-2}, derived using a non-LTE model including both inelastic and reactive collisions and radiative pumping, is similar to that in previous absorption line studies, while our limits on the OH^+/H_2O^+ and OH^+/H_3O^+ ratios are higher than seen before.

Non-LTE models of the excitation of OH^+ show that the unusual appearance of the OH^+ lines in emission is the combined result of inelastic electron collisions, far-infrared radiative pumping by dust, and chemical pumping through the O^+ + H_2 and O + H_3^+ channels. The same conditions may apply to extragalactic sources of H_nO^+ line emission. In the future, high-resolution maps of Galactic and extragalactic OH^+ line emission with ALMA will shed further light on the chemistry of this reactive ionic species.

Our observed H_nO^+ column densities are qualitatively reproduced by a model of the Orion Bar (using the Meudon PDR code) using a radiation field of $\chi=10^4\ \chi_0$ and a pressure of $P=10^8$ K cm^{-3} as suggested by previous observations. Analysis of the main formation and destruction paths of the ions indicates that our high OH^+/H_2O^+ and OH^+/H_3O^+ ratios are due to the high UV radiation field and electron density in the Orion Bar. Destruction of OH^+

and H_2O^+ by photodissociation and electron recombination limits the formation of H_2O^+ and H_3O^+.

Quantitatively, the Meudon PDR models underpredict the absolute OH^+ column density by a factor of $\sim$2.5. To match the observed line intensity with an OH^+ column density similar to that in the PDR model, the electron density would have to be $\approx 100\,\mathrm{cm}^{-3}$, which is much higher than the PDR model predicts at the depth where the H_nO^+ ions are abundant, as seen in Fig. 10 of Nagy et al. (2013) (Chapter 4). However, raising the pressure in the PDR model by $\approx$50% would increase the predicted $N(\mathrm{OH}^+)$ to the value suggested by the RADEX models. Such an increase is consistent with the CH^+ and SH^+ observations, and is also suggested by observations of high-J CO lines with PACS (Joblin et al, in prep.). Furthermore, the Meudon PDR model uses a scaling of the average interstellar radiation field, while realistic models should use direct observations of the dominant hot star θ^1C Ori for the H-ionizing part of the spectrum and the wavelength range where OH photoionization occurs, which could contribute significantly to the formation of OH^+.

Acknowledgements The authors thank Sébastien Bardeau and Jérôme Pety (IRAM) for help with the data reduction, Franck le Petit (Paris-Meudon) for assistance with the PDR model calculations, Arturo Rodríguez-Franco (Madrid) for sending his CN map in electronic form, Xander Tielens (Leiden) for useful discussions, Inga Kamp (Groningen) for a careful reading of the manuscript, and Christine Joblin (Toulouse) & Javier Goecoechea (Madrid) for sharing their PACS observations of the [OIII] line. AF acknowledges support by the Agence Nationale de la Recherche (ANR-HYDRIDES), contract ANR-12-BS05-0011-01.

HIFI has been designed and built by a consortium of institutes and university departments from across Europe, Canada and the US under the leadership of SRON Netherlands Institute for Space Research, Groningen, The Netherlands with major contributions from Germany, France and the US. Consortium members are: Canada: CSA, U.Waterloo; France: CESR, LAB, LERMA, IRAM; Germany: KOSMA, MPIfR, MPS; Ireland, NUI Maynooth; Italy: ASI, IFSI-INAF, Arcetri-INAF; Netherlands: SRON, TUD; Poland: CAMK, CBK; Spain: Observatorio Astronómico Nacional (IGN), Centro de Astrobiología (CSIC-INTA); Sweden: Chalmers University of Technology - MC2, RSS & GARD, Onsala Space Observatory, Swedish National Space Board, Stockholm University - Stockholm Observatory; Switzerland: ETH Zürich, FHNW; USA: Caltech, JPL, NHSC.

6

The UV-illuminated surface of Orion S traced by reactive ions

Nagy, Z., Van der Tak, F. F. S., Plume, R., Bergin, E. A., & Tolls, V. [1]

---

[1] In preparation, to be submitted to Astronomy & Astrophysics.

Abstract

Photon-dominated regions (PDRs) are key environments to study the feedback effect of star-formation on the surrounding molecular clouds and to probe chemical reactions triggered by enhanced UV illumination.

We estimate the physical properties of the UV-illuminated surface of the Orion S massive molecular condensation. We study the chemistry of PDR surface tracers, including the reactive ions CH^+, SH^+, and CO^+, that are thought to form via reactions with vibrationally excited H_2.

The HIFI instrument on board the Herschel Space Observatory covers a number of transitions that trace molecular line emission in PDRs. We analyze CH^+, SH^+, and CO^+ emission toward Orion S using radiative transfer and PDR models.

We detected the CH^+ J=1-0, CO^+ N=5-4, and SH^+ $N_J=1_2 - 0_1$ transitions toward Orion S in emission. The observed line widths of these ions are similar to those measured in the Orion Bar, including that of [CII]. The observed CH^+, SH^+, and [CII] line intensities are consistent with a PDR model illuminated by a radiation field derived by earlier studies toward the Orion S position ($\chi \sim 10^5 \chi_0$, Draine 1978) and a pressure of $\sim 10^8$ K cm^{-3}. This pressure is similar to that which is necessary to explain the emission of CH^+ and SH^+ in the nearby Orion Bar PDR. The models also indicate that the previously poorly constrained inclination of the PDR at the Orion S position is around 45° rather than face-on.

The difference in the observed CH^+ 1-0/2-1 line intensity ratio between the Orion Bar and Orion S regions cannot be explained by a simple non-LTE radiative transfer model and by isobaric PDR models. The detection of the CO^+ N=5-4 transition toward Orion S but not toward the Orion Bar is likely to be related to different excitation conditions between the regions rather than to differences related to the chemistry.

6.1 Introduction

Photon-dominated regions (PDRs) are UV-illuminated interfaces in molecular clouds where different chemical layers form due to the penetration of the UV radiation into the cloud. One of the best studied examples is the nearly edge-on Orion Bar (Van der Wiel et al. 2009 and references therein) located in the OMC-1 region. The Orion Bar is part of an extended region of the OMC-1 cloud that is illuminated by the Trapezium cluster (e.g. Stacey et al. 1993). The warm surface region of PDRs ($A_V \leq 1.5$) is well traced by reactive ions, such as CH^+, SH^+, and CO^+, that require a strong UV radiation field for their formation via reactions with vibrationally excited H_2.

CH^+, SH^+, and CO^+ ions have previously been studied in various PDRs and other environments with strong FUV/X-ray radiation fields. However, there are only a limited number of PDRs/XDRs or other irradiated regions, such as a protostellar envelope, where at least two of these ions are detected. Several transitions of CH^+, SH^+, and CO^+ were detected toward the Orion Bar (CO^+: Störzer et al. 1995, Fuente et al. 2003, Hogerheijde et al. 1995, CH^+: Habart et al. 2010, Naylor et al. 2010a, CH^+ and SH^+: Nagy et al. 2013). Other detections of reactive ions in PDRs include Mon R2 (CO^+, Rizzo et al. 2003) and NGC 7027 (CO^+: Fuente et al. 2003, Latter et al. 1993, CH^+: Cernicharo et al. 1997). CO^+ and CH^+ were both detected toward the envelope of the high-mass protostar AFGL 2591 using the JCMT (Stäuber et al. 2007) and Herschel/HIFI (Bruderer et al. 2010), respectively. SH^+ emission was detected toward W3 IRS5 (Benz et al. 2010), possibly also related to UV-irradiated outflow walls of protostars, such as the hydride ions detected in AFGL 2591 (Bruderer et al. 2010, Stäuber et al. 2007).

Recently Nagy et al. (2013) presented Herschel observations of CH^+ and SH^+ toward the Orion Bar. These observations and previous CO^+ detections toward the Orion Bar (Hogerheijde et al. 1995, Störzer et al. 1995, Fuente et al. 2003) show a significant difference between the line widths of these ions with a related chemistry initiated by reactions with vibrationally excited H_2. While SH^+ and CO^+ are observed with a width of $\sim$3 km s^{-1}, consistent with the widths of dense-gas tracers in the Orion Bar (Hogerheijde et al. 1995), CH^+ has a significantly broader line width of $\sim$5 km s^{-1}(Nagy et al. 2013, Chapter 4). A possible explanation is an origin in a different temperature/density component. Alternatively, CH^+ and CO^+, being destroyed on a short timescale, are not thermalized and therefore their width traces conditions of their formation rather than those of the region they originate in. Distinguishing between these possible explanations requires additional data.

We present detections of CH^+, SH^+, and CO^+ in emission toward the UV-illuminated surface of the Orion S molecular core. The Orion S (OMC 1S) massive molecular condensation is located about $1'$ southeast of the Trapezium cluster (Figure 6.1). Orion S is not part of the OMC-1 region like the nearby

Orion BK/KL but is an isolated molecular core located in the HII region around the Trapezium stars (O'Dell et al. 2009). The size of the Orion S region is similar to that of Orion BN/KL, but its 1.3 mm bolometric luminosity of $10^4 L_\odot$ is an order of magnitude lower than that of the BN/KL source (Mezger et al. 1990). This difference in luminosity, combined with molecular line emission detected toward this region, may be interpreted as the Orion S is less evolved compared to Orion BN/KL (e.g. McMullin et al. 1993). Orion S is an active site for star formation, as indicated by the number of outflows and Herbig-Haro flows detected in the region (e.g. Zapata et al. (2006) and references therein). Part of the molecular line emission detected toward Orion S is related to the UV radiation field created by the Trapezium cluster, that is estimated to be $\chi \sim 1.5\times10^5 \chi_0$ (Draine 1978 units, with $\chi_0 = 2.7 \times 10^{-3}$ erg s^{-1} cm^{-2}.) at the position of Orion S (Herrmann et al. 1997), about a factor of 10 higher than that in the Orion Bar.

This chapter aims to characterize the UV-illuminated surface of the Orion S condensation and to study the chemistry of the CH^+, SH^+, and CO^+ ions. We also aim to study the differences between the Orion S and the Orion Bar regions.

6.2 Observations and data reduction

The transitions used in this paper (Table 6.1) were observed as spectral scans as a part of the HEXOS (Herschel/HIFI Observations of EXtraOrdinary Sources: The Orion and Sagittarius B2 Star-forming Regions, Bergin et al. 2010) key program using the Heterodyne Instrument for the Far-Infrared (HIFI, De Graauw et al. 2010) of the Herschel Space Observatory (Pilbratt et al. 2010). The observations were pointed toward the R.A. (J2000.0)= $05^{\rm h}35^{\rm m}13.^{\rm s}44$, Dec. (J2000.0)= $-05°24'08.''1$ position, shown on Fig. 6.1 overlaid on a ^{13}CO 3-2 map of the OMC-1 region, taken from the James Clerk Maxwell Telescope (JCMT)[2] archive[3]. The data were reduced using the Herschel Interactive Processing Environment (HIPE, Ott 2010) pipeline version 10.0. The velocity calibration of HIFI data is accurate to ~0.5 km s^{-1} or better. The sideband deconvolution was done using the *doDeconvolution* task in HIPE. In this paper we use data from bands 1a (SH^+ $N_J = 1_2 - 0_1$), 1b (CO^+ $J = 5 - 4$), 3a (CH^+ $J = 1 - 0$), 6b (CH^+ $J = 2 - 1$), and 7b (CII). The scans were observed using dual beam switch (DBS) observing mode. The Wide Band Spectrometer (WBS) backend was used for band 1a. The WBS has a spectral resolution of 1.1 MHz. Both the High Resolution Spectrometer (HRS) and WBS were used for bands 1b, 3a, 6b, and 7b. Scans 1a, 1b, and 3a have a redundancy of 6; 6b

---

[2] The James Clerk Maxwell Telescope is operated by The Joint Astronomy Centre on behalf of the Science and Technology Facilities Council of the United Kingdom, the Netherlands Organisation for Scientific Research, and the National Research Council of Canada.

[3] `http://www1.cadc-ccda.hia-iha.nrc-cnrc.gc.ca/jcmt`

and 7b have a redundancy of 2. The total integration times corresponding to the scans are 1.9 h (band 1a), 2.1 h (band 1b), 1.7 h (band 3a), 2.1 h (band 6b), and 1.8 h (band 7b). The beam sizes and main beam efficiencies in Table 6.1 are based on Roelfsema et al. (2012). The main beam efficiencies correspond to that measured at the center of each band, and the beam sizes are calculated based on Eqn. 3 in Roelfsema et al. (2012). The spectroscopic parameters are based on the Cologne Database for Molecular Spectroscopy (CDMS, Müller et al. 2005) and on Müller (2010) for the observed CH$^+$ transitions.

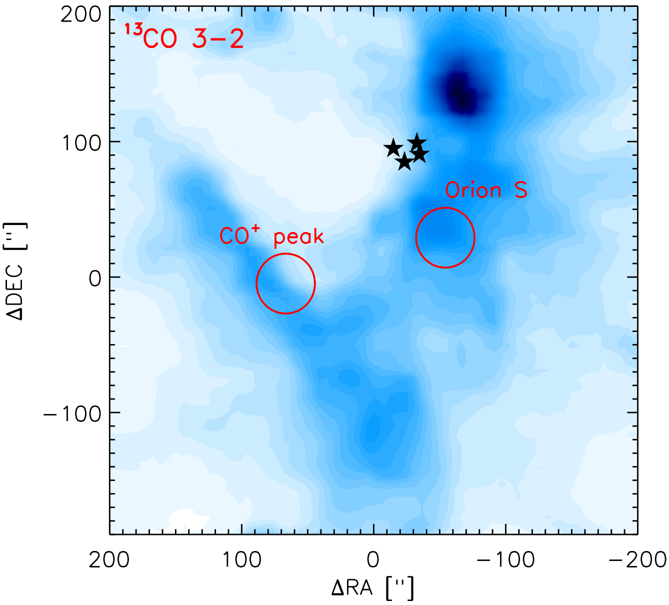

Figure 6.1 — ^{13}CO 3-2 integrated intensity map of the Orion Bar and Ridge region observed with the JCMT. The largest beam size corresponding to our observations ($\sim44''$) is overlaid toward the Orion S and Orion Bar CO$^+$ peak (Störzer et al. 1995) positions. The black symbols show the position of the Trapezium stars. The (0,0) position corresponds to R.A. (J2000.0)= $05^{\rm h}35^{\rm m}16.^{\rm s}4$, Dec. (J2000.0)= $-05^\circ24'51''$.

Table 6.1 — Summary of the transitions used in this paper.

Species / Transition		ν (MHz)	$E_{\rm up}$ (K)	$A_{\rm ij}$ (s^{-1})	Beam ($''$)	$\eta_{\rm mb}$
CO^+	J=5–4, F=11/2–9/2	589872.2	85.0	7.37×10^{-3}	36.0	0.76
CH^+	J=1–0	835137.5	40.1	6.36×10^{-3}	25.4	0.75
CH^+	J=2–1	1669281.3	120.2	6.10×10^{-2}	12.7	0.72
SH^+	$N_J=1_2–0_1$, F=3/2–1/2	526038.7	25.3	7.99×10^{-4}	40.4	0.76
SH^+	$N_J=1_2–0_1$, F=5/2–3/2	526047.9	25.3	9.59×10^{-4}	40.4	0.76
SH^+	$N_J=1_2–0_1$, F=3/2–3/2	526124.9	25.3	1.60×10^{-4}	40.4	0.76
[CII]	$^2P_{3/2}$-$^2P_{1/2}$	1900536.9	91.2	2.30×10^{-6}	11.2	0.69

6.3 Results

6.3.1 Line profiles

The CH^+ J=1-0 line detected toward Orion S (Fig. 6.2) has a similar line intensity to that detected toward the Orion Bar, however, unlike for the Orion Bar, where CH^+ has been detected up to the J=6-5 transition, there are no higher-J transitions of CH^+ detected toward Orion S. Its width (FWHM= 4.4 km s^{-1}) is slightly higher than the typical line width of other PDR envelope tracers in Orion S, such as SH^+ and CO^+ (Table 6.2), but not as large as that of the CH^+ 1-0 line detected toward the Orion Bar (FWHM= 5.5 km s^{-1}, Nagy et al. 2013, Chapter 4).

The $F = 3/2 - 1/2$ and $F = 5/2 - 3/2$ hyperfine components of the SH^+ $N_J = 1_2 - 0_1$ line have been detected toward Orion S (Fig. 6.3), with a similar width to the same lines detected in the Orion Bar (FWHM$\sim 2-3$ km s^{-1}, Nagy et al. 2013). The $F = 3/2 - 3/2$ transition, that is only a tentative detection toward the Orion Bar, has not been detected toward Orion S.

We included the [CII] 158 μm line as a typical PDR tracer in our line sample. The detected line profile (Figure 6.4) shows two components. A component that peaks near source velocity ($v_{\rm LSR}$ = 7 km s^{-1}, e.g. McMullin et al. 1993) and has a width of FWHM$\sim$3.7 km s^{-1} can be related to the UV-illuminated envelope of the Orion S molecular condensation. The other blue-shifted component at $v_{\rm LSR} \sim 0.5$ km s^{-1}(FWHM$\sim$2.8 km s^{-1}) corresponds to a foreground cloud of the OMC region and is likely related to the Orion's veil (e.g. Abel et al. 2004, 2006, Van der Werf et al. 2013). HF is seen in absorption at a similar velocity to the [CII] component around $v_{\rm LSR} \sim 0.5$ km s^{-1} for Orion S as well as toward the Orion Bar (Van der Tak et al. 2012). HI data from the Leiden/Argentine/Bonn (LAB[4], Kalberla et al. 2005) survey shows self-absorption at a similar velocity (Fig. 6.4).

---

[4] `http://www.astro.uni-bonn.de/hisurvey/profile`

We have detected the CO$^+$ $N = 5 - 4$, $F = 11/2 - 9/2$ transition (Fig. 6.5) with a width ($\Delta v \sim 3.3$ km s^{-1}) similar to that of the detected SH$^+$ lines and the envelope component of C II. Its width is also consistent with that detected toward the Orion Bar.

Table 6.2 — Line parameters based on the average spectrum of H and V polarizations.

Line	$\int T_{\rm mb} {\rm d}V$ (K km s^{-1})	$V_{\rm lsr}$ (km s^{-1})	ΔV (km s^{-1})	$T_{\rm mb}$ (K)	rms (K)
CO$^+$ N=5–4, J=11/2–9/2	0.43±0.06	8.32±0.24	3.28±0.50	0.12±0.01	0.03
CH$^+$ J=1–0	25.01±0.12	8.23±0.01	4.36±0.02	5.39±0.20	0.09
CH$^+$ J=2–1	≤2.23[a]			≤0.21	
SH$^+$ N_J=1$_2$–0$_1$, F=3/2–1/2	0.34±0.04	8.71±0.24	3.00[b]	0.11±0.03	0.03
SH$^+$ N_J=1$_2$–0$_1$, F=5/2–3/2	0.45±0.05	8.27±0.18	3.00[b]	0.14±0.03	0.03
SH$^+$ N_J=1$_2$–0$_1$, F=3/2–3/2	≤0.11[a]			≤0.02	
C$^+$ 'envelope'	386.93±0.87	8.50[b]	3.69±0.01	98.59±3.40	1.0
C$^+$ 'blue-shifted'	24.76±0.78	0.50[b]	2.80±0.11	8.30±3.40	1.0

---

[a] 3σ upper limit on the integrated intensity derived as $I(3\sigma)$ [K kms^{-1}] = 3 rms $\sqrt{2\ dv\ \mathrm{FWHM}}$, with the channel width dv in km s^{-1} and the rms noise level derived in a velocity range of ±5 km s^{-1} around the expected velocity.

[b] Fixed parameter in the fit.

6.3.2 Column densities

For a simple estimate of the column densities of the observed molecules, we used the RADEX radiative transfer code (Van der Tak et al. 2007). This method allows a simple comparison between the line emission measured in the Orion Bar (Chapter 4) and Orion S regions, however, the assumption of a single temperature and density component over-simplifies the interpretation. For a more accurate interpretation of the observations including information on the chemical processes that form and destroy the observed molecules, we use PDR models in Section 6.3.3. As CH$^+$ and CO$^+$ are very reactive, inelastic collision rates with H, H$_2$ and electrons are similar to the chemical reaction rates with these species (e.g. Stäuber & Bruderer 2009). Therefore, we consider the chemical formation and destruction rates in the statistical equilibrium calculation (e.g. Van der Tak et al. 2007). The statistical equilibrium for states i = 1 - N of energy E_i that is solved in the RADEX code is given by the time-independent rate equations:

$$\frac{dn_i}{dt} = \sum_{j\neq i}^{N} n_j P_{ji} - n_i \sum_{j\neq i}^{N} P_{ij} + \mathcal{F}_i - n_i \mathcal{D}_i \quad \mathrm{cm}^{-3}\ \mathrm{s}^{-1}$$

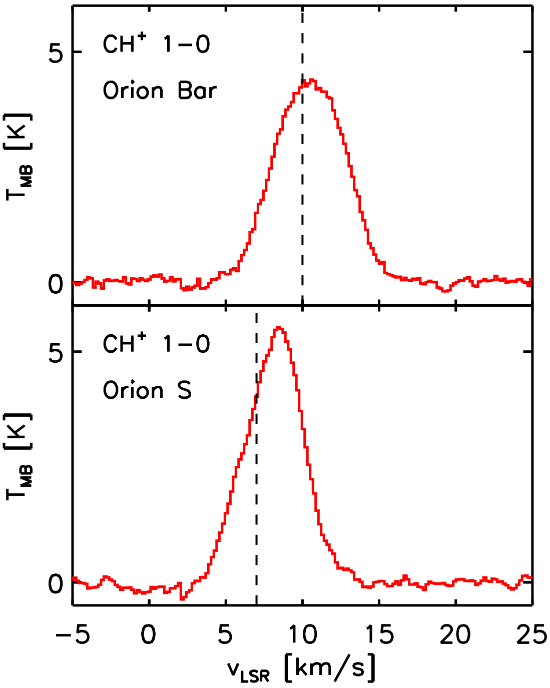

Figure 6.2 — The CH$^+$ 1-0 transition observed by Herschel/HIFI toward Orion S and toward the CO$^+$ peak of the Orion Bar. The dotted lines denote the systemic velocity of the Orion Bar ($V_{\rm LSR} \sim 10$ km s^{-1}) and Orion S ($V_{\rm LSR} \sim 7$ km s^{-1}).

where

$$
\begin{aligned}
P_{ij} &= A_{ij} + B_{ij}\bar{J} + C_{ij} \quad (E_i > E_j) \\
&= B_{ij}\bar{J} + C_{ij} \quad (E_i < E_j)
\end{aligned}
$$

and A_{ij} and B_{ij} are the Einstein coefficients, $\bar{J}$ is the mean intensity at the frequency of transition $i \to j$, C_{ij} is the sum over all collision partners of the rates of inelastic, collision-induced transitions $i \to j$, n_i is the number density (cm^{-3}) of molecules in level i, and $\mathcal{D}_i$ is the rate of destruction of the molecule in level i. When detailed knowledge of the state-specific formation process is lacking, the formation rate $\mathcal{F}_i$ (cm^{-3} s^{-1}) into level i is expressed as a Boltzmann distribution over all states at an effective formation temperature T_f,

$$\mathcal{F}_i \propto g_i \exp(-E_i/kT_f)$$

where g_i is the statistical weight of level i. The formation temperature is introduced to describe the effect of formation in excited levels by a single

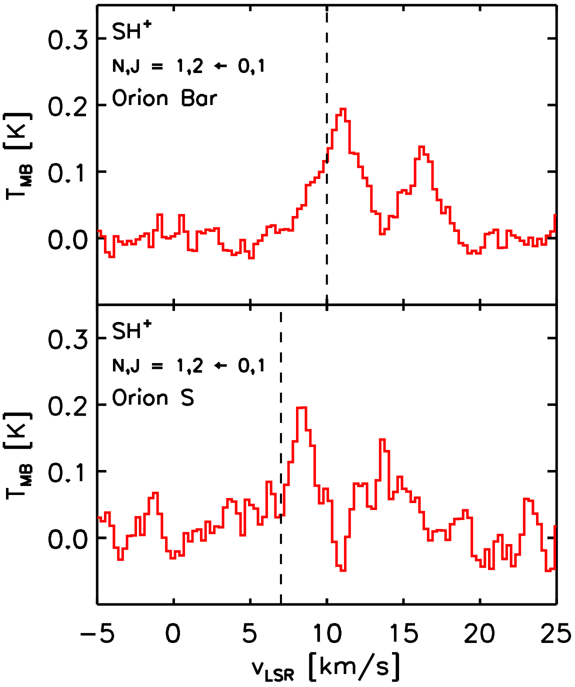

Figure 6.3 — A comparison of the SH^+ $1_2 - 0_1$ line profiles observed toward the CO^+ peak of the Orion Bar (Nagy et al. 2013) and toward Orion S using Herschel/HIFI. The dotted lines denote the systemic velocity of the Orion Bar ($V_{\rm LSR} \sim 10$ km s^{-1}) and Orion S ($V_{\rm LSR} \sim 7$ km s^{-1}).

parameter. In general, it differs from the gas kinetic temperature and the excitation temperature. Here we assume a balance between the formation and destruction of CH^+ and CO^+. In RADEX the radiative transfer is solved independently of the chemical processes, i.e. $\mathcal{F}_i$ and $\mathcal{D}_i$ are zero. Thus, we treat the chemical pumping effect described above for both CH^+ (such as in Chapter 4) and CO^+ by adding an artificial level to the CH^+ and CO^+ level systems, representing the dissociated state, that is populated with a rate equivalent to the reaction rate of CH^+ and CO^+ with H, H_2, and e^- (Woodall et al. 2007).

For inelastic CH^+-H_2 collisions, we use excitation rates from Turpin et al. (2010), that are available for temperatures in the range between 10 K and 200 K, covering transitions up to the 5-4 transition ($E_{\rm up}$ = 599.5 K). These rates have been scaled from CH^+ −He to CH^+−H_2 based on Schöier et al. (2005). The details on including reactive collisions in the excitation calculation, and on the used formation temperature can be found in Nagy et al. 2013 (Chapter 4)

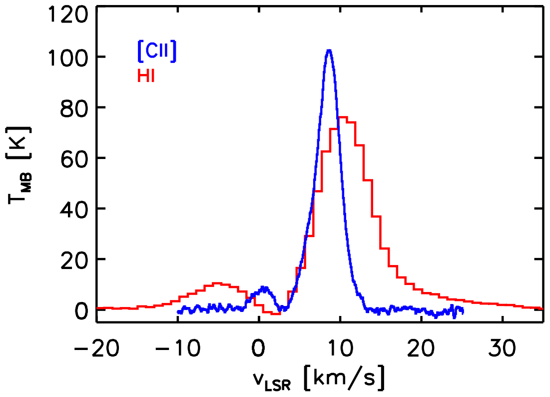

Figure 6.4 — [CII] detected with Herschel/HIFI toward Orion S and the HI λ21-cm line detected as a part of the LAB Survey at the position of Orion S.

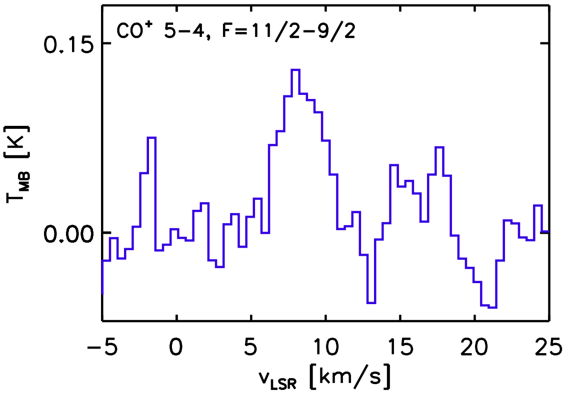

Figure 6.5 — CO$^+$ $N = 5-4$ $J = 11/2-9-2$ transition detected with Herschel/HIFI toward Orion S.

As CH$^+$ and CO$^+$ were found to trace high temperatures of ≥500 K near the surface of PDRs in a region with relatively low molecular fraction (e.g. Stäuber & Bruderer 2009 and references therein), we assume a kinetic temperature of ≥500 K and $n(H_2) \leq 10^5$ cm^{-3}. A kinetic temperature of 500 K, an H_2 volume density of 10^5 cm^{-3}, and a column density of 5×10^{14} cm^{-2} reproduces the observed CH$^+$ 1-0 line intensity with an accuracy of ∼70% (under-prediction), and inconsistently, over-predicts the intensity of the 2-1 transition by about a factor of two. RADEX models for a large range of parameters ($T_{\rm kin} \sim 100-1000$ K, $n(H_2)\sim 10^4$-10^6 cm^{-3}, Fig. 6.6) around the expected temperature and density under-predict the observed line ratio of CH$^+$ 2-1/CH$^+$ 1-0$\gtrsim$0.09. The closest values to the observed ratio are predicted for the lowest temperatures and densities used to compute the line intensity ratios. However, PDR models (see Sect. 6.4) predict higher temperatures and densities for the region in the PDR where most CH$^+$ forms.

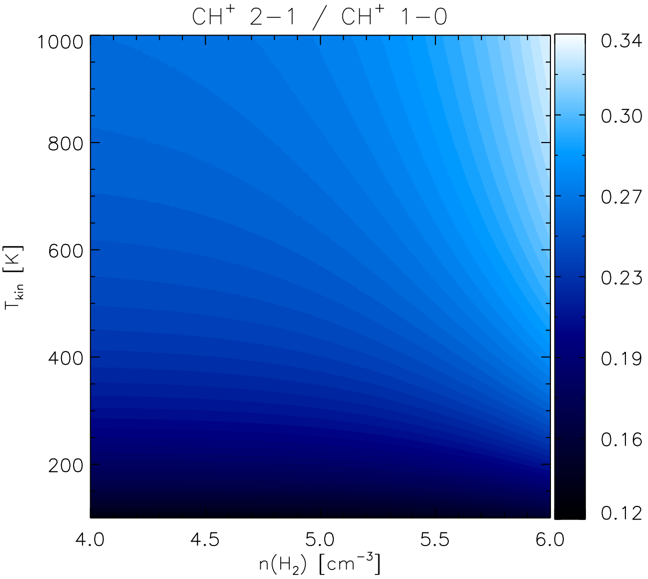

Figure 6.6 — Line intensity ratios of the CH$^+$ 2-1 to the CH$^+$ 1-0 transition calculated with RADEX for a grid of kinetic temperatures (100-1000 K) and a grid of H_2 volume densities (10^4-10^6 cm^{-3}). The upper limit on the observed CH$^+$ 2-1 to the CH$^+$ 1-0 line ratio is 0.09.

For CO$^+$, collision rates with H_2 are not available, therefore, we use the rates for HCO$^+$-H_2 as in previous works (e.g. Störzer et al. 1995 and Stäuber & Bruderer 2009). These rates were calculated for temperatures between 10 K and 400 K and rotational levels up to $J = 20$ (Flower 1999), and were extrapolated by Schöier et al. (2005) to include energy levels up to $J = 30$ and temperatures up to 2000 K. We used the same rate for each hyperfine transition. Despite the 49% higher dipole moment and a 24% smaller rotational constant of CO$^+$ compared to HCO$^+$, HCO$^+$-H_2 excitation rates are expected to match the CO$^+$-H_2 rates within a factor of 2-3 (e.g. Schöier et al. 2005). We include CO$^+$-H excitation using CO$^+$-H collision rates calculated by Andersson et al. (2008) corresponding to $T = 300$ K and assume H/H_2=1. The HCO$^+$-H_2 and CO$^+$-H excitation rates match within a factor of 2-3. We apply a formation temperature of 10 K, as suggested by Stäuber & Bruderer (2009) based on a comparison of radiative transfer models and CO^+ observations in several PDRs including the Orion Bar, where the CO^+ observations by Fuente et al. (2003) are consistent with a model using $n(H_2)\sim10^5$ cm^{-3}, $T_{\rm kin}\sim 600$ K and $T_{\rm form}\sim 10$ K. Calculating with a kinetic temperature of 500 K and $n(H_2)\sim10^5$ cm^{-3} the intensity of the observed transition can be reproduced with a column density of 8×10^{11} cm^{-2}. This is slightly below, but close to $N(CO^+)$=1-2.7$\times10^{12}$ cm^{-2} measured toward the Orion Bar (Störzer et al. 1995, Fuente et al. 2003).

To test the effect of the adopted formation temperature on the CO^+ column density, we consider formation temperatures closer to the upper level energy of the observed N=5−4 transition (85 K) and to the expected gas kinetic temperature in the region where CO^+ originates in. For the same kinetic temperature and H_2 volume density ($T_{\rm kin}\sim 500$ K, $n(H_2)\sim10^5$ cm^{-3}), adopting a formation temperature of 50 K, 100 K, and 500 K leads to CO^+ column densities of 4×10^{12} cm^{-2}, 5×10^{12} cm^{-2}, and 6×10^{12} cm^{-2} respectively.

As there are no excitation rates available for inelastic H_2-SH^+ collisions, we used scaled radiative rates to probe SH^+ excitation (J. Black, priv. comm.). Adopting the same parameters that provide a reasonable column density estimate for CH^+ and CO^+ ($T_{\rm kin}\sim 500$ K, $n(H_2)\sim10^5$ cm^{-3}) would imply an SH^+ column density $\sim 8\times10^{13}$ cm^{-2}. A gas component with parameters of $T_{\rm kin}\sim 160-220$ K, $n\sim10^{6-7}$ cm^{-3} was found to explain OH emission near the ionization front of the Orion Bar Goicoechea et al. 2011. The same parameters can also reproduce the SH^+ line intensities measured toward the CO^+ peak of the Orion Bar (Nagy et al. 2013, Chapter 4). Therefore, as a comparison, we apply the same parameters to calculate the SH^+ column density in Orion S. A kinetic temperature of 200 K and $n(H_2)$=10^6 cm^{-3} would imply an SH^+ column density of 8×10^{12} cm^{-2}.

The column densities derived in this section are summarized in Table 6.3.

6.3.3 Chemistry driven by vibrationally excited H_2

CH^+, SH^+, and CO^+ have similar formation pathways in UV-illuminated regions initiated by reactions with vibrationally excited H_2 (e.g. Sternberg & Dalgarno 1995). CH^+ and SH^+ form directly through endothermic reactions with vibrationally excited H_2, with high activation barriers:

$$C^+ + H_2^* \rightarrow CH^+ + H\ (-4640\ \mathrm{K}) \tag{6.1}$$

$$S^+ + H_2^* \rightarrow SH^+ + H\ (-9860\ \mathrm{K}), \tag{6.2}$$

while CO^+ forms directly from OH and C^+, where OH has an endothermic formation channel from O and H_2^*:

$$\begin{aligned} O + H_2^* &\rightarrow OH + H\ (-3150\ \mathrm{K}) \\ OH + C^+ &\rightarrow CO^+ + H \end{aligned} \tag{6.3}$$

OH formation via Eqn. 6.3 is the dominant formation route in regions with high FUV radiation fields such as Orion. Other OH formation routes include H_2O photodissociation and dissociative recombination of H_2O^+, H_3O^+, and HCO^+. We probe the formation and excitation of CH^+, SH^+, and CO^+ using version 1.4.4 of the Meudon code (Le Petit et al. 2006, Goicoechea & Le Bourlot 2007, Le Bourlot et al. 2012). This version includes the Langmuir Hinshelwood and Eley-Rideal mechanisms to describe the formation of H_2 on grain surfaces. We apply a radiation field of $1.5\times10^5\chi_0$, as was estimated by earlier studies (e.g. Herrmann et al. 1997) for the position of Orion S. We use isobaric models, where the pressure is kept constant, and the thermal balance is computed. Isobaric models represent the simplest equation of state for gas in steady state, stationary molecular clouds, where gravitation is negligible. A model with a pressure[5] of 10^8 K cm^{-3} provides a reasonable fit to the measured CH^+, SH^+, and [CII] line intensities. The predicted integrated intensities depends on the assumed inclination of the PDR at the Orion S position, which was a subject of a few previous studies including (Mesa-Delgado et al. 2011). Mesa-Delgado et al. (2011) derive a tilt angle of 48° ± 13° with respect to the line-of-sight, and find evidence for a significant spatial change in the orientation of the ionization front at the North-East of the Orion S region within their observed $16'' \times 16''$ field centered on $05^{\rm h}35^{\rm m}14.^{\rm s}5$ $-05°23'36.''0$ at a $1''$ spatial resolution. Thus, we expect the inclination to be in the range between 0° (face-on) and ∼50°. Figure 6.10 shows the variation of the modeled line intensities as a function of the inclination. The CH^+ line intensities predicted by the model do not change significantly for different inclinations only decreasing by about 10% between a face-on model and an inclination of 50°. Therefore, the CH^+ 1-0 and 2-1 line intensities do not constrain the inclination. The CII and SH^+ line intensities both increase by about a factor of 1.5 for i=50° compared to a face-on model. As the modeled face-on CH^+ 1-0 and CII line intensities are already close to the observed values for the used pressure and radiation field (Fig. 6.9), our results imply an inclined rather than a completely face-on model. For a pressure of 10^8 K cm^{-3} and a radiation field of $1.5\times10^5\chi_0$ our result is consistent with the inclination of 48° ± 13° with respect to the line-of-sight that was suggested by Mesa-Delgado et al. (2011).

A PDR model with an inclination of 45° reproduces the observed line intensities with an ∼80% accuracy for CH^+ 1-0 (under-estimation), within a factor of 4 for CH^+ 2-1 (over-estimation), within a factor of 3-4 for the observed SH^+ transitions, and with a ∼70% accuracy for the envelope component of CII. As no state-to-state formation rates are available for SH^+, unlike for CH^+ (Agúndez et al. 2010), the factor of 3-4 under-prediction of the SH^+ intensities may be within the uncertainties. The observed CH^+ 1-0/2-1 line intensity ratios are not well reproduced by this model which will be further addressed in Section 6.4. Models with the applied pressure and radiation field result in very similar

---

[5] Defined as $P = n_{\rm H} \times T$ (K cm^{-3}), with a proton density of $n_{\rm H}$=n(H)+2 × n(H_2)+n(H^+).

line intensities for a large range of cosmic ray ionization rates (2×10^{-15}-2×10^{-17} s^{-1} / H_2 molecule). Figure 6.7 shows the CH^+, SH^+, and CO^+ abundances calculated in the model. The abundances peak at high temperatures (400-1000 K) in a region corresponding to a visual extinction of $A_V \sim 1.5-3$. This region is located further into the PDR (at higher visual extinctions) compared to that in the Orion Bar, as the radiation field is about a factor of 10 higher. The $[SH^+]/[CH^+]$, $[CO^+]/[CH^+]$, and $[CO^+]/[SH^+]$ abundance ratios predicted by the model for depths equivalent to a visual extinction of $A_V \sim 1-4$ (including the region where the CH^+, SH^+, and CO^+ abundances peak) are shown in Fig. 6.8.

The column densities corresponding to the model for an inclination of 45° for C^+, CH^+, SH^+, and CO^+ are summarized in Table 6.3. The C^+ and CH^+ column densities are consistent within a factor of 2, and the CO^+ column density within a factor of 3.5 (for a formation temperature of 10 K). The larger difference in the CO^+ column densities may also be related to applying HCO^+-H_2 excitation rates as a proxy of the CO^+-H_2 excitation rates in the RADEX calculation. The more than a factor of 10 difference in the SH^+ column densities is dominated by the inaccuracy of the used state-to-state SH^+ formation in the Meudon code. The CO^+ column densities derived using the two different methods (RADEX and PDR models) suggest a formation temperature around 10 K. Such low formation temperatures have previously been found for CO^+ observations (Stäuber & Bruderer 2009 and references therein), such as for the Orion Bar, where the low formation temperatures together with the low observed excitation temperatures (~10 K, e.g. Fuente et al. 2003) have led to the conclusion that CO^+ in the Orion Bar was excited upon formation.

As the observed differences compared to the previously studied Orion Bar PDR may be due to different contributions of formation and destruction paths of the observed ions, we study the chemistry of CH^+, SH^+, and CO^+ at the depths where the abundances peak, including $A_V \sim 2$ (at $T\sim780$ K) and $A_V \sim 3$ (at $T\sim430$ K) (Table 6.4). The dominant formation channels of CH^+, SH^+, and CO^+ are initiated by reactions with vibrationally excited H_2 (Eqn. 6.1, 6.2, 6.3). An alternative formation route for CH^+ contributes about 11% of the CH^+ production at $A_V \sim 2$, but is not significant at $A_V \sim 3$:

$$CH_3^+ + h\nu \rightarrow H_2 + CH^+ \tag{6.4}$$

An alternative formation route for CO^+ compared to Eqn. 6.3 via CH^+ contributes about 24% of CO^+ production at $A_V \sim 2$ and ~6% at $A_V \sim 3$:

$$O + CH^+ \rightarrow H + CO^+ \tag{6.5}$$

The main destruction paths of CH^+, SH^+, and CO^+ and the corresponding rates (at $A_V \sim 2$ and 3) are summarized in Table 6.4 and are based on the 2006 version of the UMIST database (Woodall et al. 2007).

The most efficient destruction routes for CH^+ at a depth of $A_V \sim 2$ are via collisions with H (61.5% of CH^+ destructions) and H_2 (36.4%). A very small percentage of CH^+ (2.0%) is destroyed via collisions with electrons. At a depth equivalent to $A_V \sim 3$, where the molecular fraction is higher, H_2 becomes the dominant destruction partner for CH^+ (92.8%). H and electrons only destroy a small percentage of CH^+ at this depth (4.7 and 2.5%, respectively). Unlike for CH^+, SH^+ destruction via H_2 is negligible in this regime. SH^+ is mainly destroyed via reactions with H, electrons, and by FUV photons. At a depth equivalent to $A_V \sim 2$, H collisions dominate (∼74%), while electrons and photons destroy additional 20.2 and 5.7% of SH^+, respectively. Similar to CH^+, CO^+ is also destroyed via collisions with H, H_2, and electrons. However, CO^+ destruction via H_2 results in both HCO^+ and HOC^+ production. At a depth equivalent to $A_V \sim 2$, 55.8% of CO^+ is destroyed via collisions with H. Another 2×20.6% is equally destroyed by H_2 and forms HCO^+ and HOC^+. Electrons destroy another 2.9% of CO^+. At a depth equivalent to $A_V \sim 3$ reactions with H_2 dominate the destruction of CO^+ and forms HCO^+ (46.4%) and HOC^+ (46.4%). Another 3.8% and 3.5% are destroyed by H and electrons, respectively. Though HCO^+ is one of the end-products of CO^+ destruction in the outer layers of PDRs where the abundance of CO^+ and other reactive ions peak, this reaction does not affect the total HCO^+ column density much, as most HCO^+ forms in the inner parts of the PDR through other reactions.

Table 6.3 — Column densities based on RADEX (for CH^+, SH^+, and CO^+) and the Meudon code.

Species	Column density [cm^{-2}]		
	Non-LTE[a]		PDR model[b]
	$T_{\mathrm{kin}} = 500$ K $n(H_2)=10^5$ cm^{-3}	$T_{\mathrm{kin}} = 200$ K $n(H_2)=10^6$ cm^{-3}	
C^+	2×10^{18}		1.4×10^{18}
CH^+	5×10^{14}		3.4×10^{14}
SH^+	8×10^{13}	8×10^{12}	5.4×10^{12}
CO^+	8×10^{11}[c]		2.4×10^{11}

---

[a] See Sect 6.3.2

[b] For an inclination of 45°.

[c] Corresponding to a formation temperature of 10 K.

6.4 Discussion

We detected the CH^+ J=1-0, SH^+ $N_J = 1_2 - 0_1$, and CO^+ $N = 5-4$ transitions in emission toward the Orion S massive molecular condensation, possibly tracing

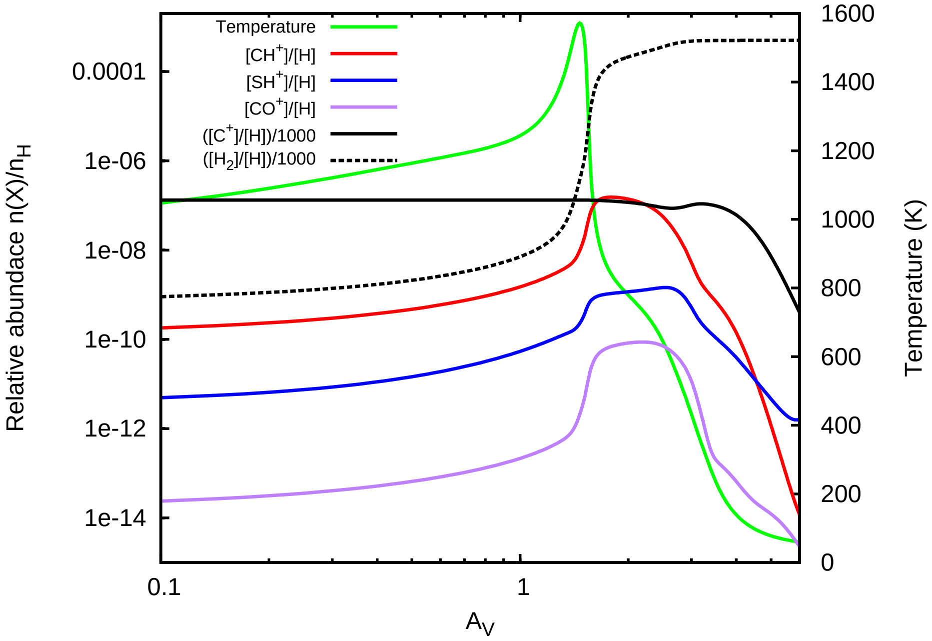

Figure 6.7 — Relative abundances of CH^+, SH^+, CO^+, [CII], and H_2 as a function of visual extinction (A_V) near the PDR surface corresponding to the $P = 10^8$ K cm^{-3} and $\chi = 1.5 \times 10^5 \chi_0$ PDR model.

the UV-irradiated surface of the cloud. A PDR-model with a radiation field of χ ~$1.5\times10^5\chi_0$ and a pressure of ~10^8 K cm^{-3} gives a reasonable fit to the [CII], CH^+, and SH^+ observed line intensities for an inclination of ~45°.

6.4.1 Comparison to the Orion Bar

Our observations of species that are expected to trace the UV-illuminated surface of Orion S show a number of similarities between the Orion Bar and Orion S regions and key differences that are expected to be related to differences between the physical properties of the two regions. One difference is that as the Orion S cloud is closer to the irradiation source θ^1 Ori C, the radiation field at that position ($1.5\times10^5\chi_0$, Herrmann et al. 1997) is about a factor of 10 higher compared to that toward the Orion Bar ionization front ($1-4\times10^4\chi_0$). Another key difference is the geometry of the two PDRs: while the Orion Bar is nearly edge-on with a suggested inclination in the range between 75° (Neufeld et al. 2006) and 87° (Hogerheijde et al. 1995, Jansen et al. 1995), the ionization front at the Orion S position is tilted with ~48° ± 13° with respect to the line-of-

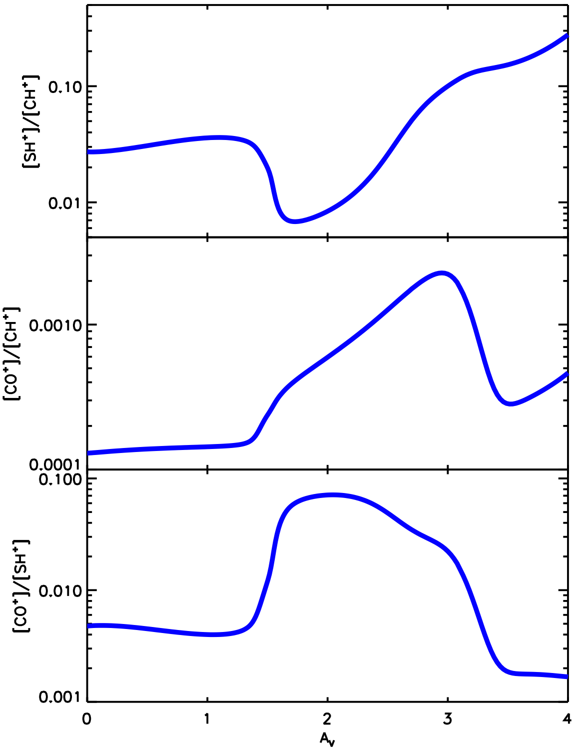

Figure 6.8 — The predicted abundance ratios (CH^+/SH^+, CO^+/CH^+, CO^+/SH^+) corresponding to the PDR model with $\chi = 1.5 \times 10^5 \chi_0$ and $P = 10^8$ cm^{-3} K in the range between A_V =1–4, including the region where CH^+, SH^+, and CO^+ abundances peak.

sight (Mesa-Delgado et al. 2011). This is consistent with our SH^+ and C^+ observations that suggest a tilted geometry with an inclination of ~45° rather than a face-on orientation.

One of the main observational differences between the two regions is the non-detection of CH^+ 2-1 toward Orion S despite the similar line intensity of the CH^+ 1-0 line to that observed toward the Orion Bar CO^+ peak position where CH^+ was detected up to its $J = 6 - 5$ transition. For the Orion Bar the observed line intensities can be well reproduced by a RADEX model with a density component of 10^5 cm^{-3} and similarly, by an isobaric PDR model with a pressure of 10^8 K cm^{-3} (Chapter 4). For Orion S the observed CH^+ line intensity ratio is poorly reproduced both by simple models with RADEX and by isobaric models with the Meudon code. Figure 6.11 shows the effect of changing the pressure on the CH^+ 2-1 to CH^+ 1-0 line intensity ratio as calculated in the

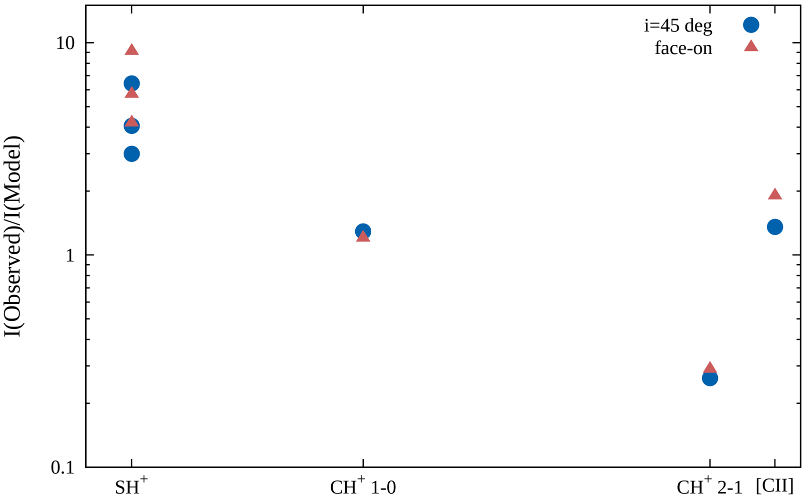

Figure 6.9 — Observed vs modeled line intensities of the detected CH$^+$, SH$^+$, and [CII] transitions corresponding to the PDR model with $\chi = 1.5 \times 10^5 \chi_0$ and $P = 10^8$ cm^{-3} K for a face-on geometry and an inclination of 45°.

Table 6.4 — The main destruction paths of CH$^+$, SH$^+$, and CO$^+$ and their rates at depths corresponding to $A_V \sim 2$ (at a gas temperature of ∼779 K and a total gas density of 1.3×10^5 cm^{-3}). and $A_V \sim 3$ (at a gas temperature of ∼432 K and a total gas density of 2.3×10^5 cm^{-3}). The total gas density is defined as the proton density in cm^{-3}: $n_H = n(H) + 2 \times n(H_2) + n(H^+)$.

Destruction path	Rate (cm^{-3} s^{-1}) $A_V = 2$	$A_V = 3$
$CH^+ + H \rightarrow H_2 + C^+$	1.3×10^{-6}	2.1×10^{-8}
$CH^+ + H_2 \rightarrow H + CH_2^+$	7.4×10^{-7}	4.2×10^{-7}
$CH^+ + e^- \rightarrow H + C$	4.1×10^{-8}	1.1×10^{-8}
$SH^+ + H \rightarrow H_2 + S^+$	1.5×10^{-9}	3.1×10^{-10}
$SH^+ + e^- \rightarrow H + S$	4.2×10^{-10}	1.5×10^{-9}
$SH^+ + h\nu \rightarrow H + S^+$	1.2×10^{-10}	2.6×10^{-11}
$CO^+ + H \rightarrow CO + H^+$	7.5×10^{-10}	4.7×10^{-11}
$CO^+ + H_2 \rightarrow H + HCO^+$	2.8×10^{-10}	5.8×10^{-10}
$CO^+ + H_2 \rightarrow H + HOC^+$	2.8×10^{-10}	5.8×10^{-10}
$CO^+ + e^- \rightarrow C + O$	3.9×10^{-11}	4.4×10^{-11}

Meudon code. Even though the CH$^+$ 2-1 to CH$^+$ 1-0 line intensity ratio is closer

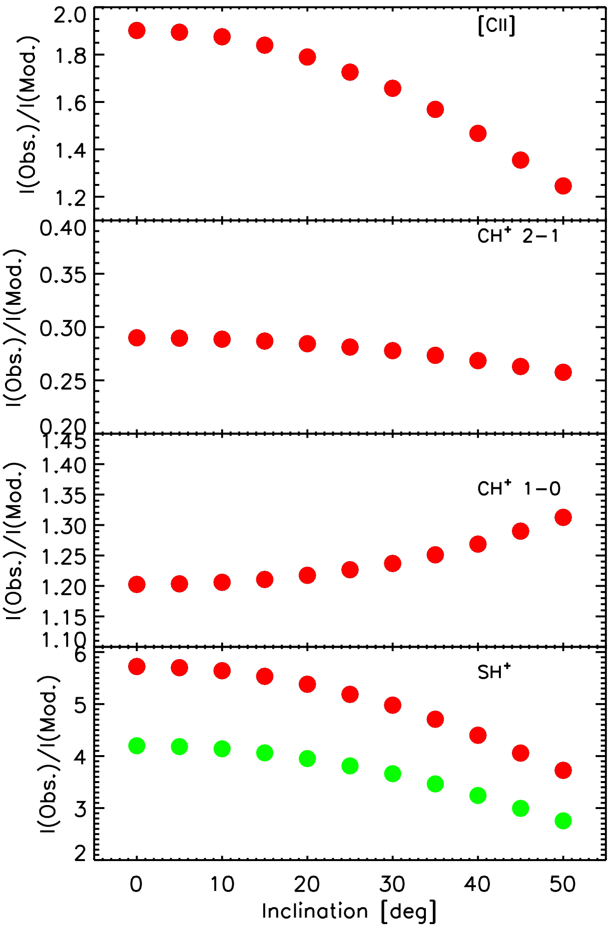

Figure 6.10 — Variations of the modeled line intensities (with respect to the observed values) as a function of the inclination. The CH^+, SH^+ $N_J = 1_2 - 0_1$ $F = 3/2 - 1/2$ (red) and $F = 5/2 - 3/2$ (green), and [CII] line intensities correspond to a PDR model with $\chi = 1.5 \times 10^5 \chi_0$ and $P = 10^8$ cm^{-3} K.

to the observed value for pressures below 10^8 K cm^{-3}, the absolute intensity of the CH^+ 1-0 line is by a factor of three under-predicted in the model with a pressure of $P = 5 \times 10^7$ cm^{-3} K. A more accurate excitation model that includes the effect of continuum radiation in the RADEX calculation will be created to address this question.

Another difference is the detection the strongest hyperfine transition of CO^+ $N = 5 - 4$ toward Orion S, while it is not detected toward the Orion Bar for

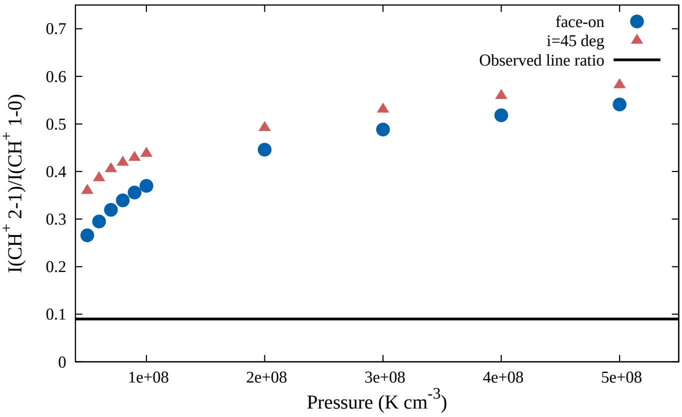

Figure 6.11 — The effect of changing the pressure on the CH^+ 2-1 to the CH^+ 1-0 line intensity ratio, as predicted by isobaric PDR models with a radiation field of $1.5{\times}10^5\chi_0$ and pressures in the range between $P = 5\times10^7$ cm^{-3} K and $P = 5\times10^8$ cm^{-3}.

a similar rms noise level. As the column densities predicted using the Meudon code are very similar for Orion Bar and Orion S conditions ($\sim$5.0$\times10^{11}$ cm^{-2} for an inclination of 75° and 2.4×10^{11} cm^{-2} for an inclination of 45°, respectively), this difference is likely a result of different excitation conditions between these regions. However, our information on CO^+ excitation is limited toward Orion S due to the lack of other, lower-N transitions. These transitions are accessible from the ground (e.g. with instruments including the IRAM 30-m and APEX telescopes) and will be measured as a part of a future investigation. Measuring the excitation temperature would also help to constrain the origin of CO^+. The low ($\sim$10 K) excitation temperatures measured for a number of sources (Stäuber & Bruderer 2009 and references therein) were interpreted by the fact that the excitation and destruction time-scales of CO^+ are similar, and therefore, its translational motions never become thermalized (e.g. Black 1998, and Chapter 4 for CH^+). Higher excitation temperatures are expected if CO^+ is formed via the ionization of CO^+ by energetic photons or particles (cosmic rays, such as discussed by Pellegrini et al. 2009), when the rotational excitation of CO^+ will be similar to that of CO.

6.4.2 Reactive ions as PDR chemistry diagnostics

In previous work on reactive ions in the Orion Bar (Nagy et al. 2013, Chapter 4) possible interpretations of the difference between the observed line widths of CH^+, SH^+, and CO^+ are discussed. The spectrally resolved CH^+ 2-1 and 1-0 lines in the Orion Bar are observed with widths of ∼5 km s^{-1}, while SH$^+$ and CO$^+$ (based on Störzer et al. 1995, Fuente et al. 2003, and Hogerheijde et al. 1995) have widths of ∼3 km s^{-1}. One possible explanation for this difference is an origin in a different gas component. Due to the known clumpiness of PDRs, different gas components contribute to the observed line emission. Several gas components have been proposed to explain line emission in the Orion Bar. Many molecular lines originate in an “interclump medium” with a mean gas density of $10^4 - 10^5$ cm^{-3} and gas kinetic temperature of ∼85 K (Hogerheijde et al. 1995) or in dense clumps with densities of $\sim 6 \times 10^6$ cm^{-3} and gas of temperatures $\lesssim$50 K (Lis & Schilke 2003). Goicoechea et al. (2011) found evidence for small unresolved clumps of warm ($T_{\rm kin} \sim 160 - 220$ K) and dense ($n_{\rm H} \sim 10^6 - 10^7$ cm^{-3}) gas near the ionization front of the Orion Bar. This component is also consistent with the observed SH$^+$ line emission in the Orion Bar. The Orion S region is more complicated than the prototypical Orion Bar PDR, as only part of the line emission observed toward this region corresponds to the UV-irradiated surface. However, it can be expected that several gas components may contribute to the line emission toward Orion S for the molecules that originate in the PDR surface.

Alternatively, as CH$^+$ and CO$^+$ are destroyed rapidly via reactions with H and H$_2$, they may never become thermalized, therefore their observed line width may be determined by their endothermic formation rather than the physical properties of the region they originate in. See Chapter 4 for more details. The line widths of SH$^+$ and CO$^+$ toward Orion S are similar to that in the Orion Bar and are ∼3 km s^{-1}. Though the width of the CH$^+$ 1-0 transition observed toward Orion S (∼4.4 km s^{-1}) is not as large as those detected toward the Orion Bar, it is still above that for CO$^+$ and SH$^+$. As the CH$^+$ line observed toward Orion S is also broader than the C$^+$ line (ΔV=3.7 km s^{-1}), the explanation related to an origin of the ions in different gas components is unlikely as C$^+$ and CH$^+$ are expected to trace the same gas component. The difference between the CH$^+$ line widths observed toward the Orion Bar and Orion S may be due to a higher CH$^+$ optical depth in the Orion Bar. To test the hypothesis that the CH$^+$ and CO$^+$ line widths are related to their chemistry and not to the physical conditions of the region they originate in more observations are needed. For example, spectrally resolved SH$^+$ and CO$^+$ maps toward the Orion Bar and Orion S can be obtained using single-dish ground based telescopes such as APEX. The SH$^+$ and CO$^+$ maps can be compared to a spectrally resolved HIFI map of the CH$^+$ 1-0 transition obtained toward a large region in Orion (Goicoechea et al., in prep.) covering both the Orion Bar and Orion S.

6.5 Summary and future plans

We detected several transitions of the CH^+, SH^+, and CO^+ reactive ions in emission toward the Orion S region using *Herschel*/HIFI at high spectral resolution. Our main results can be summarized in the following points:

- Our CH^+, SH^+, and C^+ observations are consistent with a PDR model using a radiation field of $\chi \sim 10^5 \chi_0$ and a pressure of $P = 10^8$ cm^{-3} K. A comparison of the observed line intensities to models with different inclinations suggest an inclination ∼45° rather than a completely face-on model. This is consistent with a previous study by Mesa-Delgado et al. (2011).
- The relative intensities of the CH^+ 1-0 and 2-1 (upper limit) transitions are underestimated by a factor of 4-5 by our PDR and radiative transfer models. To address this question, a more accurate excitation model with RADEX will be created that includes the effect of continuum radiation.
- The detection of CO^+ $N = 5 - 4$ for Orion S but not for the Orion Bar is more likely related to different excitation conditions than to differences in the formation and destruction processes of CO^+ due to the different physical conditions. To constrain the excitation, however, further CO^+ transitions need to be observed. Furthermore, models with the Cloudy program (Ferland et al. 2013) of the full molecular, atomic, and ionized gas will be used to constrain the role of possible ion sources.
- A comparison between results of a PDR model ($\chi \sim 10^5 \chi_0$, $P = 10^8$ cm^{-3} K) and a radiative transfer model with a correction for chemical formation and destruction of CO^+ in excited levels according to a given formation temperature suggests a low ($T \sim 10$ K) formation temperature. This is consistent with the results of Stäuber & Bruderer (2009).

In the future, ground-based observations (e.g. with APEX) of lower-N CO^+ observations will constrain its excitation in the PDR surface of Orion S. CO^+ and SH^+ data observed toward a larger sample of PDRs using ground-based telescopes and a spectrally resolved CH^+ map toward Orion (Goicoechea et al., in prep.) covering both the Orion Bar and Orion S will provide the missing information related to the line width difference seen for the CH^+, SH^+, and CO^+ ions.

Acknowledgements We thank John Black and Volker Ossenkopf for useful discussions. HIFI has been designed and built by a consortium of institutes and university departments from across Europe, Canada and the US under the leadership of SRON Netherlands Institute for Space Research, Groningen, The Netherlands with major contributions from Germany, France and the US.

Consortium members are: Canada: CSA, U.Waterloo; France: CESR, LAB, LERMA, IRAM; Germany: KOSMA,MPIfR,MPS; Ireland, NUIMaynooth; Italy: ASI, IFSI-INAF, Arcetri-INAF; Netherlands: SRON, TUD; Poland: CAMK, CBK; Spain: Observatorio Astronomico Nacional (IGN), Centro de Astrobiología (CSIC-INTA); Sweden: Chalmers University of Technology - MC2, RSS & GARD, Onsala Space Observatory, Swedish National Space Board, Stockholm University - Stockholm Observatory; Switzerland: ETH Zürich, FHNW; USA: Caltech, JPL, NHSC. HIPE is a joint development by the Herschel Science Ground Segment Consortium, consisting of ESA, the NASA Herschel Science Center, and the HIFI, PACS and SPIRE consortia.
This research used the facilities of the Canadian Astronomy Data Centre operated by the National Research Council of Canada with the support of the Canadian Space Agency.

7

Summary

The interstellar medium (ISM) is a key component of a galaxy as it is the place of birth of new generations of stars. The ISM itself is dependent on earlier generations of stars that influence its chemical composition and physical structure over the life-time of galaxies.

The formation of stars typically occurs in large, cold, massive, and dense (compared to the average density of the ISM) interstellar clouds that have average temperatures of $T = 10$ K, densities of $n = 200$ cm^{-3}, typical sizes of $D = 40$ pc[1], and masses of $M = 4 \times 10^5$ solar mass ($M_\odot$)[2]. The formation of stars is initiated by a gravitational collapse in the densest parts of interstellar clouds, where gravity overcomes the magnetic, turbulent, and thermal pressure of the interstellar medium. Once star-formation has started in a molecular cloud, temperatures and densities vary in a large range compared to the average properties quoted above due to the feedback effects (such as radiation and shocks) related to the young stars and protostars.

The earliest stages of star formation are related to dark clouds, that have no emission at optical wavelengths. Some of these clouds are also 'dark' at infrared wavelengths. Such infrared-dark clouds are often related to the formation of massive ($M \gtrsim 8\ M_\odot$) stars and clusters.

Once gravitationally unstable regions of molecular clouds start to collapse, the collapsing fragments ('clumps') go through various observable stages.

One of these observable stages is the 'hot core' phase. Collapsing clumps contain protostellar objects, which, due to their excess angular momentum, drive jets and outflows into the surrounding ISM. Due to heating by the protostars and their outflows, the clumps reach temperatures of a few times 100 K. At

---

[1] 1 pc$\sim$3.26 light years. For comparison, the distance to the nearest star outside of the Solar System (Proxima Centauri) is $\sim$1.3 pc.

[2] $M_\odot = 2 \times 10^{30}$ kg

these temperatures, complex organic molecules (such as methanol and ethanol) are evaporated off dust grains, resulting in a complex chemistry.

In the Hypercompact/Ultracompact (HC/UC) HII region phase, the most massive stars in the forming stellar cluster have started the fusion of hydrogen. Their radiation destroys complex molecules and ionizes the gas in a ∼0.01-0.1 pc region around the stars (HC/UC HII regions).

The newly formed stars, especially high-mass stars, influence their environment in different ways. The physical and chemical structure of molecular clouds is influenced by the heating of embedded newly formed stars. The impact of shocks results in the formation of some molecules and the destruction of others in regions close to protostars and young stellar objects. The Far Ultraviolet (FUV) radiation ($6\ \mathrm{eV} < h\nu < 13.6\ \mathrm{eV}$) of young massive stars creates different chemical layers as it penetrates into the surrounding molecular clouds. Photon-Dominated Regions or Photodissociation Regions (PDRs) are the regions around young massive stars where the mainly ionized medium changes into mainly molecular. Studying chemical reactions in this region is one of the subjects of the present thesis.

High-mass star forming regions near and far

This thesis focuses on two Galactic high-mass star forming regions.

The Orion region is one of the nearest high-mass star-forming regions ($d \sim 420$ pc). Part of this region is illuminated by the Trapezium cluster of four massive stars, including the most massive θ^1Ori C[3], which ionizes its surroundings and has created an HII region.

The prototypical Orion Bar PDR is located in this region. Its nearly edge-on geometry allows us to directly study the stratification (chemical layering) and therefore, it is often used as a template for other PDRs.

The FUV radiation field at the ionization front is $\sim 1-4\times10^4$ times above the average interstellar radiation field. The average gas temperature of the region is 85 K, while the average H_2 volume density is $\sim 10^5$ cm^{-3}. The classical description of the region has dense clumps detected in dense gas tracers such as HCN, with a volume density of $1.5-6\times10^6$ cm^{-3}, embedded in an interclump medium with a density of 10^4–2×10^5 cm^{-3}.

The Orion S (OMC1-S, S6) molecular condensation is another part of the Orion region that is illuminated by the Trapezium cluster, as it is located ∼0.1 pc southwest of the Trapezium stars. Part of the molecular line emission detected toward this region is related to hot cores and outflows embedded in the Orion S condensation. Due to the irradiation by the nearby Trapezium cluster,

---

[3] θ^1Ori C has a ∼43300 K temperature at its surface and is much hotter than our Sun with its $T \sim 5800$ K surface temperature.

the part of the Orion S region facing the Trapezium cluster has a PDR surface irradiated by an FUV radiation field of 1.5×10^5 above the average interstellar radiation field, that is about a factor of 10 higher than that of the Orion Bar.

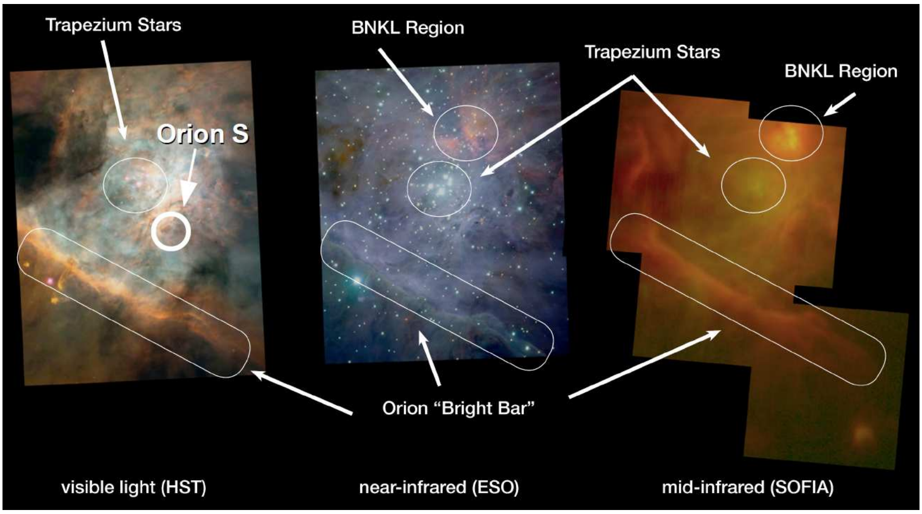

Figure 7.1 — The multiwavelength view of the Orion region around the Trapezium cluster. Credit: Visible-light image: NASA/ESA/HST/AURA/STScI/O'Dell & Wong; Near-IR image: ESO/McCaughrean et al.; Mid-IR image: NASA/DLR/SOFIA/USRA/DSI/FORCAST Team

The W49A region is located at a distance about 30× larger than the OMC-1 region ($d \sim 11.4$ kpc). Therefore, it requires interferometric observations to resolve individual objects such as hot cores and Ultracompact (UC) HII regions. With its luminosity[4] of $\sim 10^7$ solar luminosity ($L_\odot$)[5], equivalent to that of 100 massive stars similar to θ^1Ori C mentioned above, it is one of the best Galactic analogues of the starburst phenomenon seen in starburst galaxies[6]. Although its luminosity is orders of magnitude below that of external galaxies with a global starburst phenomenon, the W49A region is a template of starburst galaxies in terms of star-formation efficiency.

Many studies aimed at explaining the large amount of massive stars currently seen in W49A. The competing explanations include a large-scale inside-out gravitational collapse and a collision of two clouds, based on molecular

---

[4] The amount of electromagnetic energy a body radiates per unit of time.

[5] $L_\odot \sim 3.8 \times 10^{26}$ Watt

[6] A galaxy that undergoes an exceptionally high rate of star formation compared to that of most galaxies, such as the Milky Way. The starburst phenomenon in these galaxies is triggered by interactions or mergers with other galaxies.

line observations that typically show double-peaked line profiles with infall signatures.

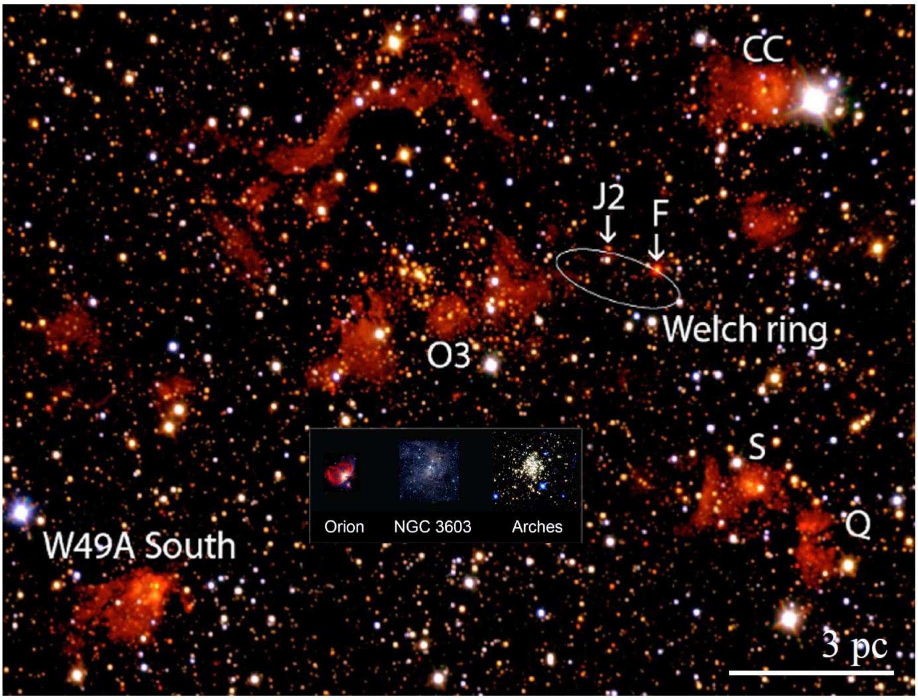

Figure 7.2 — A size comparison between the W49A region and other Galactic massive star-forming regions. The background is a JHK$_S$ composite image of W49A from Alves & Homeier (2003a). The labels show the known continuum sources (De Pree et al. 1997). The figure is based on Alves & Homeier (2003b).

Interpretation of molecular line observations

Information on the physical properties and chemistry of molecular clouds can be inferred from molecular line observations at sub-mm and infrared wavelengths.

Comparing these observations to radiative transfer models, abundances and column densities can be derived for the detected molecular species and physical parameters such as temperatures and densities of the emitting regions can be constrained.

In the simplest case, when the density of the medium is large enough that collisions determine the excitation, Local Thermodynamic Equilibrium (LTE) applies, with an excitation temperature equal to the kinetic temperature in the region. Column densities of observed molecular species can be derived in this approximation based on knowledge or assumption of the gas kinetic temperature.

At low densities, the contribution of radiative decay is comparable to that of collisional excitation, which leads to an excitation temperature below the kinetic temperature. Non-LTE models take collisional and radiative processes into account to calculate the level populations of molecules. In most non-LTE radiative transfer codes it is assumed that the formation and destruction of the molecules occurs on longer time-scales compared to their inelastic collisional excitation, and chemical processes are not taken into account while calculating column densities. In most cases this is a reasonable assumption, while for some species such as the reactive CH^+ and CO^+ ions, formation and destruction processes need to be considered for realistic column density estimates. This chemical pumping effect is taken into account in the chemical models in this thesis.

In the literature, chemical models are available for many different environments including shocks, turbulent dissipation regions, X-ray dominated regions, and PDRs. Part of this thesis (Chapters 4, 5, and 6) uses PDR models to interpret molecular line observations. For an assumed geometry and chemical network, PDR codes typically 1) calculate the structure of irradiated regions by solving the chemical balance to determine densities; 2) solve the energy balance to estimate the physical properties (temperatures, pressures, and level populations) at each position of the cloud; and 3) solve the radiative transfer to obtain a model spectrum of the cloud, to be compared with observations.

The simplest PDR models assume steady-state stationary clouds, where the chemical reactions have much shorter time-scales compared to the dynamical time scales or the time scales for significant change in the FUV flux. This is not the case for time-dependent and non-stationary PDR models where the chemical abundances and temperatures change as a function of time. Time-dependent effects become important when the radiation field or the density change on a time-scale shorter than the time-scale of the chemical reactions.

This thesis

This thesis analyses data from single-dish sub-mm and far-infrared line surveys toward two high-mass star-forming regions, the nearby Orion region and the luminous and distant W49A. These data allow us to study the radiative and mechanical feedback of young massive stars on their surrounding molecular material. In this thesis we have

- studied the physical and chemical structure of the Galactic starburst analogue W49A in key molecular line tracers to probe how it compares to starburst galaxies.

- studied the feedback effects of young massive stellar clusters and forming massive stars (hot cores, UC HII regions) on their environment.

- probed radiative feedback in a more nearby environment, the Orion region, using molecular ion lines that trace the warm surface of PDRs.

The physical and chemical structure of the Galactic starburst template W49A

To study the physical and chemical structure of the luminous high-mass star-forming region W49A, we have analysed a sub-mm line survey of the source (Chapters 2 and 3). The line survey was carried out using the James Clerk Maxwell Telescope (JCMT) Spectral Legacy Survey and covers the frequency range between 330-373 GHz, with a resolution of $\sim15''$ ($\sim$0.8 pc). As our line survey covers an extended field of view ($2' \times 2'$, equivalent to a physical size of 6.6×6.6 pc), it allows to trace the variations of physical properties in different parts of the region.

Toward the center of W49A, 260 lines were detected in the SLS survey range (**Chapter 2**), which correspond to 59 molecular species. Excitation conditions can be probed for 19 molecules, including the complex organic molecules CH_3CCH, CH_3CN, and CH_3OH. The detected species suggest the importance of shock-, PDR-, and hot core chemistry. Many molecular lines show a significant spatial extent across the maps including CO and its isotopes, high density tracers (e.g. HCN, HNC, CS, HCO^+) and tracers of UV-irradiation (e.g. CN and C_2H). Molecules that can be related to shock chemistry are confined to a $20'' \times 20''$ region around the center of the source.

The line intensity ratios of the H_2CO and HCN molecules trace physical conditions such as gas kinetic temperatures and densities. Several H_2CO and HCN transitions were covered by the SLS survey and have been detected over a large part of the observed region. Comparing the observed line intensity ratios to predictions of non-LTE radiative transfer models, our data revealed an extended region (about $1' \times 1'$, equivalent to $\sim$3×3 pc at the distance of W49A) of warm (>100 K) and dense (>10^5 cm^{-3}) molecular gas, with a mass of $2 \times 10^4 - 2 \times 10^5$ $M_\odot$ (by applying abundances derived for other regions of massive star-formation).

These temperatures and densities in W49A are comparable to those found in clouds near the center of the Milky Way and in starburst galaxies. The highly excited gas is likely to be heated via shocks from the winds of embedded O-type stars or alternatively due to UV irradiation, or possibly a combination of these two processes. Cosmic rays, X-ray irradiation, and gas-grain collisions are less likely to be the source of the gas heating in the case of W49A.

The chemistry of ions in the Orion PDR

Some reactive ions such as CH^+ and SH^+ have highly endothermic formation channels, which means that they require a large energy input for their formation. Several mechanisms have been proposed to overcome the high activation barriers, including shocks, turbulence, and reactions with vibrationally excited H_2. We have studied the chemistry and excitation of these ions toward the prototypical Orion Bar PDR (Chapter 4) and toward the FUV-illuminated surface of the Orion S dense molecular core (Chapter 6) based on data from Herschel/HIFI and PACS which we interpret by a comparison to non-LTE radiative transfer and PDR models.

We detected the rotational transitions from $J = 1-0$ to $6-5$ of CH^+ toward the Orion Bar using Herschel HIFI and PACS (**Chapter 4**). We also detected three hyperfine components of the SH^+ $1_2 - 0_1$ line. A comparison to PDR models for physical conditions that are expected for the Orion Bar confirms a formation via a reaction with vibrationally excited H_2 for CH^+. This is the most likely formation mechanism for SH^+ as well. The PDR models predict CH^+ and SH^+ formation close to the surface of the PDR at temperatures between 500 and 1000 K.

Toward the UV-illuminated surface of Orion S, only the 1–0 transition of CH^+ was detected (**Chapter 6**). Two hyperfine components of SH^+ $1_2 - 0_1$ were also detected. A key difference between the Orion Bar and Orion S regions is the non-detection of the CH^+ 2–1 transition in Orion S. Another difference is the detection of CO^+ $N = 5-4$ toward Orion S, but not toward the Bar, where lower$-N$ CO^+ transitions were previously detected. The observed line intensities are consistent with a PDR model illuminated by a radiation field derived by earlier studies toward the Orion S position ($\sim 10^5$ times the average interstellar radiation field) and a pressure of $\sim 10^8$ K cm^{-3}. The models also indicate that the previously not completely well constrained inclination of the PDR at the Orion S position is around 45° rather than face-on. The line intensities of the detected reactive ions (CH^+ $J = 1-0$, CO^+ $N = 5-4$, and SH^+ $1_2 - 0_1$) and the upper limit for CH^+ $J = 2-1$ suggest a lack of lower density gas ($\sim 10^5$ cm^{-3}) toward Orion S compared to the Orion Bar. This may also explain why OH^+ was not detected toward Orion S but only toward the Orion Bar (Chapter 5).

Other molecules that trace the warm surface of the Orion PDR include the reactive OH^+, H_2O^+, and H_3O^+ ions (collectively called H_nO^+). These ions are widespread in the interstellar medium, as shown by detections of their lines in Galactic diffuse clouds in absorption toward strong continuum sources. Their appearance in emission has so far only been reported for some active galactic nuclei.

In **Chapter 5** we showed the first example of a Galactic source of H_nO^+ line emission toward the Orion Bar. An additional HIFI map of a 0.2×0.1 pc region toward the Orion Bar shows that OH^+ line emission is extended over

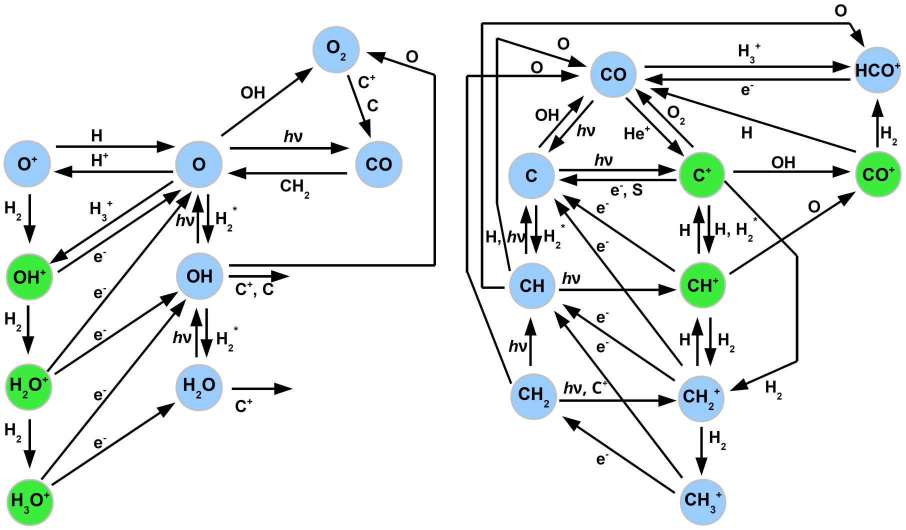

Figure 7.3 — The most important reactions involved in PDR chemistry of Oxygen-bearing (left) and Carbon-bearing (right) species. The ions shown with green colors are subjects of chapters 4, 5, and 6. Based on Figure 5 in Hollenbach & Tielens (1997).

a $\sim$0.1×0.1 pc region. While OH^+ is seen in emission and with a significant spatial extent, H_2O^+ and H_3O^+ are not detected in our line survey. Using the non-LTE radiative transfer code RADEX we derived an OH^+ column density of $\sim 1.5 \times 10^{14}$ cm^{-2}, that is similar to those toward other Galactic regions. PDR models suggest that the OH^+/H_2O^+ ratio of $\gtrsim 2$ is naturally explained by the high UV radiation field and electron density in the Orion region combined with the low molecular fraction in the region where these ions form. The appearance of the OH^+ lines in emission is the result of the high electron density, radiative pumping by dust, and chemical pumping (by reactive collisions) in the Orion Bar. Similar conditions may apply to extragalactic nuclei where OH^+, H_2O^+, and H_3O^+ lines are seen in emission.

Future perspectives

In this thesis, we have probed the physical and chemical structure of the Galactic starburst template W49A on a scale of $\sim$0.8 pc (Chapters 2 and 3). To fully resolve sub-structure (such as individual objects like UC HII regions and hot cores) and identify the origin of the detected molecular line emission, higher resolution observations are needed. One of the opportunities is given by the Atacama Large Millimeter/ submillimeter Array (ALMA), a radio telescope that consists of an ensemble of sixty-six 12- and 7-meter diameter antennas to achieve sub-arcsecond resolution in the frequency range between 84 and 950 GHz.

The other part of the thesis (Chapters 4, 5, and 6) focused on the chemistry of ions that trace the warm surface layers of PDRs. Open questions related to the chemistry of the ions discussed in this thesis can be addressed by single dish telescopes that provide a high spectral resolution. Such telescopes include the Atacama Pathfinder EXperiment (APEX), a 12-m telescope at mm and sub-mm wavelengths at a spatial resolution of $\sim$5-30$''$. Several transitions of ions are accessible with this telescope, including a number of SH^+, CO^+, and OH^+ lines. Using spectrally resolved maps of these ions a few open questions related to the chemistry of these species (chapters 4, 5, and 6) can be addressed.

Higher-resolution molecular line observations (such as with ALMA) will provide information on the small-scale structure of PDRs, including the Orion Bar. Such data may provide direct evidence of unresolved dense clumps that have been suggested to exist near the PDR surface, where the spectral lines discussed in Chapters 4 and 5 likely originate.

Another opportunity to probe the structure of star-forming regions including PDRs is given by the ongoing SOFIA (Stratospheric Observatory For Infrared Astronomy) mission. SOFIA is based on a Boeing 747SP wide-body aircraft modified to carry a 2.5-meter diameter telescope to altitudes of 12-14 km, above the main terrestrial water vapor layer. Its GREAT (German REceiver for Astronomy at Terahertz frequencies) spectrometer will provide high spectral resolution molecular line observations of key molecular line tracers including OH, OD, and SH.

8

Nederlandse samenvatting

Het interstellaire medium (ISM) is een belangrijk onderdeel van een sterrenstelsel omdat het de geboorteplaats van nieuwe generaties van sterren is. Het ISM zelf is afhankelijk van eerdere generaties van sterren die tijdens de levensloop van het sterrenstels de chemische samenstelling en fysische structuur van het ISM beïnvloeden.

Stervorming treedt meestal op in grote, koude, massieve en dichte (vergeleken met de gemiddelde dichtheid van het ISM) interstellaire wolken die een gemiddelde temperatuur van $T = 10$ K, dichtheid van $n = 200$ cm^{-3}, grootte van $D = 40$ pc [1], en massa van $M = 4 \times 10^5$ zonsmassa ($M_\odot$) [2] hebben. De vorming van sterren wordt ingeleid door een gravitationele ineenstorting van de dichtste delen van interstellaire wolken, waar de zwaartekracht de magnetische, turbulente, en thermische druk van het interstellaire medium overwint. Zodra de stervorming in een moleculaire wolk begonnen is, variëren de temperatuur en dichtheid in een breed bereik ten opzichte van de gemiddelde bovengenoemde eigenschappen, door de feedback effecten (zoals straling en schokken) van de jonge (proto-)sterren.

De vroegste stadia van stervorming zijn gerelateerd aan donkere wolken, die geen straling op optische golflengten uitzenden. Sommige van deze wolken zijn ook 'donker' op infrarode golflengten. Zulke 'infrarood-donkere' wolken zijn vaak gerelateerd aan de vorming van massieve ($M \gtrsim 8\ M_\odot$) sterren en clusters.

Als instabiele gebieden van moleculaire wolken beginnen in te storten door de zwaartekracht, gaan de instortende delen ('klonten') door verschillende waarneembare fasen.

---

[1] 1 pc$\sim$3.26 lichtjaar. Ter vergelijking, de afstand tot de dichtstbijzijnde ster buiten het zonnestelsel (Proxima Centauri) is $\sim$1.3 pc.

[2] $M_\odot = 2 \times 10^{30}$ kg

Een van deze waarneembare fasen is de 'hot core' ('hete kern') fase. Instortende klonten bevatten protostellaire objecten, die vanwege hun overtollige impulsmoment, straalstromen ('outflows') in het omringende ISM veroorzaken. Door de straling van de protosterren en hun outflows wordt het gas verhit tot honderden K. Bij deze temperaturen worden complexe organische moleculen (zoals methanol en ethanol) van stofdeeltjes afgedampt, waardoor een complexe chemie ontstaat.

In hyper- en ultra-compacte (HC/UC) HII gebieden hebben de meest massieve sterren in de vormende stellaire cluster de fusie van waterstof gestart. Hun straling vernietigt complexe moleculen en ioniseert het gas in een gebied van ~0.01-0.1 pc rond de sterren (HC/UC HII gebieden).

De nieuw gevormde sterren, met name hoge-massa sterren, beïnvloeden hun omgeving op verschillende manieren. De fysische en chemische structuur van moleculaire wolken wordt beïnvloed door de warmte van ingebedde nieuw gevormde sterren. De invloed van schokken resulteert in de vorming van sommige moleculen en de afbraak van andere in de gebieden dicht bij de protosterren en de jonge stellaire objecten. De ver-ultraviolette (FUV) straling ($6\ \text{eV} < h\nu < 13.6\ \text{eV}$) van jonge massieve sterren creëert verschillende chemische lagen zodra deze doorgedrongen is in de omringende moleculaire wolken. Foton-gedomineerde gebieden ofwel fotodissociatie-gebieden (PDRs) zijn gebieden rond jonge massieve sterren, waar het voornamelijk geïoniseerde medium in een voornamelijk moleculair medium verandert. Een van de onderwerpen van dit proefschrift is het bestuderen van chemische reacties in dit overgangsgebied.

Hoge-massa stervormingsgebieden nabij en ver weg

Dit proefschrift richt zich op twee Galactische hoge-massa stervormingsgebieden.

De Orion-nevel is een van de dichtstbijzijnde hoge-massa stervormingsgebieden ($d \sim 420$ pc). Een deel van dit gebied wordt verlicht door de Trapezium-cluster van vier massieve sterren, waaronder de meest massieve θ^1Ori C [3], die zijn omgeving ioniseert en een HII gebied heeft gecreëerd.

De prototypische Orion Bar PDR ligt in dit gebied. De bijna edge-on geometrie maakt het mogelijk de stratificatie (chemische gelaagdheid) direct te bestuderen en daarom wordt het vaak gebruikt als een blauwdruk voor andere PDRs.

Het FUV stralingsveld aan het ionisatiefront is $\sim 1-4 \times 10^4$ maal boven het gemiddelde interstellaire stralingsveld. De gemiddelde temperatuur van het gas in het gebied is 85 K, terwijl de gemiddelde H_2 volume dichtheid $\sim 10^5$ cm^{-3} is.

---

[3] θ^1 Ori C heeft een $\sim$ 43300 K temperatuur aan het oppervlak, veel heter dan onze zon met zijn $T \sim 5800$ K oppervlaktetemperatuur.

De klassieke beschrijving van het gebied bevat dichte klonten gezien in dichte gas tracers zoals HCN, met een volume dichtheid van $1.5-6\times10^6$ cm^{-3}, ingebed in een 'interclump medium' met een dichtheid van 10^4–2×10^5 cm^{-3}.

De Orion S (OMC1-S, S6) moleculaire condensatie is een ander deel van de Orion-nevel die door de Trapezium-cluster wordt verlicht, want het ligt ∼0.1 pc ten zuidwesten van de Trapezium-sterren. Een deel van de moleculaire lijnemissie gedetecteerd in de richting van dit gebied is gerelateerd aan hot cores en outflows die in de Orion S condensatie ingebed zijn. Door bestraling van de nabijgelegen Trapezium-cluster heeft het deel van de Orion-nevel aan de kant van de Trapezium-cluster een PDR-oppervlak dat door een FUV-stralingsveld van 1.5×10^5 boven het gemiddelde interstellaire stralingsveld bestraald wordt, dus ongeveer een factor 10 hoger dan bij de Orion Bar.

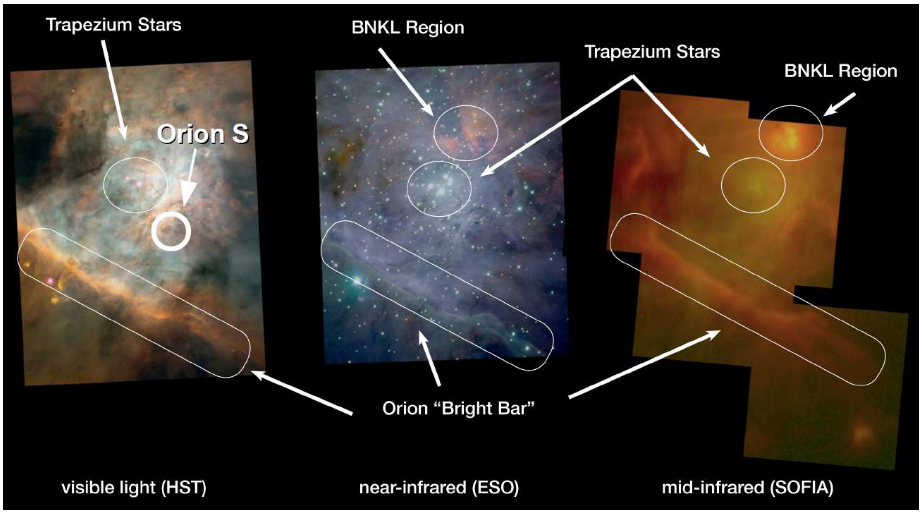

Figure 8.1 — De meerdere golflengten uitzicht van de Orion regio rond het Trapezium cluster. Krediet: Zichtbaar-licht afbeelding: NASA/ESA/HST/AURA/STScI/O'Dell & Wong; Near-IR afbeelding: ESO/McCaughrean et al.; Mid-IR afbeelding: NASA/DLR/SOFIA/USRA/DSI/FORCAST Team

Het gebied W49A ligt op een ongeveer 30× grotere afstand dan het OMC-1-gebied ($d\sim11.4$ kpc). Daarom moeten interferometrische waarnemingen gedaan worden om afzonderlijke objecten zoals hot cores en ultracompacte HII gebieden op te lossen. Met zijn lichtkracht[4] van $\sim10^7$ zonslichtkracht ($L_\odot$)[5], gelijkwaardig is aan die van de 100 massieve sterren vergelijkbaar met θ^1Ori C in Orion, is het een van de beste Galactische analogen van het 'starburst' fenomeen

---

[4] De hoeveelheid elektromagnetische energie die een object uitstraalt per tijdseenheid.

[5] $L_\odot\sim3.8\times10^{26}$ Watt

zoals gezien in sommige actieve sterrenstelsels [6]. Hoewel de lichtkracht ordes van grootte lager is dan die van externe sterrenstelsels met een globale starburst, is de regio W49A een blauwdruk van starburst-stelsels in termen van efficiëntie van stervorming.

Er zijn veel studies gericht op het verklaren van de grote hoeveelheid massieve sterren die op dit moment te zien is in W49A. De concurrerende verklaringen omvatten een grootschalige gravitationele ineenstorting van binnen naar buiten, en een botsing van twee wolken, gebaseerd op moleculaire lijnwaarnemingen die dubbel-gepiekte lijnprofielen met tekenen van instorting laten zien.

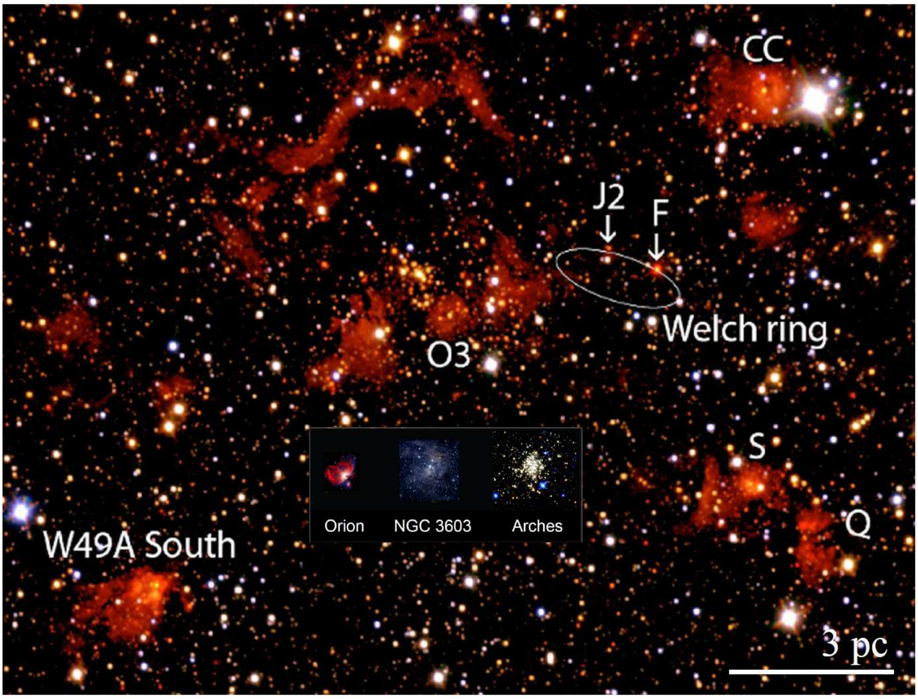

Figure 8.2 — Een grootte vergelijking tussen de regio W49A en andere Galacticsche massieve stervormingsgebieden. De achtergrond is een JHK$_S$ samengestelde afbeelding van W49A uit Alves & Homeier (2003a). De labels geven de bekende continum bronnen (De Pree et al. 1997). Het afbeelding is gebaseerd op Alves & Homeier (2003b).

---

[6] Een sterrenstelsel dat een uitzonderlijk hoge mate van stervorming ondergaat in vergelijking met de meeste sterrenstelsels, zoals de Melkweg. Het 'starburst' fenomeen in deze sterrenstelsels wordt veroorzaakt door interacties of fusies met andere sterrenstelsels.

De interpretatie van moleculaire lijnwaarnemingen

Informatie over de fysische eigenschappen en de chemie van moleculaire wolken kan worden afgeleid uit moleculaire lijnwaarnemingen op sub-mm en infrarode golflengten.

Door het vergelijken van deze waarnemingen met stralingstransportmodellen kunnen abondanties en kolomdichtheden worden afgeleid voor de gedetecteerde moleculaire species en kunnen fysische parameters zoals de temperatuur en de dichtheid van het gas worden bepaald.

In het eenvoudigste geval, wanneer de dichtheid van het medium groot genoeg is dat botsingen de excitatie bepalen, is Locaal Thermodynamisch Evenwicht (LTE) van toepassing, met een excitatie temperatuur die gelijk is aan de kinetische temperatuur in het gebied. Kolomdichtheden van waargenomen moleculaire species worden afgeleid, in deze benadering, gebaseerd op kennis of aanname van de kinetische gastemperatuur.

Bij lage dichtheden is de bijdrage van stralingsverval vergelijkbaar met die van botsingsexcitatie, hetgeen leidt tot een excitatie temperatuur die lager is dan de kinetische temperatuur. Non-LTE-modellen houden rekening met zowel botsings- als stralingsprocessen voor de bepaling van de moleculaire excitatie. In de meeste non-LTE stralingstransport codes wordt er aangenomen dat de vorming en afbraak van de moleculen gebeurt op langere tijdschalen vergeleken met hun inelastische botsingsexcitatie, en chemische processen worden niet in aanmerking genomen voor de berekening van kolomdichtheden. In de meeste gevallen is dit een redelijke aanname, maar soms, zoals bij de reactieve ionen CH^+ en CO^+ moeten vormings- en afbraakprocessen in aanmerking worden genomen voor realistische schattingen van hun kolomdichtheden. Met deze effecten wordt rekening gehouden in de chemische modellen in dit proefschrift.

Chemische modellen zijn beschikbaar in de literatuur voor vele verschillende omgevingen, waaronder schokken, turbulente dissipatie gebieden, gebieden met sterke Röntgenstraling, en PDRs. Een deel van dit proefschrift (hoofdstukken 4, 5, en 6) gebruikt PDR-modellen om moleculaire lijnwaarnemingen te interpreteren. Voor een aangenomen geometrie en chemisch netwerk berekenen PDR-codes 1) de structuur van bestraalde gebieden door het oplossen van de chemische balans om dichtheden te bepalen, 2) de fysische eigenschappen (temperatuur, druk en niveau populaties) door het oplossen van de energiebalans op elke positie van de wolk; en 3) het stralingstransport om een model-spectrum van de wolk te verkrijgen, dat kan worden vergeleken met waarnemingen.

De eenvoudigste PDR-modellen veronderstellen tijdsonafhankelijke stationaire wolken, waar de chemische reacties veel kortere tijdschalen hebben vergeleken met de dynamische tijdschalen en de termijnen voor significante verandering in de FUV flux. Dit is niet het geval voor tijdsafhankelijke en niet-stationaire PDR-modellen waarbij de chemische abondanties en temperaturen veranderen als functie van de tijd. Tijdsafhankelijke effecten worden belangrijk als het stralingsveld of de dichtheid op een tijdschaal korter dan de tijdschaal van de chemische reacties veranderen.

Dit proefschrift

Dit proefschrift analyseert de gegevens van single-dish sub-mm en ver-infrarode lijnsurveys in de richting van twee hoge-massa stervormingsgebieden, de nabijgelegen Orion nevel en het lichtsterke en verre gebied W49A. Deze gegevens stellen ons in staat om de stralings- en mechanische terugkoppeling van jonge massieve sterren op het omringende moleculaire materiaal te bestuderen. In dit proefschrift hebben we

- de fysische en chemische structuur van het Galactische starburst-analoog W49A bestudeerd in belangrijke moleculaire lijn-tracers om te zien hoe het zich verhoudt tot starburst-stelsels.
- de feedback effecten van jonge massieve sterclusters en zich vormende massieve sterren (hete kernen, UC HII gebieden) op hun omgeving bestudeerd.
- stralingsfeedback onderzocht in een meer nabije omgeving, de Orion nevel, met behulp van moleculaire ion-lijnen die het warme oppervlak van PDRs traceren.

De fysische en chemische structuur van het Galactische starburst-analoog W49A

Om de fysische en chemische structuur van het lichtsterke hoge-massa stervormingsgebied W49A te bestuderen hebben we een sub-mm lijn-survey van de bron geanalyseerd (Hoofdstukken 2 en 3). De lijn-survey werd uitgevoerd met behulp van de James Clerk Maxwell Telescoop (JCMT) Spectral Legacy Survey en bestrijkt het frequentiegebied van 330-373 GHz, met een resolutie van $\sim 15''(\sim 0.8$ pc). Daar onze lijn-survey een uitgebreid beeldveld heeft ($2' \times 2'$, gelijk aan een fysieke grootte van 6.6×6.6 pc), is het mogelijk om de variaties van de fysische eigenschappen in verschillende delen van het gebied te traceren.

In het midden van W49A werden 260 moleculaire lijnen gedetecteerd in de SLS survey range (**Hoofdstuk 2**). Deze 260 gedetecteerde lijnen komen overeen met 59 moleculaire species. Excitatie-condities kunnen worden bepaald voor 19 moleculen, waaronder de complexe organische moleculen CH_3CCH, CH_3CN en CH_3OH. De gedetecteerde moleculen soorten suggereren het belang van schok-, PDR- en 'hot core'-chemie. De emissie in vele moleculaire lijnen is ruimtelijk uitgebreid over de kaarten, waaronder CO en zijn isotopen, hoge dichtheid tracers (bijvoorbeeld HCN, HNC, CS, HCO^+) en tracers van UV-bestraling (bijv. CN en C_2H). Moleculen die kunnen worden gerelateerd aan schok-chemie zijn beperkt tot een klein ($20'' \times 20''$) gebied rond het midden van de bron.

De verhoudingen van de lijn-intensiteiten van de moleculen H_2CO en HCN traceren fysische condities, met name kinetische temperaturen en gasdichtheden. Verschillende H_2CO en HCN overgangen werden gedekt door de SLS survey en waren over een groot deel van het beeldveld gedetecteerd. Uit vergelijking van de waargenomen intensiteitsverhoudingen met voorspellingen van non-LTE stralingstransport modellen bleek het bestaan van een uitgebreid gebied (ongeveer $1' \times 1'$, ofwel $\sim$3×3 pc op de afstand van W49A) van warm ($>$ 100 K) en dicht ($>10^5$ cm^{-3}) moleculair gas, met een massa van $2 \times 10^4 - 2 \times 10^5$ $M_\odot$ (door toepassing van abondanties afgeleid voor andere gebieden van massieve stervorming).

Deze temperaturen en dichtheden in W49A zijn vergelijkbaar met die gevonden in wolken nabij het centrum van de Melkweg en in starburst-stelsels. Het hoge-excitatie gas wordt waarschijnlijk verwarmd door schokken van de winden van ingebedde O-type sterren of door UV-straling, of mogelijk door een combinatie van deze twee processen. Kosmische straling, röntgenstraling, en gas-stof botsingen zijn minder waarschijnlijk als bron van de gasverwarming in het geval van W49A.

De chemie van ionen in de Orion PDR

Sommige reactieve ionen zoals CH^+ en SH^+ hebben sterk endotherme vormingskanalen, wat betekent dat ze een grote energie-input voor hun vorming vereisen. Verschillende mechanismen zijn voorgesteld om de hoge activatiebarrières te overwinnen, waaronder schokken, turbulentie, en reacties met vibrationeel aangeslagen H_2. Wij hebben de chemie en de excitatie van deze ionen onderzocht in de richting van de prototypische Orion Bar PDR (Hoofdstuk 4) en in de richting van het FUV-verlichte oppervlak van de dichte moleculaire kern Orion S (Hoofdstuk 6), gebaseerd op gegevens van Herschel / HIFI en PACS die wij interpreteren door vergelijking met non-LTE stralingstransport en PDR-modellen.

We hebben de rotationele lijnovergangen van $J = 1 - 0$ tot $6 - 5$ van CH^+ gedetecteerd in de richting van de Orion Bar met Herschel HIFI en PACS (**Hoofdstuk 4**). We hebben ook drie hyperfijncomponenten gevonden van de $1_2 - 0_1$ overgang van SH^+. Een vergelijking met PDR modellen met parameters die representatief geacht kunnen worden voor de Orion Bar, bevestigen de vorming van CH^+ door middel van een reactie met vibrationeel aangeslagen H_2. Dit is ook het meest waarschijnlijke vormingssccenario voor SH^+. De PDR modellen voorspellen dat de vorming van CH^+ en SH^+ plaatsvindt in de oppervlaktelagen van de PDR bij temperaturen tussen 500 en 1000 K.

In de richting van het UV-verlichte oppervlak van Orion-S is alleen de 1–0 overgang van CH^+ gedetecteerd (**Hoofdstuk 6**). Twee hyperfijn componenten van de SH^+ $1_2 - 0_1$ lijn zijn ook gedetecteerd. Een belangrijk verschil tussen de Orion Bar en Orion-S is het niet detecteren van de CH^+ 2–1 lijn in de richting van Orion-S. Een ander verschil is de detectie van CO^+ $N = 5 - 4$ in de richting van Orion-S, maar niet in de richting van de Orion Bar, waar lager gelegen CO^+ lijnen wel gedetecteerd zijn. De gemeten lijnintensiteiten zijn consistent met een PDR-model aangedreven door een eerder afgeleid ultraviolet stralingsveld ($\sim 10^5$ zo sterk als het gemiddelde stralingsveld in onze Melkweg) en met een gasdruk van $\sim 10^8$ K cm^{-3}. De modellen laten ook zien dat de inclinatie van de PDR in Orion-S ongeveer 45° is in plaats van 0°.

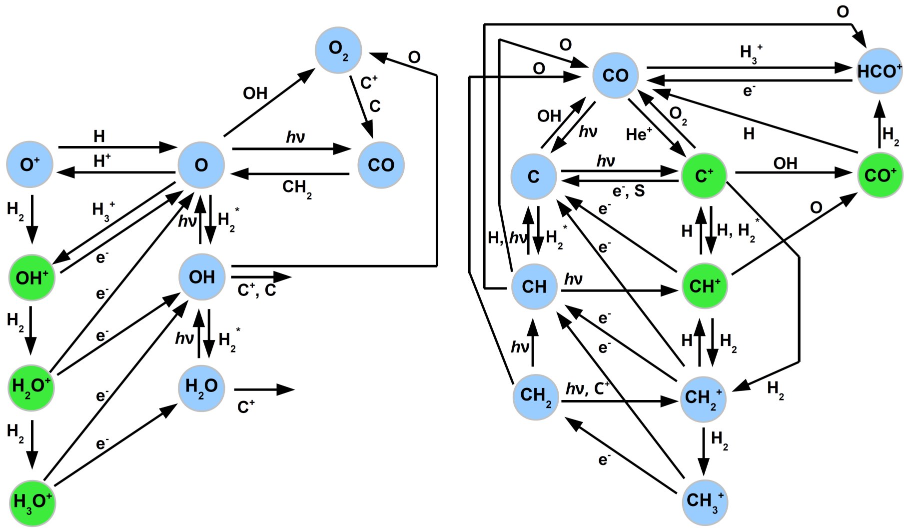

Figure 8.3 — Figuur 3 geeft een overzicht van de meest belangrijke reacties in de chemie van een PDR voor moleculen met zuurstof en koolstof. De ionen besproken in dit proefschrift (Hoofdstuk 4, 5 en 6) zijn angegeven met een groene kleur

Andere moleculen die zich bevinden in de warme oppervlaktelagen van de Orion PDR zijn de chemisch reactieve OH^+, H_2O^+ en H_3O^+ ionen (gezamenlijk aangeduid als H_nO^+). Deze ionen komen veel voor in interstellair gas, zoals blijkt uit detecties van hun lijnen in diffuse wolken in absorptie tegen sterke continuumbronnen in onze Melkweg. In emissie zijn ze tot nu toe alleen in kernen van actieve sterrenstelsels gezien.

Hoofdstuk 5 laat het eerste Galactische voorbeeld van H_nO^+ lijnemissie zien in de richting van de Orion Bar. Een andere HIFI waarneming, een kaart van 0.2 × 0.1 pc in dezelfde richting, laat zien dat de OH^+ lijnstraling uitgebreid is over een 0.1 × 0.1 pc gebied. Hoewel OH^+ te zien is in emissie en in een uitgestrekt gebied, detecteren we H_2O^+ en H_3O^+ niet in onze lijnscan. Gebruikmakend van de non-LTE stralingtransportcode RADEX leiden we een

OH^+ kolomdichtheid af van $\sim 1.5\times 10^{14}$ cm^{-2}, heel vergelijkbaar met waardes gevonden in de richting van andere bronnen in onze Melkweg. Modellering van de PDR laat zien dat de OH^+/H_2O^+ verhouding een natuurlijk gevolg is van het hoge ultraviolette stralingsveld en de elektrondichtheid in Orion, samen met de geringe hoeveelheid moleculen daar waar de ionen ontstaan. Dat de OH^+ lijnen in emissie zijn is het resultaat van een hoge elektrondichtheid, excitatie door de straling van het aanwezige stof en chemische excitatie van het ion door reactieve botsingen. Dit soort condities zijn waarschijnlijk ook te vinden in actieve kernen van melkwegstelsels waar OH^+, H_2O^+ en H_3O^+ ook in emisie gevonden zijn.

Plannen voor de toekomst

In dit proefschrift hebben we de fysische en chemische condities bepaald op een schaal van ∼0.8 pc voor W49A, een blauwdruk voor een "star-burst" in onze eigen Melkweg (Hoofdstukken 2 en 3). Om de substructuur te vinden (zoals de individuele ultracompacte Hii gebieden en "hot cores") en de oorsprong te vinden van de moleculaire lijnstraling zijn hogere resolutie waarnemingen nodig. Met de Atacama Large Millimeter Array (ALMA), een grote radio telescoop bestaand uit zesenzestig 12- en 7-meter antennes, wordt het mogelijk beeldscherptes beter dan een boogseconde te verkrijgen tussen 84 en 950 GHz.

Het tweede gedeelte van dit proefschrift (Hoofdstukken 4, 5 en 6) richt zich op de chemie van ionen in de warme oppervlaktelagen van PDRs. Veel vragen over de chemie in dit soort lagen kunnen worden aangepakt met single-dish telescopen met instrumenten met een hoge spectrale resolutie. Eén zo'n telescoop is de Atacama Pathfinder EXperiment (APEX), een 12-m telescoop voor mm en submm golflengtes met een beeldscherpte van ∼5-30″. Met deze telescoop kunnen we verschillende spectraallijnen van SH^+, CO^+ en OH^+ waarnemen. Door kaarten te maken in de spectraallijnen is het mogelijk vragen over de chemie van deze ionen te beantwoorden.

Hogere beeldscherpte in moleculaire spectraallijnen (zoals mogelijk met ALMA) zal ons meer leren over de kleine schaalstructuur van PDRs, zoals de Orion Bar. Dat soort data kan mogelijk direct bewijs leveren over het bestaan van dichte ophopingen van gas, waarvan men denkt dat ze bestaan vlakbij de rand van de PDR, de rand waar de lijnemissie besproken in Hoofdstukken 4 en 5 waarschijnlijk vandaan komt.

Een andere nieuwe mogelijkheid om de structuur van stervormingsgebieden en PDRs te bestuderen wordt geboden door de SOFIA (Stratospheric Observatory For Infrared Astronomy) missie. SOFIA is een Boeing 747SP, aangepast om een telescoop van 2,5 m diameter te herbergen, die waarnemingen doet op een kruishoogte van 12-14 km, boven de meeste waterdamp van onze atmosfeer. Het GREAT (German REceiver for Astronomy at Terahertz frequencies) instrument levert hoge spectrale resolutie waarnemingen van belangrijke moleculen zoals OH, OD en SH.

9

Magyar összefoglaló

A csillagközi anyag a galaxisok fontos alkotóeleme, hiszen új csillagok generációi keletkezésének helye. A már meglévő csillagok maguk is befolyásolják a csillagközi anyag szerkezetét és kémiai összetételét a galaxisok élete során. A csillagok nagy része óriás molekulafelhőkben keletkezik, amelyek hidegek, nagy tömegűek és sűrűek (a csillagközi anyag átlagos sűrűségéhez képest). Ezek a molekulafelhők átlagosan 10 K hőmérséklettel, $n = 200$ cm^{-3} sűrűséggel és $D = 40$ pc[1] mérettel rendelkeznek és $M = 4 \times 10^5$ naptömegnyi $(M_\odot)$[2] anyagot tartalmaznak. A csillagok keletkezése gravitációs kollapszussal kezdődik a csillagközi felhők legsűrűbb részein, amikor a gravitáció dominál a csillagközi anyag mágneses, turbulens, és termális nyomásával szemben. Miután a csillagkeletkezés beindult egy molekulafelhőben, a hőmérséklet és sűrűség lokálisan nagyságrendekkel eltér a fent említett átlagos értékektől, a keletkezett fiatal csillagok és protocsillagok hatására (pl. sugárzás és lökéshullámok).

A csillagkeletkezés legkorábbi fázisa sötét molekulafelhőkben zajlik. Ezek a felhők nem rendelkeznek optikai emisszióval. Egy részük infravörös hullámhosszakon is 'sötét'. A sötét molekulafelhők ezen utóbbi csoportját tartják számon mint a nagytömegű csillagok ($M \gtrsim 8\ M_\odot$) születési helyét.

Amint egy molekulafelhőben beindult a gravitaciós kollapszus, az összeomló felhőmagokat több fázison keresztül tanulmányozhatjuk. Az egyik ilyen fázis a 'hot core' állapot. Az összeomló felhőmagok ebben a fázisban protocsillagokat tartalmaznak. Ezek a protocsillagok a többlet impulzusmomentumuk következtében molekuláris kiáramlásokat produkálnak. A protocsillagok sugárzásának és kiáramlásainak hatására az összeomló felhőmagok hőmérséklete több 100 K-re emelkedik. Ezen a hőmérsékleten az előzőleg a csillagközi

---

[1] 1 pc$\sim$3,26 fényév. Összehasonlításként, a Naprendszerhez leközelebb eső csillag (Proxima Centauri) távolsága $\sim$1,3 pc.

[2] $M_\odot = 2 \times 10^{30}$ kg

por felszínere fagyott komplex szerves molekulák (pl. metanol vagy etanol) elpárolognak és ezáltal megváltoztatják a csillagközi gáz kémiai összetételét.

A Hiperkompakt/Ultrakompakt (HC/UC) HII régió fázisban a keletkezésben lévő csillaghalmaz legnagyobb tömegű csillagaiban beindult a hidrogén fúziója. Ezeknek a csillagoknak a sugárzása felbontja a komplex szerves molekulák kötéseit illetve ionizálja a gázt a csillagok körüli $\sim$0,01-0,1 pc területen (HC/UC HII régió).

Fiatal csillagok, különösen a nagytömegűek, többféle módon befolyásolják a környezetükben lévő csillagközi anyagot. A molekulafelhők szerkezetét és kémiai összetételét az újonnan keletkezett csillagok sugárzasa alakítja azok környezetében. A többek között a molekuláris kiáramlások által beindított lökéshullámok hatására kémiai reakciók indulnak be a csillagok környezetében. A nagytömegű csillagok távoli ultraibolya tartományban (6 eV $< h\nu <$ 13,6 eV) kibocsátott sugárzásának hatására különböző kémiai zónak alakulnak ki, ahogy a sugárzás behatol a környező molekulafelhőbe. Fotodisszociációs területek alakulnak ki a fiatal nagytömegű csillagokhoz közel. Ezek határterületek a főleg ionizált állapotban lévő gáz és a főleg molekuláris állapotban lévő gáz között. Ennek a dolgozatnak az egyik fő témája a kémiai reakciók tanulmányozása fotodisszociációs területeken.

Nagytömegű csillagkeletkezési régiók közel és távol

Ebben a dolgozatban két galaktikus nagytömegű csillagkeletkezési régió irányában mért adatokat elmzünk.

Az Orion csillagkeletkezési régió az egyik legközelebb eső nagytömegű csillagkeletkezési terület ($d \sim$ 420 pc). Ennek a csillagkeletkezési területnek egy része a Trapezium fiatal csillaghalmaz és annak θ^1Ori C komponense közelében található, amelynek sugárzása ionizálta a környezetében lévő gázt, HII régiót alkotva. Az Orion Bar fotodisszociácios terület is része az Orion csillagkeletkezési területnek. Kedvező elhelyezkedésének következtében az egyes kémiai régiók a fotodisszociációs terület felszínétől (ionizációs front) való távolság függvényében közvetlenül tanulmányozhatók. Ezáltal más fotodisszociációs területek értelmezéseben is fontos szerepet játszik. Az Orion Bar legkülsőbb rétegeire eső távoli ultraibolya sugarzási tér $\sim 1-4 \times 10^4$-szerese az átlagos csillagközi sugárzási térnek. A gáz átlagos hőmérséklete 85 K, a sűrűsége pedig $\sim 10^5$ H_2 molekula / cm^3.

Mérési adatok alapjan az Orion Bar régió klasszikus értelmezése egy 10^4–2×10^5 H_2 molekula / cm^3 sűrűségű gáz komponenst tartalmaz, amelyben helyenként sűrűsödések (1,5-6×10^6 H_2 molekula / cm^3) figyelhetők meg olyan molekulák vonalaiban, amelyek a legsűrűbb gáz eloszlását jelölik (pl. HCN).

Az Orion S molekulafelhő is az Orion csillagkeletkezési területnek a Trapezium halmazhoz közeli részén található, attól $\sim$0,1 pc távolságra. Az ennek a felhőnek az irányában detektált molekulavonalak egy része a felhőben lévő ’hot core' területekhez és protocsillagok kiáramlásaihoz kapcsolódik. A Trapezium halmaz közelsége miatt az Orion S régiónak a Trapezium irányába eső részén fotodisszociációs terület alakult ki, amire az Orion Barhoz képest 10-szer erősebb távoli ultraibolya sugárzási tér esik.

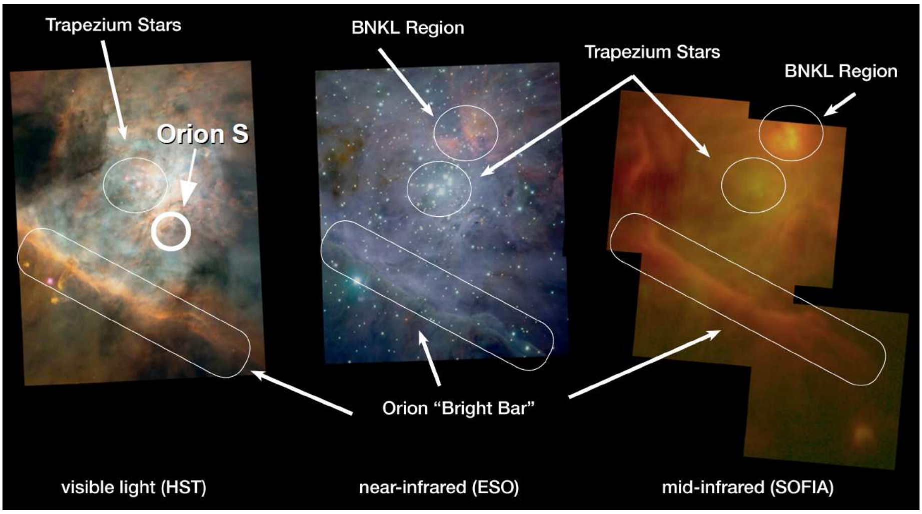

Figure 9.1 — Az Orion csillagkeletkezési régió Trapezium halmaz körüli területe optikai (forrás: NASA/ESA/HST/AURA/STScI/O'Dell & Wong), közeli infravörös (forrás: ESO/McCaughrean et al.), és közepes hullámhosszú infravörös (forrás: NASA/DLR/SOFIA/USRA/DSI/FORCAST Team) tartományban.

A W49A régió az Orion csillagkeletkezési régiónal harmincszor távolabb található ($d \sim 11,4$ kpc). Ennek következtében az egyedi objektumok, mint 'hot core' és UC HII régiók felbontásához interferometrikus mérésekre van szükség. Luminozitása[3] $\sim 10^7$-szerese a Napénak ($L_\odot$)[4]. Ez ekvivalens azzal a luminozitással, amit 100 nagytömegű, a fent említett θ^1Ori C csillaghoz hasonló objektum produkálna. Ennek következtében a W49A régiót a galaxisok egy részénél megfigyelhető 'starburst'[5] jelenség galaktikus analógiájaként tartják számon. (Mivel a W49A terület luminozitása nagyságrendekkel a starburst galaxisoké alatt marad, azokra inkább a csillagkeletkezés hatékonysága szempontjából hasonlít.) Egy sor cikkben elemezték a W49A területen nagy számban található nagytömegű csillag eredetét. Az elméletek egy része egy, a molekulafelhő nagy részére kiterjedő gravitációs kollapszust ír le. Egy másik

---

[3] Az egységnyi felületre eső elektromágneses energia amit egy objektum sugároz egységnyi idő alatt.

[4] $L_\odot \sim 3,8 \times 10^{26}$ W

[5] A 'starburst' galaxisok olyan galaxisok, amelyekben a normális galaxisokéhoz képest sokkal intenzívebb csillagkeletkezés mérhető. A magas csillagkeletkezési ráta ezekben a galaxisokban más galaxisokkal való kölcsönhatás következménye.

részük két külön molekulafelhő ütközésére épül. Az elméletek a mérésekből eredő kinematikai információkon alapulnak, amelyek egy része több molekula vonalában megfigyelhető jelenségből következik. Ez alapján a gáz a terület központi része felé áramlik.

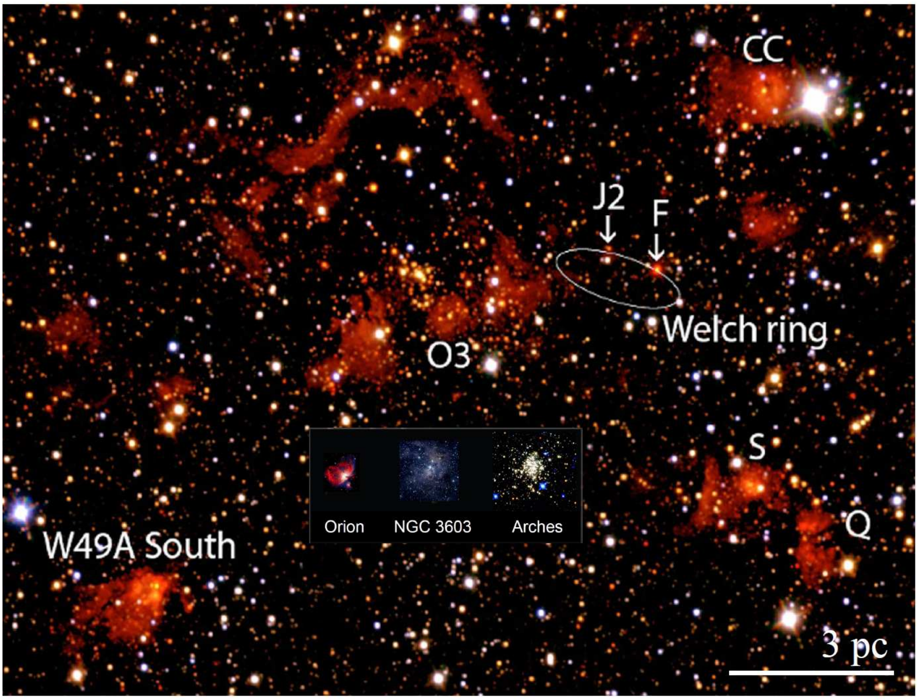

Figure 9.2 — A W49A csillagkeletkezési terület méretének más galaktikus csillagkeletkezési területekével való összehasonlítása. A háttérben a W49A terület egy kompozit JHK_S mérése látható. A feliratok az azonosított kontinuum forrásokat jelölik (De Pree et al. 1997). Az ábra az Alves & Homeier (2003b) cikkben található ábrán alapul.

Molekulavonal mérések értelmezése

Molekulák energia-átmeneteinek szubmilliméteres és infravörös hullámhosszakon mérhető vonalai alapján meghatározhatók a molekulafelhők fizikai paraméterei és kémiai összetétele. A méréseket radiatív transzfer modellek eredményeivel összehasonlítva meghatározható az egyes molekulák számsűrűsége/oszlopsűrűsége illetve a molekulafelhők fizikai paraméterei, pl. a gáz hőmérséklete és sűrűsége.

A legegyszerűbb esetben (lokális termodinamikai egyensúly, LTE) a gáz sűrűsége elég nagy ahhoz, hogy ütközések határozzák meg az egyes molekulák gerjesztését. Ebben az esetben a gerjesztési hőmérséklet a gáz kinetikus hőmérsekletével egyezik meg. Az egyes molekulák oszlopsűrűsége ebben az esetben a kinetikus hőmérséklet ismeretében vagy feltételezésével meghatározható.

Alacsonyabb gázsűrűség esetén az ütközéses gerjesztés mellett a sugárzás útján történő energiaveszteség is jelentős, így a molekulák gerjesztési hőmérséklete a gáz kinetikus hőmérséklete alatt marad. A lokális termodinamikai egyensúlyt nem feltételező (non-LTE) radiatív transzfer modellek mind ütközések, mind a sugárzási folyamatok hatását kombinálva határozzák meg az egyes molekulák energiaszintjeinek populáltságát. A legtöbb non-LTE radiatív transzfer kód esetén feltételezés, hogy a molekulák keletkezése és kémiai reakciója hosszabb időskálán történik, mint azok gerjesztése. Így a kémiai reakciókat nem kell számítasba venni az egyes molekulák oszlopsűrűségének meghatározásához. A legtöbb molekula esetében ez a feltételezés igaz. Reaktív ionok esetében (pl. CH^+ és CO^+) azonban az oszlopsűrűségek meghatározásához figyelembe kell venni a kémiai reakciókat is. Kémiai modellek ezt a hatást is figyelembe veszik.

Kémiai modellek több különböző objektum esetén léteznek, pl. olyan objektumok esetén, ahol lökéshullámok, a turbulencia disszipációja, röntgen- illetve ultraibolya sugárzás (fotodiszszociációs területek) határozzák meg a gáz fizikai paramétereit és kémiai összetételét.

Ennek a dolgozatnak egy része (4., 5. és 6. fejezet) fotodisszociációs területek kémiai modelljein alapul. Egy feltételezett geometria és kémiai összetétel esetén a fotodisszociációs régiókat leíró kódok általában 1) meghatározzák a forrás szerkezetét és a molekulák sűrűségét, kémiai egyensúlyt feltételezve; 2) energia-megmaradást feltételezve meghatározzák a fizikai paramétereket (pl. hőmérséklet, nyomás, molekulák energiaszintjeinek populáltsága) a molekulafelhők minden pontjában és 3) radiatív transzfer számítást végeznek. A legegyszerűbb fotodisszociációs terület modellek stacionárius, időben állandó területeket feltételeznek, ahol a kémiai reakciók hosszabb időskálán mennek végbe, mint amilyen időskálán a távoli ultraibolya sugárzás változik. Egyes fotodisszociációs régiókat leíró modellek térbeli és időbeli változásokat is figyelembe vesznek. Az időfüggő effektusok fontossá válnak, ha a sugárzási tér vagy a gáz sűrűsége rövidebb időskálán változik, mint a kémiai reakciók.

A dolgozat

Ebben a dolgozatban két, szubmilliméteres illetve távoli infravörös hullámhosszakon végzett spektroszkópiai felmérést elemzünk két különböző csillagkeletkezési terület, a közeli Orion régió és a távoli W49A régió irányában. Ezek az adatok információt adnak a fiatal csillagoknak sugárzás és mechanikai effektusok (pl. kiáramlások) útján a környezetükre kifejtett hatásáról. Ebben a dolgozatban

- a galaktikus starburst analóg W49A régió fizikai paramétereit és kémiai összetételét tanulmányozzuk molekulavonal-mérések alapján, és összehasonlítjuk starburst galaxisok adataival
- a fiatal csillaghalmazok és a csillagkeletkezési régiókban előforduló különböző fázisok (pl. hot core és UC HII régiók) környező molekulafelhőre kifejtett hatását vizsgáljuk
- a közeli Orion régióban tanulmányozzuk a sugárzásnak a kémiai összetételre kifejtett hatását, különösen az ionok kémiája esetében fotodisszociációs régiók felszínéhez közel.

A W49A csillagkeletkezési terület szerkezete

A W49A csillagkeletkezési régió fizikai paramétereinek és kémiai összetételének tanulmanyozására egy szubmilliméteres spektroszkópiai felmérést elemzünk (2. és 3. fejezet). A felmérés a James Clerk Maxwell teleszkóppal (JCMT) készült a 330–373 GHz frekvenciatartományban, $\sim$15$''$ ($\sim$0,8 pc) felbontással. Mivel a felmérés kiterjedt régiót fed le ($\sim$6,6$\times$6,6 pc), információt ad a fizikai paraméterek változasairól a mért területen. 260 vonalat detektáltunk a mért frekvenciatartományban a W49A régió központja irányában (2. fejezet). Ezek a vonalak 59 különböző molekulához tartoznak. Gerjesztési hőmérséklet és oszlopsűrűség meghatározása 19 molekula esetén lehetséges egyszerre több átmenet detektálása esetén, többek között a CH_3CCH, CH_3CN és CH_3OH komplex szerves molekulák esetén. A detektált molekulák alapján mind a lökéshullámok, a távoli ultraibolya sugárzás, és a 'hot core' régiók jelentősen befolyásolják a terület kémiai összetételét. Több molekula vonalát detektáltuk a mért terület jelentős részén, többek között a CO molekulát, nagy sűrűségű gázra utaló molekulákat (pl. HCN, HNC, CS, HCO^+), illetve ultraibolya sugárzás hatását jelölő molekulákat (pl. CN es C_2H). Lökéshullámok hatására keletkező molekulákat a terület központja körüli 20$''$ × 20$''$-es régióban detektáltunk.

A H_2CO és HCN molekulák különböző átmenetei intenzitásának aránya alapján fizikai paramétereket (pl. a gáz hőmérsékletét és sűrűségét) lehet meghatározni. Több H_2CO és HCN molekulavonalat detektáltuk a felmérésünk által lefedett terület jelentős részén. A mért vonalak intenzitásarányának non-LTE radiatív transzfer modellekkel történő összehasonlítása során egy kiterjedt régióban ($\sim$3$\times$3 pc) magas hőmérsékletű (>100 K) és sűrűségű ($>10^5$ cm^{-3}) gázkomponenst azonosítottunk, amelynek tömege $2 \times 10^4 - 2 \times 10^5$ $M_\odot$ (a molekulák számsűrűségére más csillagkeletkezési területek irányában meghatározott értékeket feltételezve). Ezek a hőmérsékletek és sűrűségek összemérhetők azokkal az értékekkel, amelyeket a galaxisunk középpontja irányában és starburst galaxisokban mértek. Ez a magas hőmérsékletű gáz valószínűleg fiatal csillagok csillagszeléhez vagy molekuláris kiáramlásaihoz kapcsolódó lökéshullámok vagy a csillagok ultraibolya sugárzásának eredménye, avagy e két hatás kombinációja. Kozmikus sugárzás, röntgensugárzás, illetve gáz- és porrészecskék kölcsönhatásából származó hűtés kevésbé valószínű, hogy hozzájárulnak ennek a magas hőmérsékletű gázkomponensnek a fűtéséhez.

Ionok kémiája az Orion fotodisszociációs területen

Egyes reaktív ionok, mint a CH^+ és SH^+ molekulák endoterm reakciók útján keletkeznek, ami azt jelenti, hogy jelentős energiára van szükségük a kialakulásukhoz. Több elmélet is vonatkozik ennek az energiának az eredetére. Ezek az elméletek lökéshullámokat, turbulenciát, illetve vibrációsan gerjesztett állapotban lévő H_2 molekulákkal való reakciót feltételeznek, mint a szükséges energia forrását. Ezeknek a molekuláknak a gerjesztését és kémiáját tanulmányoztuk az Orion Bar fotodisszociációs régió (4. fejezet) illetve az Orion S molekulafelhő felszínének (6. fejezet) esetében Herschel/HIFI és PACS mérések alapján. Ezeket az adatokat non-LTE radiatív transzfer illetve fotodisszociációs területek kémiai modelljeivel hasonlítottuk össze.

A CH^+ ion $J = 1-0, ..., 6-5$ forgási átmeneteit detektáltuk az Orion Bar régió irányában a Herschel HIFI és PACS mérések alapján (4. fejezet). Az SH^+ ion $1_2 - 0_1$ átmenetének mindhárom hiperfinom átmenetét detektáltuk. Fotodisszociációs terület kémiai modelljével összehasonlítva a méréseket igazoltuk, hogy a CH^+ ion vibrációsan gerjesztett H_2 molekulával történő reakció során keletkezik. Ez a legvalószínűbb keletkezési módja az SH^+ ionnak is az Orion Bar régió fizikai paramétereinek megfelelő környezetben. A modellben a CH^+ és SH^+ ionok nagy része a fotodisszociációs régió felszínéhez közel keletkezik, ahol a gáz hőmérséklete 500–1000 K között van.

Az Orion S molekulafelhő irányában a CH^+ ionnak egyedül a J=1–0 forgási átmenetét detektáltuk (6. fejezet). Az SH^+ $1_2 - 0_1$ átmenetének két hiperfinom komponensét is detektáltuk. Az egyik különbség az Orion Bar és Orion S régiók között, hogy a CH^+ 2–1 átmenetét nem detektáltuk az Orion S régió irányában. A másik különbség a CO^+ $N = 5-4$ átmenet detektálása az Orion S régió esetén az Orion Bar régióval ellentétben, ahol korábban egyéb CO^+ átmeneteket detektáltak. A mért vonalintenzitások egy $\sim 10^8$ K cm^{-3} nyomású[6] gázra és az átlagos csillagközi sugárzási tér feletti $\sim 10^5$-szeres sugárzási térre (korábbi mérésekkel összhangban) utalnak. Egy 45°-os inklinációjú modell adja a legpontosabb egyezést a mérésekkel. Az Orion Bar és Orion S régiók közötti különbségek leginkább azzal magyarázhatók, hogy kevesebb $\sim 10^5$ cm^{-3} sűrűségű gáz található az Orion S terület irányában az Orion Barhoz képest. Ez azzal is összhangban van, hogy az OH^+ iont, amit az Orion Bar irányában detektáltunk (5. fejezet), nem detektáltuk az Orion S régió irányában.

---

[6] Amit az $n_H = n(H) + 2n(H_2) + n(H^+)$ protonsűrűségnek és a gáz hőmérsékletének szorzataként definiálunk.

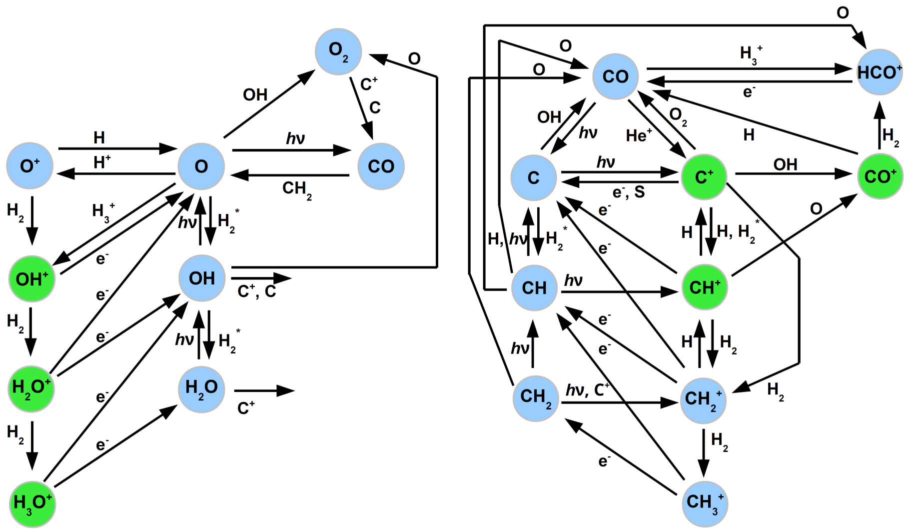

Figure 9.3 — A fotodisszociációs területek kémiájában résztvevő legfontosabb kémiai reakciók oxigént tartalmazó molekulák esetében (balra) illetve szént tartalmazó molekulák esetében (jobbra). A zöld színnel jelzett molekulákat elemezzük a 4., 5. és 6. fejezetben. Az ábra a Hollenbach & Tielens (1997) cikk 5. ábrája alapján készült.

Egyéb molekulák, amik fotodisszociációs területek magas hőmérsékletű felszínéhez kapcsolódnak, a reaktív OH^+, H_2O^+ és H_3O^+ ionok (együttesen H_nO^+ ionok). Ezeket az ionokat a csillagközi anyag számos területén detektálták. Vonalaikat abszorpcióban detektálták diffúz csillagközi felhőkben távoli csillagkeletkezési területek irányában. Vonalaik detektálása emiszszióban eddig egyedül aktív galaxisokban fordult elő. Az első galaktikus H_nO^+ detektálást elemezzük az 5. fejezetben, az Orion Bar irányában. A 0,2×0,1 pc-es régióról készült HIFI térkép ~0,1×0,1 pc-es területén detektáltunk OH^+ emissziót. Az OH^+ ionnal ellentétben a H_2O^+ és H_3O^+ ionokat nem detektáltuk. A RADEX non-LTE radiatív transzfer kód alapján $\sim 1{,}5 \times 10^{14}$ cm^{-2} OH^+ oszlopsűrűséget határoztunk meg. Hasonló értékeket mértek más galaktikus régiók irányában is. Fotodisszociációs régió modellekkel összehasonlítva a mért $OH^+/H_2O^+ \gtrsim 2$ arány a magas sugárzási tér és elektronsűrűség, illetve a fotodisszociációs terület felszínéhez (ahol a legtöbb H_nO^+ ion található) közeli gáz főleg atomos állapotának következménye. Az OH^+ vonalak emisszióban való megjelenése a magas elektronsűrűség, a csillagközi por által elnyelt és kibocsátott sugárzás, illetve a kémiai reakciók rövid időskálájának az OH^+ ion gerjesztésére kifejtett hatása eredménye. Hasonló fizikai paraméterek befolyásolhatják ezeknek az ionoknak a gerjesztését és kémiáját azokban az aktív galaxisokban, ahol emisszióban mérhetők.

A 9.3. ábra a fotodisszociációs területek kémiájában legfontosabb kémiai reakciókat foglalja össze oxigént illetve szént tartalmazó molekulák esetében. Az ebben a dolgozatban szereplő ionok zöld színnel vannak kiemelve.

Jövőbeli lehetőségek

Ebben a dolgozatban a galaktikus starburst analóg W49A csillagkeletkezési régió fizikai paramétereit és kémiai összetételét tanulmányoztuk ∼0,8 pc felbontással (2. es 3. fejezet). Önálló objektumok (pl. UC Hii zónák és 'hot core' régiók) felbontásához, illetve azoknak a spektroszkópiai felmérésünkben detektált molekulák intenzitásához való hozzájárulása tanulmányozásához ennél nagyobb felbontású mérésekre van szükség. Erre az egyik legjobb lehetőséget az Atacama Large Millimeter/ submillimeter Array (ALMA) rádióteleszkóp-hálózat jelenti, ami hatvanhat 12- illetve 7 méteres átmérőjű antennából áll. Ezek együttesen egy ívmásodperc alatti felbontást biztosítanak a 84–950 GHz frekvenciatartományban.

A dolgozat egy másik részében (4., 5. és 6. fejezet) olyan ionok kémiáját tanulmányoztuk, amik fotodisszociációs területek magas hőmérsékletű felszínéhez tartoznak. Az ehhez kapcsolódó megválaszolatlan kérdésekre a jövőben magas spektrális felbontást biztosító teleszkópok adhatnak választ. Ezek egyike az Atacama Pathfinder EXperiment (APEX), egy 12 méter átmérőjű mm-es és szubmilliméteres hullámhosszakon mérő távcső, amely ∼5–30″ szögfelbontást biztosít. Több ion vonalai esnek az APEX által elérhető hullámhossztartományba, többek között az SH^+, CO^+ és OH^+ vonalaké. Magas spektrális felbontással feltérképezve ezeknek az ionoknak a térbeli eloszlását, a 4., 5. és 6. fejezetekben tárgyalt megválaszolatlan kérdések egy részével kapcsolatban információt szerezhetünk.

Finomabb felbontású molekulavonal-mérések (pl. az ALMA teleszkóppal) a fotodisszociációs területek legkisebb skálájú szerkezetéről adnak majd információt, pl. az Orion Bar esetében. Ezek az adatok bizonyítékot szolgáltathatnak azokról az eddig fel nem bontott sűrűsödésekről, amiket az Orion Bar régió felszínéhez közel (többek között az ebben a dolgozatban a 4. és 5. fejezetben elemzett pozíció irányában) feltételeztek mérések és modellek összehasonlítása során.

Egy másik lehetőség csillagkeletkezési területek és fotodisszociációs régiók tanulmányozására a SOFIA (Stratospheric Observatory For Infrared Astronomy) teleszkóp. A 2,5 méter átmérőjű SOFIA teleszkópot egy Boeing 747SP repülőgép módosított változata szállítja 12–14 km magasságra, a földi atmoszféra vízpárát tartalmazó rétegei fölé. A SOFIA teleszkóp GREAT (German REceiver for Astronomy at Terahertz frequencies) spektrométere magas spektrális felbontású méréseket tesz lehetővé fontos molekulák (pl. OH, OD és SH) vonalaiban.

Bibliography

Abel, N.P., Brogan, C.L., Ferland, G.J. et al. 2004, ApJ, 609, 247

Abel, N.P., Ferland, G.J., O'Dell, C.R. et al. 2006, ApJ, 644, 344

Agúndez, M., Goicoechea, J. R., Cernicharo, J., Faure, A., & Roueff, E. 2010, ApJ, 713, 662

Aladro, R., Martín-Pintado, J., Martín, S., Mauersberger, R., & Bayet, E. 2011, A&A, 525, A89

Aladro R., Martín, S., Martín-Pintado, J. et al. 2011, A&A 535, A84

Aladro, R., Viti, S., Bayet, E. et al. 2013, A&A 549, A39

Allers, K. N., Jaffe, D. T., Lacy, J. H., Draine, B. T., & Richter, M. J. 2005, ApJ, 630, 368

Aloisi, A., Tosi, M. & Greggio, L. 1999, ApJ 118: 302-322

Alves, J. & Homeier, N. 2003, ApJ 589: L45-L49

Alves, J. & Homeier, N. 2003, Msngr 114, 35

Andersson, S., Barinovs, Ģ., & Nyman, G. 2008, ApJ, 678, 1042

Arab, H., Abergel, A., Habart, E., et al. 2012, A&A, 541, A19

Arce, H. G., Santiago-García, J., Jørgensen, J. K., Tafalla, M., & Bachiller, R. 2008, ApJ, 681, L21

Bachiller, R. & Pérez Gutiérrez, M. 1997, ApJ 487, L93

Bally, J., O'Dell, C. R., & McCaughrean, M. J. 2000, AJ, 119, 2919

Batrla, W. & Wilson, T. L. 2003, A&A, 408, 231

Bayet, E., Gerin, M., Phillips, T. G. & Contursi, A. 2004, A&A 427, 45

Benz, A. O., Bruderer, S., van Dishoeck, E. F., et al. 2010, A&A, 521, L35

Bergin, E. A.; Langer, W. D.; Goldsmith, P. F. 1995, ApJ 441, 222

Bergin, E. A., Phillips, T. G., Comito, C., et al. 2010, A&A, 521, L20

Bergin, E. A. & Tafalla, M. 2007, ARA&A, 45, 339

Beuther, H., Sridharan, T. K., Saito, M., 2005, ApJL 634, L185

Bik, A., Henning, T., Stolte, A., et al. 2012, ApJ, 744, 87

Black, J. H. 1983, in IAU Symposium, Vol. 103, Planetary Nebulae, ed. D. R. Flower, 91–100

Black, J. H. 1998, Faraday Discussions 109, 257

Black, J. H. & van Dishoeck, E. F. 1991, ApJ, 369, L9

Blagrave, K. P. M. & Martin, P. G. 2004, ApJ, 610, 813

Blake, G. A., Sandell, G., van Dishoeck, E. F., et al. 1995, ApJ, 441, 689

Bonnell, I. A., Larson, R. B., & Zinnecker, H. 2007, in Protostars and Planets V, ed. B. Reipurth, D. Jewitt, & K. Keil (Tucson: University of Arizona Press), p. 149

Bonnell, I. A., Bate, M. R. 2005, MNRAS 362, 915

Bonnell I. A., Bate M. R., & Vine, S. G. 2003, MNRAS 343, 413

Bonnell, I. A., Bate, M. R., Clarke, C. J., Pringle, J. E., 1997, MNRAS, 285, 201

Bonnell, I. A., Bate, M. R., Clarke, C. J., Pringle, J. E., 2001, MNRAS 323, 785

Bruderer, S., Benz, A. O., van Dishoeck, E. F., et al. 2010, A&A, 521, L44

Bradford, C. M., Nikola, T., Stacey, G. J., Bolatto, A. D., Jackson, J. M., Savage, M. L., Davidson, J. A., & Higdon, S. J. 2003, ApJ, 586, 891

Brogan, C. L. & Troland, T. H. 2001, ApJ 550, 799

Bruderer, S., Benz, A. O., Doty, S. D., Van Dishoeck E. F., & Bourke, T. L., 2009, ApJ, 700, 872

Bruderer, S., Benz, A. O., van Dishoeck, E. F., et al. 2010, A&A, 521, L44

Buckle, J. V., Hills, R. E., Smith, H., et al. 2009, MNRAS, 399, 1026

Buckley, H. D. & Ward-Thompson, D. 1996, MNRAS 281, 294

Cernicharo, J., Liu, X.-W., González-Alfonso, E. et al. 1997, ApJ, 483, 65

Chavarría, L., Herpin, F., Jacq, T. et al. 2010, A&A 521, L37

Chu, S.-I. & Dalgarno, A. 1974, Phys. Rev. A, 10, 788

Churchwell & Hollis 1983, ApJ 272, 591

Clark P. C. & Bonnell, I. A. 2005, MNRAS, 361, 2

Commerçon, B., Hennebelle, P., Henning, T., 2011, ApJ, 742L, 9

Corey, G. C. & McCourt, F. R. 1984, J. Chem. Phys., 81, 3892

Coutens, A.; Vastel, C.; Caux, E. et al. 2012, A&A 539, 132

Cravens, T. E. & Dalgarno, A. 1978, ApJ, 219, 750

Davies, M. B., Bate, M. R., Bonnell, I. A., Bailey, V. C., Tout, C. A., 2006, MNRAS 370, 2038 de Almeida, A. A. & Singh, P. D. 1981, A&A, 95, 383

Dedes, C., Röllig, M., Mookerjea, B., et al. 2010, A&A, 521, L24

De Graauw, T., Helmich, F. P., Phillips, T. G., et al. 2010, A&A, 518, L6

De Pree, C. G., Mehringer, D. M., & Goss, W. M. 1997, ApJ, 482, 307

De Pree, C. G., Wilner, D. J., Mercer, A. J., Davis, L. E., Goss, W. M., & Kurtz, S. 2004, ApJ, 600, 286

De Vicente, P. Martín-Pintado, J. & Wilson, T. L. 1997, A&A 320, 957

Douglas, A. E., & Herzberg, G. 1941, ApJ, 94, 381

Draine, B. T., 2011, Physics of the Interstellar and Intergalactic Medium (Princeton University Press)

Draine, B. T. 2003, ARA&A 41, 241

Draine, B. T. 1978, ApJS, 36, 595

Dubernet, M. L. et al 2012, submitted to A & A, 2012

Dumouchel, F., Faure, A., Lique, F. 2010, MNRAS 406, 2488

Falgarone, E., Godard, B., Cernicharo, J., et al. 2010a, A&A, 521, 15

Falgarone, E., Ossenkopf, V., Gerin, M., et al. 2010b, A&A, 518, 118

Faure, A. & Lique, F. 2012, MNRAS, 425, 740

Faure, A. & Tennyson, J. 2001, MNRAS, 325, 443

Federer, W., Villinger, H., Howorka, F., et al. 1984, Physical Review Letters, 52, 2084

Ferland, G. J., Porter, R. L., van Hoof, P. A. M., et al. 2013, Rev. Mexicana Astron. Astrofis., 49, 137

Ferrière K., Gillard, W. and Jean, P. 2007, A&A 467, 611

Flower, D. R. 1999, MNRAS, 305, 651

Flower, D. R., & Pineau des Forêts, G. 2003, MNRAS, 343, 390

Frerking, M. A.; Wilson, R. W.; Linke, R. A.; & Wannier, P. G. 1980, ApJ 240, 65

Fuente, A., Martín-Pintado, J., Cernicharo, J., & Bachiller, R. 1993, A&A, 276, 473

Fuente, A., Rodríguez-Franco, A., García-Burillo, S., Martín-Pintado, J., and Black, J. H. 2003, A&A 406, 899

Fuente, A., Rodríguez-Franco, A., & Martín-Pintado, J. 1996, A&A 312, 599

Genzel, R., Downes, D., Moran, J. M., et al. 1978, A&A, 66, 13

Gerin, M., Goicoechea, J. R., Pety, J., and Hily-Blant, P. 2009 A&A 494, 977

Gerin, M., de Luca, M., Black, J., et al. 2010, A&A, 518, L110

Gerlich, D., Disch, R., & Scherbarth, S. 1987, J. Chem. Phys., 87, 350

Gezari, D. Y., Backman, D. E., & Werner, M. W. 1998, ApJ, 509, 283

Ginard, D., González-García, M., Fuente, A., et al. 2012, A&A 543, 27

Glassgold, A. E., & Langer, W. D. 1973, ApJ, 179, L147

Godard, B., Falgarone, E., & Pineau des Forêets, G. 2009, A&A, 495, 847

Godard, B., Falgarone, E., Gerin, M., et al. 2012, A&A, 540, 87

Goicoechea, J. R., & Le Bourlot, J. 2007, A&A, 467, 1

Goicoechea, J. R., Joblin, C., Contursi, A., et al. 2011, A&A, 530, L16

Goicoechea, J. R., Pety, J., Gerin, M., 2006, A&A 456, 565

Goldsmith, P. F. & Langer, W. D. 1978, ApJ 222, 881

Goldsmith, P. F. & Langer, W. D. 1999, ApJ, 517, 209

González-Alfonso, E., Fischer, J., Bruderer, S., et al. 2013, A&A, 550, A25

Gonzalez Garcia, M., Le Bourlot, J., Le Petit, F. & Roueff, E. 2008, A&A 485, 127

Gorti, U. & Hollenbach, D. 2002, ApJ 573, 215

Graf, U. U., Simon, R., Stutzki, J. et al. 2012, A&A 542, L16

Green, S. 1991, ApJS, 76, 979

T. R. Greve, P. P. Papadopoulos, Y. Gao, and S. J. E. Radford 2009, ApJ 692, 1432

Griffin, M. J., Abergel, A., Abreu, A., et al. 2010, A&A, 518, L3

Gupta, H., Rimmer, P., Pearson, J. C., et al. 2010, A&A, 521, L47

Gusdorf, A., Cabrit, S., Flower, D. R., Pineau Des Forêts, G., 2008, A&A, 482, 809

Guzmán, V.; Pety, J.; Gratier, P. et al. 2012, A&A 543, 1

Gwinn, C. R., Moran, J. M., & Reid, M. J. 1992, ApJ, 393, 149

Habart, E., Dartois, E., Abergel, A., et al. 2010, A&A, 518, L116

Habing, H. J. 1996, A&AR, 7, 97

Helmich, F. P., & van Dishoeck, E. F., 1997, A&AS 124, 205

Hennebelle P. & Commerçon B., 2012, to appear in The Labyrinth of Star Formation, D. Stamatellos, S. Goodwin, and D. Ward-Thompson, eds., Springer, arXiv:1209.1786

Hennebelle, P., Commerçon, B., Joos,M., Klessen, R. S., Krumholz,M., Tan, J. C. & Teyssier, R. 2011, A&A, 528, A72

Hennebelle, P., & Falgarone, E. 2012, A&A Rev., 20, 55

Henney, W. J., O'Dell, C. R., Zapata, L. A., et al. 2007, AJ, 133, 2192

Herbst, E. & Van Dishoeck, E. F. 2009, Annu. Rev. Astron. Astrophys. 47, 427

Herrmann, F., Madden, S. C., Nikola, T. et al. 1997, ApJ 481, 343

Herzberg, G. & Lew, H. 1974, A&A, 31, 123

Hierl, P. M.,Morris, R. A., & Viggiano, A. A. 1997, J. Chem. Phys., 106, 10145

Hirota, T., Bushimata, T., Choi, Y. K., et al. 2007, PASJ, 59, 897

Hirota, T., Bushimata, T., Choi, Y. K., et al. 2008, PASJ, 60, 37

Hobbs, L. M., York, D. G., Snow, T. P., et al. 2008, ApJ, 680, 1256

Hogerheijde, M. R. & Van der Tak, F. F. S. 2000, A&A, 362, 697

Hogerheijde, M. R., Jansen, D. J., & van Dishoeck, E. F. 1995, A&A, 294, 792

Hollenbach, D., Kaufman, M. J., Neufeld, D., Wolfire, M., & Goicoechea, J. R. 2012, ApJ, 754, 105

Hollenbach, D.; Kaufman, M. J.; Bergin, E. A.; & Melnick, G. J. 2009, ApJ 690, 1497

Hollenbach, D. J. and Tielens, A. G. G. M. 1997, Annu. Rev. Astron. Astrophys. 35, 179

Homeier, N. & Alves, J. 2005, A&A 430, 481

Houde, M., Dowell, C. D., Hildebrand, R. H., et al. 2004, ApJ, 604, 717

Hüttemeister, S., Wilson, T. L., Bania, T. M. & Martín-Pintado, J. 1993, A&A 280, 255

Ikeda, M., Ohishi, M., Nummelin, A., Dickens, J. E., Bergman, P., Hjalmarson, Å., & Irvine, W. M. 2001, ApJ, 560, 792

Indriolo, N. & McCall, B. J. 2012, ApJ, 745, 91

Indriolo, N., Neufeld, D. A., Gerin, M., et al. 2012, ApJ, 758, 83

Jaffe, D. T., Harris, A. I., & Genzel, R. 1987, ApJ, 316, 231

Jansen, D. J., Spaans, M., Hogerheijde, M. R., & Van Dishoeck, E. F. 1995, A&A, 303, 541

Jeans, J. H., 1928, Astronomy and Cosmogony, p. 340. Cambridge, U.K.: Cambridge Univ. Press

Kalberla P. M. W., Burton W. B., Hartmann D., Arnal E. M., Bajaja E., Morras R., Pöppel W. G. L., 2005, A&A, 440, 775

Kamenetzky, J., Glenn, J., Rangwala, N., et al. 2012, ApJ, 753, 70

Kennicutt, Robert C. & Evans, Neal J., 2012, ARA&A 50, 531

Keto, E., 2007, ApJ 666, 976

Klessen, R. S., Spaans, M. & Jappsen, A.-K. 2007, MNRAS 374, L29

Krełowski, J., Beletsky, Y., & Galazutdinov, G. A. 2010, ApJ, 719, L20

Kritsuk, A. G., Norman, M. L., Padoan, P. 2006, ApJ, 638, L25

Krumholz, M., Klein, R., McKee, C. 2007, ApJ, 665, 478

Larsson, M., Geppert, W. D., & Nyman, G. 2012, Reports on Progress in Physics, 75, 066901

Latter,W. B., Walker, C. K., & Maloney, P. R. 1993, ApJ, 419, L97

Le Bourlot, J., Le Petit, F., Pinto, C., Roueff, E., & Roy, F. 2012, A&A, 541, A76

Le Petit, F., Nehmé, C., Le Bourlot, J., & Roueff, E. 2006, ApJS, 164, 506

Leurini, S., Rolffs, R., Thorwirth, S., et al. 2006, A&A, 454, L47

Lim, A. J.; Rabadán; I. & Tennyson, J. 1999, MNRAS 306, 473

Lindberg, J. E.; Aalto, S.; Costagliola F. et al. 2011, A&A 527, A150

Lis, D. C., Serabyn, E., Keene, J., et al. 1998, ApJ, 509, 299

Lis, D. C. & Schilke, P. 2003, ApJ, 597, L145

Loenen, A. F., Spaans, M., Baan, W. A. & Meijerink, R. 2008, A&A 488, 5

López-Sepulcre, A., Kama, M., Ceccarelli, C., et al. 2013, A&A, 549, A114

Lucas, R. & Liszt, H. S. 2000, A&A 355, 327

Mackey & Lim 2010, MNRAS 403, 714

Magnani, L. & Salzer, J. J. 1989, AJ, 98, 926

Magnani, L. & Salzer, J. J. 1991, AJ, 101, 1429

Mangum, J. G., Darling, J., Menten, K. M., & Henkel, C. 2008, ApJ, 673, 832

Mangum, J. G. & Wootten, A. 1993, ApJS, 89, 123

Mauersberger, R., Henkel, C., Weiß, A., Peck, A. B. & Hagiwara, Y. 2003, A&A 403, 561

McCauley, P. I., Mangum, J. G. & Wootten, A. 2011, ApJ 742, 58

McKee, C. F. & Ostriker, E. C., 2007. Annu. Rev. Astron. Astrophys. 45, 565

McMullin, J. P.; Mundy, L. G. & Blake, G. A. 1993, ApJ 405, 599

Meijerink, R. & Spaans, M. 2005, A&A 436, 397

Meijerink, R., Spaans, M., & Israel, F. P. 2006, ApJ, 650, L103

Meijerink, R., Spaans, M., & Israel, F. P. 2007, A&A, 461, 793

Melnick, G. J., Tolls, V., Goldsmith, P. F., et al. 2012, ApJ, 752, 26

Menten, K. M., Reid, M. J., Forbrich, J., & Brunthaler, A. 2007, A&A, 474, 515

Menten, K. M., Wyrowski, F., Belloche, A., et al. 2011, A&A, 525, A77+

Mesa-Delgado, A., Núñez-Díaz, M., Esteban, C., López-Martín, L., & García-Rojas, J. 2011, MNRAS, 417, 420

Mezger, P. G., Zylka, R., & Wink, J. E. 1990, A&A, 228, 95

Millar, T. J., & Herbst, E. 1990, A&A, 231, 466

Millar, T. J. & Hobbs, L. M. 1988, MNRAS, 231, 953

Milligan, D. B. & McEwan, M. J. 2000, Chemical Physics Letters, 319, 482

Mufson, S. L., & Liszt, H. S. 1977, ApJ, 212, 664

Mundy, L. G.; Evans, N. J., II; Snell, R. L.; Goldsmith, P. F.; Bally, J. 1986, ApJ, 306, 670

Mühle, S., Seaquist, E. R. & Henkel, C. 2007, ApJ 671, 1579

Müller, H. S. P., Schlöder, F., Stutzki, J., & Winnewisser, G. 2005, Journal of Molecular Structure, 742, 215

Müller, H. S. P. 2010, A&A 514, L6

Müller, H. S. P., Thorwirth, S., Roth, D. A., & Winnewisser, G. 2001, A&A, 370, L49

Nagy, Z., Van der Tak, F. F. S., Fuller, G. A., Spaans, M. & Plume, R. 2012, A&A 542, 6

Nagy, Z., Van der Tak, F. F. S., Ossenkopf, V., et al. 2013, A&A, 550, A96

Naylor, D. A., Dartois, E., Habart, E., et al. 2010, A&A, 518, L117

Naylor, B. J. et al. 2010, ApJ 722, 668

Neufeld, D. A., Lepp, S. & Melnick, G. J. 1995, ApJS 100, 132

Neufeld, D. A., Schilke, P., Menten, K. M., et al. 2006, A&A, 454, L37

Neufeld, D. A., Goicoechea, J. R., Sonnentrucker, P., et al. 2010, A&A, 521, L10

Nisini, B., Codella, C., Giannini, T. et al. 2007, A&A 462, 163

O'Dell, C. R., Hartigan, P., Lane, W. M., et al. 1997, AJ, 114, 730

O'Dell, C. R., & Henney, W. J. 2008, AJ, 136, 1566

O'Dell, C. R., Henney, W. J., Abel, N. P., Ferland, G. J., & Arthur, S. J. 2009, AJ, 137, 367

Ossenkopf, V., Müller, H. S. P., Lis, D. C., et al. 2010, A&A, 518, L111

Ossenkopf, V., Röllig, M., Neufeld, D. A., et al. 2013, A&A, 550, A57

Ott, S. 2010, in Astronomical Society of the Pacific Conference Series, Vol. 434, Astronomical Data Analysis Software and Systems XIX, ed. Y. Mizumoto, K.-I. Morita, & M. Ohishi, 139

Ott, J., Weiß, A., Henkel, C. & Walter, F. 2005, ApJ 629, 767

Palla, F. & Stahler, S.W. 1993, ApJ, 418, 414

Papadopoulos, P., Van der Werf, P., Xilouris, E. M., Isaak, K. G., Gao, Y. & Mühle, S. 2011, submitted

Pascucci, I., Wolf, S., Steinacker, J., et al. 2004, A&A, 417, 793

Pellegrini, E. W., Baldwin, J. A., Ferland, G. J. et al. 2009, ApJ 693, 285

Peng, T.,Wyrowski, F., van der Tak, F. F. S., Menten, K. M., & Walmsley, C. M. 2010, A&A, 520, A84

Persson, C. M., Olofsson, A. O. H., Koning, N., et al. 2007, A&A, 476, 807

Phillips, T. G., van Dishoeck, E. F., & Keene, J. 1992, ApJ, 399, 533

Pickett, H. M., Poynter, R. L., Cohen, E. A., et al. 1998, J. Quant. Spec. Radiat. Transf., 60, 883

Pilbratt, G. L., Riedinger, J. R., Passvogel, T., et al. 2010, A&A, 518, L1

Pineau des Forêts G., Flower, D. R., Hartquist, T. W., & Dalgarno, A. 1986, MNRAS, 220, 801

Plume, R., Fuller, G. A., Helmich, F., et al. 2007, PASP, 119, 102

Plume, R., Jaffe, D. T., Evans, N. J., II, Martin-Pintado, J., & Gomez-Gonzalez, J. 1997, ApJ, 476, 730

Poglitsch, A., Waelkens, C., Geis, N., et al. 2010, A&A, 518, L2

Rangwala, N., Maloney, P. R., Glenn, J., et al. 2011, ApJ, 743, 94

Reach, W.T. & Boulanger, F., 1998, Lecture Notes in Physics Berlin Springer Verlag, 506, 353

Rigopoulou, D., Kunze, D., Lutz, D., Genzel, R. & Moorwood, A. F. M. 2002, A&A 389, 374

Rizzo, J. R., Fuente, A., & García-Burillo, S. 2005, ApJ, 634, 1133

Rizzo, J. R., Fuente, A., Rodríguez-Franco, A., & García-Burillo, S., 2003, ApJ, 597, 153

Roberts, H., & Millar, T. J. 2007, A&A, 471, 849

Roberts, H., Van der Tak, F. F. S., Fuller, G. A., Plume, R., & Bayet, E. 2011, A&A, 525, 107

Rodríguez-Fernández N. J. , Tafalla, M., Gueth, F. and Bachiller, R. 2010, A&A 516, A98

Rodriguez-Franco, A., Martin-Pintado, J., & Fuente, A. 1998, A&A, 329, 1097

Rodríguez-Franco, A., Wilson, T. L., Martín-Pintado, J., & Fuente, A. 2001, ApJ, 559, 985

Roelfsema, P. R., Helmich, F. P., Teyssier, D., et al. 2012, A&A, 537, A17

Röllig, M., Ossenkopf, V., Jeyakumar, S., Stutzki, J., & Sternberg, A. 2006, A&A, 451, 917

Röllig, M. et al. 2007, A&A 467, 187

Scalo, J. M., & Slavsky, D. B. 1980, ApJ, 239, L73

Schilke, P., Pineau des Forets, G., Walmsley, C. M., & Martín-Pintado, J. 2001, A&A, 372, 291

Schilke, P., Walmsley, C. M., Pineau des Forets, G., & Flower, D. R., 1997, A&A, 321, 293

Schöier, F.L., van der Tak, F.F.S., van Dishoeck E.F., Black, J.H. 2005, A&A 432, 369

Scoville, N. Z., Sargent, A. I., Sanders, D. B., et al. 1986, ApJ, 303, 416

Simon, R., Stutzki, J., Sternberg, A., & Winnewisser, G. 1997, A&A, 327, 9

Serabyn, E., Guesten, R., & Schulz, A. 1993, ApJ, 413, 571

Shu, F. H., Adams F. C., Lizano S. 1987, Annu. Rev. Astron. Astrophys. 25, 23

Sievers, A. W., Mezger, P. G., Bordeon, M. A., Kreysa, E., Haslam, C. G. T., Lemke, R. 1991, A&A 251, 231

Schmid-Burgk, J., Muders, D., Müller, H. S. P., & Brupbacher-Gatehouse, B. 2004, A&A, 419, 949

Sharpee, B. D., Slanger, T. G., Huestis, D. L., & Cosby, P. C. 2004, ApJ, 606, 605

Smith, N.; Whitney, B. A.; Conti, P. S.; De Pree, C. G. & Jackson, J. M. 2009, MNRAS 399, 952

Snell, R. L., Goldsmith, P. F., Erickson, N. R., Mundy, L. G., & Evans, N. J., II. 1984, ApJ, 276, 625

Snow, T. P., & McCall, B. J. 2006, ARA&A, 44, 367

Solomon, P. M. & Vanden Bout, P. A. 2005, Annu. Rev. Astron. Astrophys. 43, 677

Spinoglio, L., Pereira-Santaella, M., Busquet, G., et al. 2012, ApJ, 758, 108

Stacey G. J.; Jaffe, D. T.; Geis, N. et al. 1993, ApJ 404, 219

Stäuber, P., Benz, A. O., Jørgensen, J. K. et al. 2007, A&A 466, 977

Stäuber, S. & Bruderer, S. 2009, A&A 505, 195

Sternberg, A. & Dalgarno, A. 1995, ApJS 99, 565

Stone, J. M., Ostriker, E. C. , Gammie, C. F. 1998, ApJL 508, L99

Störzer, H., Stutzki, J., & Sternberg, A. 1995, A&A, 296, L9

Stutzki, J., Stacey, G. J., Genzel, R. et al. 1988, ApJ 332, 379

Swings, P. & Page, T. 1950, ApJ, 111, 530

Tercero, B.; Cernicharo, J.; Pardo, J. R.; & Goicoechea, J. R., 2010, A&A 517, A96

Thi, W.-F., Ménard, F., Meeus, G., et al. 2011, A&A, 530, L2

Tielens, A. G. G. M. et al. 1993, Science 262, 86

Tielens, A. G. G. M. 2005, The Physics and Chemistry of the Interstellar Medium (1st ed.; Cambridge: Cambridge Univ. Press)

Troscompt, N., Faure, A., Wiesenfeld, L., Ceccarelli, C. & Valiron, P. 2009, A&A 493, 687

Tsujimoto, M., Hosokawa, T., Feigelson, E. D., Getman, K. V., & Broos, P. S. 2006, ApJ, 653, 409

Turner, B. E. 1991, ApJS, 76, 617

Turner, B. E. 1992, ApJ 396, L107

Turpin, F.; Stoecklin, T.; Voronin, A. 2010, A&A 511, 28

Van Dishoeck, E. F., & Black, J. H. 1986, ApJS, 62, 109

Van der Tak, F. F. S., in IAU Symposium. (2011), pp. 449

Van der Tak, F. F. S., Black, J. H., Schöier, F. L., Jansen, D. J., & van Dishoeck, E. F. 2007, A&A, 468, 627

Van der Tak, F. F. S., Ossenkopf, V., Nagy, Z., et al. 2012, A&A, 537, L10

Van der Tak, F.F.S., Van Dishoeck, E.F. and Caselli, P. 2000, A&A 361, 327

Van der Tak, F. F. S. & van Dishoeck, E. F. 2000, A&A, 358, L79

Van der Werf, P. P., Goss, W. M., & O'Dell, C. R. 2013, ApJ 762, 101

Van der Werf, P. P., Isaak, K. G., Meijerink, R., et al. 2010, A&A, 518, L42

van der Werf, P., Stutzki, J., Sternberg, A., & Krabbe, A. 1996, A&A, 313, 633

Van der Wiel, M. H. D., & Shipman, R. F. 2008, A&A 490, 655

Van der Wiel, M. H. D., van der Tak, F. F. S., Ossenkopf, V., et al. 2009, A&A, 498, 161

Van der Wiel, M. H. D. 2011, PhD thesis, Univ. Groningen

Van Leeuwen, F. 2007, A&A, 474, 653

Van Zadelhoff, G.-J., Dullemond, C. P., van der Tak, F. F. S. et al. 2002, A&A, 395, 373

Vastel, C., Spaans, M., Ceccarelli, C., Tielens, A. G. G. M., & Caux, E. 2001, A&A 376, 1064

Walmsley, C. M., Natta, A., Oliva, E., & Testi, L. 2000, A&A, 364, 301

Ward-Thompson, D. & Robson, E. I. 1990, MNRAS 244, 458

Weiß, A., Requena-Torres, M. A., Güsten, R., et al. 2010, A&A, 521, L1

Welch, W. J., Dreher, J. W., Jackson, J. M., Terebey, S., & Vogel, S. N. 1987, Science, 238, 1550

Werner, H.-J., Rosmus, P., & Reinsch, E.-A. 1983, J. Chem. Phys., 79, 905

Williams, J. A., Dickel, H. R., & Auer, L. H. 2004, ApJS, 153, 463

Wilner, D. J., De Pree, C. G., Welch, W. J. & Goss, W. M. 2001, ApJ 550, L81

Wilson, T., L.; Muders, D.; Dumke, M. et al. 2011, ApJ 728, 61

Wilson, T. L., & Rood, R. 1994, ARA&A, 32, 191

Woodall, J., Agúndez, M., Markwick-Kemper, A. J., & Millar, T. J. 2007, A&A, 466, 1197

Wu, J., Evans, N. J., II, Shirley, Y. L., & Knez, C. 2010, ApJS, 188, 313

Wyrowski, F.; Schilke, P.; Hofner, P. & Walmsley C. M., 1997, ApJ, 487, L171

Wyrowski, F., Menten, K. M., Güsten, R., & Belloche, A. 2010, A&A, 518, A26

Yorke, H. W. & Sonnhalter, C., 2002, ApJ 569, 846

Young Owl, R. C., Meixner, M. M.,Wolfire, M., Tielens, A. G. G.M., & Tauber, J. 2000, ApJ, 540, 886

Zapata, L. A., Ho, P. T. P., Rodríguez, L. F. et al. 2006, ApJ 653, 398

Zapata, L. A., Rodríguez, L. F., Ho, P. T. P. et al. 2005, ApJ, 630, L85

Zinnecker, H. & Bate, M. R. 2002, Hot StarWorkshop III: The Earliest Stages of Massive Star Birth, ASP Conf. Proc., Vol. 267. San Francisco: ASP

Zinnecker, H. & Yorke, H. W. 2007, Annu. Rev. Astron. Astrophys. 45, 481

Ziurys, L. M. and Snell, R. L. and Dickman, R. L. 1989, ApJ341, 857

Zhu, M., Seaquist, E. R. & Kuno, N. 2003, ApJ 588, 243

Acknowledgments

This thesis is the result of four years of work in Groningen. This work was done in collaboration with many colleagues whom I wish to acknowledge here.

Most of the work was done in collaboration with my promotor ***Floris van der Tak***, and involves quite some time spent on discussing the project at various stages. *Floris, thank you for all your time in the past four years. But most of all, thank you for the opportunity to be able to get involved in a research that I liked so much that I will continue in the future.*

The part of this thesis I enjoyed working on the most was my Orion Bar work, which was done in collaboration with ***Volker Ossenkopf***. *Volker, thank you for your contributions over the past few years. I am looking forward to working with you in Cologne from October.*

I thank all the other members of the 'Orion Bar team' who contributed to my project: ***Ted Bergin***, ***John Black***, ***Alexandre Faure***, ***Maryvonne Gerin***, ***Javier Goicoechea***, ***Christine Joblin***, ***Jacques Le Bourlot***, ***Franck Le Petit***, ***Zoltán Makai***, and ***Markus Röllig***.

I thank many members of the HEXOS team for useful discussions related to both science and data reduction. I thank ***Ted Bergin***, ***Rene Plume***, and ***Volker Tolls*** for their contribution to my chapter on Orion S.

My very first project and paper was about W49A, in collaboration with ***Gary Fuller***, ***Rene Plume***, and ***Marco Spaans***. *Gary, Rene, and Marco - thank you for all your advices, you made my first paper writing experience much easier.*

I thank the members of my reading committee, ***Maryvonne Gerin***, ***Inga Kamp***, and ***Gary Fuller***, for their careful reading of this thesis and for many useful comments.

I thank my Kapteyn/SRON and Leiden colleagues for many interesting science discussions during group meetings and other occasions, especially to ***Yunhee Choi***, ***Frank Helmich***, ***Evgenia Koumpia***, ***Matthieu Marseille***, ***Ke Wang***, ***Kuo-Song Wang***, and ***Matthijs van der Wiel***. I am very grateful to ***Andrey Baryshev*** for translating my thesis summary into Dutch.

Köszönöm ***Frey Sándor***nak, hogy átolvasta a magyar nyelvű összefoglalómat.

Most of this thesis is based on data from *Herschel*/HIFI. I thank the members of the HIFI ICC and the data reduction team of the HEXOS key program for their help with my data reduction related questions.

This work was funded by both the Kapteyn Astronomical Institute of the University of Groningen and SRON. I thank for the - secretarial, computer, etc. - support in the past four years. Additional travel funding from LKBF is acknowledged.

A legnagyobb köszönet a családomat illeti: Nélkületek tényleg nem tudtam volna végigcsinálni az elmúlt négy évet.